

# THE BELL SYSTEM TECHNICAL JOURNAL

Volume 47

May-June 1968

Number 5

Copyright © 1968, American Telephone and Telegraph Company

## The Design of Active Distributed Filters

By ROBERT E. PARKIN

(Manuscript received July 13, 1967)

*We develop a synthesis method which leads to simple realizations of low-pass and high-pass active filters using distributed resistance-capacitance networks. In the low-pass filter there is one distributed network terminated, through a negative impedance converter, in a load consisting of a lumped network or another distributed network. Thus we can obtain a Chebyshev-like low-pass filter which has a faster cutoff than a four pole Chebyshev realization with the same ripple. In the high-pass filter design an additional feedback element is involved. We can obtain a complex pole pair to be placed anywhere in the complex frequency plane except the real frequency axis. Design charts are given.*

### I. INTRODUCTION

In a recent book, P. M. Chirlian covers the main filter synthesis techniques using distributed resistance-capacitance networks.<sup>1</sup> This paper takes a more practical design-oriented approach. Consistent with the original terminology of Wyndrum,<sup>2</sup> we call the uniform distributed RC network  $\overline{\text{URC}}$ . The aim here is to design active distributed filters with minimal circuit element complexity. We consider the two basic types of  $\overline{\text{URC}}$  shown in Figure 1, the single  $\overline{\text{URC}}$ , and the common ground high-pass double  $\overline{\text{URC}}$ . The low-pass filters are synthesized with a single  $\overline{\text{URC}}$  and a Linvill realization<sup>3</sup> and the high-pass filters by a common ground high-pass double  $\overline{\text{URC}}$  and a Yanagisawa realization.<sup>4</sup>

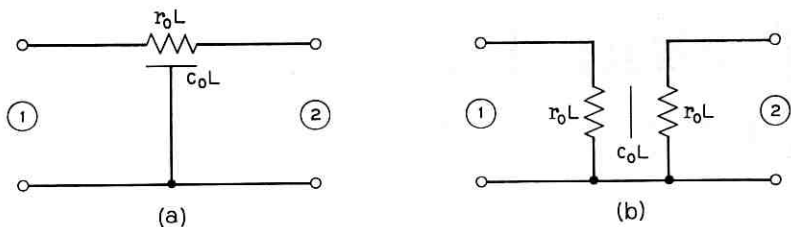


Fig. 1—The circuit symbols for (a) the single D.C.R. and (b) the cross-connected double D.C.R.

II. THE LOW-PASS FILTER DERIVATION

2.1 The Poles of the Transfer Function

The transfer function for the circuit shown in Figure 2(a) can be shown to be<sup>5</sup>

$$\frac{V_2}{V_1} = \frac{1}{\cosh \theta - y_{NL} \frac{\sinh \theta}{\theta} + z_{NS}(\theta \sinh \theta - y_{NL} \cosh \theta)} \quad (1)$$

where

$$\begin{aligned} \theta &= \sqrt{pr_0c_0L^2}, \\ y_{NL} &= r_0Ly_L, \\ z_{NS} &= z_S/r_0L, \end{aligned}$$

$r_0$  is the resistance per unit length,  $c_0$  is the capacitance per unit length,  $L$  is the length of the network, and  $p$  is the complex frequency variable.

If  $z_S = 0$ , the poles are given by

$$y_{NL} = \frac{\theta}{\tanh \theta} \quad (2)$$

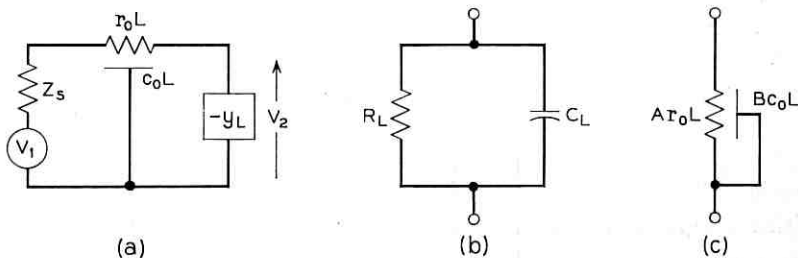


Fig. 2—The basic low-pass filter circuit.

Notice that since  $p = k\theta^2$ , the negative real axis in the  $p$  plane is the imaginary axis in the  $\theta$  plane.

## 2.2 Lumped Load

If the load  $y_L$  is the RC combination shown in Figure 2(b), and if  $\theta = x + jy$ , equation (2) becomes

$$y_{NL} \equiv \frac{1}{U} + (x + jy)^2 W = \frac{x + jy}{\tanh(x + jy)} \quad (3)$$

where

$$U = \frac{R_L}{r_0 L} \quad \text{and} \quad W = \frac{C_L}{c_0 L}.$$

An infinity of roots of equation (3) lie on the  $j$  axis of the  $\theta$  plane for any  $U$  or  $W$ , and these poles are free to move<sup>6</sup> a maximum distance of  $\pi$ . When  $W = 0$  (the case of resistive loading) the dominant pole pair in the  $\theta$ -plane can lie at  $\pm j\pi$  when  $U = 0$ , can move to the origin when  $U = 1$ , or move along the real axis towards  $\pm \infty$  as  $U \rightarrow 0$ .

If  $U = \infty$ ,

$$W = \frac{1}{\theta \tanh \theta} \quad (4)$$

and a pole pair caused by the capacitance loading, the loading pole pair, lies on the real axis in the  $\theta$ -plane for  $W > 0$ . As  $W \rightarrow 0$ , the loading poles tend to  $\pm \infty$  and in the limit  $W = 0$  do not cause instability.

It is possible to choose values for  $U$  and  $W$  so that the unbounded loading and dominant poles can combine and produce roots of equation (3) for  $x$  and  $y$  nonzero. The graph of  $U$  and  $W$  for values of  $x$  and  $y$  nonzero is given in Figure 3.

The stability plot of  $U$  and  $W$  is shown in Figure 4; the plane of reference is the  $p$  plane.

Feeding the URC by a current source, the poles of  $V_2/I_1$  can be shown to be<sup>5</sup>

$$y_{NL} = \theta \tanh \theta. \quad (5)$$

Again, there is a unique solution of equation (5) for  $x$  and  $y$  nonzero. For the load considered previously, the solution of equation (5) is given in Figure 5.

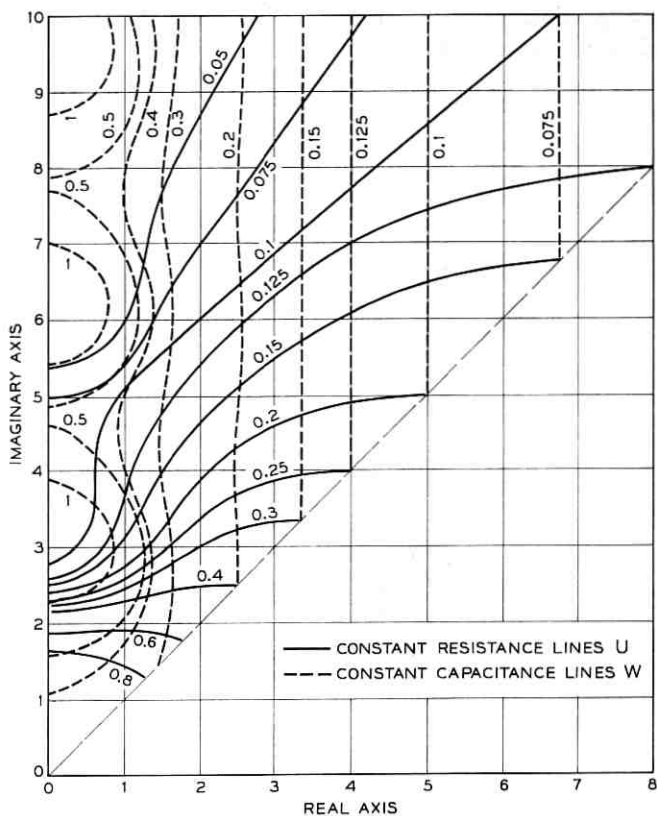


Fig. 3.—The values of  $U$  and  $W$  for complex poles at  $\vartheta = x + jy$  when  $z_s = 0$ .

### 2.3 Distributed Load

If load  $y_L$  in Figure 2(a) is the shorted  $\overline{\text{URC}}$  shown in Figure 2(c), for  $z_s = 0$  the transfer function is given by

$$\frac{V_2}{V_1} = \frac{1}{\cosh \theta - \frac{\sqrt{B/A} \sinh \theta}{\tanh(\sqrt{AB} \cdot \theta)} + \theta \cdot z_{NS} \left[ \sinh \theta - \frac{\sqrt{B/A} \cosh \theta}{\tanh(\sqrt{AB} \cdot \theta)} \right]} \quad (6)$$

where  $Ar_0$  and  $Bc_0$  are the resistance and capacitance per unit length of the load.

When  $z_s = 0$ , the poles are given by

$$\tanh \theta = \sqrt{A/B} \cdot \tanh (\sqrt{AB} \cdot \theta). \quad (7)$$

It is possible by suitable choice of  $A$  and  $B$  to place a pole anywhere in the  $\theta$  plane. In addition, depending on the values taken by  $A$  and  $B$ , more than one complex pair of roots can occur for  $x$  and  $y$  nonzero, but no matter what values  $A$  and  $B$  assume, positioning one complex pole pair fixes all the poles of the system. When a root is positioned near the  $x = y$  line in the  $\theta$  plane with all other roots in the stable region, to obtain an equiripple filter, the other complex roots (if they occur) are close to the  $x = 0$  line.

The solution of equation (7) for the section of the  $\theta$ -plane near the  $x = 6$  line is shown in Figure 6.

### III. LOW-PASS FILTER DESIGN CHARTS

#### 3.1 Lumped Load

From equation (1) and the load of Figure 2b, it can be seen that the position of the complex pole is determined by  $U$ ,  $W$ , and  $z_{NS}$ . By choosing these three factors, the ripple in the passband is fixed. When

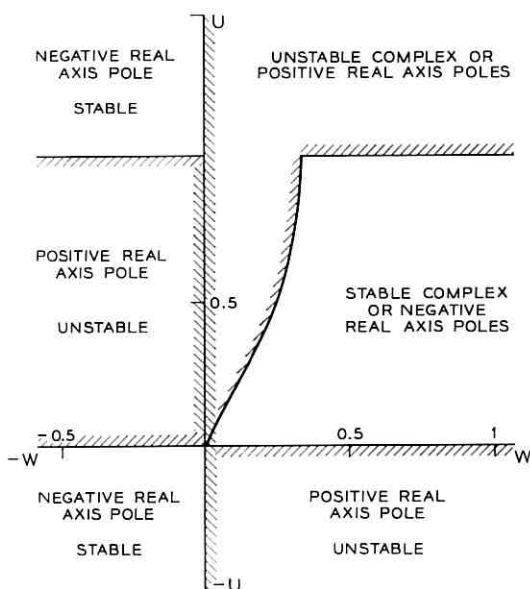


Fig. 4 — Stability plot of the low-pass lumped load filter when  $z_s = 0$ .

the ripple is small the complex pole pair is near the origin. When the ripple is large the complex pole pair is a long way from the origin and close to the  $x = y$  line, the  $j\omega$  axis in the  $p$  plane. The design chart of Figure 7 was obtained by setting  $\theta = x + j(x + \delta x)$  for some value of  $z_{NS}$ , where  $\delta x$  is small, and determining  $U$  and  $W$  for this condition. With  $W$  held constant,  $U$  was decreased until equiripple conditions were achieved. This was repeated for a complete range of values  $x$  and  $z_{NS}$ . In addition, Figure 7 shows the conditions for constant  $p_c$ , where  $p_c$  is the 3 dB cutoff frequency.

### Example

Suppose it were required to synthesize a low-pass filter with a fast cutoff having a 3 dB cutoff frequency of 75 kHz, source resistance of

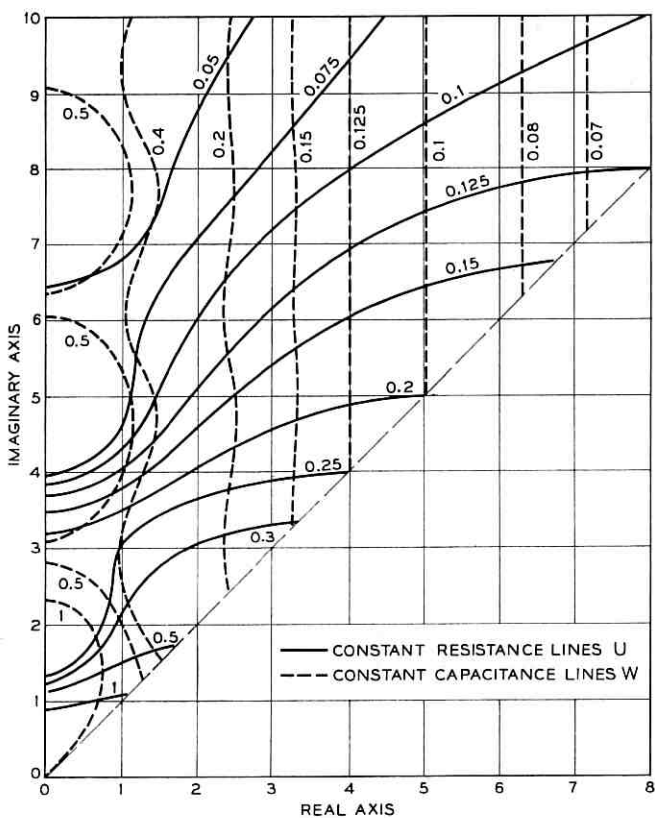


Fig. 5 — The values of  $U$  and  $W$  for complex poles at  $\theta = x + jy$  when  $z_s = \infty$ .

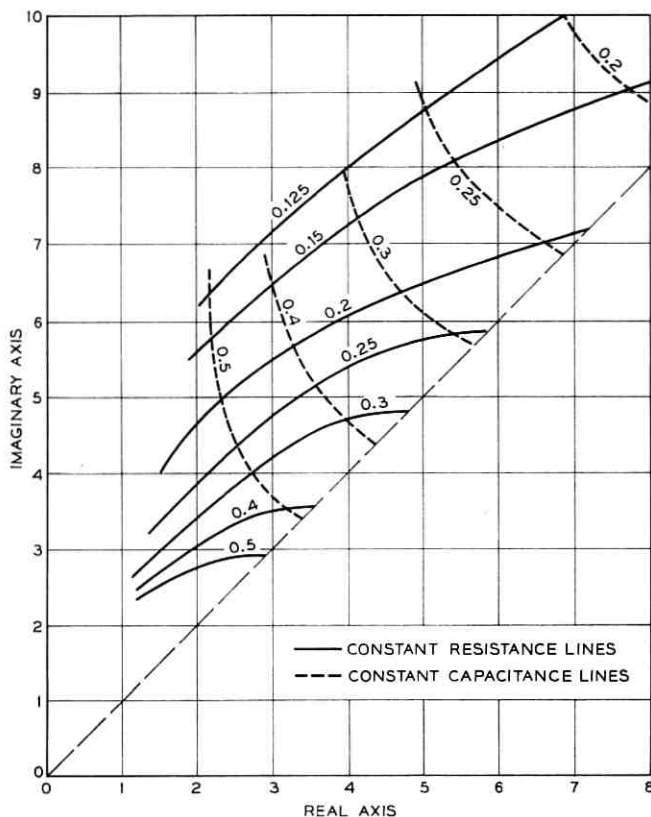


Fig. 6—The values of  $A$  and  $B$ , the distributed load factors, for complex poles at  $\theta = x + jy$  when  $z_s = 0$ .

$5K \Omega$  and working into another circuit with a driving point resistance of  $10K \Omega$ , and the maximum ripple tolerated in the passband is to be 1 dB.

If  $p_c$  is the normalized cutoff frequency,

$$r_0 L c_0 L = \frac{p_c}{7.5 \times 10^4},$$

and

$$z_{N.S} = \frac{5 \times 10^3}{r_0 L}.$$

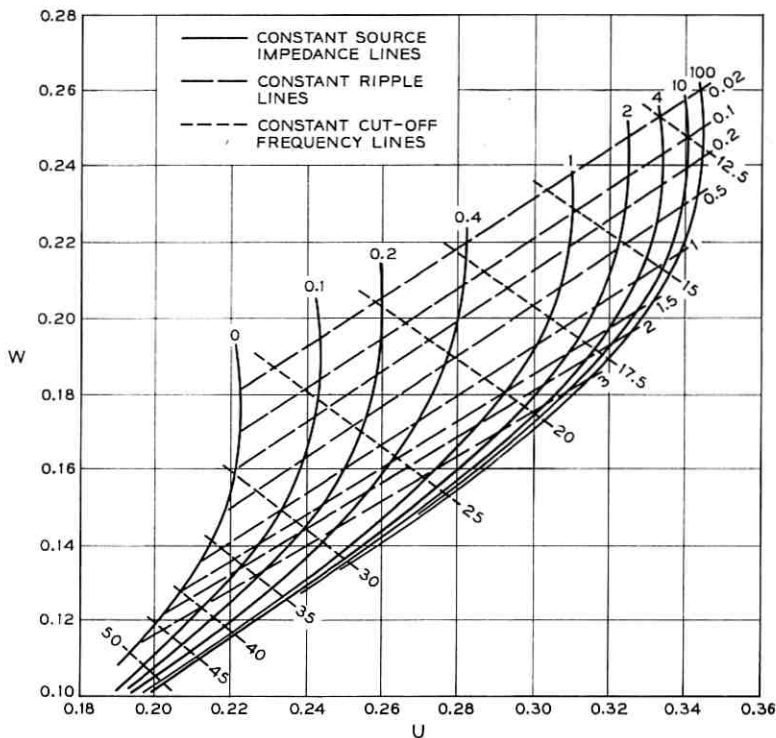


Fig. 7—The lumped load low-pass filter design chart.

One factor can now be chosen from Figure 7,  $z_{NS}$ ,  $r_oL$ , or  $c_oL$ . Letting  $r_oL = 5 \times 10^4$ , then

$$z_{NS} = 0.1$$

$$p_c = 30 \text{ Hz}$$

$$U = 0.2335$$

$$W = 0.150$$

Thus  $c_oL = 8260$  pF. The value  $U$  is the total normalized resistor load comprising  $R_L$  and the  $10\text{K } \Omega$  driving point impedance of the next stage. The realization of the circuit is shown in Figure 8. The theoretical and measured frequency responses of this circuit are shown in Figure 9; notice the close correlation between the two. The negative impedance converter used in making the measurements is

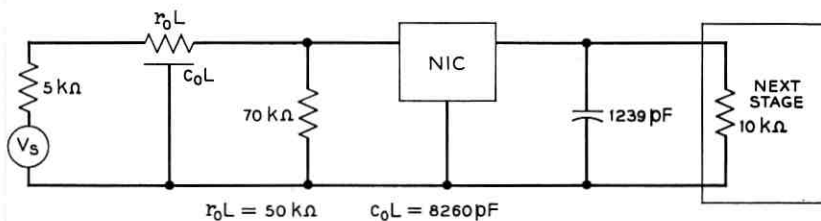


Fig. 8 — A low-pass filter circuit having lumped loading.

the NIC of Drew and Gorski-Popiel.<sup>7</sup> The rate of fall of the response at cutoff is 20.75 dB per octave, and the rate at the 10 dB point is 26.4 dB per octave.

### 3.2 Distributed Load

The design procedure proceeds as before, by placing the complex pole on the  $x = y$  line and increasing  $A$  until equiripple conditions

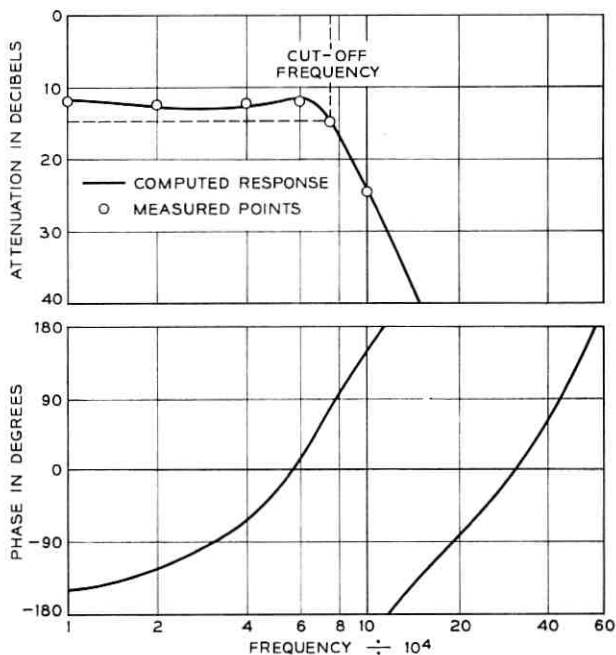


Fig. 9 — The response of the filter circuit of Fig. 8.

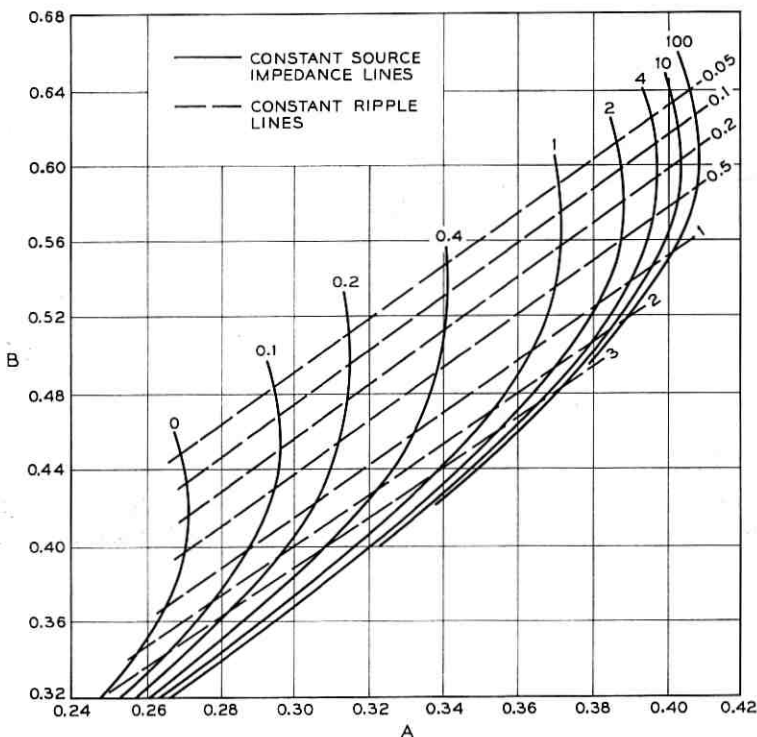


Fig. 10 — The distributed load low-pass filter design chart.

are achieved. The poles of the transfer function are given by

$$\frac{\sqrt{B/A}}{\tanh(\sqrt{AB} \cdot \theta)} = \frac{(\cosh \theta + \theta \cdot \sinh \theta \cdot z_{NS})}{(\sinh \theta + \theta \cdot \cosh \theta \cdot z_{NS})} = \alpha + j\beta. \quad (8)$$

If  $(AB)^{1/2} \cdot \theta = x' + jx''$ , the left side of equation (8) can be split into real and imaginary parts, so that

$$\frac{\alpha}{\beta} = -\frac{\sinh x' \cosh x''}{\sin x' \cos x''}. \quad (9)$$

Thus  $(AB)^{1/2} \cdot \theta$  is calculated, and substituting in equation (8),  $A$  and  $B$  are known explicitly.

Figure 10 shows the design chart for a low-pass filter with distributed load. It was found that  $p_c$  was independent of  $A$  for any value of  $B$ , so that cutoff frequency lines were not shown in Figure 10 but were given in Figure 11.

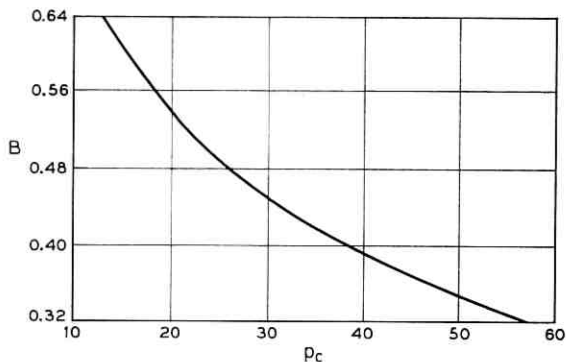


Fig. 11 — The relation between  $p_e$  and  $B$ .

*Example*

Using the low-pass filter with distributed load to synthesize a filter having the same requirements as in the previous example, but this time neglecting the effect of loading of the next stage, then

$$\begin{aligned}
 A &= 0.323, \\
 B &= 0.446, \\
 z_{NS} &= 0.33, \\
 r_0L &= 1.514 \times 10^4, \\
 c_0L &= 0.0274 \mu\text{f},
 \end{aligned}$$

for  $p_e = 31$  Hz. The circuit is given for this filter in Figure 12. The measured and theoretical frequency responses are given in Figure 13. Again, notice the close correlation between the theoretical and measured frequency response. The slope of the response at cutoff is 21 dB per octave, and at the 10 dB point it is 26.75 dB per octave.

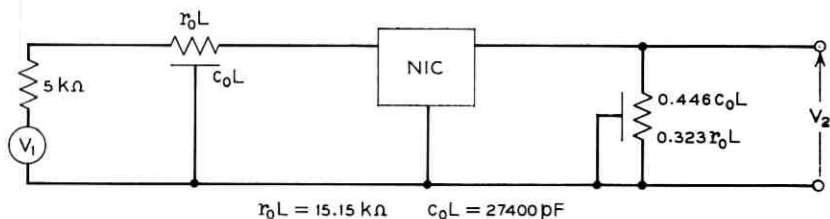


Fig. 12 — A low-pass filter circuit having distributed loading.

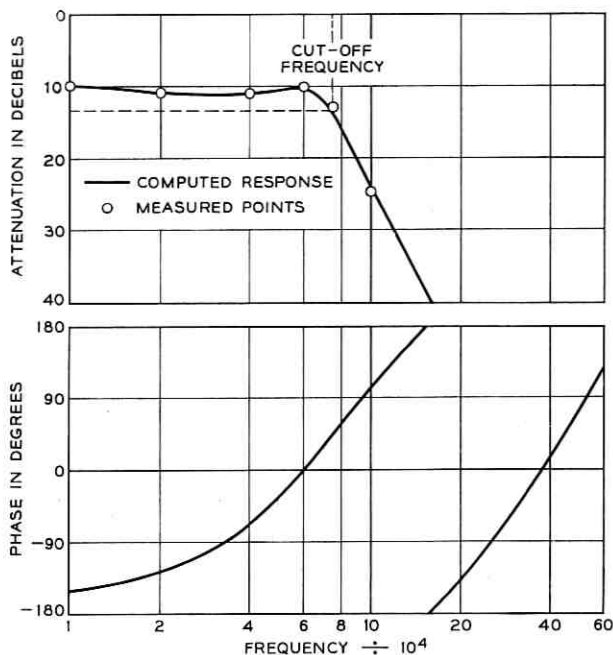


Fig. 13 — The response of the filter circuit of Fig. 12.

### 3.3 Elimination of Inband Loss

The inband loss obtained in the examples of Sections 3.1 and 3.2 can be eliminated or set to any value required by adjustment of the active device. For instance, if  $-y_L$  is realized by  $y_L$  and a current inversion negative impedance converter described by

$$v_{IN} = kv_{out}$$

$$i_{IN} = ki_{out},$$

the equivalent form of equation (1) for  $z_s = 0$  is given by

$$\frac{V_2}{V_1} = \frac{1}{k \left( \cosh \theta - \frac{y_{NL} \cdot \sinh \theta}{\theta} \right)}$$

$k$  is the factor controlling the inband loss.

IV. THE HIGH-PASS FILTER

4.1 Transfer Function Singularities

The parameters of the common ground high-pass URC have been developed by Hager.<sup>8</sup> Imbedding this element with the current negative impedance converter (current NIC) and  $y_A - y_B$  networks as shown in Figure 14, the transfer function can be found as

$$\frac{V_2}{V_1} = \frac{\frac{\Psi}{\tanh \Psi} - 1 - 2y_{NA}}{2y_{NA} + 2y_{NB} - 1 - \frac{\Psi}{\tanh \Psi} + z_{NS} \left[ y_{NB} \left( 1 + 2y_{NA} + \frac{\Psi}{\tanh \Psi} \right) - \frac{2\Psi}{\tanh \Psi} \right]} \quad (10)$$

where

$$\Psi = \sqrt{2pr_0c_0L^2}.$$

Notice that replacement of the current NIC by a voltage NIC does not yield the same result.<sup>5</sup> It can be seen from Equation (10) that the loss at high frequencies is zero if and only if  $z_S \rightarrow 0$  as  $p \rightarrow \infty$ .

When  $z_S = 0$ , the poles of equation (10) are given by

$$y_{NB} = \frac{1}{2} + \frac{\Psi}{2 \tanh \Psi} - y_{NA} \quad (11)$$

and the zeros by

$$y_{NA} = \frac{1}{2} \left( \frac{\Psi}{\tanh \Psi} - 1 \right), \quad (12)$$

where

$$y_{NA} = r_0Ly_A \quad \text{and} \quad y_{NB} = r_0Ly_B.$$

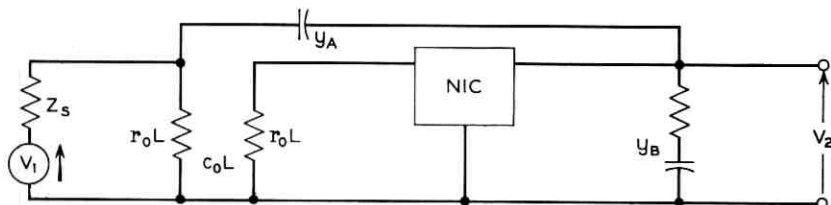


Fig. 14—The basic high-pass filter circuit.

## 4.2 Lumped Load and Feedback

If  $y_A$  and  $y_B$  have the form shown in Figure 14, for a second order zero at the origin, equation (10) yields

$$\frac{\Psi \left( 1 + \frac{\Psi^2}{2!} + \dots \right)}{\left( \Psi + \frac{\Psi^3}{3!} + \dots \right)} - 1 - \Psi^2 W_F = 0 \quad (13)$$

where  $W_F = y_A / (pc_0L)$ .

Letting  $\Psi \rightarrow 0$  in equation (13),  $W_F = 1/3$ . Substituting in equation (11)

$$y_{NB} = \frac{1}{2} + \frac{\Psi}{2 \tanh \Psi} - \frac{\Psi^2}{3}. \quad (14)$$

There is a unique solution of equation (14) for  $x$  and  $y$  nonzero, when  $x + jy = \Psi$ .

## 4.3 Distributed Load and Feedback

The common ground high-pass  $\overline{\text{URC}}$  is still used as the central filtering element in this high-pass filter, but the lumped elements are replaced by  $\overline{\text{URCs}}$  as shown in Figure 15. Substituting for  $y_{NA}$  and  $y_{NB}$  in equation (10), and for  $z_{NS} = 0$ ,

$$\frac{V_2}{V_1} = \frac{\frac{\vartheta}{\tan \vartheta} - 1 - \left[ \frac{\Psi}{\frac{1}{\tanh \Psi} + \frac{\cosh \Psi - 1}{\cosh \Psi + 1} A} \right]}{A \left( \cosh \Psi + \frac{\sinh \Psi (\cosh \Psi + 1)}{\cosh \Psi + 1} \right) - 1 - \frac{\vartheta}{\tanh \vartheta} - \frac{4\nu \sinh \nu}{\alpha(\nu \sinh \nu + 2(\cosh \nu + 1))}} \quad (15)$$

where

$$\vartheta = \sqrt{2pr_0c_0L^2}$$

$$\Psi = \sqrt{2pAr_0Bc_0L^2} = \sqrt{AB} \cdot \vartheta$$

$$\nu = \sqrt{2p\alpha r_0\beta c_0L^2} = \sqrt{\alpha\beta} \cdot \vartheta$$

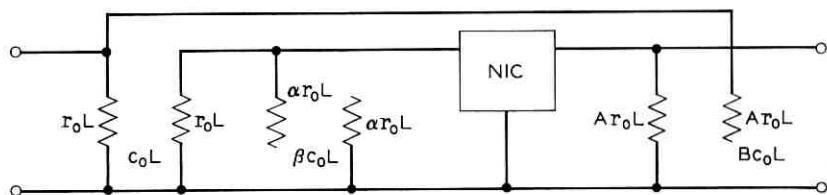


Fig. 15 — The completely distributed high-pass filter circuit.

For second order zeroes to occur at the origin,  $B = 1/3$ .  
Notice the similarity to the previous result.

#### V. HIGH-PASS FILTER DESIGN

A high-pass filter can be realized from the circuit of Figure 14 by replacing  $y_B$  with a resistor  $R_L$  and capacitor  $C_L$  in series, and  $y_A$  by a capacitor. Unfortunately, to place the complex poles where required could require  $R_L > 0$ ,  $C_L < 0$ . To make  $C_L > 0$ , connect another resistor  $R_1$  on the other port of the NIC.

To assess the best position for the complex poles, three factors can be used which, when minimized simultaneously, produce desirable properties in the filter.

- (i) Make the slope at cutoff as near as possible to 12 dB per octave, the low-frequency rate of change of attenuation.
- (ii) Make the difference between the frequency at which the response crosses the constant attenuation line passing through the high-frequency attenuation, and the frequency at which a 12 dB per octave line drawn at the cut-off point would cross the high-frequency line, a minimum.
- (iii) Make the overshoot a minimum.

These three factors are shown in Figure 16, where  $G_1 = 12$ , the slope of the response line at cutoff in dB per octave,  $G_2 =$  the frequency at which the response attenuation is equal to the high-

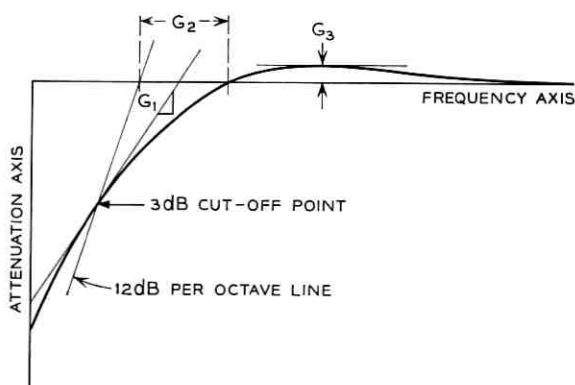


Fig. 16 — Three factors governing the quality of the high-pass filter.

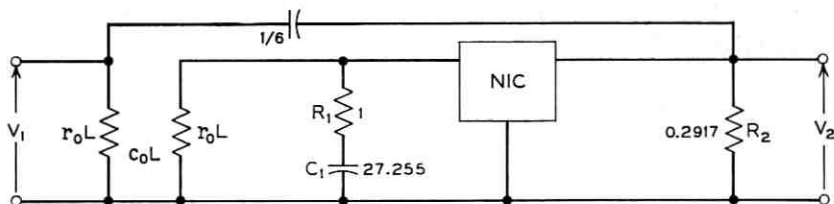


Fig. 17 — A lumped load and feedback high-pass filter.

quency attenuation  $-1.25 \times$  (cutoff frequency), and  $G_3 =$  peak overshoot. Combining these three factors together as

$$G = G_1 + G'_2 + G_3$$

where

$$G'_2 = \frac{40G_2}{1.25 \times (\text{cutoff frequency})}$$

and minimizing  $G$ , the best filter under these circumstances if  $z_s = 0$  and the overshoot is limited to 1.25 dB, is shown in Figure 17. The response of this filter is shown in Figure 18. Notice that  $G'_2$  is slightly

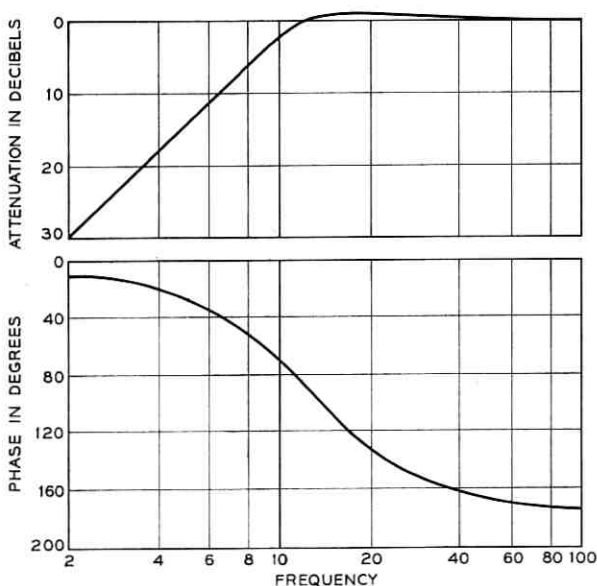


Fig. 18 — The response of the circuit of Fig. 16.

modified to  $G'_2$  to normalize for the cutoff frequency, and to introduce a loading factor.

#### VI. CONCLUDING REMARKS

It is evident that for best filtering characteristics, the  $\overline{\text{URC}}$  must be connected to use its transmission line properties. The low pass filters use a  $\overline{\text{URC}}$  as a transmission line, and the negative-valued loads serve merely to boost the high-frequency responses and extend the cutoff frequencies in a way not unlike that employed in video amplifiers, where an inductor is often used to compensate the high-frequency capacitive drop in the response.<sup>9</sup>

The completely distributed low-pass filter has a faster cutoff than the partially distributed filter. The difference in response is caused by the slightly different noncomplex pole positions near the origin; the further away the first negative real axis pole in the  $p$  plane is from the origin, and so closer to the other noncomplex poles, the further away the complex poles must be from the origin and nearer the limit of stability line to obtain an equiripple filter. Thus, the cutoff frequency is higher, the effect of the nondominant poles lying on the negative real axis of the  $p$  plane on the transfer function at frequencies about cutoff is more pronounced, and a faster cutoff results.

For frequencies up to the 20 dB point, to obtain an equivalent response to that of the distributed low-pass filter in lumped circuitry, would require at least five resistors and five capacitors.

To improve the response of the high-pass filters would require a higher order zero at the origin than the second order zero now obtained. Until this is achieved with a minimum of active devices, the distributed high-pass filters of the type considered here will show less promise than the low-pass filters.

Sensitivity has not been considered in this paper; to do justice to the subject would require a depth of study sufficient to warrant another paper. However, for the low-pass filters, the information contained in Figures 7 and 10 could provide a basis for future sensitivity studies.

#### REFERENCES

1. Chirlian, P. M., *Integrated and Active Network Analysis and Synthesis*, New York: Prentice-Hall, 1967.
2. Wyndrum, R. W. Jr., "The Exact Synthesis of Distributed RC Networks,"

- N. Y. U. Technical Report 400-76, (May 1963). Abbreviated version, "The Realization of Monomorphic Thin Film Distributed RC Networks" IEEE Conv. Record, 1965, part 10, pp. 90-95.
3. Linvill, J. G., "RC Active Filters," Proc. IRE, Vol. 42, March 1954, pp. 555-564.
  4. Yanagisawa, T., "RC Active Networks Using Current Inversion Type Negative Impedance Converters," IRE Trans. Circuit Theory, *CT-4*, No. 3 Linvill (September 1957), pp. 140-144.
  5. Castro, P. S. and Happ, W. W., "Distributed Parameter Circuits and Microsystems Electronics," Proc. Nat. Elec. Conf., Chicago, Ill., 16 (October 1960), pp. 448-460.
  6. Parkin, R. E., "Approximations to the Equations Describing Distributed RC Networks," IEEE Trans. Circuit Theory, *CT-12*, No. 4 (December 1965), pp. 598-601.
  7. Drew, A. J. and Gorski-Popiel, J., "Directly Coupled Negative Impedance Converter," Proc. IEEE, 111, No. 7 (July 1964), pp. 1282-1283.
  8. Hager, C. K., "Network Design of Microcircuits," Electronics, September 4, 1959, pp. 44-49.
  9. Terman, F. E., *Electronic and Radio Engineering*, New York: McGraw-Hill, 1955, p. 292.

# Design of Monopulse Antenna Difference Patterns with Low Sidelobes\*

By E. T. BAYLISS

(Manuscript received August 9, 1967)

*The flexibility of modern monopulse radar antenna systems makes possible the independent optimization of sum and difference patterns. The two parameter difference pattern, developed here for the circular aperture antenna, is designed to have nearly equal sidelobes similar to those of the Taylor sum pattern. The difference pattern is asymptotic to a model difference pattern which has the greatest slope (angle sensitivity) for a given sidelobe level. The model function is unrealizable because it has uniform sidelobes which are infinite in extent. The two parameter difference pattern is realizable and is expressed in a Fourier-Bessel series of  $N$  terms in a manner similar to Taylor's treatment of the sum pattern. The other parameter,  $A$ , controls sidelobe level.*

*Comprehensive tables of the Fourier-Bessel coefficients are given for both the circular aperture series and the difference pattern series. Directivity and angle sensitivity are investigated and found to have maximum values that decrease as sidelobe level decreases. The monopulse system performance using the asymptotic difference pattern and the Taylor sum pattern compares favorably with a maximum likelihood angle estimation system. Development of a line source difference pattern is presented in the appendix.*

## I. INTRODUCTION

Monopulse radar systems have, in recent years, achieved a high degree of flexibility in their antenna patterns. This flexibility is the result of development of multihorn feed structures and array antennas. It now appears feasible to optimize independently the sum and difference patterns of the monopulse system. A good deal of work has been done to improve the sidelobe performance for sum beam pat-

\* This work was supported by the Army Materiel Command under Contract DA-30-069-AMC-333(Y) through the Nike-X Project Office, Redstone Arsenal, Alabama.

terns.<sup>1</sup> However, less attention has been paid to improving the angle sensitivity and sidelobe performance of the circular aperture difference pattern.

The objective of this investigation was to develop a difference pattern which possesses characteristics that are compatible with those of the Taylor sum pattern. Specifically, the goal was to obtain the maximum angle sensitivity commensurate with a given sidelobe level. Low sidelobes are desirable in both sum and difference patterns for the suppression of near-target clutter, ground clutter, and jammers. Requiring large angle sensitivity and low sidelobes for the difference pattern is analogous to requiring a narrow beamwidth and low sidelobes in the case of the sum beam. The pattern that meets these requirements must be produced by a reasonably well behaved aperture illumination.

This paper solves the problem of generating difference patterns by using a technique that parallels Taylor's approach to the sum pattern design. The problem is first detailed in terms of making good angle estimates. It is attacked by applying a general synthesis technique to the approximation of a model difference pattern. Finally, the resulting asymptotic difference pattern is examined for angle sensitivity. Pertinent design information is presented.

## II. THE PROBLEM—ANGULAR ESTIMATION IN NOISE USING ANTENNA DIFFERENCE PATTERNS

A monopulse system can make a maximum likelihood angle estimate<sup>2</sup> under one of the following assumptions:

- (i) The primary source of noise is spatially and temporally uncorrelated noise from the radiation field
- (ii) The primary source of noise is thermal noise which is independent in the sum and difference channels.

The angle estimate is made by correlating the sum and difference channel outputs. The sum and difference patterns required to make the maximum likelihood estimate unfortunately have quite high sidelobes (for example, the difference pattern first sidelobe is only 14.5 dB below the sum beam maximum). For applications where clutter or active noise sources are a problem, such high sidelobes are clearly unacceptable. Techniques used to suppress sidelobes can be expected to reduce the angle sensitivity. (This tradeoff is examined in Section IV.) Thus, the problem is to suppress antenna sidelobes in *both* the

difference and sum patterns without severely degrading the angle sensitivity of the system.

The objective of this paper is to provide a unified approach to difference pattern design for the monopulse system. Specifically, the objectives are to:

(i) Design a difference pattern with equal sidelobes, similar to sidelobes of Taylor sum pattern.

(ii) Solve the practical problem of generating the aperture function for the circular aperture.

(iii) Balance sidelobe level and angle sensitivity to get the best angle sensitivity for a given sidelobe level.

(iv) Compute and tabulate such design parameters as angle sensitivity, directivity, sidelobe level and, of course, the aperture generating functions.

### III. THE SOLUTION—AN ASYMPTOTIC PATTERN FUNCTION WITH UNIFORM SIDELOBE LEVEL

#### 3.1 Aperture and Pattern Functions

The aperture screen concept is very useful in the analysis of planar antennas. It is well known that from the tangential  $\mathbf{E}$  and  $\mathbf{H}$  fields on a surface enclosing a source one can, in principle, calculate the radiated fields. If the enclosing surface is an infinite plane, then some useful simplifications can be made. The equivalence principle and image theory<sup>3</sup> can be used to determine the field in the source-free half-space ( $z > 0$ ) from its tangential components on the plane ( $z = 0$  in Fig. 1). For this special case the  $\mathbf{E}$ -field can be determined solely from the  $\mathbf{E}$ -field on the plane.<sup>3</sup>

Plonsey<sup>4</sup> has pointed out that it is possible to describe the field in the Fraunhofer region for all  $\theta < \pi/2$  where the usual Kirchhoff scalar diffraction approximation<sup>5</sup> is good only for small  $\theta$ .

The aperture and pattern expression can be put in standard form by making the following change of variables:

$$u = \frac{2a}{\lambda} \sin \theta \quad \text{and} \quad p = \frac{\pi}{a} \rho \quad (1)$$

where  $u$  is the angle variable measured in standard beamwidths,  $p$  is the normalized aperture variable and  $a$  is the radius of the antenna, (Fig. 1). It is of interest to consider the case where the vector field

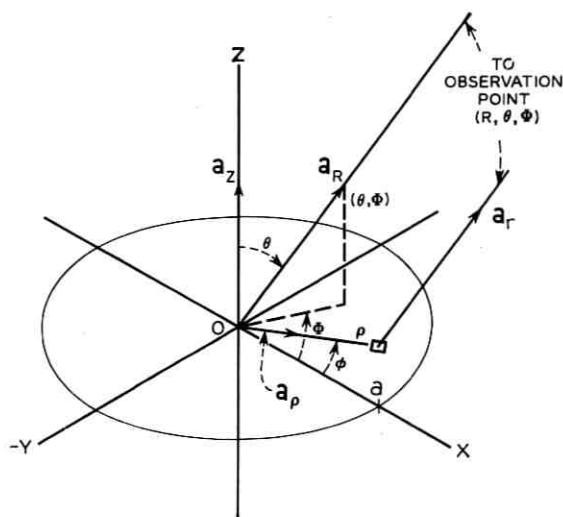


Fig. 1—Aperture geometry.

in the aperture is factorable:

$$\mathbf{E}\left[p, \frac{\pi}{2}, \varphi\right] = \begin{cases} (\mathbf{a}_z + \gamma \mathbf{a}_v)g(p, \varphi); & p \leq \pi \\ 0; & \text{elsewhere} \end{cases} \quad (2)$$

where  $\gamma$  is a complex constant,  $\mathbf{a}_i$  is a unit vector and  $g(p, \varphi)$  is the complex scalar aperture function. Notice for linear polarization,  $\gamma = 0$ , and for circular polarization,  $\gamma = \pm j$ . Under the above assumptions and with the usual Fraunhofer approximations (that is,  $\rho \ll R$ ,  $1 \ll kR$ )

$$\mathbf{E}(R, \theta, \Phi) = \frac{-je^{-ikR}}{kR} \{\mathbf{a}_R \times [\mathbf{a}_z \times (\mathbf{a}_z + \gamma \mathbf{a}_v)]\} \left(\frac{2a}{\lambda}\right)^2 F(u, \Phi); \quad \theta < \frac{\pi}{2} \quad (3)$$

where

$$F(u, \Phi) = \frac{1}{2\pi} \int_0^{2\pi} d\varphi \int_0^\pi g(p, \varphi) \exp[jup \cos(\Phi - \varphi)] p dp. \quad (4)$$

The pattern function,  $F(u, \Phi)$ , which is the Fourier-Hankel transform of the aperture function,  $g(p, \varphi)$ , will be the starting point for the next section.

### 3.2 Synthesis Method for Circular Apertures

The procedure for synthesizing an arbitrary pattern function with a circular aperture is an application of Woodward's technique to the circular aperture synthesis problem.<sup>6</sup>

The aperture function can be represented as a Fourier-Bessel series

$$g(p, \varphi) = \sum_{k=-\infty}^{\infty} \sum_{l=0}^{\infty} a_{kl} e^{ik\varphi} J_k(\mu_{kl}p); \quad p \leq \pi. \quad (5)$$

This series has orthogonality and completeness properties for appropriately chosen  $\mu_{kl}$ . It converges in the mean to an arbitrary aperture function,  $\hat{g}(p, \varphi)$ , when the complex coefficients,  $a_{kl}$ , are found by taking the inner product of the function with each orthogonal function.

The Sturm-Liouville boundary conditions give rise to the eigenvalues for the angular and radial eigenfunctions:

(i) The angular eigenfunctions must satisfy periodic boundary conditions. Thus their eigenvalues are the integers  $k$ .

(ii) The radial eigenfunctions must satisfy one of two cases:

1.  $J_k(\mu_{kl}\pi) = 0$ ;  $\mu_{kl} > 0$ ,  $k \geq 0$ ,  $l = 0, 1, 2, \dots$
2.  $cJ_k(\mu_{kl}\pi) + \mu_{kl}\pi J'_k(\mu_{kl}\pi) = 0$ ;  $c \geq 0$ ,  $c^2 + k^2 > 0$ ,  $\mu_{kl} > 0$  for  $l = 0, 1, 2, \dots$  except when  $c = k = 0$  then  $\mu_{00} = 0$ .

The selection of case 1 or 2 and the constant  $c$  determine the set of positive distinct eigenvalues to be used in the radial eigenfunctions of (5).

The aperture function expansion that allows nonzero boundary values (case 2) is to be preferred in the expansion of equal sidelobe patterns because:

(i) As Taylor<sup>1</sup> has shown, the slowest far sidelobe decay rate results from nonzero boundary values.

(ii) The "central region" ( $|u| < \mu_{kN}$ ) zeros are confined to a smaller region. This means that better sidelobe control can be obtained in the central region for a given main-beam performance and a fixed number of terms,  $N$ .

Thus, choosing case 2, let  $c = 0$ . The synthesis of a difference pattern allows simplification of (5) because of the symmetry required. The difference pattern requires an antiphase aperture [one sign reversal,  $\hat{F}(u, \Phi) = -\hat{F}(u, \Phi + \pi)$ ], thus only first order Fourier components are required ( $k = \pm 1$ ). Thus choosing  $k = 1$ , the boundary conditions reduce to\*

\* Primes denote differentiation with respect to the argument.

$$J'_l(\mu_l \pi) = 0 \quad l = 0, 1, \dots \quad (6)$$

where the  $k$  subscript on  $\mu_{ki}$  has been dropped. See Table I for values of  $\mu_l$ .

To further simplify the choice of coefficients, let the difference axis be  $\varphi = \Phi = 0$ . This requires setting  $a_{li} = -a_{-li} = B_l/2$  and gives

$$\tilde{g}(p, \varphi) = \cos \varphi \sum_{l=0}^{N-1} B_l J_1(\mu_l p); \quad p \leq \pi. \quad (7)$$

The  $N$ -term approximation to the required function  $\tilde{g}$  or  $\tilde{F}$  is designated by a tilde  $\tilde{g}$  or  $\tilde{F}$ . The pattern function expansion corresponding to  $\tilde{g}(p, \varphi)$  in equation (7), that is, transformed by (4), is

$$\tilde{F}(u, \Phi) = j \cos \Phi \sum_{l=0}^{N-1} B_l J_1(\mu_l \pi) \frac{u J'_1(\pi u)}{\mu_l^2 - u^2}. \quad (8)$$

The terms of (8)

$$J_1(\mu_l \pi) \frac{u J'_1(\pi u)}{\mu_l^2 - u^2},$$

are shown in Figure 2.

The pattern function series (8) has the important "sampling" property which many approximation techniques use. If (8) is set equal to the required pattern function,  $\tilde{F}(u, \Phi)$ , at the sample point  $(\mu_m, 0)$  then the  $m$ th coefficient,  $B_m$ , can be evaluated because all other terms of (8) are zero there. Equation (8) is evaluated at  $(\mu_m, 0)$  by applying L'Hôpital's rule, substituting Bessel's equation and the boundary value (6) to obtain

$$\tilde{F}(\mu_m, 0) = B_m j \frac{\pi^2}{2} J_1^2(\mu_m \pi) [1 - (\pi \mu_m)^{-2}]. \quad (9)$$

TABLE I—BESSEL FUNCTION ZEROS,  $J'_l(\mu_l \pi) = 0$

$l$	$\mu_l$	$l$	$\mu_l$	$l$	$\mu_l$	$l$	$\mu_l$
0	0.5860670	5	5.7345205	10	10.7417435	15	15.7443679
1	1.6970509	6	6.7368281	11	11.7424475	16	16.7447044
2	2.7171939	7	7.7385356	12	12.7430408	17	17.7450030
3	3.7261370	8	8.7398505	13	13.7435477	18	18.7452697
4	4.7312271	9	9.7408945	14	14.7439856	19	19.7455093

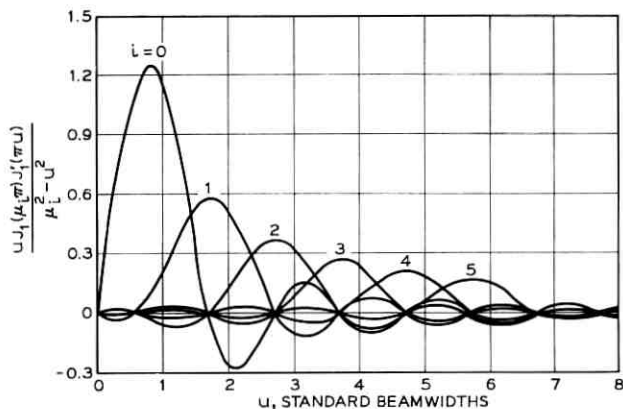


Fig. 2—Bessel series pattern function terms.

Now setting (9) equal to  $\hat{F}(u, \Phi)$  at the sample points, the coefficients of (8) are evaluated

$$B_m = \hat{F}(\mu_m, 0) \frac{2}{j\pi^2} J_1^{-2}(\mu_m \pi) [1 - (\pi \mu_m)^{-2}]^{-1};$$

$$m = 0, 1, 2, \dots, N - 1. \quad (10)$$

In Section 3.4 (10) is used to evaluate the coefficients from sample points on the model function,  $F_M$ , and thus determine the aperture function (7) and pattern function (8).

### 3.3 Construction of a Model Pattern Function

The previous section provides a method of expanding any realizable pattern function. In this section a model difference pattern function is developed. It will serve as a model for the construction of the asymptotic difference pattern in the next section. Thus its role is analogous to Taylor's "ideal function."<sup>1</sup>

The main characteristic desired in a model function is maximum angular sensitivity for a given sidelobe level. It has been shown<sup>7</sup> for an array that the pattern function that produces the greatest angular sensitivity with a given sidelobe level must also have sidelobes of equal height. This theorem is analogous to that proved by Dolph for the sum pattern.<sup>8</sup>

Two important differences occur when the above result for an array is extended to the case of the continuous aperture:

(i) The pattern function has maximum slope for a given sidelobe level (not maximum sensitivity).

(ii) The pattern function is not a realizable antenna pattern.

These two characteristics result from requiring the difference pattern to have sidelobes of equal height. These equal sidelobes now are infinite in extent (for all  $u$ ). Any pattern function whose sidelobes do not decay at least as  $u^{-3/2}$  is not realizable because it requires an unbounded aperture function. Because the function is unrealizable its angular sensitivity is undefined. Nevertheless it does have the maximum slope for a given sidelobe level and will serve as a model function for synthesis of a realizable asymptotic difference pattern in Section 3.4.

Thus, the main characteristics of the model function are:

(i) Maximum slope at the origin for a given peak-to-sidelobe ratio.

(ii) Sidelobes of uniform magnitude and infinite in extent.

Price and Hyneman pointed out that an exact functional form for such a function is not known. What follows is a method for constructing a very close approximation to the equal sidelobe difference pattern function.

The ideal sum pattern used by Taylor<sup>1</sup> is of the form

$$F_{\Sigma}(u) = \cos \pi \sqrt{u^2 - A^2} \quad (11)$$

where  $A$  is a parameter that determines the sidelobe level. This function has equal sidelobes that are infinite in extent. Taking the derivative of the ideal sum pattern a difference pattern is obtained.

$$F_{\Delta}(u) = \pi(u^2 - A^2)^{-1/2} u \sin \pi(u^2 - A^2)^{+1/2}. \quad (12)$$

The first few sidelobes of this function are not of equal height as can be seen from the dashed curves in Figure 3. However, it is possible to modify the first few sidelobes of the above function so that they are equal to the asymptotic sidelobe level. The zeros of the above function are given by

$$z_n = \begin{cases} 0; & n = 0 \\ \pm(A^2 + n^2)^{1/2}; & n = 1, 2, 3, \dots \end{cases} \quad (13)$$

A model difference function can be constructed by moving the first  $T$  zeros on either side of the origin so that the sidelobes are made

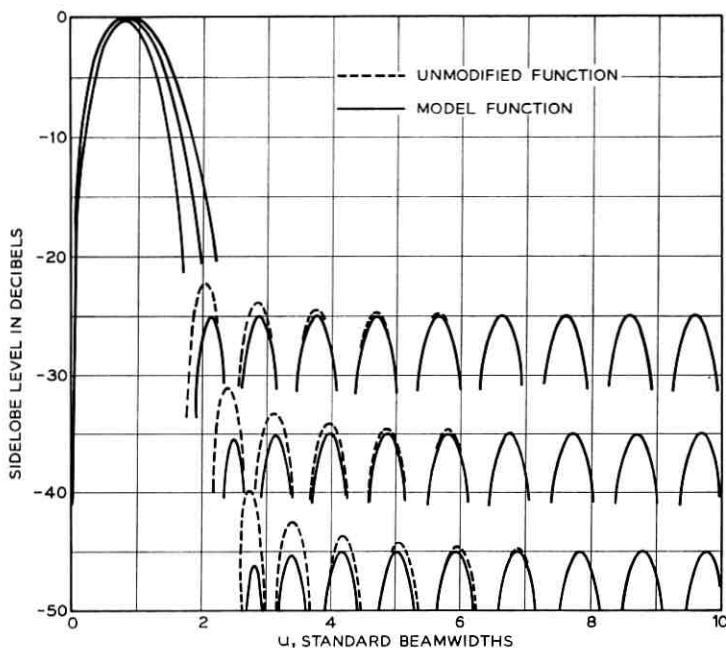


Fig. 3—Model difference pattern compared with unmodified function for sidelobe levels of 25, 35, and 45 dB.

equal. The model difference function is given by

$$F_M(u) = F_\Delta(u) \prod_{n=1}^T \frac{\xi_n^2 - u^2}{z_n^2 - u^2} \quad (14)$$

where the zeros,  $z_n$ , are moved to  $\xi_n$ . The location of the new zero  $\xi_n$  which make the sidelobes equal can be found by an iterative procedure.<sup>9</sup> Very good results were obtained by moving only the first four zeros on either side of the origin. The constructed model functions are shown in Figure 3 as solid curves.

To expedite future computations the sidelobe parameter  $A$  and the zeros were fitted as polynomial functions of the sidelobe level in dB. Fourth degree polynomials were fitted to values of  $A$ ,  $\xi_n$ , and the location of the difference peak,  $p_0$ , that were obtained from the iterative computation. Curves of the parameters along with their polynomial coefficients can be found in Figure 4.

The use of fitted polynomials inevitably leads to errors in the results. The effect of these errors is more pronounced in the low side-

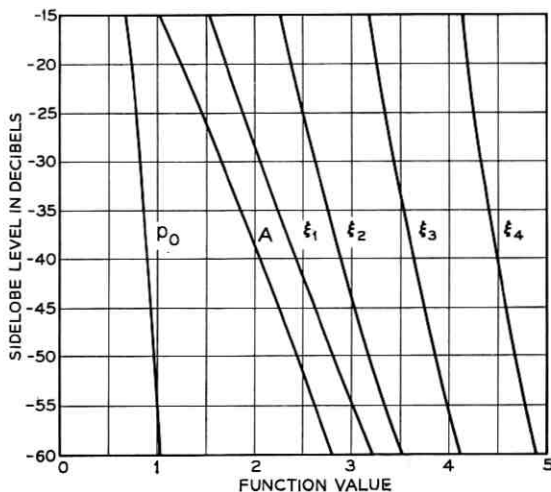


Fig. 4 — Model difference pattern parameters.

Polynomial Name	Polynomial Coefficients				
	$C_0$	$C_1$	$C_2$	$C_3$	$C_4$
$A$	0.30387530	-0.05042922	-0.00027989	-0.00000343	-0.00000002
$\xi_1$	0.98583020	-0.03338850	0.00014064	0.00000190	0.00000001
$\xi_2$	2.00337487	-0.01141548	0.00041590	0.00000373	0.00000001
$\xi_3$	3.00636321	-0.00683394	0.00029281	0.00000161	0.00000000
$\xi_4$	4.00518423	-0.00501795	0.00021735	0.00000088	0.00000000
$p_0$	0.47972120	-0.01456692	-0.00018739	-0.00000218	-0.00000001

lobe pattern. For example, notice the depressed first sidelobe in the -45 dB pattern of Figure 3 (and later in Figure 8). If good fidelity is desired for low sidelobe patterns it is advisable to use the calculated zeros directly and avoid use of the polynomials.

### 3.4 Synthesis of Asymptotic Difference Patterns

Now the problem of approximating the model function using the synthesis method described in Section 3.2 is considered. In this section an asymptotic form of the model function is developed. The asymptotic form is expressed in terms of the Fourier-Bessel series.

In Section 3.3 the model function for the ideal difference pattern  $F_M$  is generated in equations (12) and (14). The outstanding feature of this model function is its equal sidelobes.  $F_M$  is an entire function

of  $u$  and is completely described by its zeros,

$$Z_n = \begin{cases} 0; & n = 0 \\ \pm \xi_n; & n = 1, \dots, T. \\ \pm (A^2 + n^2)^{1/2}; & n = T + 1, \dots \end{cases} \quad (15)$$

For large  $|u|$  the zeros approach  $\pm n$  asymptotically. The model function is not realizable because it does not have decaying sidelobes (nonfinite energy).

The steps in constructing the asymptotic difference pattern are illustrated in Figure 5. The behavior of the model function in the far sidelobe region is changed so that it conforms to the asymptotic behavior of a realizable pattern function with decaying sidelobes. To do this, the zeros,  $Z_n$ , of  $F_M$  for all  $n \geq N$  are moved to  $\mu_n$ . These new far sidelobe zeros are zeros of the truncated pattern function series (8). This series must represent a realizable pattern function.

These zeros also satisfy (6). By changing only the far sidelobe zeros we have retained the essential model function characteristics in the central region. This central region behavior is embodied in the central zeros,  $Z_n$  for  $n < N$ . The  $N$ th zero pair of the model function,  $\pm Z_N$ , and the  $N$ th zero pair of the realizable function,  $\pm \mu_N$ , do not coincide.

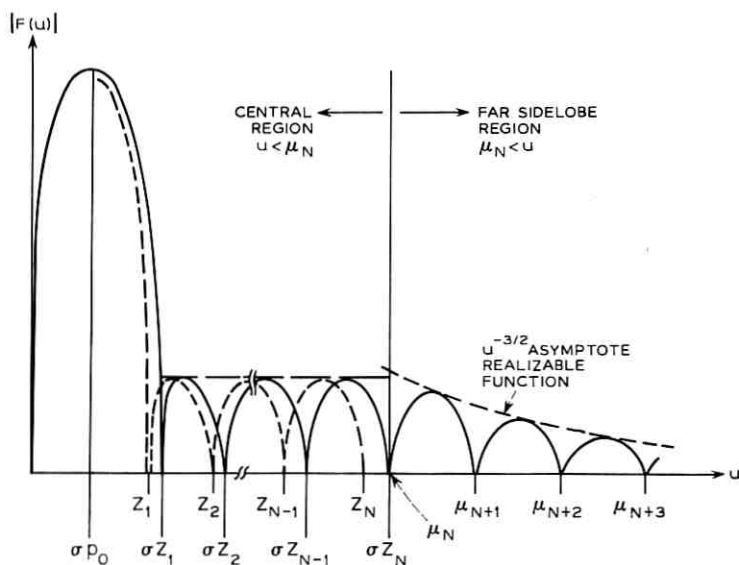


Fig. 5—Construction of asymptotic difference pattern.

Usually, the distance between  $Z_{N-1}$  and  $\mu_N$  is somewhat greater than one. Such a situation will give rise to a rather large sidelobe at the transition between central region and far sidelobe region.

To eliminate this high transition sidelobe the zeros of the central region will be dilated by a factor  $\sigma$  which makes  $Z_N$  and  $\mu_N$  coincide

$$\sigma = \frac{\mu_N}{Z_N}. \quad (16)$$

For sufficiently large  $N$ ,  $\sigma$  will always be greater than one.

The steps illustrated by Figure 5 are:

(i) A realizable pattern function with decaying sidelobes replaces the model function in the far sidelobe region.

(ii) The model function (dashed curve) is dilated so that the zero ( $\sigma Z_N$ ) coincides with the first zero of the far sidelobe region at  $u = \mu_N$ .

The asymptotic form of the model function is essentially complete. It can be expressed as a cononical product of its zeros

$$F_a(u, \Phi) = C u \pi \cos \Phi \prod_{n=1}^{N-1} \left[ 1 - \left( \frac{u}{\sigma Z_n} \right)^2 \right] \prod_{n=N}^{\infty} \left[ 1 - \left( \frac{u}{\mu_n} \right)^2 \right] \quad (17)$$

where  $C$  is a constant. The second product term must be reduced to closed functional form for this expression to have any practical value. The zeros in the second product of (17) satisfy  $J'_1(\mu_n \pi) = 0$ . Thus the second product term in (17) in closed form is equal to the first term of (8) with all zeros removed for  $|u| < \mu_N$ .

$$\prod_{n=N}^{\infty} \left\{ 1 - \left( \frac{u}{\mu_n} \right)^2 \right\} = [2J'_1(u\pi)] \left\{ \prod_{l=0}^{N-1} 1 - \left( \frac{u}{\mu_l} \right)^2 \right\}^{-1}. \quad (18)$$

Combining (17) and (18)

$$F_a(u, \Phi) = C (\cos \Phi) 2\pi u J'_1(u\pi) \frac{\prod_{n=1}^{N-1} \left[ 1 - \left( \frac{u}{\sigma Z_n} \right)^2 \right]}{\prod_{l=0}^{N-1} \left[ 1 - \left( \frac{u}{\mu_l} \right)^2 \right]}. \quad (19)$$

$F_a(u, \Phi)$  is a realizable asymptotic difference pattern. It is nearly equal to the model function in the central region (that is,  $|u| < \mu_N$ ). In fact, as the size of the central region increases without bound, the asymptotic function approaches the model function

$$\lim_{N \rightarrow \infty} F_a(u, \Phi) = F_M(u, \Phi). \quad (20)$$

The limit can be deduced from (17) by noting that asymptotic behavior of  $\mu_N$  (6) gives

$$\sigma = \frac{\mu_N}{[A^2 + N^2]^{\frac{1}{2}}} \approx 1 + \frac{3}{N}, \quad 1 < T \ll N. \quad (21)$$

Now as  $N$  is increased  $\sigma \rightarrow 1$ . Thus as  $N$  goes to infinity (and  $\sigma \rightarrow 1$ ) the second product term (17) disappears and only the first remains. The first product term (with  $\sigma = 1$ ) is exactly equal to the model function. Thus  $F_a(u, \Phi)$  is truly asymptotic to  $F_M(u, \Phi)$ .

The asymptotic function (19) is expressed as a Fourier-Bessel series using equation (10) to evaluate the coefficients. First evaluate  $F_a(u, \Phi)$  at the sample points  $(\mu_m, 0)$

$$\hat{F}(\mu_m, 0) = F_a(\mu_m, 0) = C2\pi\mu_m \frac{\prod_{n=1}^{N-1} \left[ 1 - \left( \frac{\mu_m}{\sigma Z_n} \right)^2 \right]}{\prod_{\substack{l=0 \\ l \neq m}}^{N-1} \left[ 1 - \left( \frac{\mu_m}{\mu_l} \right)^2 \right]} \text{Lim}_{u \rightarrow \mu_m} \frac{J_1'(u\pi)}{\left[ 1 - \left( \frac{u}{\mu_m} \right)^2 \right]} \quad (22)$$

$$m = 0, 1, \dots, N-1.$$

Evaluating the limit and substituting Bessel's equation yields

$$F_a(\mu_m, 0) = C(\pi\mu_m)^2 [1 - (\pi\mu_m)^{-2}] J_1(\mu_m\pi) \frac{\prod_{n=1}^{N-1} \left[ 1 - \left( \frac{\mu_m}{\sigma Z_n} \right)^2 \right]}{\prod_{\substack{l=0 \\ l \neq m}}^{N-1} \left[ 1 - \left( \frac{\mu_m}{\mu_l} \right)^2 \right]} \quad (23)$$

$$m = 0, 1, \dots, N-1.$$

Notice also that because of the construction of the asymptotic function  $F_a(\mu_m, 0) = 0$  for  $m \geq N$ . Finally the coefficients from (10) are:

$$B_m = \begin{cases} \frac{-Cj2\mu_m^2 \prod_{n=1}^{N-1} \left[ 1 - \left( \frac{\mu_m}{\sigma Z_n} \right)^2 \right]}{J_1(\mu_m\pi) \prod_{\substack{l=0 \\ l \neq m}}^{N-1} \left[ 1 - \left( \frac{\mu_m}{\mu_l} \right)^2 \right]} ; & m = 0, 1, \dots, N-1 \\ 0 & ; \quad m = N, N+1, \dots \end{cases} \quad (24)$$

where  $\mu_m$  is given by (6),  $Z_n$  by (15) and  $\sigma$  by (16). The constant  $C$  is evaluated so that the peak of the asymptotic difference pattern is unity, that is,  $F_a(\sigma\rho_0, 0) = 1$ .

The pattern function expansion (8) is identically equal to the asymp-



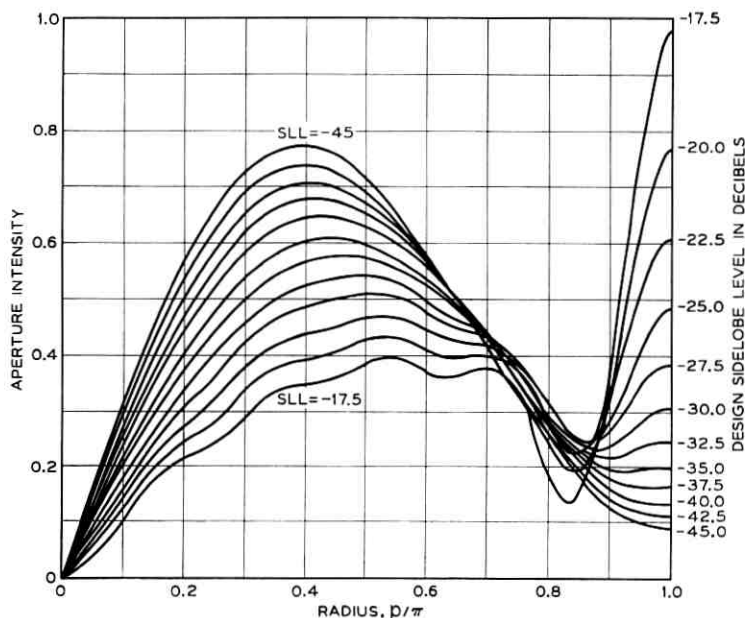
TABLE III—COEFFICIENTS FOR DIFFERENCE PATTERNS

		N = 5											
COEFFICIENTS \ SLL =		-17.5	-20.0	-22.5	-25.0	-27.5	-30.0	-32.5	-35.0	-37.5	-40.0	-42.5	-45.0
B 0		0.79738	0.78751	0.77806	0.76893	0.76033	0.75219	0.74458	0.73722	0.73042	0.72392	0.71792	0.71213
B 1		0.14654	0.26831	0.37445	0.46772	0.55036	0.62400	0.69001	0.74921	0.80278	0.85116	0.89522	0.93516
B 2		0.13474	0.06408	0.01520	-0.01692	-0.03613	-0.04535	-0.04690	-0.04252	-0.03364	-0.02137	-0.00658	0.01005
B 3		-0.15632	-0.09756	-0.05612	-0.02743	-0.00808	0.00445	0.01209	0.01623	0.01796	0.01804	0.01706	0.01544
B 4		0.09650	0.06431	0.04125	0.02488	0.01343	0.00556	0.00029	-0.00311	-0.00517	-0.00631	-0.00680	-0.00686

		N = 10											
COEFFICIENTS \ SLL =		-17.5	-20.0	-22.5	-25.0	-27.5	-30.0	-32.5	-35.0	-37.5	-40.0	-42.5	-45.0
B 0		0.81073	0.80063	0.79056	0.78064	0.77095	0.76154	0.75248	0.74367	0.73523	0.72715	0.71935	0.71189
B 1		0.02204	0.16201	0.26817	0.37274	0.46739	0.55343	0.63195	0.70372	0.76955	0.83004	0.88566	0.93694
B 2		0.26549	0.16480	0.09021	0.03053	-0.00030	-0.02345	-0.03549	-0.03846	-0.03404	-0.02362	-0.00634	0.01085
B 3		-0.37699	-0.25968	-0.17324	-0.11027	-0.06513	-0.03349	-0.01200	0.00191	0.01023	0.01451	0.01596	0.01549
B 4		0.43812	0.30936	0.21485	0.14597	0.09622	0.06071	0.03576	0.01858	0.00708	-0.00031	-0.00478	-0.00721
B 5		-0.45439	-0.32444	-0.22918	-0.15972	-0.10940	-0.07324	-0.04751	-0.02942	-0.01690	-0.00841	-0.00281	0.00074
B 6		0.42252	0.30349	0.21625	0.15259	0.10637	0.07303	0.04915	0.03219	0.02027	0.01201	0.00638	0.00262
B 7		-0.34848	-0.25158	-0.18048	-0.12840	-0.09065	-0.06323	-0.04349	-0.02935	-0.01932	-0.01227	-0.00737	-0.00401
B 8		0.24219	0.17579	0.12694	0.09111	0.06493	0.04586	0.03205	0.02208	0.01495	0.00997	0.00629	0.00380
B 9		-0.11903	-0.08696	-0.06320	-0.04580	-0.03297	-0.02356	-0.01670	-0.01171	-0.00810	-0.00550	-0.00364	-0.00232

first, when  $N$  is fixed (Figure 6), one sees that increasing the sidelobe level decreases the peak but increases the edge illumination. Conversely, when the sidelobe level is held constant (Figure 7), the effect of increasing  $N$  reduces the peak only slightly but increases the edge illumination tremendously. One of the prominent characteristics of this type of pattern synthesis is that the edge illumination increases as  $N$  increases.

Fig. 6 — Circular aperture functions for  $N = 10$ .

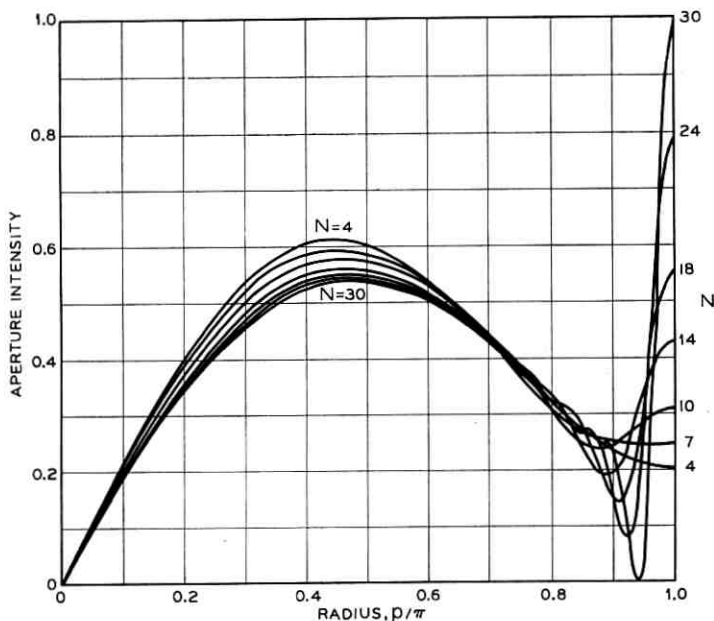


Fig. 7 — Circular aperture functions for  $-30$  dB sidelobe level.

The pattern functions exhibit a more straightforward dependence on the two parameters. The sidelobe envelopes are plotted in Figure 8 and 9 that correspond to the aperture functions in Figures 6 and 7. Only the envelope is plotted with a  $\circ$  to mark the sidelobe peak. Obviously the sidelobe parameter controls the maximum sidelobe level. The suppression of the first few sidelobes for very low sidelobe levels (Figure 8) is caused by using too small an  $N$ . When nondecreasing sidelobes are encountered the pattern is in a nonasymptotic region indicating that there are not enough terms in the series.

The effect of changing  $N$  can best be seen by keeping the sidelobe level fixed (Figure 9). As  $N$  is increased the sidelobes become more nearly equal as well as increasing the region affected. If we examine the sidelobe more closely we see that an inflection occurs at about  $u = N$ . The inflection results from the transition between the central region where the zeros have been modified and the far sidelobe region where the natural decay envelope is  $u^{-3/2}$  (Figure 10).

The asymptotic behavior of a given pattern function for large  $u$  can be examined in a manner similar to Taylor's<sup>1</sup>, giving the asymptotic

form of the pattern function as

$$F(u, \Phi) \sim \frac{(2\pi)^{\alpha+1} \Gamma(\alpha+1)}{\pi \sqrt{2} u^{(\frac{3}{2})+\alpha}}$$

$$\frac{h(\pi, \Phi) \exp \left[ j\pi \left( u - \frac{3}{4} - \frac{\alpha}{2} \right) \right] + h(\pi, \Phi + \pi) \exp \left[ -j\pi \left( u - \frac{3}{4} - \frac{\alpha}{2} \right) \right]}{2}$$

for  $|u| \rightarrow \infty$  and  $\text{Re } u > 0$ . (25)

The above notation follows Taylor's except that the aperture function is defined over the entire aperture not just on a line. The function

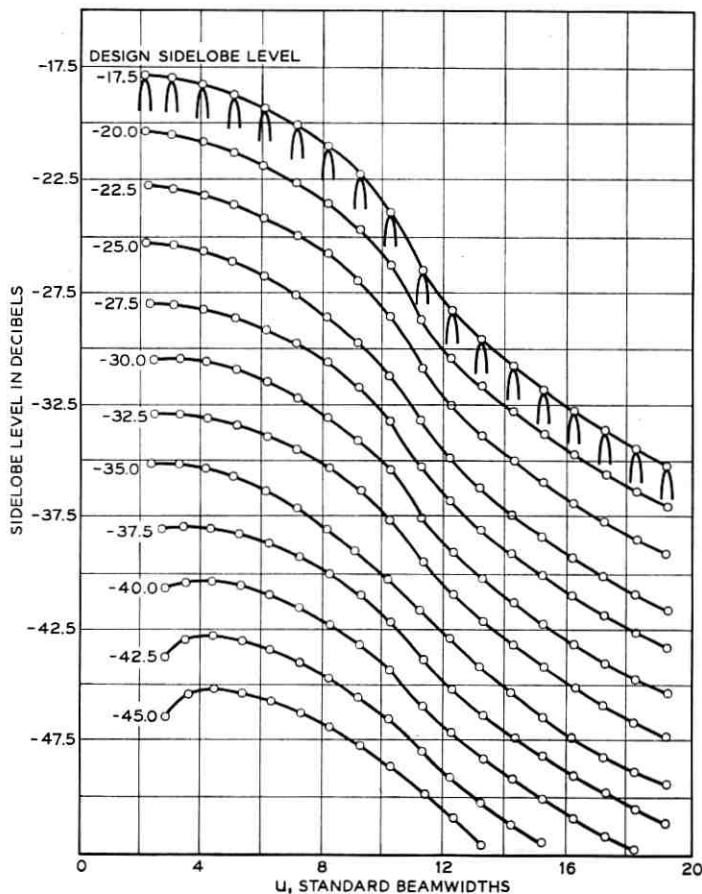


Fig. 8 — Sidelobe envelope of pattern functions for  $N = 10$ .

$h(p, \Phi)$  is the analytic part of the aperture function, that is,  $g(p, \Phi) = h(p, \varphi)(\pi^2 - p^2)^\alpha$ . For nonzero boundary values  $\alpha = 0$  and  $h(p, \varphi) = g(p, \varphi)$ . Evaluating (25) for the difference pattern gives

$$F(u, \Phi) \sim \sqrt{2} g(\pi, \Phi) \frac{\sin \pi(u - \frac{3}{4})}{u^{\frac{3}{2}}}. \quad (26)$$

As one might expect when dealing with aperture-limited functions the asymptotic form of the pattern function depends only on the aperture function behavior at the boundary of the aperture. The asymptote in Figure 10 was computed from equation (26).

To pursue the topic of asymptotic behavior further leads to considering the superdirectivity ratio and "Q" of the antenna. A rough qualitative definition would describe the superdirectivity ratio as the ratio of total power flow through the aperture to the power that is actually radiated. The definition of Q is the ratio of energy stored in the near field (evanescent waves) to that radiated per cycle. Increasing the superdirectivity increases the reactive component of power flow (also Q) and thus increases the ohmic losses in the antenna.

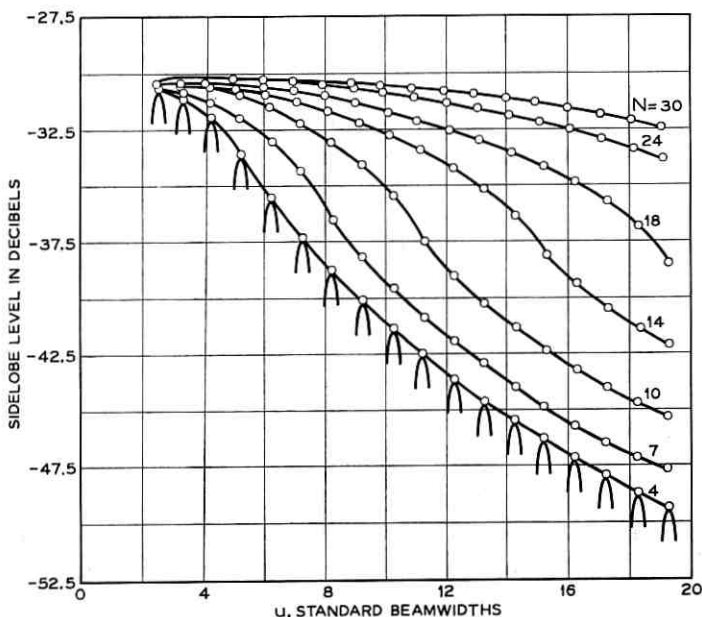


Fig. 9—Sidelobe envelope of pattern functions for -30 db sidelobe level.

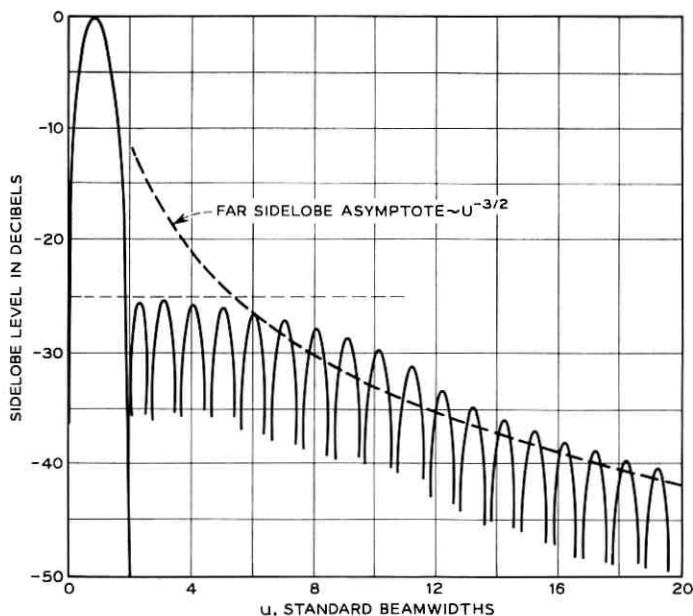
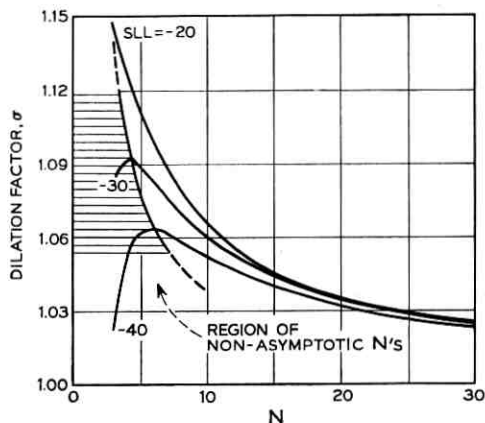


Fig. 10 — Asymptotic sidelobe behavior for  $-25\text{dB}$  sidelobe level and  $N = 11$ .

Large superdirectivity ratios are to be avoided (except in very small antennas) for a number of practical reasons: high ohmic losses, high error sensitivity, and narrow bandwidth. How then is superdirectivity affected by the choice of difference pattern? Superdirectivity increases as the integrated power of the pattern function in the region  $u > 2a/\lambda$  increases. This means that for a given sidelobe level superdirectivity increases with  $N$ . However, for a given pattern function, superdirectivity decreases with increasing antenna diameter. Because of the undesirable effect of the reactive component, the parameter  $N$  should be chosen so that  $N < 2a/\lambda$ .

The asymptotic behavior of the pattern function as  $N$  is increased is best illustrated by the dilation factor,  $\sigma$  (Figure 11). The dilation factor decreases to one as  $N$  is increased toward infinity. In the non-asymptotic region (Figure 11) the dilation actually increases with  $N$ . Because of severe sidelobe anomalies it is best to avoid using patterns with  $N$  in the nonasymptotic region. For  $N = 30$  the pattern dilation is less than 3 per cent for all sidelobe levels.

Fig. 11 — Pattern dilation factor,  $\sigma$ .

#### 4.2 Pattern Characteristics

A figure of merit by which the performance of a pattern can be measured against other patterns is a great help in selecting a specific pattern. Two such figures are directivity and angular sensitivity.

The directivity function is defined so that the aperture function can be used to find the total power

$$G(u, \Phi) = \frac{4\pi^2 a^2}{\lambda^2} \frac{\frac{4}{\pi} |F(u, \Phi)|^2}{\int_0^{2\pi} d\varphi \int_0^\pi |g(p, \varphi)|^2 p dp} \quad (27)$$

This definition is based on Silver's work,<sup>10</sup> and makes the following assumptions:

- (i) The effect of the obliquity factor is neglected.
- (ii) The antenna is large in wavelengths.
- (iii) The effects of ohmic losses in the antenna are neglected.

The maximum directivity of a uniform-phase circular aperture is

$$G_0 = \frac{4\pi^2 a^2}{\lambda^2} \quad (28)$$

The maximum directivity of a difference pattern naturally occurs at the peak of the difference beam ( $u_1, \Phi_1$ ) rather than at boresight.

The directivity at the pattern maximum normalized by the maxi-

imum aperture directivity is defined as the *relative directivity*,  $\eta$ :

$$\eta = \frac{G(u_1, \Phi_1)}{G_0} = \frac{\frac{4}{\pi} |F(u_1, \Phi_1)|^2}{\int_0^{2\pi} d\varphi \int_0^\pi |g(p, \Phi)|^2 p dp} \quad (29)$$

where  $(u_1, \Phi_1)$  is the pattern maximum.

This quantity is similar to aperture taper efficiency. Computation of relative directivity can now be carried out for the asymptotic difference pattern by noting that the coefficients computed for Tables II and III were normalized to make  $F(u_1, \Phi_1) = 1$  and that the aperture function series is orthogonal.

$$\eta = \frac{8}{\pi^4} \left\{ \sum_{l=0}^{N-1} |B_l|^2 J_1^2(\mu_l \pi) [1 - (\mu_l \pi)^{-2}] \right\}^{-1} \quad (30)$$

Relative directivity in dB ( $10 \log \eta$ ) was plotted as a function of  $N$  and sidelobe level (Figure 12). It can be seen that there is one  $N$  that gives a maximum relative directivity. The maximum is obtained when, as  $N$  increases, the power removed from the main beam by narrowing is just offset by the power added to the sidelobes by raising more sidelobes. The maximum relative directivity that can be achieved in any difference pattern (antiphase aperture) is  $-2.47$  dB.<sup>11</sup>

The most important characteristic of a difference pattern is its angle sensitivity. The angle sensitivity function is defined<sup>12</sup> using equation (27)

$$K(u) = \frac{\partial G^{\frac{1}{2}}(u, \Phi_1)}{\partial u} \text{ volt/volt/std. BW} \quad (31)$$

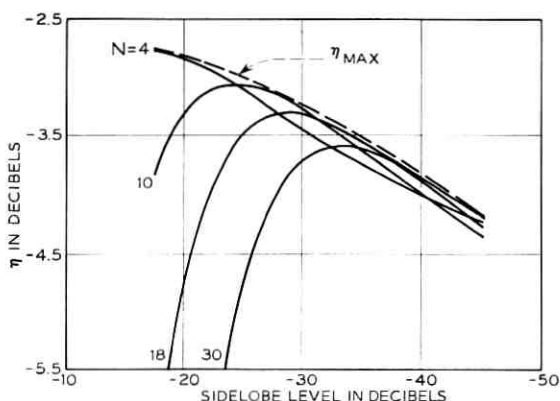


Fig. 12—Difference pattern relative directivity,  $\eta$ .

where  $\Phi_1$  is the difference pattern axis. The angle sensitivity of a pattern is  $K(0)$  which is the maximum value at boresight. The maximum angle sensitivity for any aperture is produced by a linear odd aperture function<sup>12</sup> (that is,  $g = jx$ ). For a circular aperture its pattern function is

$$F(u, 0) = \pi \frac{J_2(\pi u)}{u} \quad (32)$$

This pattern has -11.6 dB sidelobes and angle sensitivity

$$K_0 = \frac{\pi}{2} G_0^{\frac{1}{2}} \text{ volt/volt/std. BW.} \quad (33)$$

Again it is convenient to normalize to this maximum angular sensitivity and thus define *relative angle sensitivity* to be

$$\delta = \frac{K(0)}{K_0} = \frac{2}{\pi} \eta^{\frac{1}{2}} \left| \frac{\partial F(u, \Phi_1)}{\partial u} \right|_{u=0} \quad (34)$$

where  $F(u, \Phi)$  is normalized to unity.

By evaluating the partial derivative of the difference pattern function at  $u = 0$  the relative angle sensitivity is calculated as

$$\delta = \eta^{\frac{1}{2}} \sum_{l=0}^{N-1} B_l \frac{J_1(\mu_l \pi)}{\mu_l^2} \quad (35)$$

Relative angle sensitivity in dB ( $20 \log \delta$ ) was plotted as a function of  $N$  (Figure 13). The curves are very similar in behavior to those for

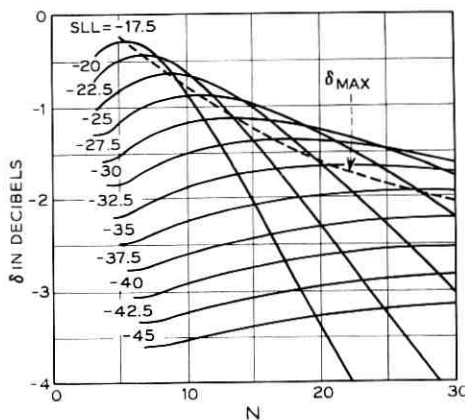


Fig. 13—Difference pattern relative angular sensitivity,  $\delta$ .

relative directivity as might be expected from equation (35). Certainly it is not unreasonable for the derivative of the directivity function at boresight to be strongly influenced by the magnitude of the peaks on either side. The dependence on sidelobe level is greater than for relative directivity. The dashed curve in Figure 13 is the maximum angle sensitivity ( $\delta_{\max}$ ) for each sidelobe level. The pattern coefficients are given in Table II for 12 sidelobe levels with  $N$  chosen to maximize  $\delta$ .

The decrease in angle sensitivity as the target moves off boresight is of interest in determining the linearity and useful angular sector of operation. The normalized angular sensitivity function,  $K(u)/K_0$  is plotted for six  $\delta_{\max}$  patterns in Figure 14. Although the boresight sensitivity is higher for high sidelobes than for low sidelobes, it also decreases more rapidly as a function of angle.

#### 4.3 System Performance

The sum and difference signals derived from the antenna just discussed can easily be put in a form that allows processing by any of the three types of angle detection systems.<sup>13</sup> The system generally used makes the angle estimate by forming a ratio of the difference to

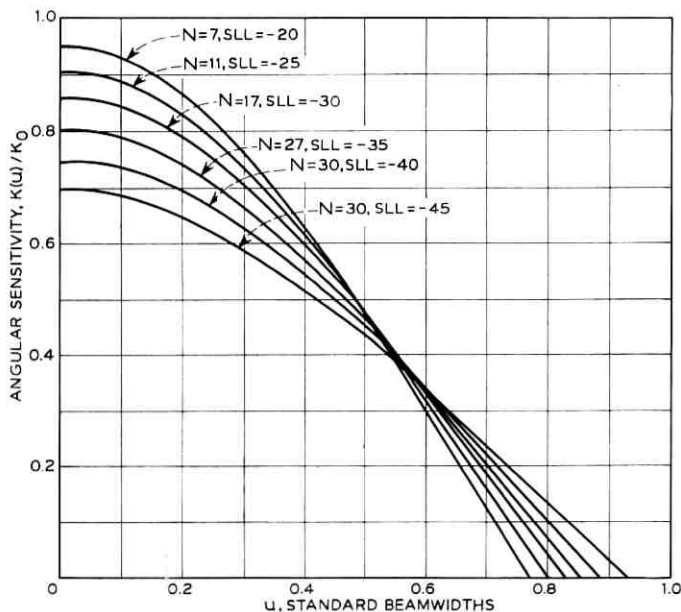


Fig. 14 — Normalized angular sensitivity function,  $K(u)/K_0$ .

sum signal. The statistic of this ratio was recently treated<sup>14</sup> with regard to maximum likelihood estimates of angle. For the high signal-to-noise case the variance of the maximum likelihood angle estimate<sup>2, 14</sup> is shown to be:

$$\sigma_{\theta}^2 = \frac{A^2}{B^2} \left( \frac{2E}{N_0} \right)^{-1} \quad (36)$$

where  $A$  and  $B$  correspond to  $G_{\Sigma}^{\frac{1}{2}}$  and  $K$  in our notation, \*  $E$  is the signal energy and  $N_0$  is the noise power per cycle of receiver bandwidth.

Manasse had shown earlier<sup>2</sup> that the minimum standard deviation for the maximum likelihood angle estimate made using a circular aperture is

$$(\sigma_u)_{\text{opt}} = (\sigma_{\theta})_{\text{opt}} \left( \frac{2a}{\lambda} \right) = \frac{2}{\pi} \left( \frac{2E_0}{N_0} \right)^{-\frac{1}{2}} \text{std. BW} \quad (37)$$

where  $2E_0/N_0$  is the output peak signal-to-noise power ratio in a perfectly matched receiver with optimum antenna system (that is, uniform aperture function).

The effects of antenna illumination on system performance can be expressed noting that realized signal energy  $E$  is also affected by antenna sum directivity. Thus  $E = E_0 \eta_{\Sigma} L$  where  $L$  accounts for losses such as filter mismatch loss, integration loss, and transmitter and propagation losses. Then (36) expressed in standard beamwidths is

$$\sigma_u = \frac{G_{\Sigma}^{\frac{1}{2}}(u)}{K(u)} \left( \frac{2E_0 \eta_{\Sigma} L}{N_0} \right)^{-\frac{1}{2}} \text{std. BW.} \quad (38)$$

Now by noting that

$$\frac{K(0)}{K_0} = \delta \quad \text{and} \quad \frac{G_{\Sigma}(0)}{G_0} = \eta_{\Sigma}; \quad \frac{K(u)}{K(0)} \cong 1 \quad \text{and} \quad \frac{G_{\Sigma}(u)}{G_{\Sigma}(0)} \cong 1$$

for  $|u| \ll 1$ , and for a circular aperture  $K_0 = (\pi/2)G_0^{\frac{1}{2}}$ , then (38) becomes

$$\sigma_u = \frac{2}{\pi \delta} \left( \frac{2E_0 L}{N_0} \right)^{-\frac{1}{2}} \text{std. BW.} \quad (39)$$

Thus at high signal-to-noise ratios the antenna dependence is

$$\sigma_u \approx \frac{1}{\delta}.$$

This dependence shows that the difference pattern angle sensitivity is of prime importance in determining the over-all system angle accuracy.

\* The subscript  $\Sigma$  refers to sum pattern parameters.

The optimum system from the standpoint of angle estimation is one with  $\delta$  and  $\eta_z$  equal to unity. As we pointed out before such a system would have unacceptably high sidelobes. The price of lower sidelobes is reduced sensitivity (Figure 15). The top curve shows the maximum relative directivity,  $\eta_{\max}(\Sigma)$ , obtainable from a Taylor sum pattern.\* Similarly, the  $N$  can be selected to maximize relative angle sensitivity,  $\delta_{\max}$ , for the asymptotic difference pattern (Figure 15).

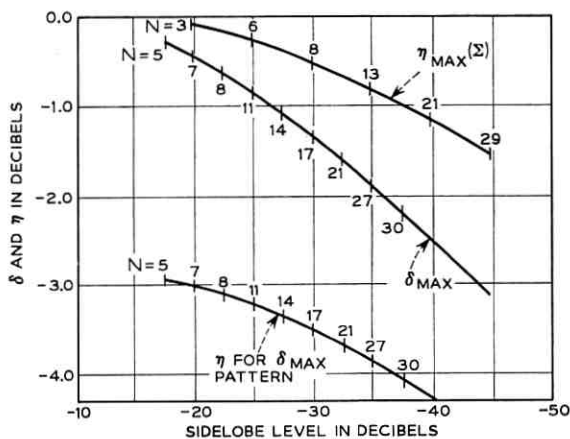


Fig. 15—Relative directivity and angular sensitivity for maximum sensitivity pattern.

The relative directivity ( $\eta$ ) of the  $\delta_{\max}$  pattern is shown at the bottom of Figure 15. Notice that it is 3 dB below the sum pattern relative directivity. Thus, to equalize the sidelobe clutter returns from the highest sidelobes in the sum and difference patterns, the difference pattern sidelobe level should be 3 dB greater than the sum patterns sidelobe level. For example, if a sum pattern with  $-30$  dB sidelobe level is chosen ( $N = 8$ ) the difference pattern sidelobe level should be  $-27$  dB, and  $\delta_{\max}$  is  $-1$  dB when  $N = 14$ .

One of the major reasons for suppression of sidelobes is the presence of clutter. Although clutter can be a problem throughout the pattern it is often more prevalent at low angles. If clutter does not occur near the main beam it might be advantageous to choose a small value of  $N$  so that the sidelobes decay rapidly (Figure 9). If clutter is very bad it may be necessary to taper the transmitter illumination, too.

\* Where  $N$  corresponds to  $\bar{n}$  in Taylor's notation.

A second reason for suppression of sidelobes is the presence of active noise sources. These are the essence of the radio astronomy problem. For the radar problem they are jammers (electronic countermeasures). They generally are considered to be point sources which may appear anywhere in the pattern. Hence the requirement to minimize the maximum sidelobe level.

In selecting a difference pattern a major practical consideration is that the aperture function be realizable. Remember that the aperture function represents the resulting field on the face of the aperture (that is, after all ohmic losses and mutual couplings have been accounted for). Certainly one could not choose an aperture function with a lip or spike at the edge for use with a horn fed antenna or array. Even in an array of independent elements it usually is not desirable to let the edge excitation exceed the peak.

These considerations along with constraints of the system problem such as required accuracy, clutter, noise, and so on, influence the selection of sidelobe level and  $N$ .

#### V. SUMMARY

Full theoretical and design documentation has been given to a new two-parameter difference pattern. The salient features of the pattern are asymptotically equal sidelobes and near optimum angle sensitivity. The two parameters,  $A$  and  $N$ , give complete control of the sidelobe level and decay behavior. The difference pattern was designed to be compatible with monopulse systems using the Taylor sum beam illumination.

#### ACKNOWLEDGMENT

The author wishes to thank G. J. Libretti for computer programing.

#### APPENDIX

##### *Asymptotic Difference Pattern for a Line Source*

The construction of an asymptotic difference pattern for a line source can be carried out in a manner similar to that described for the circular aperture. The equations for the line source difference pattern, which parallel those in the body of this report, are outlined here.

The line-source-to-pattern-function transform is a finite Fourier

transform.

$$F(u) = \int_{-\pi}^{\pi} g(x)e^{iux} dx \quad (40)$$

where  $u = 2a/\lambda \sin \theta$ ,  $\theta$  is measured from the normal,  $2a$  is the length of the line source and  $x$  is normalized to  $\pi/a$ . Expand  $g(x)$  in a sine series because an odd function is required

$$g(x) = \begin{cases} \sum_{l=0}^{N-1} B_l \sin \mu_l x; & -\pi \leq x \leq \pi \\ 0; & \text{elsewhere.} \end{cases} \quad (41)$$

A nonzero boundary value is again required for the truncated series. The eigenvalues must be  $u_l = l + 1/2$ . Now transforming the series by (40) and setting  $u_l = l + 1/2$  yields

$$F(u) = 2j \sum_{l=0}^{N-1} B_l \frac{(-1)^l u \cos u_{\pi}}{(l + \frac{1}{2})^2 - u^2}. \quad (42)$$

The desired model function,  $F_M(u)$  (see equations 12 and 14) is again described by its zeros.

The dilation factor is

$$\sigma = \frac{\mu_N}{Z_N} = \frac{N + \frac{1}{2}}{Z_N}. \quad (43)$$

The asymptotic function is given by the canonical product

$$F_a(u) = Cu \prod_{n=1}^{N-1} \left\{ 1 - \left( \frac{u}{\sigma Z_n} \right)^2 \right\} \prod_{l=N}^{\infty} \left\{ 1 - \left( \frac{u}{\mu_l} \right)^2 \right\} \quad (44)$$

where  $C$  is a constant.

The asymptotic difference pattern in closed form is:

$$F_a(u) = Cu \cos(\pi u) \left\{ \frac{\prod_{n=1}^{N-1} 1 - \left( \frac{u}{\sigma Z_n} \right)^2}{\prod_{l=0}^{N-1} 1 - \left( \frac{u}{\mu_l} \right)^2} \right\}. \quad (45)$$

The function may be expressed in series form by evaluating (45) at  $u = \mu_m$  and setting it equal to (42) to find  $B_m$ . Evaluating the series (42) at  $u = \mu_m$  gives

$$F(\mu_m) = \lim_{u \rightarrow \mu_m} F_a(u) = j\pi B_m. \quad (46)$$

Substituting  $\mu_n = n + 1/2$ , the coefficients are:

$$B_m = \begin{cases} \frac{C}{2j} (-1)^m (m - \frac{1}{2})^2 \frac{\prod_{n=1}^{N-1} \left[ 1 - \left( \frac{m + \frac{1}{2}}{\sigma Z_n} \right)^2 \right]}{\prod_{\substack{l=0 \\ l \neq m}}^{N-1} \left[ 1 - \left( \frac{m + \frac{1}{2}}{l + \frac{1}{2}} \right)^2 \right]}, & m = 0, 1, 2, \dots, N-1 \\ 0; & m = N, N+1, \dots \end{cases} \quad (47)$$

As  $N$  is allowed to increase without bound it may be noticed that  $\sigma \rightarrow 1$  from above and the zeros of  $F_a(u)$  approach those of  $F_M(u)$ . Thus

$$\lim_{N \rightarrow \infty} F_a(u) = F_M(u).$$

For small  $N$  the values of  $B_m$  can be evaluated by hand by using the model function parameters from Figure 4.

#### REFERENCES

1. Taylor, T. T., "Design of Circular Apertures for Narrow Beamwidth and Low Sidelobes," IRE Trans. Antennas and Propagation, *AP-8* (January 1960), pp. 17-22.
2. Manasse, R., "Maximum-Angular Accuracy of Tracking a Radio Star by Lobe Comparison," IRE Trans. Antennas and Propagation, *AP-8* (January 1960), pp. 50-56.
3. Harrington, R. F., *Time-Harmonic Electromagnetic Fields*, New York: McGraw-Hill, 1961, pp. 110-112.
4. Plonsey, R., "Aperture Fields," IRE Trans. Antennas and Propagation, *AP-9* (November 1961), p. 577.
5. Hansen, R. C., *Microwave Scanning Antennas*, New York: Academic Press, 1964, vol. 1, pp. 5-11.
6. Ruze, J., "Circular Aperture Synthesis," IEEE Trans. Antennas and Propagation, *AP-12* (November 1964), pp. 691-694.
7. Price, O. R. and Hyneman, R. F., "Distribution Functions for Monopulse Antenna Difference Patterns," IRE Trans. Antennas and Propagation, *AP-8* (November 1960), pp. 567-576.
8. Dolph, C. L., "A Current Distribution for Broadside Arrays Which Optimizes the Relationship between Beamwidth and Sidelobe Level," *Proc. IRE*, *34* (June 1946), pp. 335-348.
9. Sinclair, G. and Cairns, F. V., "Optimum Patterns for Arrays of Non-Isotropic Sources," IRE Trans. Antenna and Propagation, *AP-1* (February 1952), pp. 50-61.
10. Silver, S., *Microwave Antenna Theory and Design*, MIT Radiation Laboratory Series, vol. 12, New York: McGraw-Hill, 1949, p. 177.
11. Kinsey, R. R., "Monopulse Difference Slope and Gain Standards," IRE Trans. Antennas and Propagation, *AP-10* (May 1962), pp. 343-344.
12. Kirkpatrick, G. M., "Aperture Illuminations for Radar Angle-of-Arrival Measurements," IRE Trans. Aeronautical and Navigational Elec., *AE-9* (September 1953), pp. 20-27.
13. Rhodes, D. R., *Introduction to Monopulse*, New York: McGraw-Hill, 1959, p. 56.
14. McGinn, J. W., Jr., "Thermal Noise in Amplitude Comparison Monopulse Systems," IEEE Trans. Aerospace Elec. Syst., *AES-2*, (September 1966), pp. 550-556.

# Error-Controlled High Power Linear Amplifiers at VHF

By H. SEIDEL, H. R. BEURRIER, and A. N. FRIEDMAN

(Manuscript received July 21, 1967)

*Two amplifiers, each covering a different band in the VHF range, were constructed for test set applications. These amplifiers were required to meet stringent specifications beyond the general scope of previous art. These specifications related to the simultaneous availability of relatively large output power, tight linearity, minimal delay distortion across a 40 per cent band, high input and output return loss, large dynamic range, and time stability.*

*The performance problems were solved by using:*

- (i) Quadrature couplers in a corporate structure array to provide a high multiplicity of "paralleled" transistors, yielding both the power and return loss capabilities.*
- (ii) The emitter follower configuration as the basic amplifier element, providing broad band, high level performance owing to the large self degeneration of that configuration.*
- (iii) A "feed-forward," instead of a feedback, system for error control and noise cancellation.*

## I. INTRODUCTION

There are times when problems arise in device implementation that appear to be the product of the sheer perversity of the system designer. Worst of all, he can justify his need—as in the need to develop a solid-state 10-watt amplifier between 60 and 90 Mc, with low intermodulation distortion, time delay distortion, and gain ripple, with a high return loss, and with excellent time stability. Subsequently, a similar need was expressed over a band of 25 to 35 Mc.

A format of amplifier design was devised meeting these requirements and subsequent constructions justified the design philosophy. While some of the techniques used are known, we believe that the nature of their use here emphasizes latent potentialities which had

not been generally apparent. In particular, a "feed-forward" error compensation system is used which has parallels to McMillan's and Van Zelst's generalization of Black's error injection methods.<sup>1-3</sup> There is a very specific recognition here, however, of the physical role played by time, which dominates the form of the error network and which provides, among other advantages, a means of arbitrary error control of large time delay amplifiers which are intractable to feedback methods.\*

We shall describe further the use of "corporate" amplifier binary arrays using quadrature couplers and emitter-follower amplifier stages. The word "corporate" is intended to suggest the process of a corporate coordination of many sources to deliver their powers in some desired collective mode, in much the same fashion as in a corporate antenna. With respect to the emitter-follower amplifier, much to the contrary usage of that device only as a unit gain isolation stage, there are many advantages highly germane to its use as an amplifier with certain basic advantages over the common emitter and common base modes of transistor operation.

The name "feed-forward" error control scheme, coined to distinguish it from feedback, is fully descriptive. Error is detected, amplified, and injected after proper time delay in the forward time stream of the amplifier, and error cancellation is accomplished over the entire band of interest. The error, it should be emphasized, is composed of ripples in the amplifier transfer function, distortions through nonlinearity, and amplifier noise. To some extent the low level error amplifier has noise; nevertheless, there is advantage gained in noise performance by exchanging that noise for the much greater noise of the higher power amplifier. Further, the feed-forward system makes demands on the active elements of the system only within the band of interest, and great advantage is gained in using more powerful, lower quality transistors without the concerns of high frequency dispersion instabilities attendant upon conventional feedback systems.

## II. CORPORATE POWER STAGES

### 2.1 *Coupler Arrays*

High-frequency transistors generally have a smaller dynamic range than the lower frequency and power transistors. One may, however,

\* During the late stages of preparing this manuscript, we learned of a patent issued by the German Federal Republic to Heinrich Schmidt-Brücken in which he recognizes time as a factor in error compensation. In Appendix 3 we compare his implementations with present implementations, and we believe the differences are significant.

resort to transistor arrays to multiply the power capability inherent in a single stage while retaining the high-frequency performance. The notion of an array of elements to provide power is well within the framework of conventional electronics as observed in the early ring oscillator, an antecedent of the existing distributed amplifiers and oscillators.

In the ring oscillator, as in the magnetron, there is a coordination of the various elements into a collective mode. These modes comport with the rotational symmetry of the ring and so are characterized by eigenvalues which are the various rational roots of unity. Often the modes are virtually degenerate and mode strapping and mode killing techniques are a necessity to isolate the desired mode of operation. This isolation is frequently marginal and mode-hopping is a well-known consequence of improper excitation or loading of the system.

The difficulty in mode suppression stems from the requirement that, for an  $n$  degree of freedom system,  $n - 1$  modes must be suppressed without hampering the transmission qualities of the  $n$ th. Further, reactive strapping may operate, not so much to suppress, but simply to alter the dispersion characteristics of the network permitting the unwanted modes to pop out elsewhere and, often, with deleterious effects.

Seidel has examined the problems of active network synchronization,<sup>4</sup> and the resolution of the problems of stability would appear to exist through the use of hybrid or conjugate couplers with absorbing suppressors. Basically, through the use of couplers, the terminating loads on the ideally unexcited ports provide exactly the  $n - 1$  independent absorbers needed; furthermore, these absorbers are precisely where they should be to provide the necessary orthogonality against absorption of the desired mode.

As opposed to the ring, the mode structure of the hybrid coupled amplifier is not characterized by a simple eigenvalue description. Further, the forms of building the coupler array may be quite variable and the choices reflect on considerations of some moment. There are two particular considerations which are of major consequence.

- (i) Out-of-band stability of the harnessed system
- (ii) Low level of multiple reflection in interconnection of amplifier stages.

While these two considerations are phrased independently, a small interdependence can exist.

With respect to out-of-band stability, assume the possible use of a

transmission line hybrid such as, for example, a rat race or 3 dB in-phase coupler. While meeting proper in-band specifications on match or power, what are the consequences of performance of this harnessing structure upon the element whose activity persists well beyond this point? Further, with respect to the second consideration, what are the proper harnessing formats to permit arbitrary cascading of elements whose intrinsic isolations may, at best, be modest?

## 2.2 Quadrature Couplers

A solution which contains many practical advantages is the use of arrays of lumped quadrature couplers. A quadrature coupler, as an elementary device, is a matched reactive reciprocal four-port having two orthogonal axes of symmetry. This characterization suffices to endow the coupler with the following properties:

- (i) Corresponding to an excitation port, labelled 1, there exists a conjugate, or hybrid, port labelled 4.
- (ii) The entire incident power emerges in quadrature phase from the remaining ports 2 and 3.

An evident symmetry of these coupling characteristics obtains with respect to rotations about the two symmetry axes. The about results are demonstrated in Appendix 1.

When we apply the device symmetries to the above labelling scheme we find the following scattering matrix:

$$S = \begin{pmatrix} 0 & S_{12} & S_{13} & 0 \\ S_{12} & 0 & 0 & S_{13} \\ S_{13} & 0 & 0 & S_{12} \\ 0 & S_{13} & S_{12} & 0 \end{pmatrix} \quad (1)$$

Application of the unitary properties of the scattering matrix, namely the relationship  $\bar{S}S = 1$ , yields

$$S_{12}S_{13}^* + S_{13}S_{12}^* = 0 \quad (2)$$

$$S_{12}S_{12}^* + S_{13}S_{13}^* = 1. \quad (3)$$

From (2)  $S_{13}^* = -S_{13}(S_{12}^*/S_{12})$  which we substitute in (3) to provide

$$S_{12}^2 - S_{13}^2 = \frac{S_{12}}{S_{12}^*}. \quad (4)$$

Equations (2) and (4) may be put in a more useful form. Equation (2) provides that  $\text{Re } S_{12}S_{13}^* = 0$  so that  $S_{12}S_{13}^*$  is imaginary implying that  $S_{12}$  and  $S_{13}$  are in phase quadrature. Equation (4) leads to a result which we shall employ crucially:

$$|S_{12}^2 - S_{13}^2| = 1. \quad (5)$$

Equation (5) is of major importance, since it states that it is possible to use quadrature couplers in an all-pass arrangement, as shown in Fig. 1, without regard to the frequency sensitivity of  $S_{12}$  and  $S_{13}$ . Since this result is independent of the frequency sensitivities of the matrix elements of  $S$ , it is possible to use the structural elements of Fig. 1 to implement far more complex power divider arrays without sharpening the frequency characteristics of transmission. Figure 2 shows a four-way all-pass division and the extension of a  $2^n$  division is clearly evident. Figure 3 shows the harnessing of two 4-way dividers to form the 8-way divider. Shown, to, for the first time, is the placement of the elementary amplifiers.

There is a key shown in Fig. 2 which is the algorithm for patterning the phase shifter arrays which introduce the relative  $0^\circ$  and  $180^\circ$  phase additions. Given any  $2^n$  array of phase shifts, the pattern for  $2^{n+1}$  is given by forming the complement array and adjoining the latter to the former. For example, if the 8-way array from top to bottom is  $(+ - - + - + + -)$ , where  $+$  and  $-$  have substituted for  $0^\circ$  and  $180^\circ$ , respectively, the complement pattern is  $(- + + - + - - +)$  so that the 16-way pattern is  $(+ - - + - + + - ; - + + - + - - +)$ , the 32-way is  $(+ - - + - + + - - + + - - + + - - + ; - + + - + - - + + - - + + -)$ , and so forth.

Why quadrature coupler arrays instead of more conventional in-phase divider arrays? Why introduce the complexity in phasing the array? The essential answer is inherent in the simplest of the structures shown in Fig. 1. The coupler has a 3 dB split with energy incident upon each of the amplifiers having  $90^\circ$  difference. Under

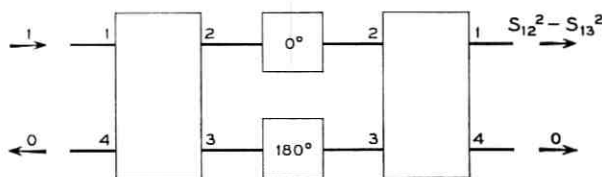


Fig. 1 — Quadrature couplers in all-pass arrangement.

reflection from identical amplifier inputs the phase difference mounts to  $180^\circ$ , as returned to the source, and a high degree of the reflection is cancelled. On the other hand, the reflected energies return in phase to the port conjugate to the input and are dissipated in a dummy load.

This technique, using 3-dB quadrature couplers to provide high input return loss to arrays of mismatched elements, was first used for short-slot couplers in radar transmit-receiver switches to prevent

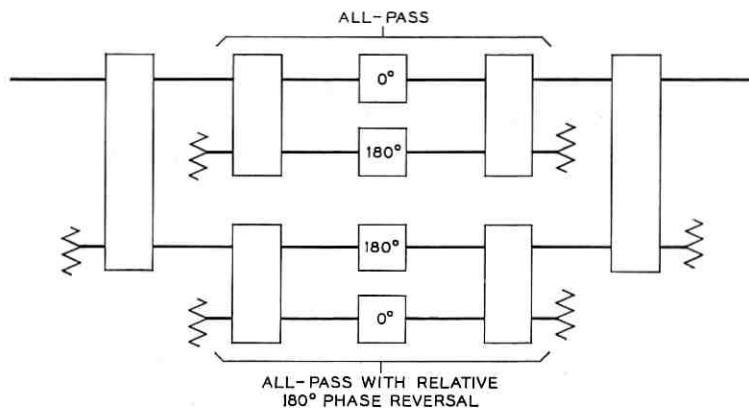


Fig. 2 — All-pass four way quadrature power divider.

mismatch back to the magnetron. While this technique has been extended to tunnel diode and transistor amplifiers, nevertheless the specific arrays shown here differ in two basic respects:

- (i) The arrays can have arbitrarily large multiplicity.
- (ii) All-pass transmission results from the use of  $180^\circ$  phase difference sections.\*

The arrays shown in Figs. 1 through 3 were developed through a graphical induction process. Their properties are, however, more clearly phrased by returning to an analytic description. In terms of the scattering coefficients, the transmission  $T$  and input reflection  $K$  of the array are

$$T = (S_{12}^2 - S_{13}^2)^n t \quad (6)$$

\* The use of  $180^\circ$  phase difference sections and their application to high multiplicity dividers was independently conceived. Original recitation of their use in two section dividers was made by E. A. Marcatilli, and D. H. Ring, IEEE Professional Groups Microwave Theory & Techniques *MTT-10* #4 (July 1962) pp. 251-8.

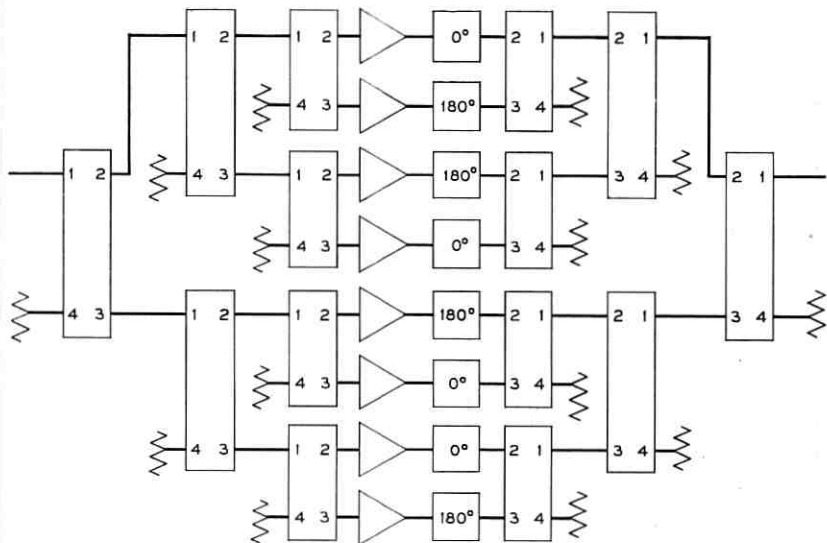


Fig. 3—Eight way quadrature divider with amplifiers.

and

$$K = (S_{12}^2 + S_{13}^2)^n k \quad (7)$$

where  $t$  and  $k$  are the transmission and reflection, respectively, of each amplifier element and where  $2^n$  is the number of amplifier elements. We observe from (5) and (6) that  $|T| = |t|$ , confirming the all-pass construction.

At the center frequency of each coupler,  $|S_{12}| = |S_{13}| = 1/(2)^{\frac{1}{2}}$  and, via (2), there always exists phase quadrature. Therefore,  $S_{12}^2 + S_{13}^2$  vanishes at centerband and, whatever the multiplicity of that zero, (7) shows the reflection zero to be raised to  $n$ th degree. Simple coupler synthesis techniques permit an arbitrary multiplicity of the degree of the zero and no major difficulty exists in obtaining octave performance and much greater.

### 2.3 Coupler Economics

It is instructive to consider the simplest couplers meeting the objectives of the amplifier to be constructed. The coupler enters into the technical design of the amplifier with respect to the return loss of the coupled amplifier array over the band together with a deterioration of the dynamic range relative to a single amplifier element. On

the other hand, the choice of coupler enters into the economics as a greater cost for a more complex coupler.

We shall find that the return loss is not the essential problem of the array but that it is the dynamic range which is limiting. While dynamic range deterioration does dominate the coupler choice, we shall see that the degree of deterioration is not major and that the feed-forward compensation may, in many instances, make the problem negligible. Let us now investigate both the return loss and the dynamic range problems.

### 2.3.1 Return Loss

We shall consider two coupler types; one and two stage couplers. Corresponding to the number of stages is the multiplicity of zeros in the reflection factor,  $k$ , of (7) over the band. We intend to discuss these couplers in detail in another publication<sup>5</sup> and we shall consider it sufficient here to state simply that the couplers are compact and are composed primarily of lumped elements. They meet the characterizations of Section 2 to a high degree over extremely wide bandwidths and all the properties described are met substantially in practice.

We shall be concerned here only with the magnitude of  $k$ . Equation (7) yields

$$|K| = \left| |S_{12}|^2 - |S_{13}|^2 \right|^n |k|, \quad (8)$$

which produces the return loss  $L$  in db;

$$L = 20n \log_{10} \left| |S_{12}|^2 - |S_{13}|^2 \right| + 20 \log_{10} |k|. \quad (9)$$

Recognizing that  $|S_{12}|^2 + |S_{13}|^2 = 1$ , from (5), equation (9) yields

$$L = 20n \log_{10} \left| 2 |S_{12}|^2 - 1 \right| + 20 \log_{10} |k|. \quad (10)$$

Let us choose a normalized frequency variable,  $\Omega$ , such that  $\Omega = 1$  at center band. We then assert for one and two stage couplers, respectively, that

$$|S_{12}|^2 = 1/1 + \Omega^2 \quad (\text{single stage}) \quad (11)$$

and

$$|S_{12}|^2 = 1/1 + [1.545\Omega \cos(20.6^\circ\Omega) - 1.195\Omega^2 \sin(20.6^\circ\Omega)]^2 \quad (\text{double stage}) \quad (12)$$

where the coefficients in the two stage unit are chosen such that the power transmitted to port 2 and the power transmitted to port 3

differ by the same amount at centerband and at the edges of a 1.5:1 bandwidth. The behavior of (12) is shown in Fig. 4.

For a specific choice of a 1.5:1 bandwidth, as was required for the 60-90 Mc amplifier, we find

$$2 |S_{12}^2| - 1 \leq 0.22 \quad (\text{single stage})$$

$$\leq 0.038 \quad (\text{double stage}).$$

If we assume that our manner of use of the amplifier elements as emitter followers produces  $|k|$  generally close to unity, we may neglect its inclusion in (10) and

$$L = -13.16n \text{ dB} \quad (\text{single stage}) \quad (13)$$

$$= -28.4n \text{ dB} \quad (\text{double stage}). \quad (14)$$

The major need for high return loss resides in the interaction between amplifiers. The dominant error produced by multiple reflections is the "third time around" incidence which is down from the initially incident signal by the sum of the return losses of the output and input of the first and second amplifiers, respectively. Since the gain per stage exceeds 6 dB for emitter follower amplifier elements, each stage is capable of feeding a next stage composed of four times as many amplifier elements. Therefore, if the first stage contains  $2^n$  elements the second contains  $2^{n+2}$ . If  $L_{1+2} \equiv L_1 + L_2$  in dB. Then, from (13) and (14)

$$L_{1+2} = -26.32(n+1) \text{ dB} \quad (\text{single stage couplers}) \quad (15)$$

$$= -56.8(n+1) \text{ dB} \quad (\text{double stage couplers}). \quad (16)$$

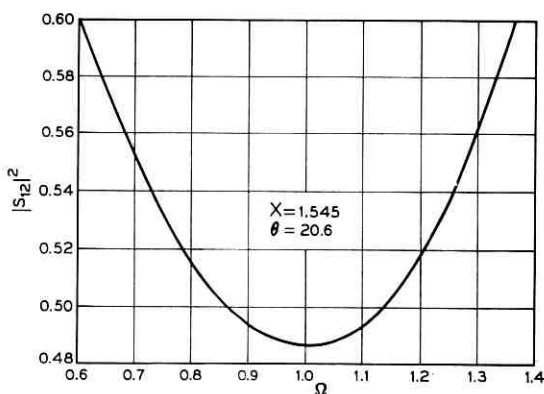


Fig. 4 — Two stage coupler designed for 1.5:1 bandwidth.

The fine structure in transmission of  $n = 1$  or greater is very small and represents extremely small power variation. This presents a negligible taxation of the power handling capabilities of the feed-forward compensation system which will wash it out. Under these circumstances, the choice between single and double stage couplers does not rest upon return loss considerations.

### 2.3.2. Saturation Power

We may find from (6) a means for characterizing the energy paths through the coupler array. In much the same way as that in which the Pascal triangle builds up the binomial expansion in terms of the number of paths connecting two points, we may use the expansion of (6) to enumerate the number of paths from input to output. As an example, consider  $n = 3$  which corresponds to an eight element amplifier stage. We have

$$T = \{S_{12}^6 - 3S_{13}^4S_{12}^2 + 3S_{12}^2S_{13}^4 - S_{13}^6\}. \quad (17)$$

As may be confirmed using Fig. 3 as a guide, we have

- (i) One path making six transitions of an  $S_{12}$  form
- (ii) Three paths making four transitions of an  $S_{12}$  form and two of an  $S_{13}$  form, together with a net  $180^\circ$  phase shift
- (iii) Three paths making two transitions of an  $S_{12}$  form and four of an  $S_{13}$  form
- (iv) One path making six transitions of an  $S_{13}$  form together with a net  $180^\circ$  phase shift.

As is evident from this enumeration, different paths contain somewhat different amplitude content because of the frequency sensitivities of the scattering parameters  $S_{12}$  and  $S_{13}$ . This suggests that the amplifiers are somewhat unevenly excited which must have deleterious consequences to the net dynamic range of the composite amplifier.

Equation (17) contains too much information in that it does not distinguish between paths prior to amplifier excitation, which would bear on saturation, and paths leading from the amplifiers which have only to do with collection, which do not bear on saturation. This dichotomy into exciting and collecting paths may be accomplished simply by factoring (6) into

$$T = (S_{12} + S_{13})^n (S_{12} - S_{13})^n t.$$

We then define two structure factors; an excitation function  $F_e$  and a collection function  $F_c$ . We have

$$F_e = (S_{12} + S_{13})^n \quad (18)$$

$$F_c = (S_{12} - S_{13})^n. \quad (19)$$

If in Fig. 3, the  $180^\circ$  phase structures had been placed prior to the individual amplifiers,  $F_e$  and  $F_c$  would have reversed in formulation.

From the point of view of saturation we are only concerned with the form of the structure factor  $F_e$ . Again considering an eight amplifier array which corresponds to  $n = 3$ , we have

$$F_e = S_{12}^3 + 3S_{12}^2S_{13} + 3S_{12}S_{13}^2 + S_{13}^3 \quad (20)$$

which provides the following excitation paths

- (i) One threefold transition  $S_{12}$
- (ii) Three twofold  $S_{12}$  transitions with one  $S_{13}$  transition
- (iii) Three single  $S_{12}$  transitions with a twofold  $S_{13}$  transition
- (iv) One threefold transition  $S_{13}$ .

To form relative magnitudes, take the relative phase of  $S_{12}$  to be  $0^\circ$  and that of  $S_{13}$  to be  $90^\circ$ . We have the following values at the lower band-edge in a 1.5:1 frequency range.

	Single-Stage Coupler	Double-Stage Coupler
$S_{12}$	0.78	0.720
$S_{13}$	<i>i</i> 0.625	<i>i</i> 0.694

In Table I are tabulated the terms of (20) where the quantity

$$\frac{1}{(2^{\frac{1}{2}})} = 0.354$$

would represent the equal term values if the coupler were an ideal 3 dB power splitter. It is evident that the amplitude variations shown in the  $F_e$  column for the single stage coupler may be quite significant and, while they are more modest for the double stage couplers, they are, nevertheless, still present. Let us propose a harsh model of saturation in which any one amplifier saturates completely at the 0.354 level. In the SAT column of Table I are listed the relative amplifier outputs after the application of saturation with the assumption of no substantial phase shift effects.

TABLE I—EXCITATION AND OUTPUT TERM VALUES  
 FOR SATURATION MODEL

Term	Multiplicity	Value for Single Stage Coupler		Value for Double Stage Coupler	
		$F_e$	SAT	$F_e$	SAT
$S_{12}^3$	1	0.474	0.354	0.386	0.354
$S_{12}^2 S_{13}$	3	$i$ 0.381	$i$ 0.354	$i$ 0.3585	$i$ 0.354
$S_{12} S_{13}^2$	3	0.3045	0.3045	0.347	0.347
$S_{13}^3$	1	$-i$ 0.244	$-i$ 0.244	$-i$ 0.334	$-i$ 0.334
$\frac{1}{2^{3/2}}$		0.354		0.354	

If we recognize that the individual amplifiers are symmetrically disposed between input and output, as shown typically in Fig. 3, then the term value corresponding to the transmission from the input terminal to the input of any one amplifier corresponds, within a minus sign, to the term value for the transmission from that amplifier to the output terminal. Therefore, to form the transmission magnitude under this model of saturation, we sum the magnitudes, respectively, of the product of multiplicity, the term value, and the value listed in the saturation column, corresponding to each of the term values. Thus, using the single couplers we have

$$\begin{aligned}
 T &= t\{0.474 \times 0.354 + 3 \times 0.381 \times 0.354 + 3 \times (0.3045)^2 + (0.244)^2\} \\
 &= 0.9095t \quad (\text{single stage coupler, 8 element amplifier}), \quad (21)
 \end{aligned}$$

while for the double stage couplers we have

$$\begin{aligned}
 T &= t\{0.386 \times 0.354 + 3 \times 0.358 \times 0.354 + 3 \times (0.347)^2 + (0.334)^2\} \\
 &= 0.9894t \quad (\text{double stage coupler, 8 element amplifier}). \quad (22)
 \end{aligned}$$

Corresponding to the single stage, eight element amplifier there is a 0.88 dB distortion at the lower band edge while, corresponding to the double stage coupler amplifier there is a 0.08 dB distortion, where these distortions occur relative to an amplifier output at eight times the saturation power of an individual elementary amplifier. The implications of these distortions must be further elaborated, however, in relating the choice of couplers on the economics of the amplifier.

The intent in design, from the beginning, was the use of a feed-forward compensation system able to "clean up" amplitude distortions of 1 dB at maximum power, namely, the use of a clean-up amplifier

having about one-fourth the output power of the main amplifier. While the 0.88 dB, corresponding to the single stage coupler, is within the 1 dB clean-up capability, it does form a reasonably large proportion of it. For many applications, however, amplifier power covers the entire spectrum of the bandwidth and the proportion of the power associated with the band edge is very much less than full power. Under these circumstances, the clean-up capabilities are quite adequate. If it is required to provide single frequency performance anywhere within the band, then about 10 per cent power output reduction is advisable.

The use of double stage couplers forms more of a fail-safe situation and the feed-forward amplifier is barely exercised. This leaves the feed-forward amplifier with its capabilities intact to handle phase and gain distortions without the excess power demand introduced by premature saturation within the main amplifier. The cost, of course, is in the use of couplers having roughly double the expense.

A further basis of choice of the double coupler lies in the use of the amplifier without the feed-forward implementation. According to the tabulation for the eight element amplifiers the term with the highest degree of saturation is  $S_{12}^3$  which has an unsaturated value of 0.386 for the two-stage coupler as opposed to the saturation level of 0.354, corresponding to a 0.72 dB saturation. Without feed-forward, this loss of capacity of the full amplifier, namely 0.72 dB, would be required to avoid *any* of the aspects of saturation. The corresponding penalty paid using the single stage coupler is 2.52 dB, which might be too high.

#### 2.4 Hybrid Power Divider Arrays

We have discussed power divider arrays using only quadrature hybrids. It might be argued that it is required, at most, to be concerned only with paired amplifiers since this is all that is required to form adequate in-band match. After having performed such a match then an arbitrary number of such pairs might be combined using in-phase, as opposed to quadrature-phase, power dividers.

There are several objections. We list and discuss them in order.

*Stability:* Quadrature couplers have excellent match characteristics from dc to, typically, greater than three times their center frequency of operation. Since match and isolation are directly related, the amplifier elements of a large quadrature coupler array stage generally do not interact over the active range of these elements, assuring stability. The control of parasitics in an in-phase divider, particularly

in a high frequency ferrite core type of divider, is not of the same degree of excellence and interactions leading to oscillation are a more severe problem.

*Match:* Assume that the array were composed of amplifier element pairs coupled via quadrature couplers, with the remainder of the array being in-phase dividers. The return loss from (13) and (14) would be 13.16 dB at the lower portion of a 1.5:1 band for a single stage coupler and 28.4 dB for a double stage, assuming the amplifier to be a perfect mismatch. The economic advantage of the single stage coupler is so major that, assuming an insistence on in-phase dividers, and all other considerations aside, a minimum single-stage quadrature coupling of four elements would be most desirable. This would lead to a 26.32 dB return loss, which is generally acceptable.

*Cost:* By far the most major advantage of the lumped quadrature coupler is its extremely low cost, particularly as a single stage device. It is reasonable to anticipate a cost of a few cents, as opposed to several dollars for other types of hybrids. In the vhf range an in-phase divider is composed of a pair, or more, of multiply-wound ferrite cores (Ruthroff transformers).<sup>6</sup> Microwave distributed couplers are vastly more complex. A hybrid array of in-phase and lumped quadrature couplers is far more costly than an array of quadrature couplers only.

*Power Handling:* Amplifier arrays under development are yielding typical average powers between 50 and 100 watts. It takes no great leap of imagination to conjecture such amplifiers in the kilowatt to multikilowatt range for any of assorted operations. Should any severe imbalances occur within the array owing to the failure of a transistor, an in-phase divider in the high power portion of the amplifier would experience large internally circulating power. If the divider contains high frequency ferrite transformers, burnout is virtually assured because of ferrite heating. Lumped quadrature couplers are air-core devices capable of tolerating kilowatt power levels without burnout; the only limitation is the dielectric strength of the insulation, which can be great.

### 2.5 A Two-Rail Array

While the authors believe the exclusively lumped quadrature coupler array to have prominent advantages over other forms of organization, it is of interest, nevertheless, to show one specific situation in which a hybrid system of in-phase and quadrature couplers has certain advantages in construction.

Consider a situation in which ferrite core implementations are not realistic to provide the  $180^\circ$  phase shifts required for all-pass operation. Such a situation occurs in the upper portion of the uhf region, and beyond, where the ferrite magnetization can no longer follow a rotation mode. Both in-phase dividers and differential  $180^\circ$  sections become much more expensive and cumbersome, but let us assume that the expenditure is warranted in providing two each of these aforementioned devices.

Figure 5 uses the in-phase dividers in a fashion reminiscent of two rail logic. Two universes are formed  $180^\circ$  apart via the in-phase dividers and the differential  $180^\circ$  sections. Whenever a  $180^\circ$  phase shift is called for it is accomplished simply by a symmetric interchange or transposition between the two universes. Thus, the cost of a large multiplicity of  $180^\circ$  sections is reduced to that of providing only two, aside from the two in-phase dividers.

Another advantage is gained in respect to saturation. Figure 5 is, in actuality, a doubled four-way quadrature divider to form an eight element amplifier and, as such, has a lower degree of compression

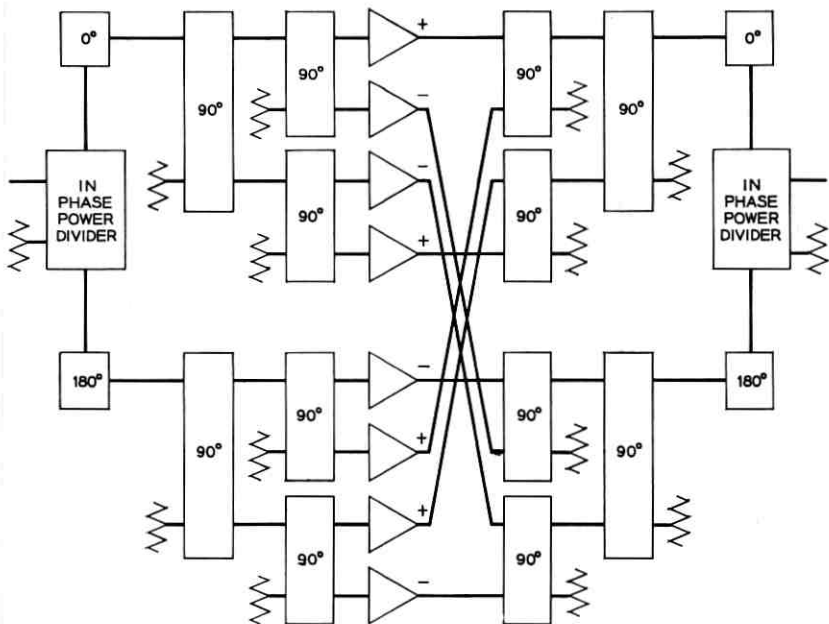


Fig. 5—Hybrid array of in-phase and quadrature couplers: doubled for way divider to form eight element amplifier.

than does a pure quadrature coupler array. Corresponding to (18) we have for  $n = 2$

$$F_e = (S_{12} + S_{13})^2 = S_{12}^2 + 2S_{12}S_{13} + S_{13}^2. \quad (23)$$

Let us now consider only the single stage coupler for which we have tabulation shown in Table II. Under the model of saturation proposed earlier we have

$$\begin{aligned} T &= t\{0.5 + 2 \times (0.487)^2 + (0.397)^2\} \\ &= t\{0.9362\}. \end{aligned} \quad (24)$$

The transmission value of  $0.9362t$ , or  $0.48$  dB, in the double-four amplifiers compares to the  $0.88$  dB compression relative to capacity of the full eight amplifier array. There is less demand on the feed-forward cleanup and power reduction is, therefore, unnecessary. Single stage couplers, therefore, produce acceptable performance and the resulting economy offsets the in-phase divider costs.

Having discussed the limitations of hybrid arrays, is Fig. 5 a workable system? The two major questions one may pose are those of power and stability. The experimental sections of this paper disclose that such a structure was successfully constructed for the 75 Mc amplifier. The ferrite loaded in-phase dividers were adequately broad, extending beyond the range of significant transistor activity, and stability was not the problem. However, the means to provide power handling capability within the ferrite transformers was a problem.

Assume that the amplifier were to be designed, not on a fail-safe basis, but on the assumption that all stages operate appropriately. Since the in-phase power divider (Ruthroff hybrid) has a conjugate antisymmetric port, can this port be used to save the need for the  $180^\circ$  differential phase shifters? The answer is negative in that the antisymmetry port would require power transformation through the ferrite. Since the core must be small to avoid circuit parasitics, the

TABLE II—SINGLE STAGE COUPLER

Term	Multiplicity	Value $F_e$	SAT
$S_{12}^2$	1	0.608	0.5
$S_{12}S_{13}$	2	$i 0.487$	$i 0.487$
$S_{13}^2$	1	-0.397	-0.397

handling of large continuous power might cause burnout. The symmetry port barely excites the ferrite and its use is indicated.

The circuitry of a simple 1:1 transformer is much less complex than that of a Ruthroff hybrid and the  $180^\circ$  section admits construction as a heavy core ferrite reversing transformer. In the event that the power might yet be too high to sustain in the reversing transformer, simple nonferrite circuits are available which produce  $180^\circ$  phase differentials over a 3:1 bandwidth.

As stated, this system does not contain the reliability feature discussed earlier. Transistor failure produces severe imbalance in the array and ferrite excitation in the transformers would result, with possibly deleterious effects at high average power. The specific amplifier design using the transformers with which the authors were concerned, related to pulsed operation, and this failure possibility was not significant.

### 2.6 Out-of-Band Filters

We have, up to now, considered in-band performance in which the return losses of the various stages were adequate to suppress multiple reflection effects. Out of band, the power split of the couplers becomes highly unequal and the input reflection into a quadrature-coupled pair of amplifiers approaches the amplifier reflection.

A simple fix for this unstable multiple interactions situation is obtained through the use of band-pass multiplex filters. In band, these filters provide excellent transmissions between various stages of the filter; out of band, all energy is transmitted reflectionlessly into dummy loads, with high isolation between the previously well coupled ports.

The multiplex, or out-of-band filters, are themselves quadrature couplers having a desired synthesis of  $|S_{12}|$ . The design through quadrature coupler techniques<sup>6</sup> is made to assure the wideband match required for stability. In the construction of the amplifier system, the use of these filters was determined on a practical basis. If stages directly feeding one another tended to oscillate, an out-of-band filter was injected between them and a large margin of stability was restored in each case.

### 2.7 Comparison with Distributed Amplifiers

The distributed amplifier is a chain of active elements in contrast to the parallel-like arrangement of the binary complex tree. Since

the excitation varies along the chain one must reduce the gain of each successive stage to preserve equal power output per stage. The implicit assumption here is that each amplifier stage has been designed for power output to the limit of its intrinsic power capability. The gains of the various stages in sequence are clearly interdependent.

There are four major advantages of the coupler array over the distributed chain:

(i) The gain profile along the chain in a distributed amplifier is tailored to accommodate to a presumed performance of each stage, and the net energizing of any one stage in the chain is a function of all those preceding it. Fluctuations of performance in time, or simple tolerance effects, are cumulative. This is not true for the coupler array in which each element is orthogonally energized.

(ii) Imperfections along a chain produce multiple internal scattering with a necessary result of rapid gain variation with frequency. In a signal flow sense, each active element of the coupler array is "hit" only once with substantially no multiple reflection.

(iii) In the event of the failure of a single element of a distributed amplifier chain, the transmission properties are greatly modified, producing no fail-safe guarantees. Through the orthogonality properties of the coupler array construction, the failure of any one active element component simply causes its ordinarily contributed voltage to be subtracted from the common mode without any catastrophic interactions with the other properly functioning components. Thus, the coupler array provides a fail-safe redundancy.

(iv) The return loss properties of a quadrature coupled array improves with complexity. The return loss of a chain, contrariwise, deteriorates with complexity.

The intrinsic return loss property of a quadrature coupled array improves with increasing complexity through the presence of an ever greater number of parasitic-mode absorbers. A chain composed of imperfectly isolated stages becomes ever more difficult to match with an increasing number of stages.

### 2.8 *Dynamic Range*

It is evident that coupler distributed systems provide increased power in proportion to the number of active elements. Notice that this increased power output comes with little expense to the system noise temperature over that of any one of the active elements, aside from the copper loss of the couplers.

The noise emission of any one amplifier is spontaneous and, as such, is entirely uncorrelated with that of any other active element. The coupler system is a  $2^n = N$  mode system and, with this lack of internal correlation, each active element as a  $\delta$  function source equally stimulates each mode. Of the  $N$  modes,  $N - 1$  are absorbed in the dummy loads, and only  $1/N$  of this power finds egress. With  $N$  individual sources, the output noise emission is  $N \times 1/N$  of the noise power of any one element, and so, is just the noise emission of one of the elements.

The dynamic range of the system is given by the ratio of the power at saturation to the noise power emitted over the amplifier bandwidth. Since the upper limit of the power has increased by a factor of  $N$ , and the noise level is unaffected, the dynamic range also increase by a factor of  $N$ . It should be recognized that the dummy loads of the coupler system occupy only ports orthogonal to the power transmission path, hence, none of these loads contributes to noise. It is concluded, therefore, that the coupler organized power multiplex increases dynamic range with insignificant noise figure deterioration.

### III. EMITTER FOLLOWER AMPLIFIERS

#### 3.1 General Considerations

The desire to deliver large power requires, in turn, a choice of an active element compatible with that power, together with a capability of supplying the circuit demands for proper frequency behavior. High power transistors always exhibit large internal capacitances and are limited in bandwidth.

The major problems arising in a general design that uses power transistors are the circuit complexities to realize the desired frequency characteristics, and the reproducibility from device to device for large variations of the internal parameters. The resolution of these problems may be carried out effectively by means of the emitter-follower amplifier.

The emitter follower, the analogue to the cathode follower, is generally used as a buffering device in transforming, at substantially a unit voltage gain, between a high impedance source and a low impedance load. While it is well recognized that power gain exists, a means for obtaining voltage gain between equal impedances has been viewed as demanding too complex a use of transformers in respect to parasitic elements. The eminent desirability of the emitter follower

comes, of course, from its large self-degeneration which makes its response fairly impervious to internal parameter variations.

### 3.2 Marriage of Emitter Followers and Quadrature Couplers

Let us review some pertinent features of the ideal emitter follower, where the connotation of ideal implies an infinite input impedance, a unit voltage gain, and very low output impedance. Figure 6 shows the insertion of an ideal emitter follower between a normalized Thevenin generator and an equal impedance load. Since the open circuit voltage is twice that delivered to a matched load, the generator is characterized by a voltage of amplitude 2. The insertion of the emitter follower, therefore, doubles the voltage ordinarily delivered by the generator to the load, and a 6 dB gain results.

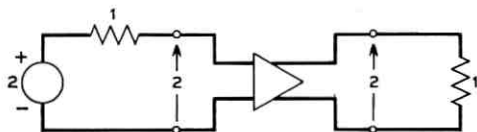


Fig. 6—Thevenin equivalent of insertion of ideal emitter follower.

This gain, however, does not lend itself to a simple transformerless cascade of emitter followers as seen in Fig. 7.\* It is evident that having achieved a voltage level of 2, this amplitude is transferred from section to section without further enhancement. The fallacy in forming this simplistic cascade is that match has not been restored from stage to stage, remembering that it was precisely through the interface of a matched source and open circuit that the 6 dB gain was achieved.

This situation is rectified by the use of quadrature couplers to pair emitter followers as shown in Fig. 8. The harnessing structure of the couplers forms an all-pass unity transmission network and the gain takes place via the mechanism of Fig. 6. Since the couplers do restore match, substantially, at the input as well as the output, this circuit is capable of iteration with return losses as given by (7). Specifically, incident waves of amplitude  $S_{12}$  and  $S_{13}$  impinge, respectively, on each of the emitter followers. Since each emitter follower is an open circuit, a voltage reflection factor of unity doubles each of these incident

\* The lack of a transformer distinguishes this cascade from a Darlington network in which cumulative power gain occurs only because of impedance transformation.

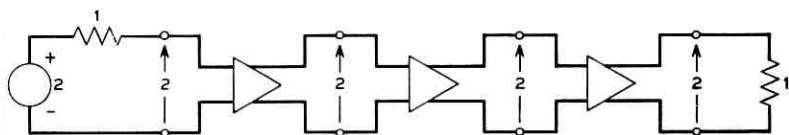


Fig. 7—Transformerless cascade of emitter followers.

voltages, forming emergent waves of  $2S_{12}$  and  $2S_{13}$ , respectively. The termination is excited by an amount  $2(S_{12}^2 - S_{13}^2)$  which, from (5), demonstrates a 6 dB gain.

Since the circuit of Fig. 8 shows an inherent 6 dB gain, no transformers are required to achieve this modest, but highly useful, gain. However, a mild input or output voltage transformation might be used to raise it somewhat beyond this value. From the point of view of power generation, the stages shown in Figs. 1 through 3 might increase at a four-fold rate. Such proliferation of circuit complexity seems not nearly so modest.

### 3.3 Real vs. Ideal Emitter Followers

The ideal emitter follower is a most imperfect representation of the real device. However, it is not too difficult to patch things up to obtain a creditable performance within the frequency range of our interest. Figure 9 is a simplified high frequency equivalent from which we may deduce the more significant features of operation.

Define the following quantities:

$$Y = 1 + i\omega C_i = 1 + i \frac{\omega}{\omega_i}$$

$$r_b C_{cb} = \frac{1}{\omega_{cb}}$$

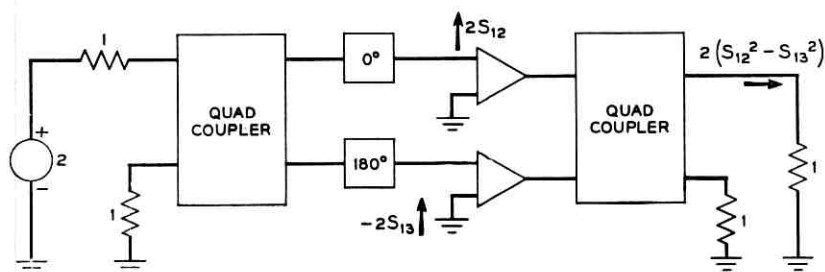


Fig. 8—Transformerless pairing of emitter followers through quadrature couplers.

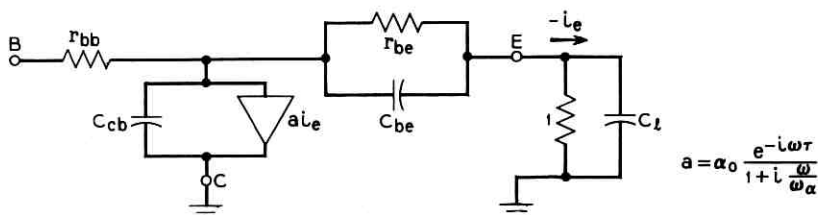


Fig. 9—Simplified high frequency equivalent of terminated emitter follower.

$E_1$  = Base signal voltage

$E_2$  = Output voltage at the emitter

$$a = \frac{\alpha_0 e^{-i\omega\tau}}{1 + i \frac{\omega}{\omega_\alpha}}$$

$\tau$  = emitter to base drift time and is of order  $0.6/\omega_\alpha$ . Analysis yields the results

$$E_1 = \left\{ 1 + \frac{i\omega}{\omega_{cb}} + r_{bb}(1-a)Y \right\} E_2 \quad (25)$$

$$Z_1 = \frac{E_1}{I_1} = \frac{\left( 1 + \frac{i\omega}{\omega_{cb}} \right) + r_{bb}Y(1-a)}{i\omega C_{cb} + Y(1-a)} \quad (26)$$

Since we are seeking nominally small gain we may, with good approximation, take  $\alpha_0 = 1$ . Expanding, and dropping terms beyond  $\omega^2$ , (25) becomes

$$E_1 = \left\{ 1 + r_{bb} \left[ 1 - \cos \omega\tau - \frac{\omega^2}{\omega_l} \left( \frac{1}{\omega_\alpha} + \tau \right) \right] + i\omega \left[ \frac{1}{\omega_{cb}} + r_{bb} \left( \frac{1}{\omega_2} + \tau \right) \right] \right\} E_2$$

The quantity  $r_{bb}$  is small relative to unit loading and we may omit the term  $r_{bb}(1/\omega_\alpha + \tau)$  in contrast to  $1/\omega_{cb}$ . We have then

$$E_1 = E_2 \left\{ \left[ 1 - \omega^2 \left( \frac{1}{\omega_\alpha \omega_l} + \frac{\tau}{\omega_l} - \frac{\tau^2}{2} \right) \right] + \frac{i\omega}{\omega_{cb}} \right\} \quad (27)$$

We perceive in (27) a negative real part resulting from the Miller effect action with respect to  $C_l$ . The tuning procedure demands flat power gain, and we may offset the decrease of the real part in (27)

against the rising imaginary portion to maintain constant magnitude. Assuming small parasitics at the frequency of operation, the constant magnitude condition yields

$$\frac{1}{\omega_{\tau b}^2} = 2r_{bb} \left( \frac{1}{\omega_2 \omega_1} + \frac{\tau}{\omega_1} - \frac{\tau^2}{2} \right). \quad (28)$$

A value of  $\omega_1$  always exists to satisfy (28).

According to (27) and (28), the voltage appearing at the base emerges with unit gain from the emitter. The question, indeed, is what voltage appears at the base? To determine it, we examine the input impedance function given in (26) to within first order terms in  $\omega$ . We find

$$Z_1 = r_{bb} + \frac{1}{i\omega \left( C_{cb} + \frac{1}{\omega_\alpha} + \tau \right)}. \quad (29)$$

While (29) has a disconcerting form with respect to dimensions, as does (28), that a unit terminating impedance is dimensionally concealed in these results. Under these circumstances,  $r_{bb}$  is small compared with unity and we momentarily neglect it in comparison with the series capacitance  $C_{cb} + 1/\omega_\alpha + \tau$ .

Assuming this capacity not to be excessively large, it may be incorporated as a terminating element of a bandpass filter that has a characteristic impedance equal to that of the generator. Over its bandwidth the generator incidence is maintained to within the time delay of the filter circuit and all the appurtenances of the ideal emitter follower are realized; an incident signal is delivered at matched impedance from the generator to the open circuit, and the voltage at the input is transmitted to the output in substantially frequency-independent fashion.

In general, this bandwidth is far larger than the 1.5:1 frequency width desired and, corresponding to this gain-bandwidth availability, tradeoff may be made with the bandwidth to enhance the gain by using appropriate input circuit design. This circuit may also compensate for  $r_{bb}$  by providing high frequency peaking to offset it.

### 3.4 Linearity

While much has been said here of the linear behavior of the emitter follower, the feedback which causes the emitter to follow the base extends well beyond the region of linear characterization. In large signal excitation the interelectrode capacitances vary throughout the

cycle, causing nonlinear interactions with the circuit environment. A particularly significant term is  $C_{ob}$ , but its variation is greatly damped by the generator impedance. Aside from the considerations of frequency characteristics, it is the desire to maintain high generator damping that vitiates a greater use of impedance transformation to yield higher gain.

In class A operation the region of linearity is limited, in any event, by current cutoff. In class AB push-pull operation the distortion takes the form of a slightly different low and high signal gain. This last distortion may well be the more insidious of the two and it is only the use of the feed-forward system which makes it acceptable. This acceptability is extremely significant because the push-pull class AB operation, when operated near the class B state, has several advantages over class A:

(i) Power supplies are substantially reduced.

(ii) Since all of the transistor current is used to produce RF power, and since twice the number of transistors are used, about four times as much power is generated for the same amount of coupler hardware.

(iii) Lower average currents yield wider band response because of lower average internal capacitance. In actual measurement the limit of the linear range seems closely identified with avalanche breakdown, for which there is the danger of thermal damage to the transistor.

There is a notable disadvantage in class AB operation, but it is not too objectionable in a 50 per cent or less duty cycle amplifier. As the excitation varies, the average current varies, shifting bias points. Further, the operating temperature may shift the quiescent point in each transistor, significantly affecting low signal distortion. However, an active clamp may be used which samples the off-signal voltages and restores proper operating levels. This clamp is described in Section 6.8.

### 3.5 *Economics of Coupler Organized Emitter Follower Amplifiers*

While it is implicit throughout the technical descriptions, one general feature which must be stressed is the significant economy possible through emitter followers. Because of its large internal negative feedback, reproduction of the transistor becomes a problem of relatively negligible proportions.

In contrast to the situation in which refined transistor devices may

be improved in yield, we have a situation in which frankly cheap devices are used to provide an adequate yield. The low potential costs of quadrature couplers and relatively inexpensive transistors, operating well beyond their traditional ranges, forms the prospect of much less expensive, high performance amplifiers.

Acceptable within this framework may be a moderate aging of semiconductor parameters, usually a bugaboo in device manufacture. Its importance is diminished not only through the degeneration offered by the emitter follower circuit, but by the feed-forward provisions as well. Thus, cheaper encapsulations might be permitted than otherwise would be, admitting possibly consequential cost reductions in transistor fabrication.

#### IV. FEED-FORWARD

##### 4.1 *Feedback vs. Feed-Forward*

Much of the development of the high power amplifier stands or falls on the ability to devise a proper error correcting system. As stated in the introduction, the choice made in the design of this system, if indeed a choice was open, was a "feed-forward" construction.

In the late 1920's, H. S. Black conceived of feed-forward as well as feedback, and his patent disclosures show either grid or plate injection of the error signal.<sup>3</sup> The grid meant back injection whereas the plate meant forward injection and either was adequate to within  $180^\circ$  of phase. Clearly, the plate injection was at a higher level and required subsidiary amplification, while grid injection ingeniously reused the same amplifier.

With an occasional, but short lived, resurrection, feed-forward fell into a general disuse until independent revivals by McMillan and Van Zelst.<sup>1, 2</sup> These were followed by further activities by Deighton, Cooke-Yarborough, Miller, and Golembeski.<sup>6, 7</sup> The essence of the McMillan and Van Zelst disclosures was to combine both techniques of Black by providing frequency shaping networks simultaneously in feedback as well as in feed-forward. The aim was to provide channel redundancy as well as parameter desensitizing. The Deighton paper uses this technique to stabilize a particular circuit of a pulse amplifier while Golembeski has represented a generalized parallel channel configuration and developed a synthesis procedure and realizable conditions.

Even though the basic inadequacy of feedback techniques were evident, we developed the feed-forward compensation system because we needed to provide stable correction to an amplifier that had a relatively large time delay. Indeed, simple physical insights not only repudiate the use of feedback but force use of the alternative, for our case.

Feedback, a technique which has been used with much success, attempts a causal contradiction: after an event has occurred, reshape its cause. This violation may be resolved only by time smearing the event to blur the distinction between "before" and "after" to an adequate degree. This smearing requires a prescribed control of spectral response; a craft too well known to presume further comment.

Feed-forward evolves from entirely different premises, avoiding causal anomaly.<sup>8</sup> Instead of seeking to reverse time, it recognizes the passage of time. Error is determined in relation to a time-shifted reference and corrected in a time sequence compatible with the main signal. No obscuration of time is permitted and frequency shaping to attain stability is irrelevant.

The fact that frequency shaping (that is, control of the return ratio function) is irrelevant is of major importance. A feedback amplifier consumes a good portion of its gain-bandwidth figure of merit in controlling the return ratio well beyond the band of interest to prevent instability.

The power transistors demanded for economical construction of the power amplifier clearly are not geared to high frequency application. To obtain the needed bandwidths, gains must be kept modest. The amplifier, then, would be built of a sufficiently large number of stages to offset the gain consumed in a feedback correction. With this number of stages, however, the excess phase would mount to such degree as to be beyond control in a feedback system.

The feed-forward system has three strikingly important features:

- (i) Feed-forward correction does not reduce amplifier gain.
- (ii) Gain-bandwidth is entirely consumed within the band of interest.
- (iii) Feed-forward realization is independent of the magnitude or shape of the amplifier time delay and it exists in general.

We demonstrate these features in the following section. The major point to be made here, however, is that it is not a question of feedback vs. feed-forward as a choice, but as a necessary engineering decision.

#### 4.2 Detailed Description of Feed-Forward Operation

Figure 10 is the general block diagram of the feed-forward correction system. Input signal is divided into two portions; that going into the amplifier and that entering a reference path. The signal is amplified through the main amplifier A and a sampling is taken through a directional coupler with very flat coupling  $1/G$ , where  $G$  approximates the in-band gain of A. This sample is compared with the reference path signal which has been delayed a time  $\tau$ , a quantity approximately equal to the time delay of the main amplifier.

A time-shifted error is thus obtained and it is amplified by a subsidiary amplifier whose gain  $G'$  is such that this error is restored to the appropriate level to cancel the error of the main amplifier. If the subsidiary amplifier consumes a time roughly equal to  $\tau'$ , a time delay of that value is inserted in the main amplifier path. The injection of the error back into the main line takes place through a reactive two-port, shown typically as a transformer.

The choice of a reactive two-port, as opposed to the use of a coupler four-port, is made irrespective of the ordinary desire of keeping the outputs of both amplifiers decoupled. While a coupler would isolate the subsidiary amplifier from the main amplifier, the cost of energy losses of the subsidiary amplifier into the dummy loading of a coupler would be unacceptable.

While we have emphasized the care to be taken with time delay, there is an implicit condition within the phase specification to produce error cancellation. Since time delay is the slope of phase with respect to frequency, assuming small phase curvature, it is adequate to adjust phase at but a single point in the band and have it track throughout. In the event that the main amplifier and the subsidiary amplifier had large phase curvatures, then  $\tau$  and  $\tau'$ , respectively, would require more complex realization than simple delay lines; they would have to incorporate the same curvatures as well. Evidently, this may be extended to yet higher phase derivatives with respect to frequency.

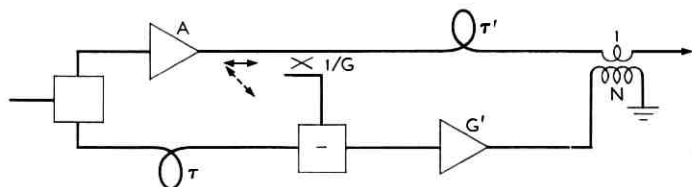


Fig. 10 — One loop feed-forward network.

As indicated, the gain and phase of A and the gain and phase of  $G'$ , are known only to within some first order tolerance. Via the coupler  $1/G$  and the time delay  $\tau$ , strict gain and phase standards are set with which to compare the amplifier A. These form a Procrustean bed such that anything within A that does not fit these standards is to be treated as error, and chopped off or stretched. In processing just this error portion through  $G'$  and  $\tau'$ , first order errors of the latter two quantities only produce negligible second order quantities in error correction.

Having "feed-forward compensated" the amplifier A in this manner, it is quite proper to consider this circuit complex as a new amplifier, B, which is to be "feed-forward compensated." Since B has desired performance to within second order errors, this new compensation would reduce the errors to third order errors. This method of successive compensation may be iteratively compounded, controlling errors to a very high degree. A two-loop system is shown in Fig. 11.

#### 4.3 Transformer Design for Error Injection Circuit

As already discussed, the use of hybrid couplers for error injection is avoided, since any such matched device leads to excessive power loss to the system. If, for example, the coupler provided equal power division, then a 3 dB power loss would be sustained by the main amplifier. If a division ratio more favorable to the main amplifier were used, the consequences to the subsidiary amplifier might well prove disastrous. It could be called on to deliver a greater power than the main amplifier, in some instances, to compensate moderate errors in that main amplifier.

We will try to design a feed-forward compensation system that can

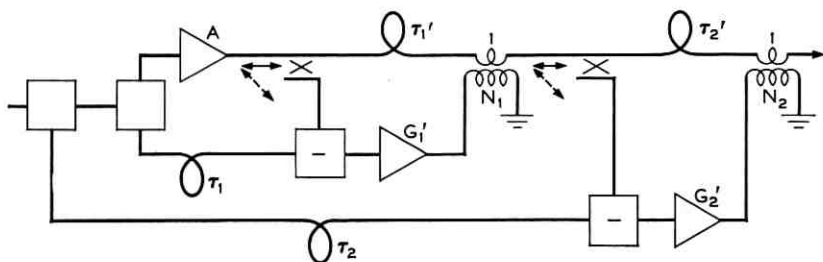


Fig. 11 — Two loop feed-forward network.

correct the main amplifier over a range of about 1 dB, using transformer injection.

Appendix 2 shows that the optimum transformer ratio is

$$N = \sqrt{\frac{1 - \delta_p}{\delta_p}}, \quad (30)$$

under the condition that the subsidiary amplifier sees a matched load when it is correcting the peak relative in-phase voltage error,  $\delta_p$ . At this point the power being delivered by the subsidiary amplifier is

$$P_s = \frac{\delta_p}{1 - \delta_p} P_m, \quad (31)$$

where  $P_m$  is the main amplifier peak power. It is shown that the mismatch introduced by the transformer results in no loss to the power output of the system, only a small loss of gain, so there appears *none* of the loss that would be associated with a hybrid coupler instrumentation. In our case of 1 dB correction,  $\delta_p = 1/8$ , for which  $N^2 = 7$ .

The analysis shows another interesting feature. If, with no feed-forward circuitry present, a relative distortion occurs at peak power approximately equal to  $2\delta_p$ , then:

(i) In the presence of feed-forward circuitry the power gain is depressed by a relative amount  $\delta_p$ , so that the power necessary to produce an undistorted output is only  $\delta_p$ .

(ii) This residual distortion power of  $\delta_p$  is contributed by the subsidiary amplifier.

(iii) In this sense, a subsidiary amplifier power capability of  $\delta_p$  controls a distortion of  $2\delta_p$ .

The above design takes into account the in-phase errors, mainly in-phase compression in the amplifier at peak power. Another consideration is the ability of the above design to compensate for phase distortion. It is shown that, if the maximum relative quadrature voltage at peak main amplifier power is  $i\delta'_p$ , the relation between this and the maximum permissible in-phase voltage error is

$$\delta'_p = \frac{1}{2}\delta_p. \quad (32)$$

Then the same system which will correct a 1 dB amplitude error with  $\delta_p = \frac{1}{8}$  will provide a phase correction of  $\pm \arctan \delta'_p = \pm 3.6^\circ$  at maximum main amplifier power.

The above might seem a small phase correction range but remem-

ber that the main amplifier consists of an array of emitter follower amplifiers. To within small variable transit time effects with high power, the emitter follower amplifier would tend to saturate as a function of instantaneous excitation. Hence, saturation effects would tend to be in phase and would not seriously tax the range of quadrature correction capability. Nevertheless, from the equalization point of view, it would be well to limit phase ripple peaks to below  $2^\circ$  before applying feed-forward correction.

We emphasize that the numerical results obtained above correspond to the worst case and should not be used inflexibly. For instance, there might be some best phase positioning of the subsidiary amplifier along its transmission path to optimize the phase correction range. Or suitable judgment might suggest an optimum trade-off between in-phase and quadrature error correction in a specific construction.

Appendix 2 also considers two questions concerning match within the system. First it shows that, even though the subsidiary amplifier is mismatched at less than maximum excitation, reflections within the error correction loop can never be phased so as to demand either more current or voltage from the subsidiary amplifier than is demanded at peak power. Second, it considers the output mismatch and the use of nonoptimal transformers.

The term nonoptimal is meant to suggest that the transformer is not optimally designed to minimize the power demand on the subsidiary amplifier. As shown, a non-optimal transformer yields the advantage of simplifying the problems in providing very high output return loss from the amplifier system, but at major cost to the subsidiary amplifier.

#### 4.4 *Circuit Modification for Optimal Noise Performance*

As discussed, the dynamic range of a coupler organized amplifier is raised at the saturation power level in proportion to the number of active elements without deteriorating the noise level of the system. This promises a dynamic range increase of only a factor of  $N$ . It is possible to obtain much more spectacular ratios by a noise exchange with a low noise subsidiary amplifier. This improvement is of major significance since the active elements are individually high power devices emitting large noise powers and advantage is to be gained, in providing dynamic range, by working at the low end of that range.

We emphasize that the subsidiary amplifier in the feed-forward system has an entirely different function in noise reduction than does an amplifier used as a low noise preamplifier. In the latter use, the

amplifier must sample the entire signal range and, intrinsically, limits dynamic range. The subsidiary amplifier, on the other hand, handles only the spontaneous error and, consequently, a negligible portion of the coherent signal range. Therefore, the dynamic range of the subsidiary amplifier may have virtually no relationship to the dynamic range of the system it controls.

#### 4.4.1. Major Considerations

The feed-forward or subsidiary amplifier has a considerably lower dynamic range than does the main amplifier. With multiple feed-forward looping, as indicated in Section 4.2, the dynamic range of the ultimately controlling amplifier may be extremely small, yet adequate. The low power requirement of the subsidiary amplifier in such use may be turned to advantage by designing for relatively low noise figure performance.

The noise of the main amplifier is an erroneous output which the feed-forward system corrects. However, noise generated by this subsidiary amplifier is introduced in the process. The advantage of such an exchange would be lost if the signal-to-noise ratio of the subsidiary amplifier were to be lessened by the use of significant power division at the input to the reference path.

Figure 12 shows a modification of Fig. 10 to achieve optimal noise performance. Couplers  $C_1$  and  $C_3$  are made to direct most of their power to the subsidiary amplifier  $G'$ . While the gain of amplifier  $A$  must be made larger to offset the coupling loss of  $C_1$ , this increase is, in principle, irrelevant. The worsened noise figure of  $A$  is of no consequence since the error cancellation of the feed-forward system simply treats the additional noise as additional error.

#### 4.4.2. Nonideal Behavior

Of course, what we have just stated is an ideal view; the cancellation is imperfect. The primary source of this imperfection lies in the varia-

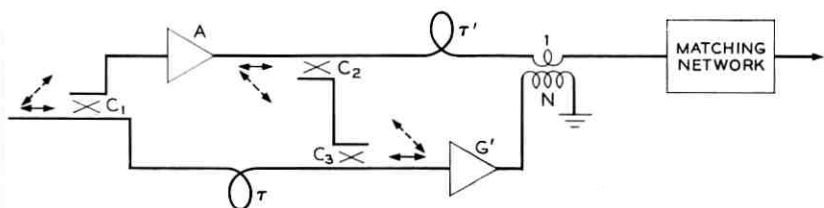


Fig. 12 — Modification of feed-forward network to improve noise performance.

tions of the subsidiary amplifier, which is uncontrolled. A realistic quantitative assumption might be a power transfer variation of  $\pm 5$  per cent over the frequency range or a peak voltage transfer variation of  $2\frac{1}{2}$  percent. This latter number limits the cancellation to a power ratio of  $(0.025)^2$  or 32 dB. Let us assume further that  $C_1$  is a 12 dB coupler, increasing the excess noise of the main amplifier by that amount. Nevertheless, even with a reduction of the 32 dB cancellation possibility by 12 dB, the net noise of the feed-forward compensated system is the sum of the excess noise of the subsidiary amplifier plus a 20 dB reduced excess noise of the main amplifier. Since the subsidiary amplifier noise is presumed minor, relative to that of the main amplifier, this represents a major gain in performance. We have neglected the small transmission loss of  $C_1$  which deteriorates the noise performance slightly.

In multilooping along the lines of Fig. 11, successive reductions of the above order may be accomplished until the noise of the lowest excess noise subsidiary amplifier stage dominates the process. Because of the rapidity of convergence it is questionable whether more than three subsidiary loops would ever be meaningful with respect to noise minimization.

#### 4.4.3. *Subsidiary Amplifier Stabilization*

Since the limit of noise cancellation of the high power amplifier relates to gain variations of the subsidiary amplifier, we suggest another form of multilooping, differing from Fig. 9, in which the subsidiary amplifier itself is feed-forward stabilized. We believe that this variant, shown in Fig. 13 is inferior to that of Fig. 11 in that a much more restrictive tolerance is placed on couplers  $C_2$  and  $C_3$ . This is so because the error determination is now only "one shot" with reference to the main amplifier as opposed to the progressive error sampling of the earlier system.

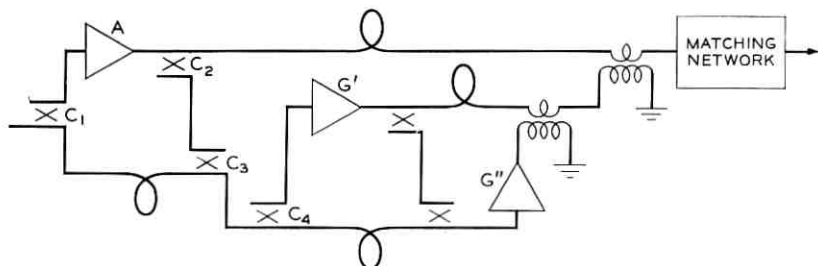


Fig. 13—Modification of low noise system in which subsidiary amplifier is stabilized.

Nevertheless, the looping progression shown in Fig. 13 requires that some weak subsidiary amplifier only be confronted with a next stage merely one degree higher in power. In contrast, Fig. 11 requires that all subsidiary stages work into the highest power level of the system. That this might be a consequential difference is not yet clear.

#### 4.5 Subsidiary Amplifier Gain

In the development to this point we have given the relationship between subsidiary amplifier gain and main amplifier gain in various implicit forms. Here we explicitly state this relationship in terms of the insertion power gain  $G_m$  of the main amplifier and  $G_s$  of the subsidiary amplifier.

Let us form a skeletal schematic of the levels of power flow in the full amplifier, which is shown in Fig. 14. We define the following quantities:

$L_m$ —Loss through input power splitter to main amplifier

$L_s$ —Loss through input power splitter to subsidiary amplifier

$L'_s$ —Loss through the error coupler to subsidiary amplifier.

If we particularize the circuit between the subsidiary amplifier output and the load,  $1 + 1/N^2$ , we find the equivalent shown in Fig. 15, whereas the output of  $G_m$  to the load is shown in Fig. 16. The amplifiers  $G_m$  and  $G_s$  are each normalized to a unit impedance and, through Figs. 12 and 13, we define the transfer functions  $T_m$  and  $T_s$  to the load,  $1 + 1/N^2$ , which we determine to be

$$T_s = \frac{N}{1 + N^2} \quad (33)$$

and

$$T_m = \frac{N^2}{1 + N^2}. \quad (34)$$

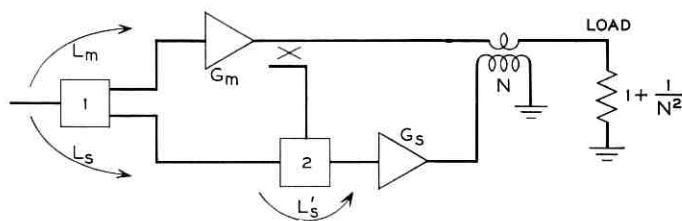


Fig. 14—Feed forward amplifier schematic.

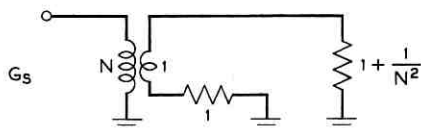


Fig. 15 — Equivalent circuit as seen by the subsidiary amplifier.

The nature of feed-forward correction is such that the overall transfer power from the input through the main amplifier path equals that through the subsidiary amplifier path. This provides

$$\frac{T_m^2}{L_m} G_m = \frac{T_s^2 G_s}{L_s L'_s},$$

which, through (33) and (34), yields

$$\frac{G_s}{G_m} = \frac{N^2 L_s L'_s}{L_m}. \quad (35)$$

Equation (35) determines the differential gain of the subsidiary amplifier over the main amplifier.

We may quantitatively evaluate the differential gain for a particular, but typical, low noise figure amplifier. For this amplifier we have

$$L_s = L'_s = 1.07 \rightarrow 0.3 \text{ dB},$$

$$L_m = 20 \rightarrow 13 \text{ dB},$$

and

$$N^2 = 9 \rightarrow 9.55 \text{ dB}.$$

The differential gain, in dB, of the subsidiary amplifier is, in this case,

$$9.55 + 0.3 + 0.3 - 13 = -2.85 \text{ dB}.$$

In this calculation we find, as a practical matter, that the subsidiary amplifier actually has a smaller gain than does the main amplifier in a low noise configuration.

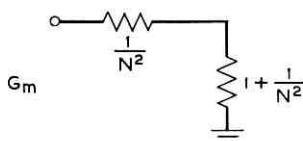


Fig. 16 — Equivalent circuit as seen by the main amplifier.

#### 4.6 Sampling Via Directional Coupling

The causal arguments, which motivate the development of this form of amplifier, imply that all sampling be done in a strictly ordered time sense. This requires sampling devices which are well isolated from reflections within the system which appear as events in improper time sequence.

Figures 12 and 13 shows the use of directional couplers for sampling. Let us assume for the moment that the output of the main amplifier, A, is perfectly matched. Under the circumstances error injection by the subsidiary amplifier G into the final transformer has only backward component of wave travel through the coupler  $C_2$  and no feedback occurs to that amplifier.

If the output port of A is mismatched, any reflections of the injected error signal create a new forward wave representing undesired signal. However, the undesired signal is sampled by  $C_2$ , treated as an error, and corrected via the correction loop.

Energy reflected back into the system from a mismatched load is similarly handled. Thus, in the steady state, the directional character of  $C_2$ , has acted to preserve the prescribed net emergent signal. To the extent that a coupler has finite directivity this ideal is blurred, but couplers with high directivities are available in practice and the idealization may be met to high degree.

Aside from its use to eliminate parasitic feedback paths, the sampling coupler stabilizes the main amplifier output impedance and provides for a high output return loss. As we have already discussed, the fixed amplifier system has an unusually high degree of linearity and, as such, is entirely describable by a Thevenin equivalent. Let us then, in gedanken fashion, measure its output impedance, which is a physically meaningful quantity.

To measure the system output impedance, a wave emanating from an external generator is made incident upon the output terminals, and its reflection measured. From Figs. 12 and 13 we can see there is a first reflection from the series impedance imaged through the 1:N transformer, and a second reflection from the main amplifier itself. However, as we have seen, this second reflection is negated via the coupling through  $C_2$  back to the subsidiary amplifier.

By design, the effect of the transformer is small and any mismatch of the subsidiary amplifier is a thoroughly negligible second order effect. The net input to the output terminals therefore appears as a resistor of normalized value  $1/N^2$  in series with a perfect absorber;

a total resistive impedance of  $1 + 1/N^2$ . Since  $N^2 = 7$ , the mismatch to unity is relatively small and a simple matching section may be used to produce a large return loss across the band of interest. Most importantly, this return loss relates only to the quality of passive circuits and is essentially independent of the active system.

A simple catechism helps us form an effective perspective in recognizing the role of directional coupler sampling in error correction in relation to the two other, better known, types.

(i) Voltage sensing produces an unvariable emergent voltage, making the source impedanceless.

(ii) Current sensing produces an unvariable emergent current, making the source admittanceless.

(iii) Incident wave sensing produces an unvariable emergent wave, making the source reflectionless.

Within this context, the use of directional couplers to provide incident wave sensing is not limited to only the feed-forward system described here to produce a highly matched generator.

#### 4.7 *Parallel Literature on Feed-Forward Technique*

It seems clear that the presently described structure is closely related to the previously mentioned class of redundancy and desensitization networks.<sup>1, 2, 7</sup> Nevertheless, we feel that we emphasize certain important points in this paper that are contained, but not obvious in the general treatments:

(i) The significant role of matched delay is cited, from causal considerations, as the basic means of providing a degree of correction realization unavailable in feedback. The degree of correction is arbitrary.

(ii) The absence of stability considerations in feed-forward.

(iii) Realization of full gain-bandwidth, fully consumed within the band of operation, without restriction on the degree of correction.

(iv) The advantages of the use of unequal amplifiers with respect to noise figure.

(v) Use of coupler sampling both for stability and high output return loss.

(vi) Transformer injection of the error correction to minimize loss of power capacity.

## V. SPECIAL COMPONENTS CONSIDERATIONS

It is intended to review the coupler art elsewhere; we are not concerned with it here. Indeed, the couplers that we used were commercially available items\* and were not, themselves, the source of any general concerns.

There were, however, certain specific concerns in the experimental developments which did not materialize. While they did not manifest themselves for our particular equipment, they still might show up in other circumstances.

### 5.1 Error Injection Transformer

While not in exact correspondence with the specific values chosen for the mathematical model, a 3:1 transformer is close enough to the value needed and generally can be constructed over the necessary bandwidth range at the frequencies of interest. The major concerns were the practical one: can a ferrite loaded transformer sustain the power levels flowing through it?; and the hypothetical one: what if the frequency range were beyond the capabilities of ferrites?

In seeking other realizations of the transformer, one must appreciate that the transformer shown in Fig. 14 is little more than a schematic format of the circuit. Specifically, the transformer is a reactive reflection isolating the subsidiary and main amplifiers. Any other reactive two-port having the same insertion loss would, according to Weissfloch,<sup>9</sup> be equivalent to the transformer to within the insertion of phase corrections at each of the ports. Further, the error injection might take the form of a dual shunt current feed as opposed to the series voltage form and, as such, there are quite flexible options in design.

While there is hardly a dearth of networks to produce the desired circuit function, we shall develop one which seemed simply suited for synthesis. Figure 17(a) shows a tee of inductances. The power transmission  $|T^2|$  vanishes at zero and at infinite frequency without any intervening singularity so that, as shown in Fig. 17(b), a stationary transmission value exists. If the circuit is modified as shown in Fig. 18(a), by introducing the shunt capacity  $C''$ , a high frequency propagating region is introduced as observed in Fig. 18(b). With appropriate proportioning of the capacitance an inflection region is introduced at the point of stationarity and a flat insertion loss region is obtained. This flat insertion loss may be corresponded to the trans-

\* Merrimac R&D Co., West Caldwell, N.J.

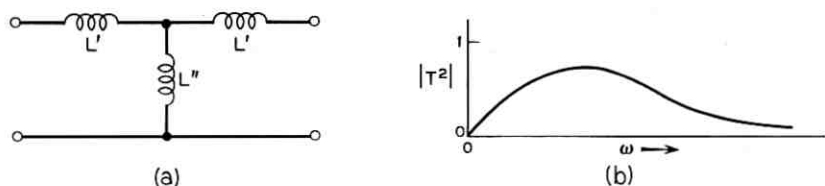


Fig. 17 — Network with stationary transmission.

former  $N$  within the Weissfloch equivalent and the various component values are shown in Fig. 19.

For completeness we provide the relevant formulations. If  $L$  is the numeric power insertion loss, we have

$$L = 1 + \frac{1}{4} \left( N - \frac{1}{N} \right)^2; \quad (36)$$

$$L = 1 + \left[ \omega L' + \frac{\sqrt{3L'^2}}{1 + 6L'^2 - 3L^4} \left( \frac{\omega}{\sqrt{3L'}} - \frac{\sqrt{3L'}}{\omega} \right) (1 + \omega^2 L'^2) \right]^2; \quad (37)$$

$$L'' = \frac{1 + 6L'^2 - 3L^4}{6L'^3}; \quad (38)$$

and

$$C'' = \frac{2L'}{1 + 6L'^2 - 3L^4}. \quad (39)$$

The net results of these machinations are shown in Fig. 20. Since the network has a relatively high inductive impedance at midband, a short transmission line  $\theta$  is used to present a resistive input. Thus input impedance is a minor perturbation and frequency effects are correspondingly small but, if desired, a low  $Q$  resonator matching network in tandem with the load may be employed for higher degree matching.

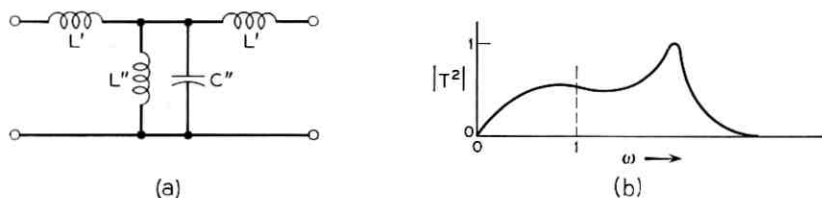


Fig. 18 — Modification to produce an inflection point.

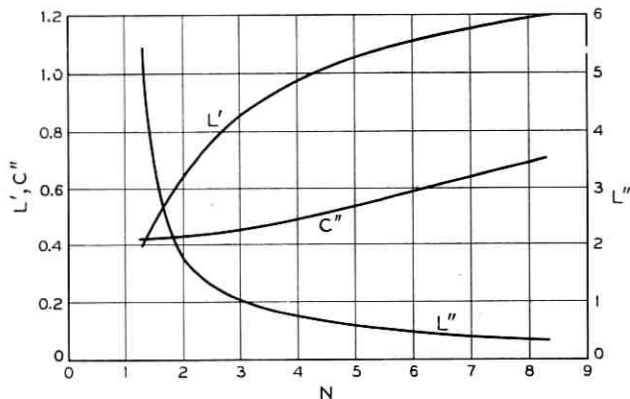


Fig. 19—Component values for equivalent transformer.

The load conductance  $G_L$  is equal to  $1 + 1/N^2$  in dual fashion to series injection form shown in Fig. 21.

5.2 180° Phase Differential Networks

The 180° phase differencing networks are staples of the interconnection formats we have described here. They can be realized to a good degree in the tens of magacycles range as a pair of mutually reversed ferrite transformers together with capacitive compensations to account for the differences in the way in which the winding capacitance is energized.<sup>10</sup> There was fear that the power handling capacity might prove excessive for the ferrite or that the parasitics might dominate. These

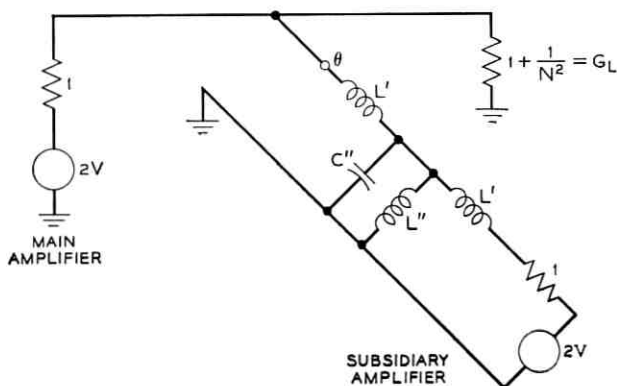


Fig. 20—Shunt error injection using transformer network equivalent.

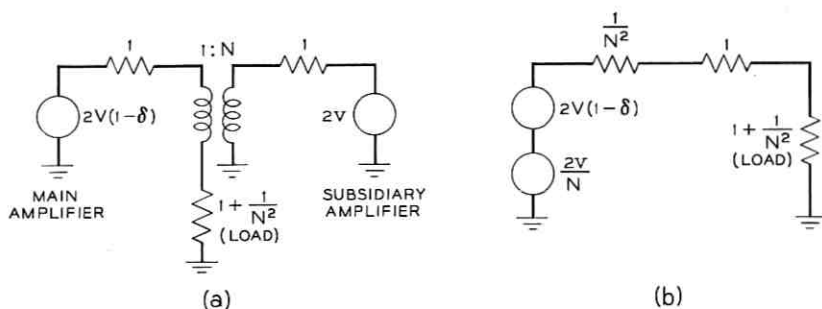


Fig. 21 — Thevenin equivalents of subsidiary amplifier feed into main amplifier output circuit.

were exactly the anticipatory fears with relation to the injection transformer and, in precisely like fashion, the fears proved groundless at the power level and the frequency range of operation.

Nevertheless, there is the question of what to do in the event that ferrite transformers are unrealistic. We use a single section quadrature coupler together with a technique credited to E. M. T. Jones to produce the desired realization. Jones's technique recognizes that the transmission between the input and its conjugate port, in a symmetrically mismatch terminated quadrature coupler, is directly proportional to the reflections terminating the coupled ports. The transmission in such a device whose coupled ports are short-circuited differs by  $180^\circ$  of phase from that same device coupled into open circuits.

Equations (10) and (11) show a single section coupler used in such application to have only a relatively narrow band for high return loss and that the transmission is more akin to that of a resonant section. Further analysis shows, indeed, that the identification with a resonator is a very good one and that the conventional technique of adding prior and subsequent resonators to form a filter chain is entirely applicable.

With the coupled ports open-circuited, the equivalent circuit is exactly a series resonator with both the inductance and capacitance corresponding perfectly to unit impedances at band center. A maximally flat three section filter chain is constructed by bounding this resonator on both sides with shunt resonators composed of elements possessing exactly double unit impedance.

If the coupled ports are short circuited, a dual situation results. The coupler equivalent is a shunt resonator composed of unit admittances and the bounding networks are series resonators composed of elements of twice unit admittance.

Since the open and short circuited couplers are perfectly dual structures, the  $180^\circ$  phase difference is perfectly maintained irrespective of frequency. The bandwidth of the structure pair is about 3:1 before the onset of any significant transmission loss; this results in an eminently practical component.

## VI. REALIZATIONS

### 6.1 Motivation

The above philosophies and design considerations have been realized in the construction of two amplifiers intended for testing dispersive ultrasonic delay lines in the 60-90 Mc and 25-35 Mc ranges. The large loss inherent in these devices made necessary large power output while the dispersive nature of the delay imposed the requirements of linear flat gain with little intermodulation distortion. Since the delay line represents a nearly lossless capacitive load on the amplifier, the latter must be a well matched device in order to prevent large interaction effects between amplifier and delay line.

### 6.2 60-90 Mc System Performance

The first development undertaken was the 60-90 Mc amplifier. During the course of this project we learned much about the operation of a feed-forward system. This increased sophistication was applied to the subsequent 25-35 Mc system. The first amplifier is shown in Fig. 22, and it is seen to be a single stage feed-forward system with its input sampling loop and its output error correction loop which is capable

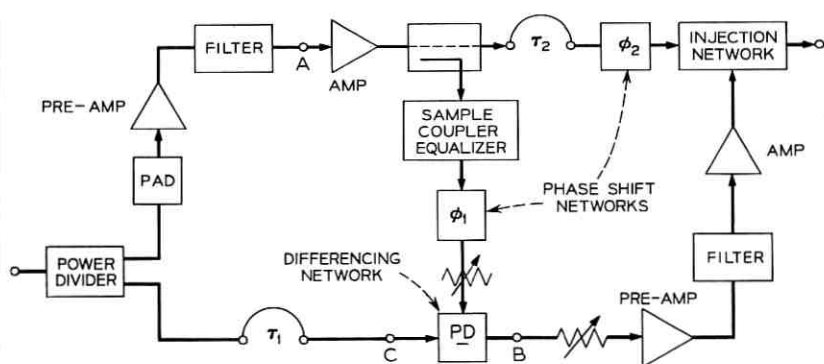


Fig. 22 — 75Mc feed forward system.

of supplying one quarter of the main amplifier power. This amplifier delivers 10 watts average power in CW operation (20 watts peak) to the 0.1 dB compression point.

At this power level the phase distortion is 1.25 degrees (see Fig. 23) at 75 Mc. The swept response across the band is shown in Fig. 24 both for small signals and at maximum power output. (The dashed curve shows the system response with the correction circuit disabled.) A sensitive measurement was made of the small signal gain and phase across the band (Figs. 25 and 26) which showed  $\pm 0.1$  dB gain ripples superimposed on a 0.5 dB slope\* and  $\pm 2^\circ$  phase deviation from con-

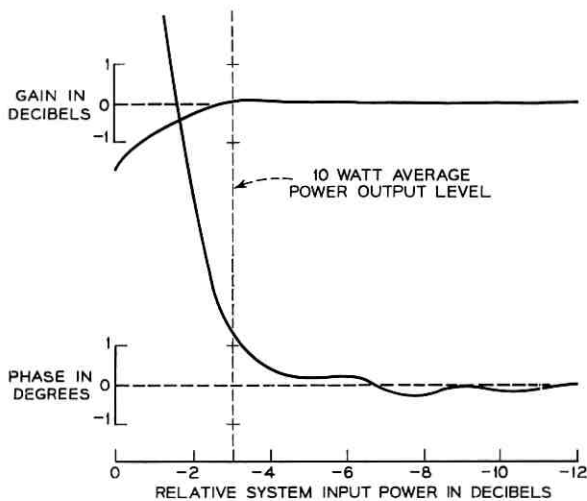


Fig. 23 — System gain and phase at 75Mc as a function of input power.

stant time delay (linear phase vs. frequency) out of a  $1300^\circ$  phase variation across the band.

### 6.3 Couplers in 60-90 Mc System

The couplers, used to pair amplifiers in the preamplifiers and in the more general harnessing in the main power amplifiers, were double stage quadrature hybrid couplers purchased from Merrimac Research and Development Co. (see Sections 1.2 and 1.3, and Fig. 27. The transfer characteristics of this coupler are shown in Fig. 28 and the input

\*The  $\pm 0.1$  dB ripples may have been partially due to a procedural error in the operation of the test set used for the measurement.

match with two identical total reflections in Fig. 29. This last figure points up one of the main advantages of the quadrature coupler type of organization; the fact that input match is maintained for arbitrary port termination as long as the two terminations are identical.

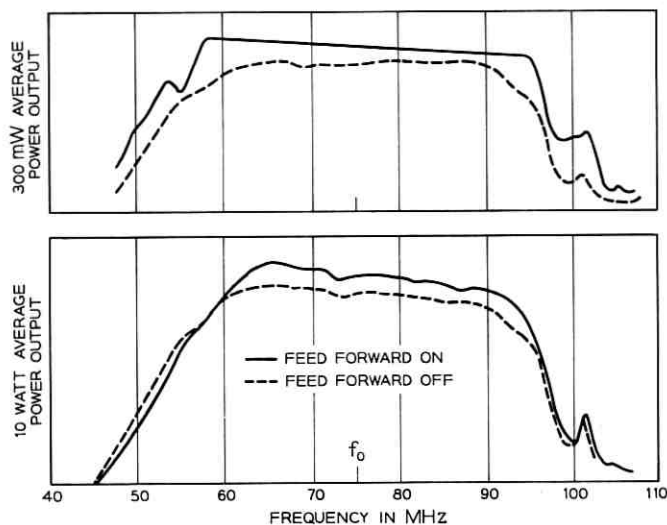


Fig. 24 — 75Mc system output as a function of frequency.

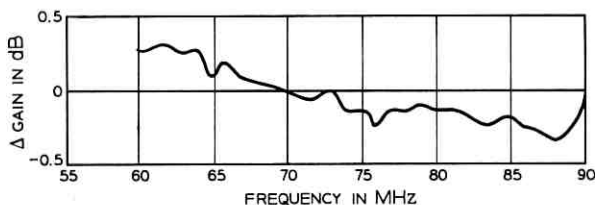


Fig. 25 — Gain variation with frequency at low power output.

#### 6.4 Amplifiers in 60–90 Mc System

The preamplifiers shown in Fig. 22 are composed of an input pair of low-level high-gain amplifiers and enough stages of intermediate power emitter follower pairs emitter follower pairs (Fig. 30) to provide sufficient power to drive the main power array of emitter followers (Fig. 31).<sup>\*</sup> All emitter followers are biased to class A operation.

<sup>\*</sup>The amplifiers used were based on designs and models provided by R. V. Goordman and R. C. Petersen.

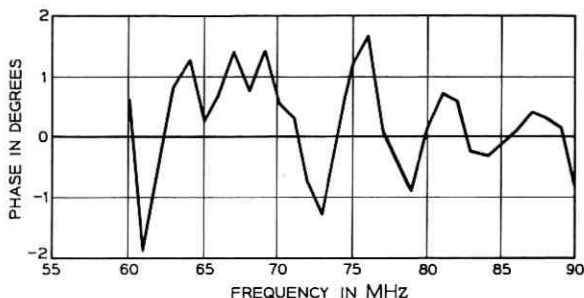


Fig. 26 — Phase deviation from linear phase vs. frequency behavior (Constant time delay). Average time delay =  $2.5\mu\text{sec}$ .

The high gain amplifiers are of a broadband design with a flat 52 dB gain from 0.2 Mc to 100 Mc and capable of 100 milliwatts output before compression at the higher frequency (greater power at lower frequency).

The drive stage emitter followers in the preamplifiers used 2N3375 transistors they have sufficiently high base impedance at these frequencies to permit some modest input transformation in order to enhance the 6 dB theoretical gain made available by driving the high

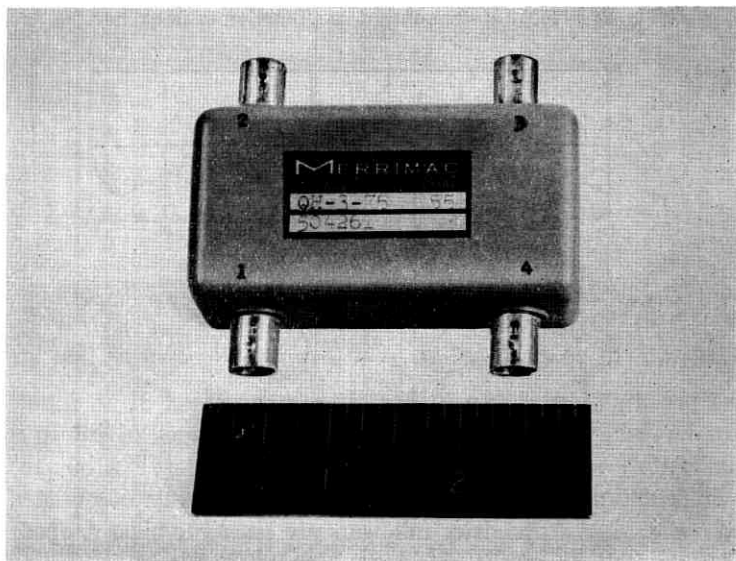


Fig. 27 — Quadrature hybrid coupler.

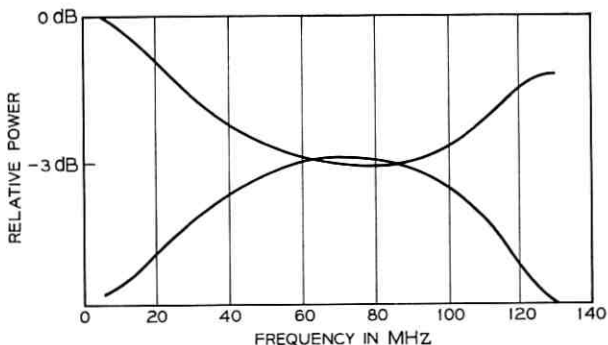


Fig. 28 — Coupling characteristics of 2 section coupler.

impedance emitter follower input from a matched source. The driver stage amplifiers had gains of 8.5 to 9 dB and were capable of 0.6 to 0.7 watts output. The 2N3632 transistors used in the power stage amplifiers, however, did not allow any transformation and, after some input tuning, had 6-7 dB gain but were capable of 1.25 watts output.

In order to realize the matching properties of the coupler organization it was found necessary to select matched pairs of transistors. The transistors were inserted in a test jig and tuned for best response with calibrated reactances. The values and final response were noted. Pairs of transistors were selected by comparison of these data. The amplifier pairs constructed using them showed typically  $> 25$  dB

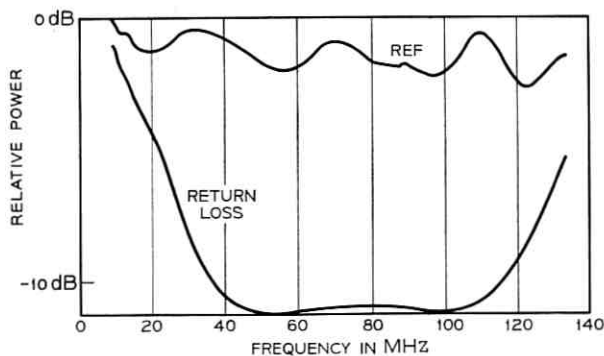


Fig. 29 — Return loss of 2 section coupler with open circuit terminations on coupled ports.

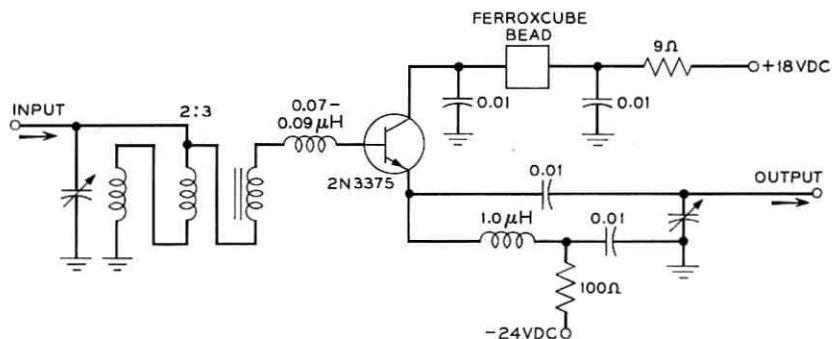


Fig. 30 — 60-90 Mc class A, 8.5-9.0 dB gain, 600-700 mW linear driver stage.

input and output return loss across the band. Interaction between the amplifiers outside of the band is prevented by using "out-of-band" filters as described in Section 2.6 (see Fig. 22).

#### 6.5 Signal Processing Components in 60-90 Mc System

In the feed-forward system, as developed in the preceding text, there are six essential signal processing operations (see Fig. 22):

- (i) Splitting off a reference signal from the input
- (ii) Delaying this reference signal for a time equal to the time of passage through the main amplifier
- (iii) Splitting off a sample of the amplified signal
- (iv) Comparison of the sample with the reference

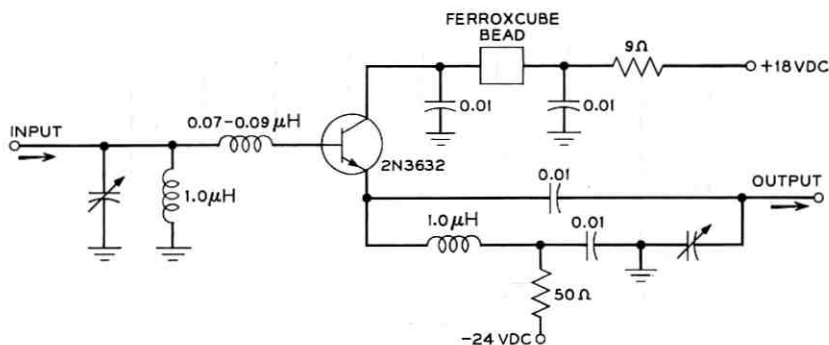


Fig. 31 — 60-90 Mc class A, 6.0-7.0 dB gain, 1.25 watt linear power stage.

- (v) Delaying the amplified signal for a time equal to the time of passage of the error through the subsidiary amplifier
- (vi) Injecting the correction into the output path.

In the 60-90 Mc system operations *i* and *ii* are carried out within in-phase power dividers (Merrimac Research and Development Co. PD-75). Operations *ii* and *v* are carried out in approximately 60- and 30-foot lengths of coaxial cable. (These lengths were first calculated from measurements of phase vs frequency within the system.) Operation *iii* is carried out in a two-section quadrature hybrid coupler similar to the ones used within the amplifiers (see Figs. 27, 28 and 29). However, instead of a 3 dB power split, this coupler was synthesized to couple out a signal 15 dB down from the input and to present only 0.27 dB loss to the main power path (see Fig. 32). The final operation, (*vi*), uses the reactive network described in Section 4.1 and Fig. 18.

The other components appearing in Fig. 22 are of secondary importance to the feed-forward concept but are quite essential to system operation. The fixed pad in the main amplifier input and the variable attenuator in the sample path insure that the power levels are appropriate to a proper differencing in the power divider. The variable attenuator in the error correction loop performs a similar function. These variable attenuators were constructed based on the transmission and match properties of the quadrature hybrid coupler. Figure 33 shows the transmission between the input and hybrid ports of a two-stage quadrature coupler both under open circuit termination of the coupled ports and with 10  $\Omega$  terminations. The use of ganged carbon rheostats as terminations (Fig. 34) produces a well-

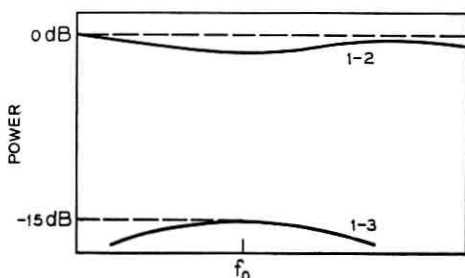


Fig. 32—Coupling characteristics of hybrid directional coupler used as sampling coupler.

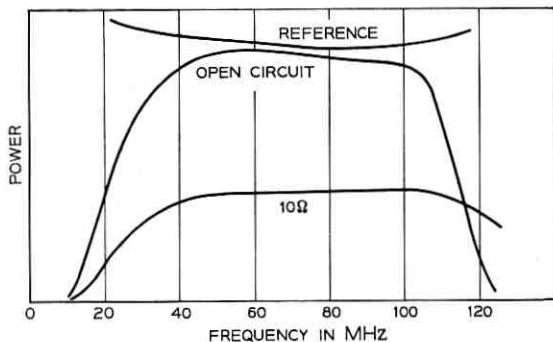


Fig. 33 — Transmission of two section coupler under open circuit and 10  $\Omega$  termination.

matched variable attenuator which is quite flat over the modest attenuation ranges needed.

The “sample coupler equalizer” is a low  $Q$  shunt resonant circuit which has a transmission characteristic that compensates for the bow in the sampled signal from the coupler, as shown in Fig. 35. The “phase shift networks” shown in Fig. 22 are also resonant equalizers. When the cable length corresponding to  $\tau_1$  was adjusted such that the time delay through the main amplifier equaled that through the reference path (equal phase vs frequency slopes), it was found that

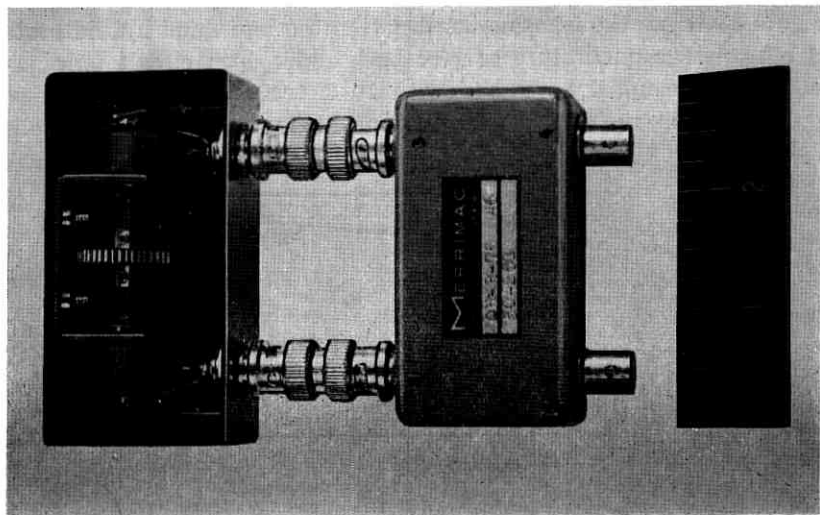


Fig. 34 — Variable attenuator.

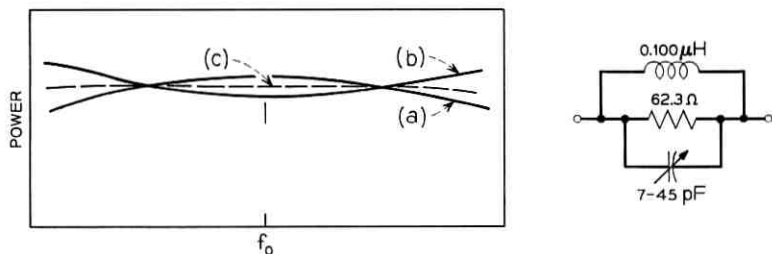


Fig. 35—Sampling coupler equalization. (a) Sample coupler characteristics. (b) Transmission of equalizer. (c) Equalized characteristics.

there was a constant  $70^\circ$  excess phase shift through the amplifier out of a total variation of  $1500^\circ$  across the band (see Fig. 36). In order to equalize this difference, use was made of the fact that a resonant circuit has zero phase shift at the resonant frequency, at which point there is an inflection in the phase vs frequency characteristic (see Fig. 37). The latter produces constant time delay at the resonant frequency. An extra length of line was then added to the reference path to produce equal phase shift at center frequency and the two-resonator network shown in Fig. 38 added to the sample path to equalize the phase slope (see Fig. 36). It was found that a two-resonator net-

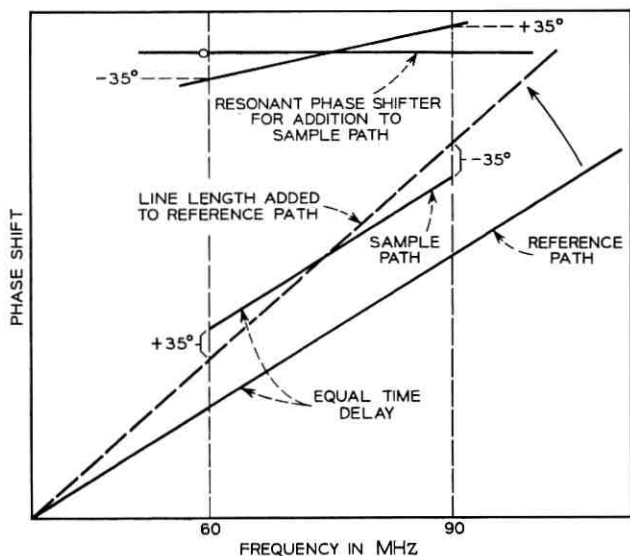


Fig. 36—Phase equalization of reference loop.

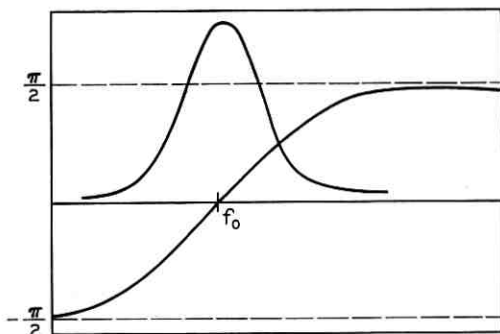


Fig. 37 — Amplitude and phase of transmission through a resonator.

work was needed, minimally, to produce sufficient flatness across the band. The insertion of the phase shift network,  $\varphi_2$ , in the correction loop relative to  $\tau_2$  is similar to the above.

#### 6.6 System Checks

With the system assembled, each of the two loops was put through an operational check, and final adjustments were made. The reference loop is checked by applying a small signal to the input and observing the output of the comparison power divider at *B*. The variable attenuator in the power sampling line was adjusted to produce the best null across the band. Small adjustments of  $\tau_1$  were made and the best null was obtained by using a sweep generator and an oscilloscope.

The error correction loop was then adjusted by feeding a swept frequency signal into the main amplifier at *A* and observing the system output. Both the variable attenuator at the input to the subsidiary amplifier, and  $\tau_2$ , were adjusted to produce a null output.

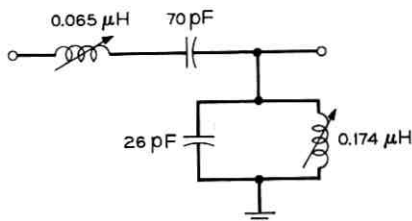


Fig. 38 — Phase shift section (values shown for 75 Mc, 70° correction) in 50  $\Omega$  system.

The final experimental proof of system performance lies in breaking (and terminating) the reference line at  $C$  in order to "fool" the error correction loop into operating as if there were no input signal, and observing the entire system between input and output ports. The excellence of the correction system may be judged by the degree of degeneration of the output. The results of this observation with the subsidiary amplifier turned off, and with the subsidiary amplifier restored are shown in Fig. 39 along with a simplified schematic indicating the measurement condition.

#### 6.7 25–35 Mc Amplifier—Differences from 75 Mc System

After experience with the 75 Mc system, the 30 Mc amplifier was designed to increase the power output several fold over the 10 watts attained above, without increasing the complexity of the system (that is, the number of coordinated branches in the power amplifier). This was done by going to class B push-pull operation rather than to a single-ended class A operation as in the previous system. In addition to doubling the number of transistors, the dc-rf power conversion capability of each was doubled. The push-pull pair (see Fig. 40) delivered 7.5 watts, linearly.

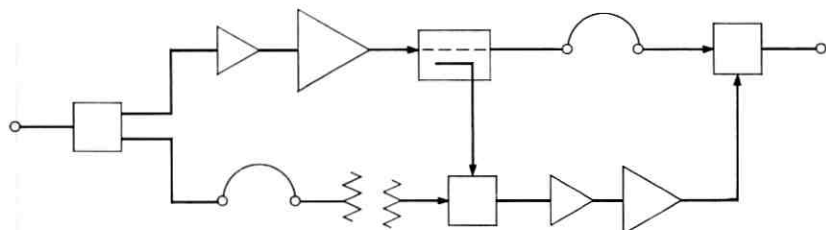
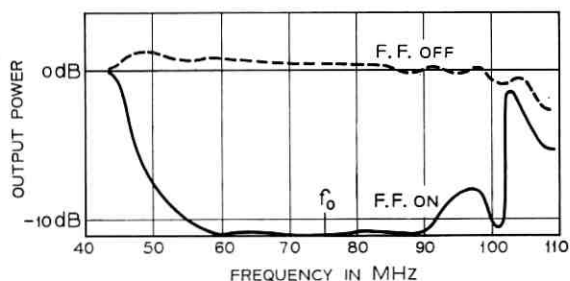


Fig. 39—System output with reference line open, feed forward switched on and off.

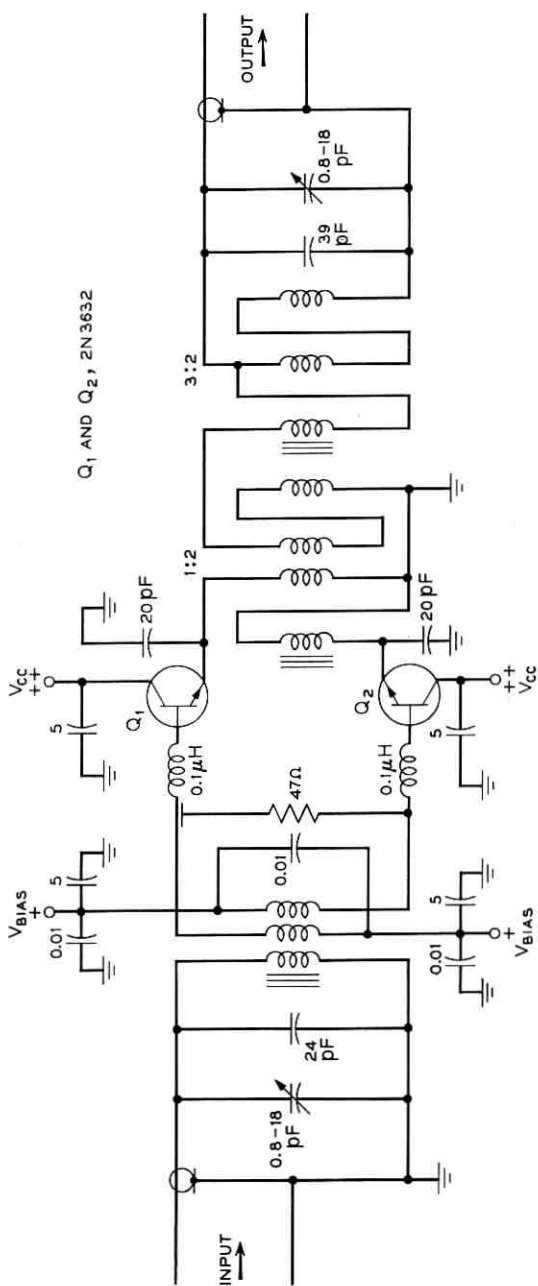


Fig. 40 — Class B push-pull amplifier for 30 Mc system (20-40 Mc, class A-B, push-pull, 7.5 watts linear).

This transition to class B operation made another design change possible. It was decided to design for low duty cycle pulsed operation and to use an "active clamp" biasing circuit which samples and restores bias voltages between pulses.

In addition to extending the dynamic range of the amplifier by increasing its power output capability, an attack was made on the system noise figure by the use of a directional coupler at the input favoring the reference path. As a further improvement the series input matching resistors ( $\sim 43 \Omega$ ) of the low-level preamplifier in the subsidiary amplifier were removed. The input match was restored by the amplifier pairing operation using quadrature couplers, which produced a matched amplifier having approximately a 4 dB noise figure.

Other changes were in the use of a series 3:1 injection transformer instead of the previously used shunt injection network, and in the use of limiting in the low-level preamplifier sections of both amplifier chains to prevent destruction of the power transistors under accidental overdrive. A schematic diagram of this system appears in Fig. 41.

### 6.8 "Active Clamp" Bias Circuit

The active clamp biasing used in the 25-35 Mc amplifier (see Figs. 42 and 43) provides a means of stabilizing the amplifier against changes in bias condition with variations in the signal power level and duty cycle. At high signal levels an unrealistically large bypass capacitor (see Fig. 44) would otherwise be required to perform this function. The clamp circuit also serves to make the bias levels insensitive to

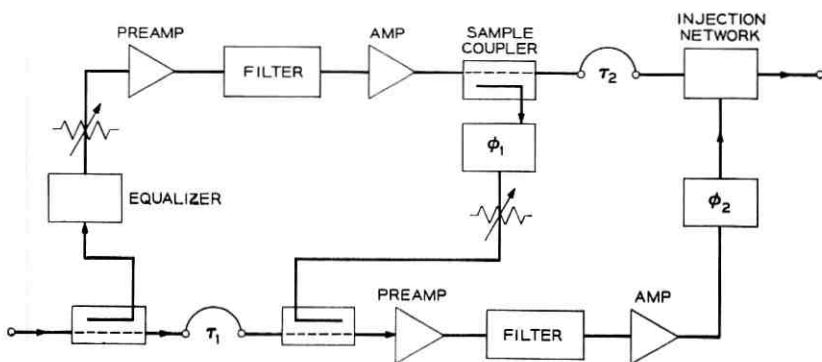


Fig. 41 — 30 Mc system.

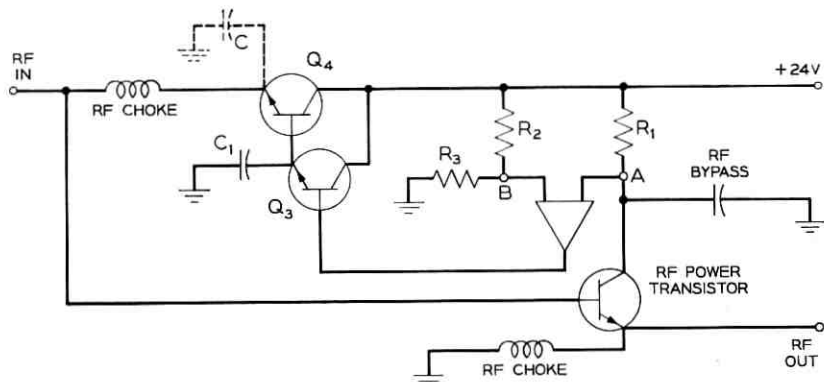


Fig. 42 — Active clamp schematic.

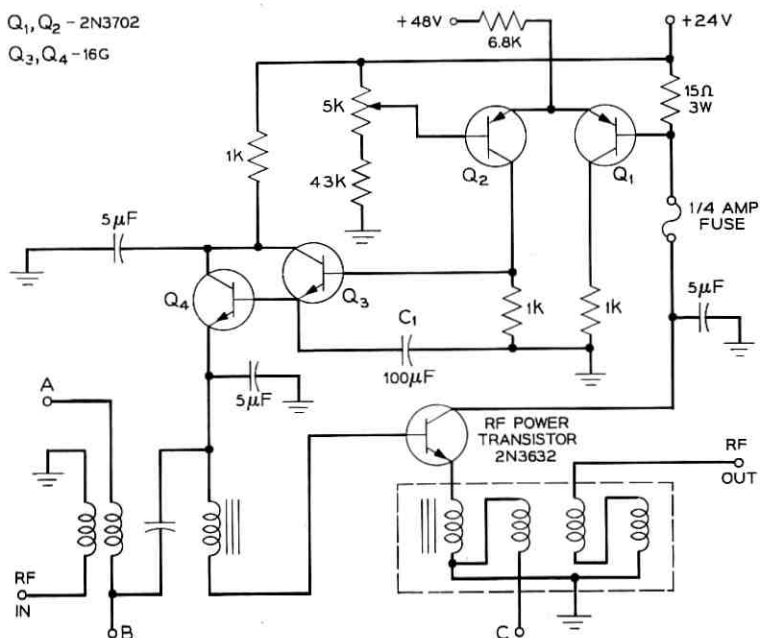


Fig. 43 — Active clamp biasing of power transistor. A, B, and C are connections to the other transistor of the push-pull pair.

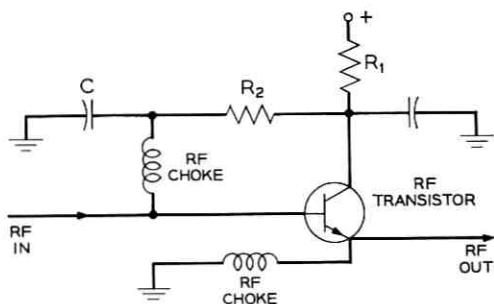


Fig. 44 — Conventional transistor biasing arrangement with DC stabilization.

thermal drift in the controlled transistor and to parameter variations between substituted transistors.

The high gain differential amplifier, shown in Fig. 42 provides the self-correcting bias condition since its output is fed into the base of the power transistor in such a way as to keep the potential at A of Fig. 3 equal to the reference potential at B. The gain of the differential amplifier also allows the use of a much smaller value of  $R_1$  ( $15 \Omega$  as in Fig. 43) than would be used in a conventional current feedback biasing scheme (shown in Fig. 44) to sense variations in quiescent current through the power transistor.

Ordinarily, as stated, a large bias bypass capacitor C, shown in Fig. 44 and dotted in Fig. 42, must be used to provide base current to the transistor during the conducting part of the cycle. It must be made adequately large to prevent substantial discharge, independently of duty cycle or drive amplitude. Transistor  $Q_4$  of Fig. 44, allows the use of a much smaller capacitor,  $C_1$ , since this capacitor need only supply a control current to its base. The transistor,  $Q_3$ , prevents the discharge of  $C_1$  into the differential amplifier during the pulse and allows a rapid recharge of  $C_1$  after the pulse because of its low emitter follower output impedance.

### 6.9 Performance of the 25–35 Mc Amplifier

The characteristics of the completed amplifier at low power are shown in Figs. 45 through 48. These figures show that the gain of the amplifier slowly oscillates  $\pm 0.1$  dB about a 0.4 dB slope across the band, the total amplification being 39 dB. The phase varies  $\pm 1^\circ$  from a constant time delay phase characteristic. Further, the spot noise

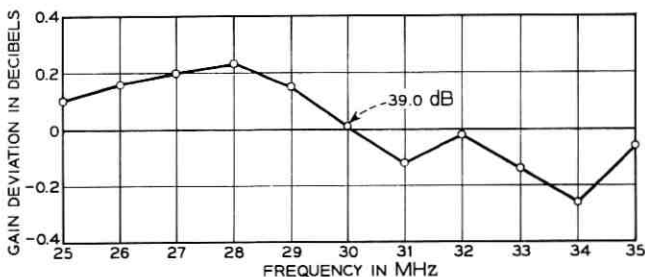


Fig. 45 — Deviation from flat gain at low power.

figure is better than 12.5 dB across the band and better than 9.5 dB over 85 percent of the band. The integrated noise figure is 8.6 dB.

Figures 49 through 51 show the gain and phase as functions of power level with the system fully functional and with the feed-forward correction loop disabled. These figures show the marked improvement obtained by the use of feed-forward correction. Notice that, as implied by the analysis in Section 3.3, when the subsidiary amplifier is called on to deliver large power to compensate for gain variation, it can no longer provide phase compensation. (It was shown that the compensation of only  $3.6^\circ$  at maximum power output requires all the power capability of the subsidiary amplifier.) The 40 watts indicated on the figures and the 8.6 dB noise figure shown above yield a dynamic range for the amplifier of 103.5 dB. Its output return loss was  $> 25$  dB (see Fig. 52).

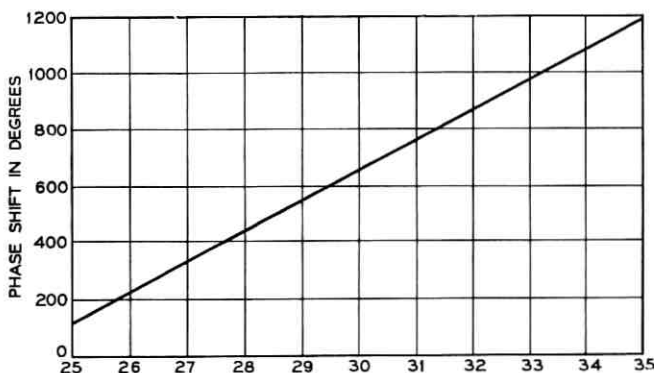


Fig. 46 — Phase shift through 30 Mc amplifier system as function of frequency (low power).

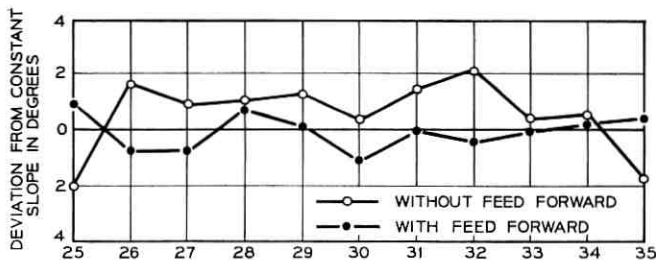


Fig. 47 — Deviation from constant time delay (low power).

## VII. CONCLUSIONS

The amplifier systems that were constructed at 30 and 75 Mc had an excellent correlation with design and showed the engineering practicability of the methods of design construction. The primary features were the use of:

- (i) Quadrature coupled corporate amplifier arrays to phase coordinate power emission of the individual active elements
- (ii) Emitter follower amplifiers as the basic elements to provide broadband, low distortion gain with transistors, otherwise incapable of producing this type of performance with a high yield
- (iii) A time-compatible or "feed-forward" error injection technique to equalize the transfer function of the amplifier, reduce distort-

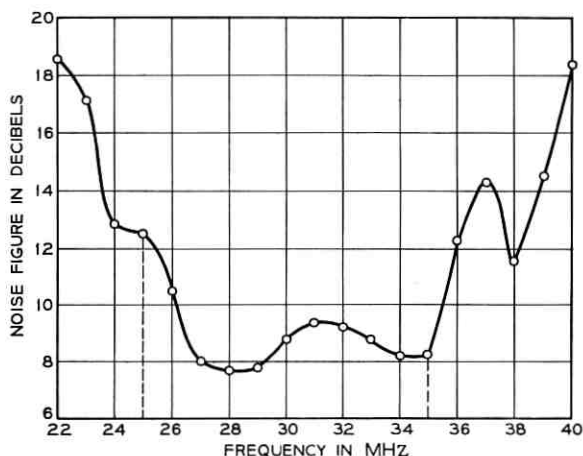


Fig. 48 — Amplifier noise figure.

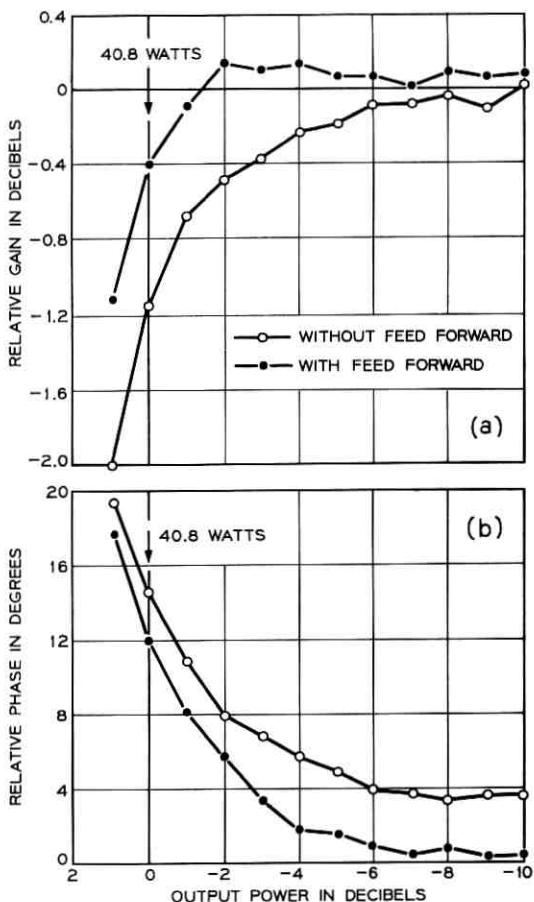


Fig. 49 — Gain (a) and Phase (b) Variation at 28 Mc.

tion and diminish noise in a system having relatively large time delay  
 (iv) Directionally coupled error sensing to produce a high return loss at the amplifier output

The 75 Mc amplifier was operated over a band of 60–90 Mc producing a 10 watt output average power with an amplitude compression there of about 0.2 dB. Its transfer function showed slow amplitude variations within 0.1 dB and phase deviations from linearity of about  $1.5^\circ$  out of a total phase spread of greater than  $1500^\circ$  across the band.

The 30 Mc amplifier had a band of operation between 25 and 35

Mc. It produced a 40 watt average power with an amplitude compression of 0.2 dB. Transfer characteristics showed slow amplitude excursion of about 0.2 dB with phase distortion about  $1^\circ$ . Output return loss was about 25 dB across the band and lent itself to simple equalization.

The 30 Mc amplifier had an 8.6 dB noise figure across the 10 Mc band of design interest which, together with its 40 watt average undistorted output capability, provided a dynamic range of 103.5 dB.

While correction did not extend beyond that of a single loop in these amplifiers, the textbook-like adherence of the results to the design elements makes it clear that further feed-forward looping would provide an arbitrary degree of correction over the prescribed bandwidth, probably with some further noise improvement. This is to be contrasted to the inability to use a feedback control for these

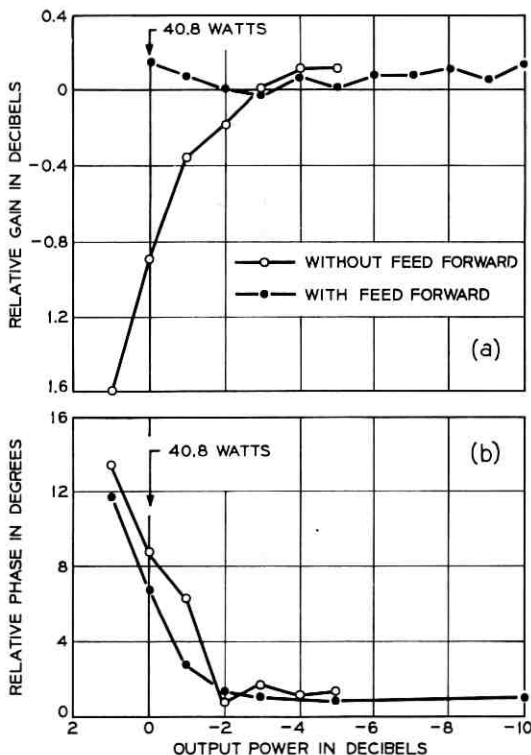


Fig. 50 — Gain (a) and Phase (b) Variation at 32 Mc.

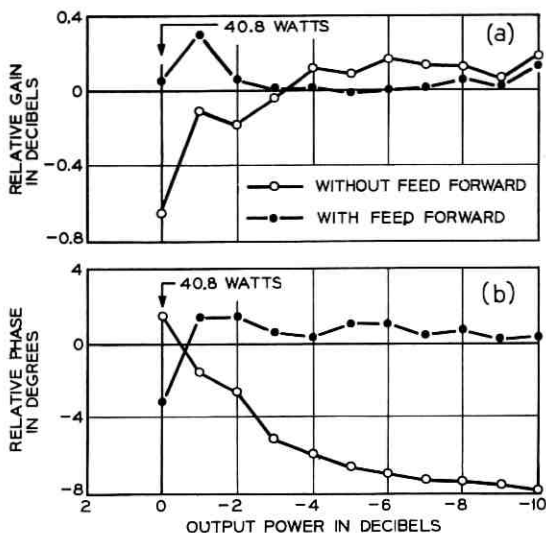


Fig. 51 — Gain (a) and Phase (b) Variation at 35 Mc.

amplifiers specifically because of excessive delay over the bandwidth, and to the limited ability of feedback, in general, to degenerate error cumulatively because of stability concerns.

The feed-forward correction scheme does not impose any concern for active element characteristics beyond the band of use, as does

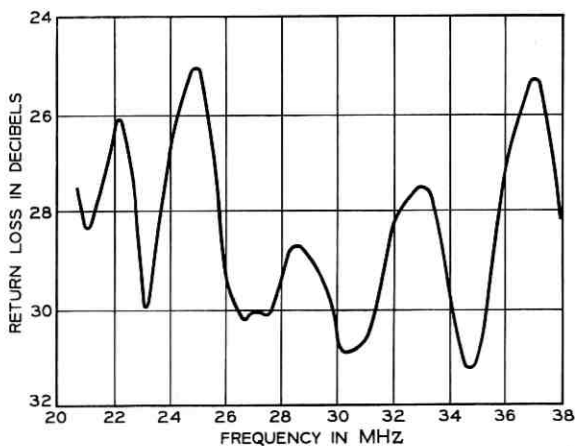


Fig. 52 — Output return loss of 30 Mc amplifier.

feedback, providing the simultaneous ability to use higher power and cheaper transistors than would ordinarily be acceptable at the frequency used. Using the self-degenerating emitter-follower mode of amplification, experience with the two amplifiers constructed showed a high degree of insensitivity to transistor selection aside from those failing catastrophically. Nothing more than a dc transistor checker was needed to construct the 30 Mc unit, while a rough rf sweep selection procedure was employed at 75 Mc to form slightly preferred transistor pairs.

The use of time-compatible error cancellation is not limited to the specific circuits described here either in frequency or in the specific active element circuitry used. It is generally applicable and, in conjunction with the corporate power accumulation available through coupler arrays, and smooth (no guard-band) frequency multiplex arrangements, there are available at least in principle, controlled, arbitrary (bandwidth, arbitrary power, capabilities virtually throughout the entire rf spectrum).

#### VIII. ACKNOWLEDGMENTS

We gratefully acknowledge the expert skills of others who helped this activity succeed. We are particularly indebted to R. V. Goordman whose teaching, consultation, and services we most often sought in the area of transistor electronics; to R. C. Petersen, for providing an initial feasibility demonstration of the linear power capabilities, at high frequency, of an overlay emitter follower transistor amplifier; to A. B. Wertz for the extensive and highly refined measurements of amplifier performance characteristics; and not least to J. J. Golembeski for his critical, and most informed, reading of the manuscript.

#### APPENDIX A

##### *Conditions for Directional Coupling*

In Section 2.2 we indicated that a sufficient condition that a passive, reciprocal, and reactive, fourport possess directional coupling properties was that it be matched and that it possess two axes of symmetry. We shall show the sufficient conditions to result from the application of simple time reversal arguments.

Figure 53 shows the fourport excited by a unit incidence into port 1 without reflection but with scatterings  $\alpha$ ,  $\beta$ , and  $\gamma$ , into ports 2, 3, and 4, respectively. If this figure is time-reversed, being reactive, the

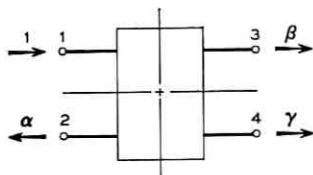


Fig. 53 — Prototype network.

fourport remains unchanged, but the scattered quantities are reversed in flow direction and their phases inverted. This result is shown in Fig. 54 which then must be an excitation format compatible and simultaneous with that of the first figure.

Use in turn incident amplitudes,  $-\beta^*$ ,  $-\gamma^*$ , and  $\alpha^*$ , into ports 3, 4, and 2, respectively, to cancel the various incident quantities of Fig. 54. The respective scattered results are shown in Fig. 55, where the two axes of symmetry and the scattering format of Fig. 53 were used. If the results of Fig. 55 are superposed, then the excitation scheme of Fig. 56 is yielded. This last figure shows only emergent waves. Since there are no incident waves, each of the emergent waves must vanish and we have

$$1 - \alpha\alpha^* - \beta\beta^* - \gamma\gamma^* = 0, \quad (40)$$

$$\alpha\gamma^* + \gamma\alpha^* = 2 \operatorname{Re} \alpha\gamma^* = 0, \quad (41)$$

$$\alpha\beta\alpha + \beta\alpha^* = 2 \operatorname{Re} \beta\alpha^* = 0, \quad (42)$$

and

$$\gamma\beta^* + \beta\gamma^* = 2 \operatorname{Re} \gamma\beta^* = 0. \quad (43)$$

Equation (40) simply confirms the conservation of energy in a reactive fourport. Equations (41) through (43) state that  $\alpha$ ,  $\beta$ , and  $\gamma$  are all mutually perpendicular phasors. Since these three phasors

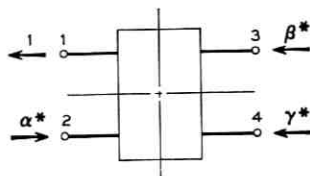


Fig. 54 — Time reversed description.

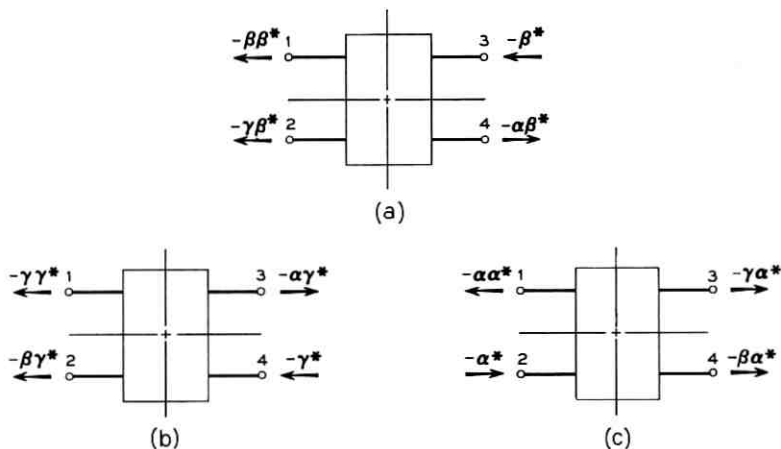


Fig. 55 — Excitation of 'beta' Port (a), 'gamma' Port (b) and 'alpha' Port (c).

are in a two-dimensional space this mutual perpendicularity is absurd unless one of the quantities vanishes. Therefore,

- (i) There exists one port "hybrid" to the incident port
- (ii) All the power is transmitted to the remaining two ports.

These two statements define a directional coupler.

APPENDIX B

*Transformer Injection*

B.1 *First Considerations*

B.1.1. *In Phase Errors*

Let us first see what is required of the circuitry of Fig. 14 to accomplish in-phase error correction then consider the correction of

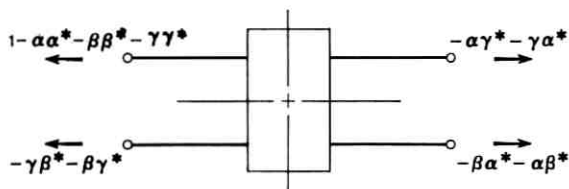


Fig. 56 — Superposed excitations.

quadrature phase errors. Our specific concern is the specification of the  $1:N$  transformer shown as the means for final injection of the error cancellation signal.

Figure 21 shows a first Thevenin equivalent of the insertion of the subsidiary, error correction, amplifier into the output circuit of the main amplifier. Both amplifiers are shown with normalized internal impedances and the external load matched to the combined impedance. We assume proportional error  $\delta$ , of the main amplifier open circuit voltage  $2V$ , and we assume further that the open circuit voltage of the subsidiary amplifier is  $2v$ .

As seen from Fig. 21(b) the reduced equivalent, the condition that the load be excited independently of  $\delta$  is given by

$$v = NV\delta. \quad (44)$$

If we isolate the subsidiary amplifier, as in Fig. 57, the amplifier has a voltage  $v'$  at its load terminals corresponding to a load current  $V/N(1 + 1/N^2)$ . At the maximum voltage of  $V$ , defined as  $V_p$ , with corresponding subscript notation on all other quantities, we would like to see the subsidiary amplifier match terminated to deliver maximum power. Accordingly,  $v'$  is half the open circuit voltage and it is equal to the current at match in the impedance normalized description. Then

$$v_p = \frac{V_p}{N\left(1 + \frac{1}{N^2}\right)} \quad (45)$$

and, using (44), we have

$$N = \sqrt{\frac{1 - \delta_p}{\delta_p}} \quad (46)$$

and

$$v_p = V_p \sqrt{\delta_p(1 - \delta_p)}. \quad (47)$$

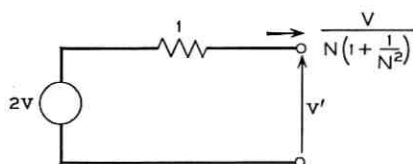


Fig. 57 — Thevenin equivalent of loaded subsidiary amplifier.

By the above construction, at peak power the subsidiary amplifier works into a match and furnishes a power  $P_s$  which compares to the main amplifier  $P_m$ , via (46), by the relationship

$$P_s = \delta_p(1 - \delta_p)V_p^2 = \frac{\delta_p}{1 - \delta_p} P_m \quad (48)$$

where  $V_p^2(1 - \delta_p)^2 = P_m$  is the peak available power of the main amplifier.

We may consolidate our results to this point under the approximation that  $\delta_p$  is small.

(i) The main amplifier power deviation is approximately  $[(1 - \delta_p)^2 - 1]P_m \simeq -2\delta_p P_m$ , at its peak power capability.

(ii) The subsidiary amplifier furnishes a correction power of approximately  $\delta_p P_m$ .

There seems a curious divergence of a factor of 2 in providing the necessary compensation. If, for example,  $\delta_p = \frac{1}{8}$ , implying a peak-power deviation of  $\frac{1}{4} P_m$ , a subsidiary amplifier having only a power capacity of  $\frac{1}{8} P_m$  would appear to be adequate for compensation.

A second feature of transformer injection may also be discerned which at first would appear unrelated to the missing factor of 2. The error injection is not without some cost to the main amplifier. As Fig. 21 shows, the subsidiary amplifier images a resistance of  $1/N^2$  into the main amplifier circuit, causing an effective generator characteristic impedance of  $1 + 1/N^2$  to be presented to the load.

The subsidiary amplifier provides the power both to equalize the irregular main-amplifier transfer characteristic and to cancel distortions produced by nonlinearities. Assume the main-amplifier power to be small such that no nonlinear distortions are observed and assume further that equalization is unnecessary. There is, therefore, no error and, consequently, no contribution from the subsidiary amplifier, and the open circuit voltage is that of the main amplifier only. The available power is decreased by an amount equal to the changed impedance and an insertion loss of

$$L = 1 + \frac{1}{N^2} = \frac{1}{1 - \delta_p} \quad (49)$$

is sustained where the results of (46) have been used.

The question exists whether this is indeed just a loss in gain or a loss in power capability. We shall now show that it is only a loss in gain and that we add to the power capability of the main amplifier by the amount of the subsidiary amplifier peak power.

From Fig. 21 we see the delivered voltage of the main amplifier to be, at peak,

$$2V_p(1 - \delta_p) - \frac{V_p}{1 + \frac{1}{N^2}}.$$

Since  $1 + 1/N^2 = 1/1 - \delta_p$  by (46), the voltage delivered reduces to  $V_p(1 - \delta_p)$ . Since the current drawn is  $2V_p/2(1 + 1/N^2) = V_p(1 - \delta_p)$ , the total power delivered by the main amplifier is

$$P_m = V_p^2(1 - \delta_p)^2. \quad (50)$$

However, (50) is, identically, the available power from the main amplifier without the subsidiary circuit, so that there is no difference in the power actually delivered by the main amplifier into the load.

The power delivered by the subsidiary amplifier is the product of its output voltage referred to the main loop,  $2v_p/N - [(1/N^2 \times V_p)/(1 + 1/N^2)]$  and the main loop current  $V_p/(1 + 1/N^2)$ . The use of equations (46) and (47) shows this power to conform to (50) producing a power

$$P_s = V_p^2(1 - \delta_p)\delta_p.$$

The total power reaching the load is  $P_m + P_s = P_L$  which is

$$P_L = V_p^2(1 - \delta_p) = \frac{P_m}{1 - \delta_p}. \quad (51)$$

Equation (51) shows most succinctly that the power reaching the load exceeds the power capability of the main amplifier and that the transformer interconnection, as characterized earlier, is vastly superior to a power divider interconnection which would have produced a 3 dB loss in power capacity. Further, the insertion loss shown in (48) is not a power loss, but a small loss in gain only.

### B.1.2. Quadrature Errors

Let us assume that the transformer  $N$  has been specified by (47) and the subsidiary amplifier by (48) in terms of some desired real peak voltage error  $\delta_p$ . We now seek to determine the peak capability of the system to correct a quadrature error  $i\delta_p'$ .

Given this quadrature error, the subsidiary amplifier output voltage is  $v = iNV_p\delta_p$  corresponding to its current  $i = V_p/N$ . The subsidiary amplifier perceives, therefore, a terminating reflection factor

$$\frac{v - i}{v + i} = \frac{iNV_p \delta'_p - \frac{V_p}{N}}{iNV_p \delta'_p + \frac{V_p}{N}}$$

which, obviously, has a unit magnitude.

Given a unit reflection, the subsidiary amplifier, depending on its electrical position relative to the load, might be called on to develop twice its rated voltage or twice its rated current. To safeguard against this possibility, the open circuit voltage must be down rated by a factor of 2, and corresponding to (47), we have

$$v'_p = \frac{iV_p}{2} \sqrt{\delta_p(1 - \delta_p)} = NV_p \delta'_p. \quad (52)$$

So that, by (46)

$$\delta'_p = \frac{1}{2} \delta_p. \quad (53)$$

Quantitatively, if  $\delta_p = \frac{1}{8}$ , corresponding roughly to a  $\pm 1$  dB correction, (53) yields  $\delta'_p = 0.0625$ . Since the phase correction has a magnitude of the arctangent of  $\delta'_p$ , the phase cleanup range is, minimally,  $3.6^\circ$  at high power.

## B.2 Further Considerations

### B.2.1. Subsidiary Amplifier Mismatch

At peak power, by design, the subsidiary amplifier is matched. Let us now go to the extreme of low power. Using Fig. 21(b) the main amplifier supplies a current  $V/(1 + 1/N^2)$  which develops a voltage

$$\left[ \frac{V}{1 + \frac{1}{N^2}} \right] \left( \frac{1}{N^2} \right) (N) = \frac{V}{N + \frac{1}{N}} \quad (54)$$

across the step-up side of the injection transforms via the subsidiary amplifier image impedance  $1/N^2$ . The main current reduces by  $1/N$ , and a current flow also equal to  $V/(N + 1/N)$  flows through the voltage step-up side of the transformer.

As at high power the subsidiary amplifier output voltage is equal to its current, but with a major difference. The voltage sense is reversed and now, instead of finding a positive resistance match, the termination is a negative match. In transition between high and low power, the termination of the subsidiary amplifier has passed through violent shift and a question exists whether, as power decreases, some

requirement existed on the subsidiary amplifier worse than that at peak main amplifier power.

Having aroused this concern, we shall now dismiss it. Equation (54) shows the negative voltage bound to be less than the positive voltage bound, since  $V$ , by hypothesis, is less than its peak voltage  $V_p$ . Similarly, the subsidiary amplifier current is always less than its peak value  $V_p/(N + 1/N)$ . The subsidiary amplifier, in actuality, is separated from the terminating transformer by a transmission line. Along this line, peak current and voltage amplitudes interchange. Since neither of these peaks ever exceeds the value supplied by the subsidiary amplifier at peak main-amplifier distortion, the initial design of the subsidiary amplifier covers the worst case.

### B.2.2. *Nonoptimal Transformers*

While the transformer design chosen optimizes the powers delivered by the main and subsidiary amplifiers, nevertheless one may wish to forego this optimization somewhat to reduce the contribution of  $1/N^2$  to the output matching problem. While this problem is not particularly serious, it is generally, a nuisance in the following sense. Very high return loss is guaranteed by the directional coupler sampling arrangement exclusive of the  $1/N^2$  contribution, and the very insertion of any matching circuit at all is a severe perturbation on the goodness of the system. The less the mismatch to be corrected, the higher the degree of return loss realization across the band.

Let us now consider a nonoptimal transformer  $n$  replacing the optimum value  $N$  deduced in earlier expressions. If  $2v'$  is the open circuit error voltage applied to the high side of the injection transformer then

$$\delta v'_p = 2nV_p\delta_p$$

and the current referred to the high turns side is

$$I'_p = \frac{V_p}{1 + \frac{1}{n^2}} \cdot \frac{1}{n}$$

The terminating transformer, together with the correlated current flow in the low turns side, provides an output impedance  $Z$  for the subsidiary amplifier which must conform to the relationship

$$1 + Z = \frac{2v'_p}{I'_p} = 2n^2 \left( 1 + \frac{1}{n^2} \right) \delta_p$$

and

$$Z = 2(n^2 + 1)\delta_p - 1. \quad (55)$$

Equation (55) shows that for  $(n^2 + 1) > 1/\delta_p$  the subsidiary amplifier, as expected, operates into a high impedance mismatch.

The subsidiary amplifier must be made to cope with the standing wave, to be capable of supplying either an excess open circuit voltage or an excess short circuit current. We assume a power capacity to be required from the subsidiary amplifier such that it can tolerate that peak through its internal impedance. Since this peak, relative to matched loading, is given by the ratio of  $2Z/(Z + 1)$ , namely  $1 + |k|$ , where  $k$  is the reflection factor, we have

$$\frac{v'_p}{v_p} = \frac{2(n^2 + 1)\delta_p - 1}{(n^2 + 1)\delta_p} \cdot \frac{n}{N} \quad (56)$$

with the corresponding peak subsidiary amplifier power ratios

$$\frac{P'_s}{P_s} = \left( \frac{2(n^2 + 1)\delta_p - 1}{(n^2 + 1)\delta_p} \right)^2 \frac{n^2}{N^2}. \quad (57)$$

Combining (57) with (46) we have, finally,

$$\frac{P'_s}{P_s} = \frac{(2(n^2 + 1)\delta_p - 1)^2 n^2}{(n^2 + 1)^2 \delta_p (1 - \delta_p)}. \quad (58)$$

The formulation of (58) shows, of course, that when  $n^2 = N^2 = 1 - \delta_p/\delta_p$ , this ratio reduces to unity. As a quantitative determination, let us increase  $n$  such that it introduces roughly one-half the mismatch it inserts under optimal conditions for  $\delta_p = \frac{1}{8}$ , our 1 dB design center. Since  $N^2 = 7$ , let us choose  $n^2 = 16$ , where the latter number is chosen to form an integral turns ratio. Equation (58) demands 7.3 times as much power as that for the matched case, a level of power for the subsidiary amplifier virtually equal to that of the main amplifier.

The quantitative example chosen, of course, represents a fairly undesirable situation; nevertheless, it shows a tradeoff possibility which is not to be ignored. In multiple looping feed-forward systems, each loop is called on to handle progressively smaller and smaller deviations. In using these progressively smaller values of  $\delta_p$ , we form a sequence of progressively higher values of  $N$ , corresponding in turn, according to (48) to lower values of  $P_s$ . Below some value, the value of  $P_s$  is no longer limiting and we may wish to use correction power as a tradeoff against mismatch.

## APPENDIX C

*Schmidt-Brücken Patent*

During the final stages of preparing this article we found a German Federal Republic patent, issued July 14, 1960 (document 1085194), to Heinrich Schmidt-Brücken, entitled "A Method For Compensating Distortion In Amplifiers."

Clearly this patent, in spirit, precedes our own activities in attempting to provide time compatible error cancellation. While it suggests a time flow correction system seemingly much similar to our own, its actual embodiment severely compromises the intent of the patent. We have reproduced Figures 1 and 3 of the Schmidt-Brücken patent as our own Figures 58 and 59. We claim the disclosure shown in Fig. 58 to be operative only in principle, and that of Fig. 59 to be generally inoperative.

We feel it relevant to pursue the dissection of these devices since they illustrate, negatively, important considerations in the format of implementation of feed-forward amplifiers. It is not, however, intended by so doing to deprive Mr. Schmidt-Brücken of a well earned recognition of his priority in recognizing time as a controllable factor in error cancellation.

A major consideration lacking in both the configurations of Figures 58 and 59 is that of directional wave sampling. Let us observe the consequences of a simple voltage sampling as used in Fig. 58 where such sampling follows the usual practice in feedback amplifiers.

If all components in Fig. 59 are matched, that system will operate. In general, however, there is no disclosure of the degree of match required in the patent, and the effect of multiple reflections are

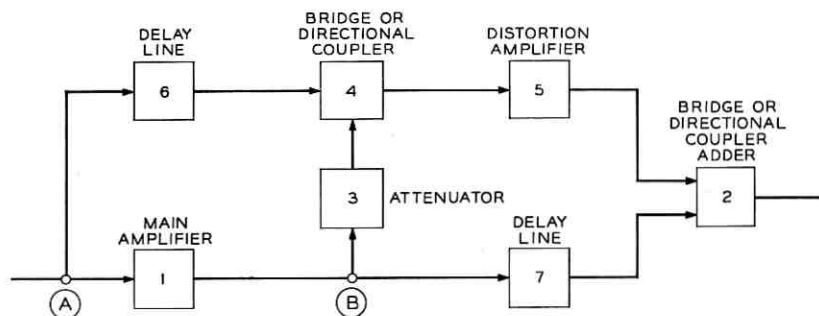


Fig. 58—Schmidt-Brücken Fig. 1.

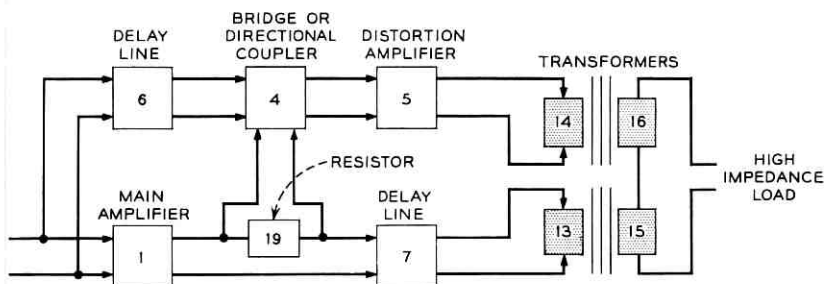


Fig. 59 — Schmidt-Brücken Fig. 3.

ignored. Let us assume, however, that all devices are matched only to within reasonable specification of return loss, and that the amplifiers, particularly, might have return losses of the order of 20 dB.

The error reference is established at point A in Fig. 58 through the use of a voltage divider network, and, consequently, the error voltage is a function of the input impedance seen looking into the delay-line labeled 6. The phase of the 10 per cent reflection factor of the distortion amplifier 5 may rotate through more than one cycle as a function of the delay line length, producing a peak to peak impedance variation of 50 per cent. The reference sampling is modulated by this order of magnitude, making a shambles of the compensation system.

Inherent in this system, therefore, is an inclusion of an active device, namely the amplifier, as part of the reference standard, greatly limiting the general practicability of this class of device. In our own embodiments, we have carefully employed directional coupler sampling, stressing the incident wave, and not the voltage, as the reference. With properly designed match, third time around incidence is not greatly significant since it is down by twice the return loss, the order of 40 dB or greater, making amplifier mismatch a secondary consideration.

The same form of argument applies to point B with respect to the adder 2. Notice that both boxes 4 and 2 are bridges or directional couplers, and that they are used to prevent spurious coupling between chains. Awareness is manifested, therefore, within the patent itself of the existence of directional coupling devices, but nowhere are these couplers applied to the crucial problem of error sampling.

Figure 59 shows a device containing not only the above fault, but adds fallacy as well. The intention is to show alternative means for

providing chain isolations by the use of constant current sources, such as pentodes, operating in parallel or, as actually shown, by the use of series connected secondaries of transformers 13 and 14 working into a relatively infinite output impedance.

The implications to multiple reflections are obvious and the consequence to the current sensing resistor 19 is disastrous. If, for example, delay line 7 passes through a half wavelength, 19 is open circuited and develops no sense voltage. The paralleling of pentode chains is equally disastrous since one of the pentodes, if viewed looking back into the delay line, may prove to be anything but a current source.

There are no considerations by Schmidt-Brücken to use his device to transfer power. All considerations of the relevant requirement of the output combiner are missing, as are considerations of output impedance. Pointedly, we differ with Schmidt-Brücken in calling for an output bridge or directional coupler, since these must be power wasting four-ports. We have expressly demanded amplifier interactions in an output three-port to conserve power. In like fashion we disagree with Schmidt-Brücken in demanding an open circuit output to avoid interaction when he does, indeed, chance to use an output three-port.

#### REFERENCES

1. McMillan, B., "Multiple Feedback Systems," U. S. Patent 2-748-201, issued May 29, 1956.
2. Zaalberg van Zelst, J. J., "Stabilised Amplifiers," Philips Technical Review, 9 (1947), pp. 25-32.
3. Black, H. S., "Translating System," U. S. Patent 1-686-792, issued October 9, 1928 and U. S. Patent 2-102-671, issued December 1937.
4. Seidel, H., unpublished work.
5. Seidel, H., and Friedman, A. N., unpublished work.
6. Deighton, M. O., Cooke-Yarborough, E. H., and Miller, G. L., "A Method of Enhancing Gain Stability and Linearity of Transistor Amplifier Systems," Proc. Northeast Regional Elec. Mfrs. Conf., Boston, 1964.
7. Golembeski, J. J., et al., "A Class of Minimum Sensitivity Amplifiers," IEEE Trans. Circuit Theory, *CT-14*, No. 1 (March 1967), pp. 69-74.
8. Seidel, H., unpublished work.
9. Weissfloch, A., "Anwendung des transformersatzes über verlustlose vierpolen auf die hinter einander schaltung, von vierpolen," Hochfreq. Tech. Electr. Akust., 61 (January 1943), pp. 19-28.
10. Friedman, A. N., and Seidel, H., unpublished work.

# Effects of Precipitation on Propagation at 0.63, 3.5, and 10.6 Microns

By T. S. CHU and D. C. HOGG

*The attenuation and scattering of laser beams by rain, fog, and snow have been calculated and measured at 0.63, 3.5, and 10.6 $\mu$ . Attenuation of the infrared wavelengths by light fog is up to one order of magnitude less than at 0.63 $\mu$ . But for dense fog, calculation shows that the attenuation at 10.6 $\mu$  can exceed 40 dB per km. It is found that attenuation by rain can be calculated to good accuracy from average path rain rates provided that forward scattering is taken into account; this scattering reduces the attenuation.*

*Measurements of propagation through precipitation over a 2.6 km path are discussed in detail and are found to be consistent with predictions. The wavelength dependence of attenuation is found to vary from one fog to another because of different drop-size distributions. Attenuation of 0.63 $\mu$  in rain showers is about 20 per cent less than at 3.5 $\mu$  and is, of course, much less than the attenuation in fog. But even for extremely heavy rain showers, the 0.63 $\mu$  attenuation never exceeded 20 dB per km, which is less than the attenuation of millimeter waves under such conditions. Both the attenuation and forward scattering properties of snow appear to be between those of fog and rain.*

## I. INTRODUCTION

It is well known that optical waves suffer much attenuation in propagation through precipitation in the atmosphere. Penetration of light through a dense fog is much more difficult than through a heavy shower. One would also expect similar phenomena for near infrared waves. However, quantitative data are necessary in order to evaluate the potential use of lasers for short range communication through the atmosphere. Attenuation by precipitation is the dominant factor in determining the feasibility of open-air laser communication systems. The interesting fluctuations of laser beams caused by turbulence in the clear atmosphere are not discussed here.

The gas lasers which provide significant amounts of power within the infrared windows of the clear atmosphere are  $3.5\mu$  and  $10.6\mu$ ;  $3.39\mu$  is not suitable because it is attenuated by the small amount of methane in the air.<sup>1</sup> The wavelengths of visible gas lasers with suitable output power are  $0.49\mu$  and  $0.63\mu$ . Since the attenuation of optical waves in a fog is largely the result of scattering by numerous small drops, it is not likely that transmission of  $0.49\mu$  and  $0.63\mu$  through a fog would differ appreciably. The literature reveals that the attenuation of blue light ( $\sim 0.49\mu$ ) through a light fog is somewhat greater than that of red light ( $\sim 0.63\mu$ ), while their attenuations in a dense fog differ little from one another.<sup>2</sup> In this study,  $0.63\mu$  is the visible wavelength used.

Some computed results of attenuation by precipitation at the wavelengths of  $0.63\mu$ ,  $3.5\mu$ , and  $10.6\mu$  are given first. The effect of forward scattering is examined using a Gaussian model for the scattering pattern of a rain drop and a single scattering model is used to describe the broadening of a laser beam by precipitation. Then the results of measurements of attenuation by precipitation over a 2.6 km path at these three wavelengths are described. Some of the measured data have been discussed briefly in previous notes.<sup>3, 4</sup>

The measured attenuation by rain is compared with that calculated from the rainfall measured on the path. Optical attenuation by fog is compared with total liquid water content derived from path-loss measurements taken on a radar operating at a wavelength of 3 mm. Similar quantitative correlations have not been made for attenuation by snow because of the lack of an independent physical measurement for this form of precipitation.

## II. ATTENUATION CALCULATIONS

### 2.1 Method of Computation

The total power removed from a laser beam by a precipitation particle, say a spherical drop of radius  $a$ , is given by

$$E = SC(a, \lambda) \quad (1)$$

where  $S$  is the magnitude of the incident Poynting vector, and  $C(a, \lambda)$  is the total or extinction cross section of the drop. The change in  $S$  upon passing through a layer of precipitation  $\Delta z$  is

$$\Delta S = -S \Delta z \int_0^{\infty} n(a)C(a, \lambda) da \quad (2)$$

where  $n(a)da$  is the number of drops per unit volume within the range  $(a, a+da)$ . Integrating equation (2) yields

$$S = S_0 e^{-\int \alpha dz} \quad (3)$$

where

$$\alpha = \int_0^{\infty} n(a)C(a, \lambda) da. \quad (4)$$

The total cross section is often normalized with respect to the geometrical cross section

$$Q(a, \lambda) = \frac{C(a, \lambda)}{\pi a^2}. \quad (5)$$

Since the energy removed is partly scattered and partly absorbed by the particle, the total cross section is divided into scattering and absorption cross sections:

$$Q_{\text{ext}} = Q_{\text{scat}} + Q_{\text{abs}}. \quad (6)$$

The  $Q$ 's are sometimes called efficiency factors. Notice that part of the energy represented by the scattering cross section is scattered forward; this leads to a decrease in attenuation as discussed in Section III.

The attention coefficient in equation (4) may be calculated if the particle-size distribution and the cross sections are given. Equation (4) gives the extinction, scattering, or absorption coefficients when the appropriate cross section is substituted.\* We take the shape of the water drops in fog and rain to be spherical. With this assumption, it is not a prohibitive task to use Mie's rigorous expressions to calculate the extinction and absorption cross sections of the drops. However, very simple approximate formulas are quite applicable here in view of the uncertain drop-size distributions and the doubtful sphericity. Using a combination of geometrical optics and Huygen's principle, Van de Hulst<sup>5</sup> obtained the following formulas for the extinction and absorption cross section:

$$Q_{\text{ext}} = 2 - 4e^{-\rho \tan \beta} \left( \frac{\cos \beta}{\rho} \right) \sin(\rho - \beta) - 4e^{-\rho \tan \beta} \left( \frac{\cos \beta}{\rho} \right)^2 \cos(\rho - 2\beta) + 4 \left( \frac{\cos \beta}{\rho} \right)^2 \cos 2\beta \quad (7a)$$

\* Extinction is often used in optical terminology for attenuation; however, it is misleading. It is more exact to designate the extinction coefficient as the attenuation coefficient without forward scattering corrections.

$$Q_{\text{abs}} = 1 + \frac{e^{-4x n'}}{2x n'} + \frac{e^{-4x n'} - 1}{8x^2 n'^2} \quad (7b)$$

where

$$\rho = \frac{4\pi a}{\lambda} (n - 1), \quad \tan \beta = \frac{n'}{n - 1}, \quad x = \frac{2\pi a}{\lambda},$$

and  $n$  and  $n'$  are the real and imaginary parts of the refractive index, respectively. The above two expressions are derived under the assumptions  $(n - 1) \ll 1$ ,  $n' \ll 1$ ,  $2\pi a/\lambda \gg 1$ . Numerical comparison indicates<sup>5</sup> that the essential features of the cross section curves using equation (7) remain correct for  $|n - 1 - in'| \lesssim 1$  and  $2\pi a/\lambda \gtrsim 1$ . When  $\rho \ll 1$ , equation (7) reduces to

$$Q_{\text{ext}} = \frac{4}{3}\rho \tan \beta + \frac{1}{2}\rho^2(1 - \tan^2 \beta) \quad (8a)$$

$$Q_{\text{abs}} = \frac{4}{3}\rho \tan \beta - \rho^2 \tan^2 \beta. \quad (8b)$$

## 2.2 Refractive Indices

Figure 1 shows the complex refractive index ( $n - in'$ ) of liquid water in the visible and near infrared region. For the wavelengths below  $18\mu$  the data have been taken from the tabulation by Centeno<sup>6</sup> except for those of  $n'$  in the  $2.8\mu$  band where Centeno's values are too low and have been replaced by the Bayly results.<sup>7</sup> No serious changes

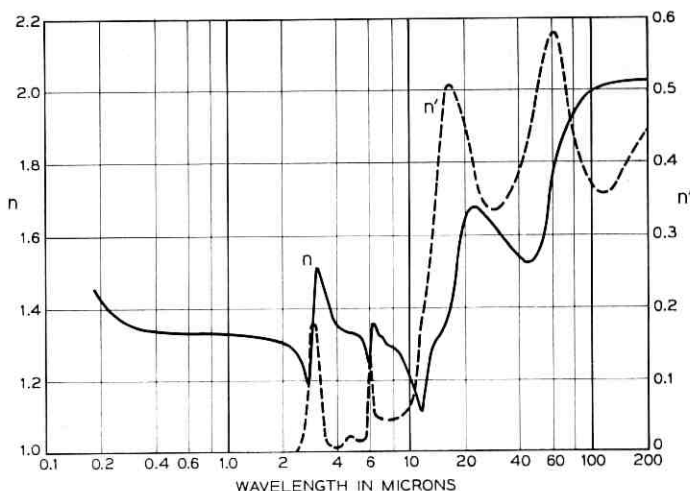


Fig. 1 — Complex refractive index ( $n - in'$ ) of liquid water.

at other wavelengths are reported in more recent literature. In particular, for the three wavelengths we investigated, the complex refractive indices of liquid water are well agreed upon:

$$\lambda = 0.63\mu, \quad n = 1.33, \quad n' \sim 10^{-6}$$

$$\lambda = 3.5\mu, \quad n = 1.42, \quad n' = 0.013$$

$$\lambda = 10.6\mu, \quad n = 1.18, \quad n' = 0.08.$$

The curves beyond  $18\mu$  in Figure 1 have been obtained from Kislovskii.<sup>8</sup> Most measurements of the refractive index of water have been conducted at  $20^\circ\text{C}$ , but it is known that as the temperature of the water is increased, the position of maximum absorption is shifted to slightly shorter wavelengths.<sup>9, 10</sup> However, detailed information on temperature dependence seems to be lacking. Much less data have been published for the complex refractive index of ice than for water. Figure 2, ice at  $-10^\circ\text{C}$ , is reproduced from Kislovskii for the sake of completeness.

### 2.3 Cross Sections and Attenuation Coefficients for Monodisperse Drop-Size Distribution

Using equations (7) and the above values of the complex refractive indices, extinction and absorption cross sections have been computed as a function of radius of water spheres for the three wavelengths we mentioned. The data are shown in Figure 3. When the radius of the water sphere becomes large, say 1 mm (that is, about the size of

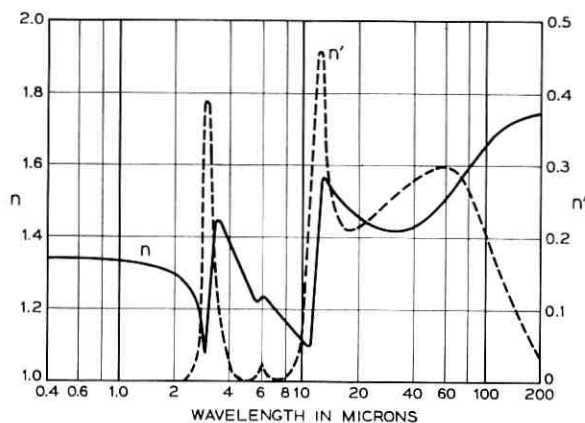


Fig. 2—Complex refractive index ( $n - in'$ ) of ice.

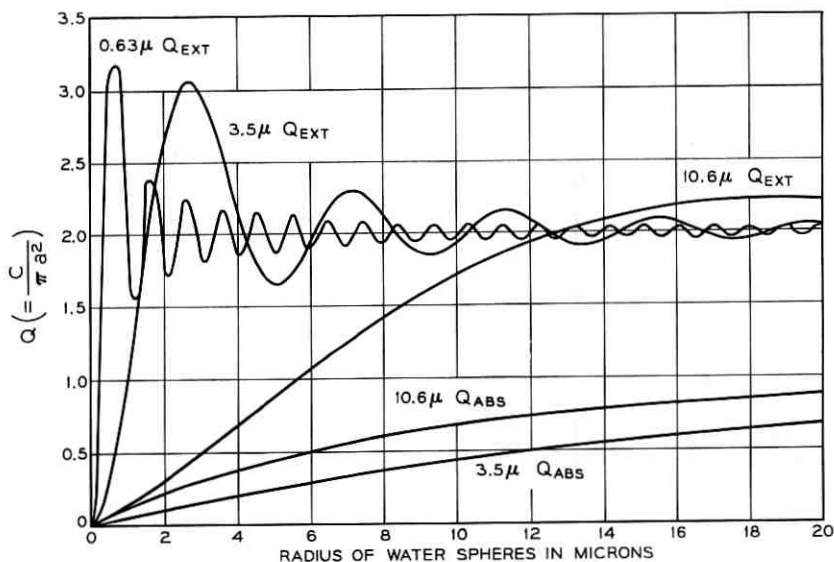


Fig. 3 — Approximate extinction and absorption cross sections.

a rain drop), the extinction cross sections approach two, while the absorptive cross sections at  $3.5\mu$  and  $10.6\mu$  approach unity. The absorption cross section of  $0.63\mu$  does not appear in Figure 3 because pure water is practically lossless at visible wavelengths. The extinction cross section for  $3.5\mu$  remains substantially less than that of  $0.63\mu$  only when the radius of water sphere is smaller than  $1\mu$ ; also, in that range, the extinction cross section of  $10.6\mu$  almost entirely results from absorption. The longer wavelength and the lower refractive index push the first maximum of the  $10.6\mu$  extinction cross section to an "a" of about  $19\mu$ .

Although fogs and rains never have drops of a single radius, it is instructive to calculate the attenuation coefficients for this ideal case. If we substitute

$$n(a) = \frac{w}{3\pi a^3} \delta(a) \quad (9)$$

into equation (4), where  $w$  is the liquid water density and  $\delta(a)$  is the Dirac delta function, then the extinction coefficient of liquid water becomes

$$\alpha = \frac{3}{4} \frac{Q_{\text{ext}} \text{ nepers}}{a \text{ km}} \Big/ \frac{\text{mg}}{\text{m}^3} = 3.25 \frac{Q_{\text{ext}} \text{ dB}}{a \text{ km}} \Big/ \frac{\text{mg}}{\text{m}^3} \quad (10)$$

where the radius of water sphere "a" is in microns. The extinction and absorption coefficients obtained using equation (10) are plotted in Figure 4.

The vast difference in attenuation by rain and fog is very clear from equation (10). Although the liquid water content of a typical heavy shower, say  $1000 \text{ mg/m}^3$ , is ten times that of a typical dense fog, say  $100 \text{ mg/m}^3$ , the fog drop radius is about one thousandth that of a rain drop. This is the primary reason why attenuation by rain is two orders of magnitude less than that of fog at optical wavelengths. For rains with drop radii about  $1 \text{ mm}$ , the extinction coefficient is only  $0.0065 \text{ (dB/km)/(mg/m}^3)$  (see Figure 4), thus a fairly heavy shower with a liquid water content of  $1 \text{ g/m}^3$  (rain rate about  $25 \text{ mm}$  per hour) has an extinction of about  $6.5 \text{ dB/km}$  for both optical and near-infrared wavelengths.

At least half of the attenuation resulting from rain at  $3.5 \mu$  and

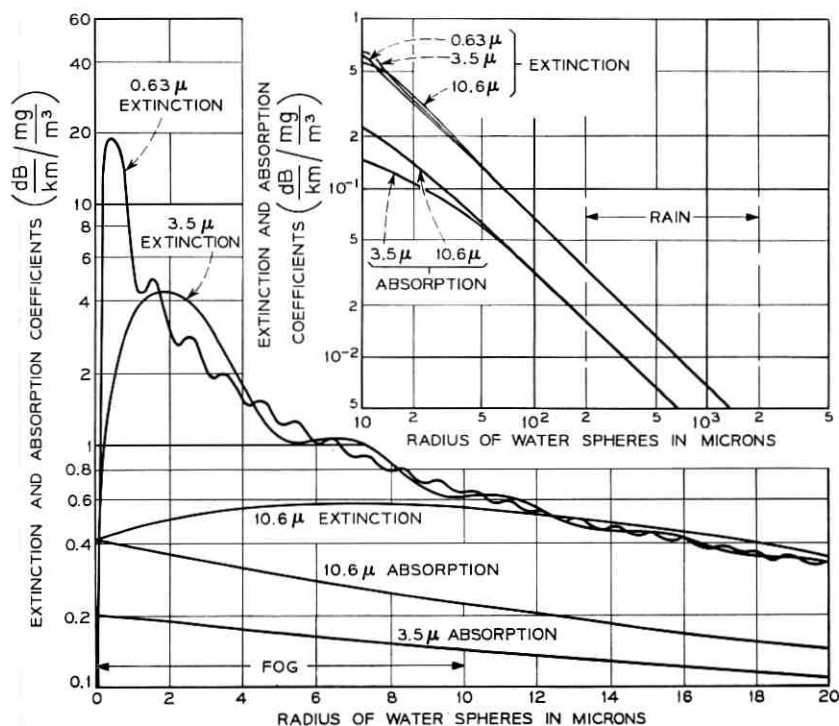


Fig. 4—Extinction and absorption coefficients of precipitation with monodisperse drop-size distribution.

$10.6\mu$  is absorptive loss while at  $0.63\mu$  it is caused almost entirely by scattering, as seen from Figure 4.

Attenuation by fog is contributed largely by water drops less than a few microns in radius, therefore much of the  $10.6\mu$  attenuation is absorptive loss, as implied by equation (8) and Figure 4. The extinction coefficient of fog is expected to be substantially less (up to one order of magnitude) at  $10.6\mu$  than at  $0.63\mu$  where scattering predominates. However, heavy fogs with liquid water contents exceeding  $0.1\text{gm}/\text{m}^3$  will attenuate  $10.6\mu$  more than 40 dB/km.

Attenuation by fog at  $3.5\mu$ , largely caused by scattering, remains significantly less than that of  $0.63\mu$  only if the fog drop radii are smaller than  $1\mu$ , as is also true for haze. Fogs which consist of drops with an average radius of  $5\mu$  are expected to attenuate about the same amount at optical and shorter near-infrared wavelengths.

#### 2.4 Calculations for Realistic Drop Size Distributions

Experimental difficulty and natural variations have caused gross inconsistency among the published data on measured fog drop-size distributions. Most of the measuring instruments fail to respond to droplets less than one micron in diameter, yet there are indications that the number density continues to increase as the diameter of fog drops decreases toward one micron. The relatively consistent information seems simply to be that the number density decreases for the larger drop radii.

For example, Eldridge's measurement shows that the number density decreases approximately with the inverse square of the drop diameter.<sup>11</sup> In searching for a realistic drop-size distribution for fog, the following model<sup>12</sup> for the number density, appeared to be plausible:

$$n\left(\frac{a}{a_m}\right) = A\left(\frac{a}{a_m}\right)^\alpha \exp\left[-B\left(\frac{a}{a_m}\right)^\gamma\right]. \quad (11)$$

Here

$$A = \left(\frac{\alpha}{\gamma}\right)^{(\alpha+1)/\gamma} \frac{\gamma}{\Gamma\left(\frac{\alpha+1}{\gamma}\right)} \frac{N}{a_m} \quad \text{and} \quad B = \frac{\alpha}{\gamma}.$$

$N$  is the number of drops per unit volume (say  $\text{cm}^3$ ),  $a_m$  the radius of the drops with the maximum number density, and  $\alpha$  and  $\gamma$ , parameters which can be adjusted to fit an observed fog particle size distribution. The liquid water density appropriate to the above model

is easily obtained by integrating equation (11).

$$W = \int_0^{\infty} n \frac{4}{3} \pi a^3 da = \frac{4\pi}{3} \left(\frac{\gamma}{\alpha}\right)^{3/\gamma} \frac{\Gamma\left(\frac{\alpha+4}{\gamma}\right)}{\Gamma\left(\frac{\alpha+1}{\gamma}\right)} a_m^3 N. \quad (12)$$

In Figure 5 four plots of equation (11) are given for several indicated combinations of parameters. Three of these exhibit a slope on the larger drop side of the maximum ( $a > a_m$ ) similar to that of Eldridge's measured distribution. The other combination of parameters ( $\alpha = 2, \gamma = 3$ ) shown in Figure 5 corresponds to the asymptotic distribution of coagulating particles<sup>13</sup> and has a sharp decreasing rate on both sides of the maximum number density.

Using these model distributions, extinction coefficients have been plotted versus the radius at maximum number density,  $a_m$ , in Figure 6. These curves merge at somewhat smaller values of  $a_m$  than do the corresponding curves for constant drop radius in Figure 4 because

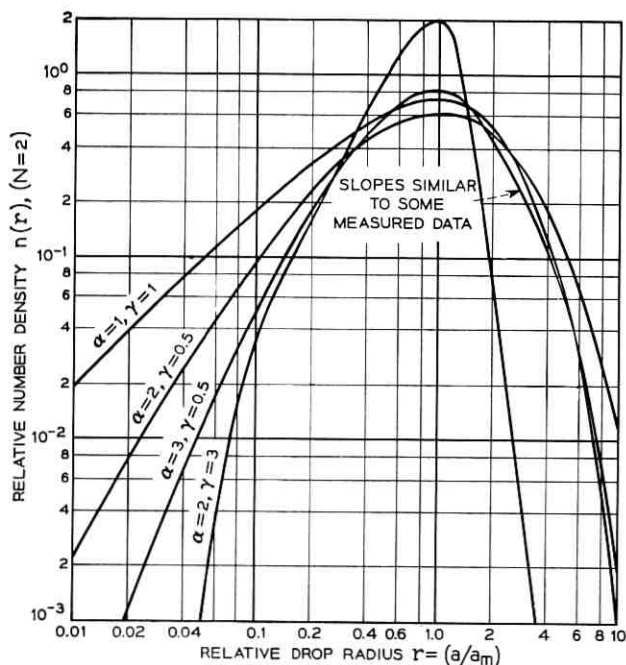


Fig. 5—Drop size distribution of fog models.  $n(r) = Ar^a \exp[-\alpha/\gamma r^\gamma]$   $A = (N/a_m) (\alpha/\gamma)^{(\alpha+3)/\gamma} \gamma/\Gamma[\alpha+1/\gamma]$ , and  $a_m$  = radius of drops with maximum number density.

the drops larger than  $a_m$  contribute more to the extinction than do smaller ones.\* The similarity between Figures 6(a) and 6(c) is attributed to the similar average slopes on the larger drop side of the corresponding distributions in Figure 5.

It is interesting to compare the above model with the Junge dis-

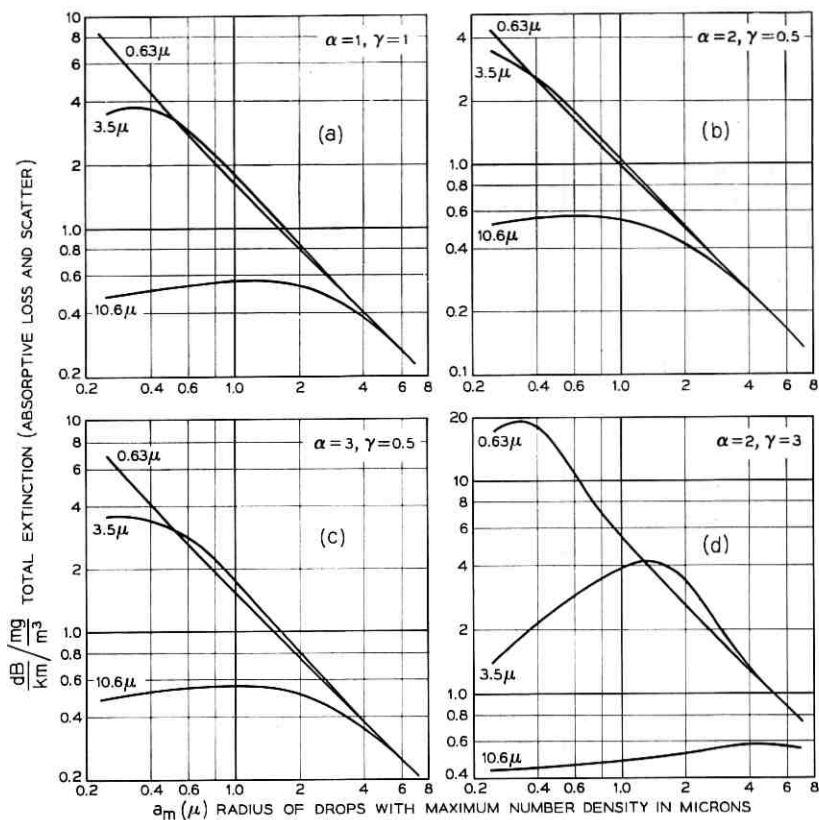


Fig. 6 — Extinction of coefficients for various fog models.

tribution<sup>14</sup> which states that  $n(a) = ca^{-p}$  where  $2 \leq p \leq 4$ .<sup>15, 16</sup> This simple relation points out the importance of decreasing number density for the larger drops; however, more parameters, such as those offered in equation (11), are needed to describe both ends of the

\* Although more extinction is obtained for the same amount of liquid water in the form of smaller drops than in the form of larger drops, the extinction cross section of a larger drop is, of course, greater than that of a smaller drop.

distribution. Since the extinction cross section is of the order of the geometrical cross section  $\pi a^2$ , the decreasing rate of larger drops can be approximated by the inverse square power ( $p \sim 2$ ) only in a limited range beyond which the number density must decrease much more rapidly to insure convergence of the integral in equation (4).

Raindrop size distributions measured at ground level seem to be fairly consistent among the published data. The Laws and Parsons<sup>17</sup> distributions which have been virtually confirmed by later workers are illustrated in Figure 7 and are readily available in tabulations.<sup>18</sup> Substituting these well-known distributions into equation (4) yields the extinction coefficient versus rain rate shown as the upper solid curve in Figure 8. Notice that the total extinction is the same for the visible and near-infrared wavelengths. Half of the extinction coefficient at  $3.5\mu$  or  $10.6\mu$  is contributed by the absorptive loss as illustrated in Figure 8.

### III. FORWARD SCATTERING

The energy intercepted by precipitation particles is partially scattered forward, toward the receiver, and this reduces the attenuation. Here is an approximate calculation for predicting the reduction of

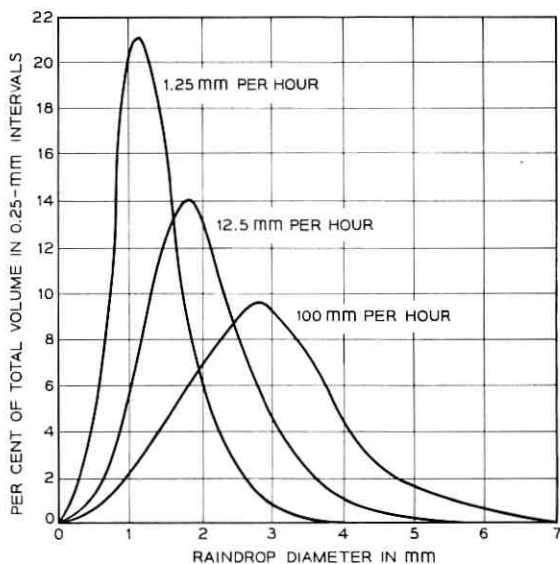


Fig. 7 — Raindrop size distributions by Laws and Parsons.

attenuation at  $0.63\mu$  and  $3.5\mu$  by forward scattering during rain, and a single-scattering model for beam broadening.

### 3.1 Approximate Correction Factor for Attenuation by Rain

The forward scattering pattern of a rain drop is assumed to be a Gaussian beam with an effective aperture area equal to the geometrical cross section of the water sphere.<sup>19</sup> Using the geometrical parameters illustrated in Figure 9, the scattering pattern of a raindrop of radius  $a$  situated at  $(\rho, \varphi, Z)$  is taken to be

$$\frac{2}{\pi w_s^2} e^{-2R^2/w_s^2}$$

where

$$w_s^2 \cong w_{os}^2 \left[ 1 + \left( \frac{\lambda(L-Z)}{\pi w_{os}^2} \right)^2 \right]$$

and the effective aperture area is  $2\pi w_{os}^2 = \pi a^2$ . The beam from the transmitter,  $T$ , is taken to be

$$\frac{2}{\pi w^2} e^{-2\rho^2/w^2}$$

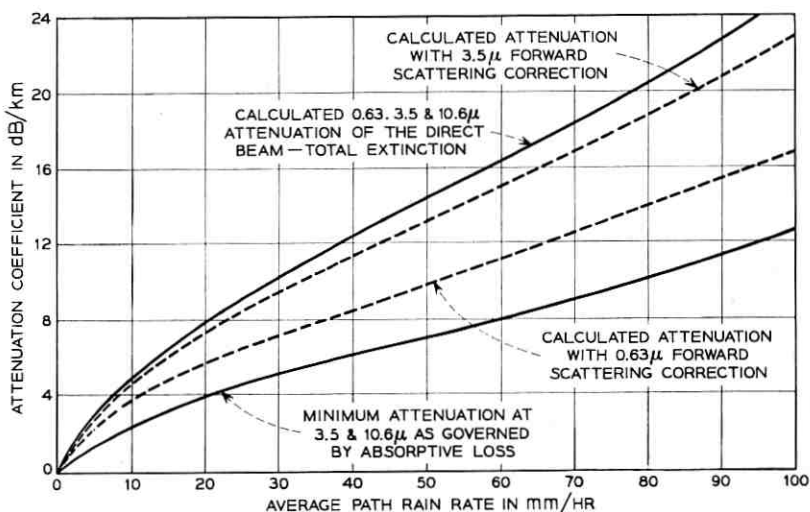


Fig. 8 — Rain attenuation coefficient for a 2.6 km path.

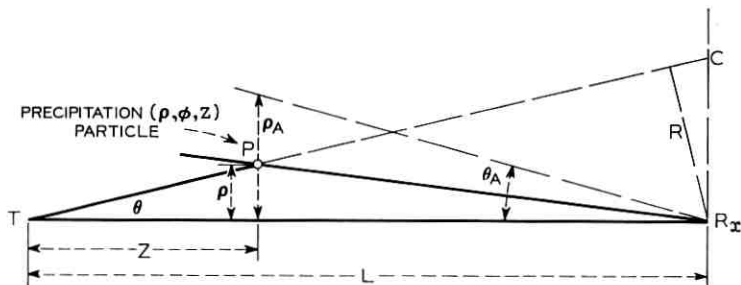


Fig. 9—Geometry for forward scattering.

where

$$w^2 = w_{oT}^2 \left[ 1 + \left( \frac{\lambda Z}{\pi w_{oT}^2} \right)^2 \right]$$

and  $w_{oT}$  is the minimum beam radius, located at the uniphase transmitting aperture. Then the attenuation in a path of length  $L$  is:

$$\alpha L(1 - \bar{\beta}) = \int_0^L \alpha dZ \left[ 1 - \frac{Q_{scn}}{Q_{ext}} \frac{1}{\frac{2}{\pi w_T^2}} \cdot \int_0^{\rho_A} \frac{2}{\pi w^2} e^{-2\rho^2/w^2} \frac{2}{\pi w_s^2} e^{-2R^2/w_s^2} 2\pi\rho d\rho \right]. \quad (13)$$

$\alpha$  is the extinction coefficient (the attenuation coefficient without forward scattering correction),  $\bar{\beta}$  the reduction factor resulting from forward scattering,  $Q_{scn}/Q_{ext}$  the fraction of the intercepted energy available for forward scattering,  $2/\pi w_T^2$  the maximum flux of the unattenuated transmitted beam at the receiver

$$\left( w_T^2 = w_{oT}^2 \left[ 1 + \left( \frac{\lambda L}{\pi w_{oT}^2} \right)^2 \right] \right),$$

and  $\rho_A/(L - Z) = \theta_A$  the acceptance angle of the receiver. It is easily shown from the geometry of Figure 9 that  $R/\rho = L \cos \theta/Z$ ; thus when  $\theta$  is small, as it is in practice,  $R \cong \rho L/Z$ . If the acceptance angle of the receiver is large compared with the scattering beamwidth of the rain drop,  $\rho_A$  can be replaced by  $\infty$ .

The above approximations simplify evaluation of the inner integral in (13) and lead to the following expression for the forward scattering

correction factor:

$$\bar{\beta} = \frac{1}{L} \frac{Q_{\text{scat}}}{Q_{\text{ext}}} \int_0^L \frac{w_T^2}{w_s^2 + w^2 \left(\frac{L}{Z}\right)^2} dZ. \quad (14)$$

Using equation (14),  $\bar{\beta}$  versus raindrop radius has been computed for  $L = 2.6$  km,  $\lambda = 3.5\mu$ ,  $w_{oT} = 0.55$  cm, and  $\lambda = 0.63\mu$ ,  $w_{oT} = 0.25$  cm. Table I gives the data. The two values of  $w_{oT}$  are the clear weather beamwidths in our experiments. Upon numerical integration over the raindrop size distribution one obtains the dashed curves in Figure 8. The above approximate calculation is essentially a crude multiple scattering model for very narrow beams because equation (13) implies that the forward scattering energy effectively rejoins the original transmitting beam.

### 3.2 A Single Scattering Model for Beam Broadening

Measurements discussed later show that various degrees of beam broadening occur when a  $0.63\mu$  laser beam propagates through precipitation. Beam broadening resulting from rain is more pronounced than that of snow and fog. Let us consider a single scattering model describing the effect of forward scattering on the attenuation, and beam broadening of a narrow laser beam. We are interested in the power distribution at the receiving plane.

Using cylindrical coordinates with origin at  $T$  as illustrated in

TABLE I—FORWARD SCATTERING CORRECTION FACTOR  $\bar{\beta}$  FOR A 2.6 KM PROPAGATION PATH

Raindrop Radius (cm)	$\lambda = 0.63\mu$ $w_{oT} = 0.25\text{cm}$	$\lambda = 3.5\mu$ $w_{oT} = 0.55\text{cm}$
0.025	0.106	0.025
0.050	0.202	0.049
0.075	0.289	0.071
0.100	0.366	0.093
0.125	0.434	0.113
0.150	0.495	0.133
0.175	0.548	0.152
0.200	0.595	0.169
0.225	0.636	0.186
0.250	0.672	0.202
0.275	0.703	0.217
0.300	0.730	0.232

$w_{oT}$  is the beam radius at which the field amplitude has fallen to  $1/e$  of its maximum value in the collimated transmitting aperture.

Figure 9, the intersection of  $TP$  with the receiving plane is  $(\rho L/Z, \phi, L)$  whereas an arbitrary point in the receiving plane is designated by  $(r, \phi', L)$ . The Cartesian coordinates of these two points in the receiving plane are  $(\rho L/Z \cos \phi, \rho L/Z \sin \phi, L)$  and  $(r \cos \phi', r \sin \phi', L)$  respectively. Since  $\theta$  is always very small for narrow laser beams, the scattering pattern of a raindrop will show negligible obliquity at the receiving plane and may be written as

$$S = \frac{2}{\pi w_s^2} \exp \left\{ -\frac{2}{w_s^2} \left[ \left( \frac{\rho L}{Z} \cos \phi - r \cos \phi' \right)^2 + \left( \frac{\rho L}{Z} \sin \phi - r \sin \phi' \right)^2 \right] \right\} \quad (15)$$

$$= \frac{2}{\pi w_s^2} \exp \left\{ -2 \left[ \frac{\left( \frac{\rho L}{Z} \right)^2 + r^2}{w_s^2} + \frac{2 \frac{\rho L}{Z} r \cos(\phi - \phi')}{w_s^2} \right] \right\}.$$

Then the scattering by a uniform rain of constant drop radius  $a$  over a path of length  $L$  is:

$$P_s = \int_0^L \alpha \frac{Q_{\text{scat}}}{Q_{\text{ext}}} dZ \left[ \frac{1}{2} \int_0^{2\pi} \int_0^\infty \frac{2}{\pi w_s^2} e^{-2\rho^2/w_s^2} S \rho d\rho d\phi \right]. \quad (16)$$

The definitions of the parameters in equations 15 and 16 are the same as in the preceding section. The integration over  $\phi$  is recognized as a Bessel function of imaginary argument

$$\int_0^{2\pi} \exp \left[ \frac{4 \frac{\rho L}{Z} r \cos(\phi - \phi')}{w_s^2} \right] d\phi = 2\pi J_0 \left( -i \frac{4\rho L r}{Z w_s^2} \right). \quad (17)$$

Using the well known identity

$$\int_0^\infty J_0(at) \exp(-p^2 t^2) t dt = \frac{1}{2p^2} \exp \left( -\frac{a^2}{4p^2} \right) \quad (18)$$

where  $a$  is an arbitrary complex number, one can perform the  $\rho$ -integration in equation 16:

$$2\pi \int_0^\infty J_0 \left( -i \frac{4\rho L r}{Z w_s^2} \right) \exp \left[ -2\rho^2 \left( \frac{1}{w_s^2} + \frac{L^2}{Z^2 w_s^2} \right) \right] \rho d\rho$$

$$= \frac{\pi}{2} \left( \frac{w^2 Z^2 w_s^2}{Z^2 w_s^2 + w^2 L^2} \right) \exp \left[ \frac{1}{8} \left( \frac{4Lr}{Z w_s^2} \right)^2 \left( \frac{w^2 Z^2 w_s^2}{Z^2 w_s^2 + w^2 L^2} \right) \right]. \quad (19)$$

Finally the  $Z$ -integration can be reduced to the following form for numerical computation:

$$P_s = \alpha \frac{Q_{\text{scat}}}{Q_{\text{ext}}} \int_0^L \frac{w_r^2}{w_s^2 + \left(\frac{L}{Z}\right)^2 w^2} \exp \left[ -\frac{2r^2}{w_s^2 + \left(\frac{L}{Z}\right)^2 w^2} \right] dZ. \quad (20)$$

Both  $\alpha$  and  $w_s$  in the above equation are functions of raindrop radius. Upon numerical integration of  $P_s$  over the raindrop size distribution one obtains the scattering pattern in the receiving plane.

Using  $L = 2.6$  km,  $\lambda = 0.63\mu$ ,  $w_{OT} = 0.25$  cm (equivalent to our experimental clear weather half-power beamwidth of twenty seconds) and the Laws-Parsons distribution, scattering patterns for a light rain 2.5 mm per hour and a heavy rain 50 mm per hour have been computed; these are shown in Figures 10(a) and 10(b), respectively. The direct beam pattern, the total power pattern, and the normalized total power pattern are also shown there. It has been tacitly assumed in the computations that the scattering and the direct beam are attenuated by the same factor,  $e^{-\alpha L}$ , and that the total power pattern is the arithmetic sum of the direct beam and the scattering. For light rain, (Figure 10a), the scattering modifies only

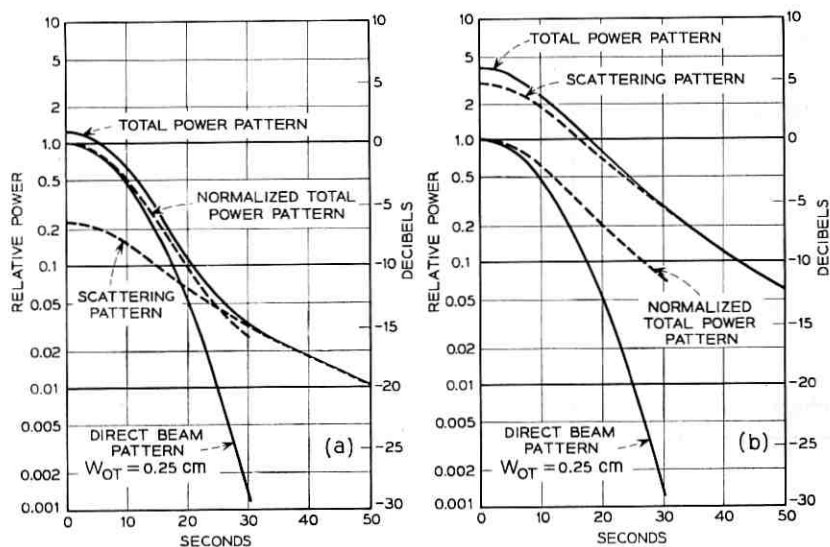


Fig. 10—Calculated scattering pattern and beam broadening. (a) Light rain, 2.5 mm per hour. (b) Heavy rain, 50 mm per hour.

slightly the clear weather or "direct" pattern. However, in heavy rain, (Figure 10b), the scattering becomes predominant.

One might expect more beam broadening the heavier the rain; however, since the average drop size increases with rain rate, the scattering pattern of a heavy rain is narrower than that of a light rain. This effect tends to offset somewhat the beam broadening by heavy rain. On the other hand, side lobes of rain drop scattering which have been neglected in the Gaussian approximation and multiple scattering effects which are inherently absent in the single scattering model will tend to increase the beam broadening. Also notice that beam broadening will be quite sensitive to inhomogeneity of the rain.

#### IV. EXPERIMENTAL EQUIPMENT

Figure 11 is a block diagram of the transmitting and receiving equipment for  $0.63\mu$  and  $3.5\mu$ . Care was taken to stabilize the transmitters both thermally and mechanically. The equipment for  $10.6\mu$  has been described by Wilson and Penzias.<sup>4</sup> Figure 12 gives the profile of the 2.6 km propagation path at Holmdel, N. J. Table II lists the parameters of the transmitting and receiving systems.

##### 4.1 $0.63\mu$ Equipment

The  $0.63\mu$  transmitter is a 50 mW multimode He-Ne laser; the cavity consists of two 10m-radius of curvature multilayer dielectric mirrors separated by 1.25m. The output is chopped mechanically at 330 cycles per second and passed through a refracting telescope which has an input lens of 5 cm focal length and an output lens of 50 cm focal length; the transmitting beam has a half power beamwidth of about 20 seconds in clear weather.

The received signal passes through attenuators, a  $3\text{\AA}$  bandwidth filter, a double-convex lens with an iris in the focal plane, and a polarizer to a photomultiplier. The receiver acceptance angle, about 10 minutes, is determined by the iris opening. Using a reference signal transmitted by telephone line, the synchronous detector gives a signal to noise ratio of 65 dB on a clear day; the limit of this sensitivity is set by the scattering of sunlight.

##### 4.2 $3.5\mu$ Equipment

The  $3.5\mu$  transmitter is a 5 mW multimode He-Xe laser; the 1.1m-long cavity consists of a plane reflecting mirror and a calcite polarizer

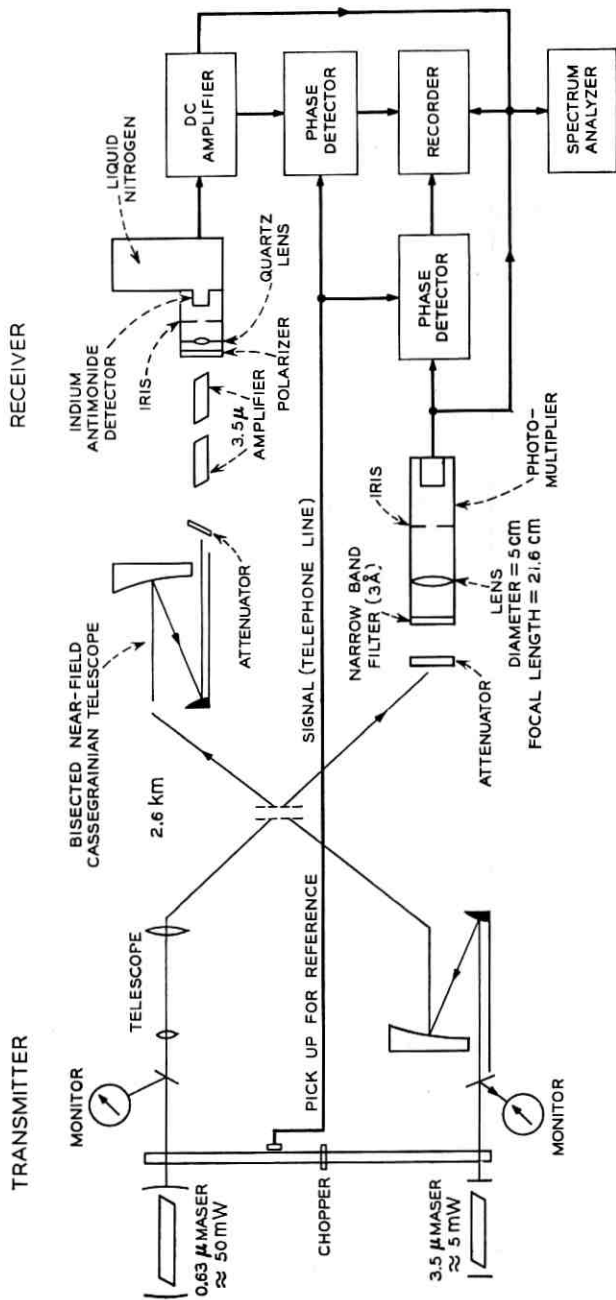


Fig. 11 — Sketch of the equipment.

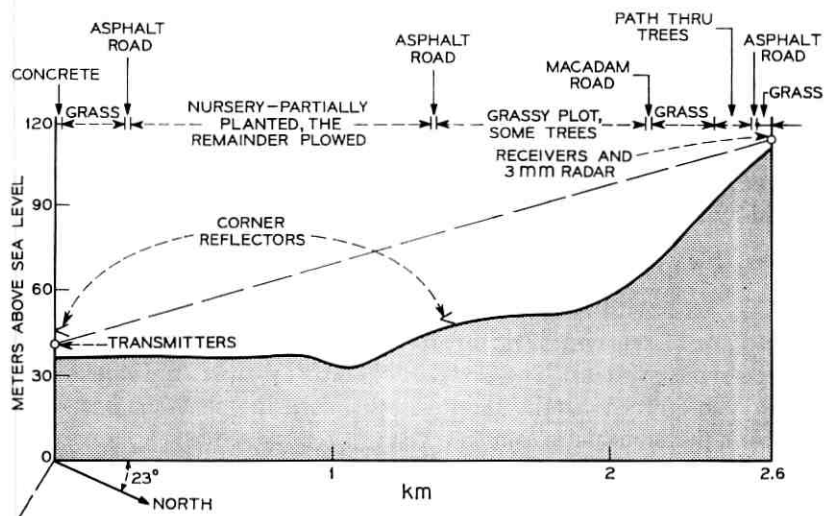


Fig. 12 — Profile of transmission path.

which acts as an output mirror. The output passes through the 330 Hz chopper to a bisected nearfield Cassegrainian telescope, a combination of two bisected confocal paraboloids. The main reflector is one half of a 38.1 cm diameter spin-cast paraboloid of 30.48 cm focal length while the subreflector has a diameter of 1.27 cm and a focal length of 1.02 cm.

Another bisected near-field telescope collects the signal for the receiver. The concentrated beam from the subreflector is amplified by two He-Xe tubes, each of about 18 dB gain. The good impedance match of the telescope plays an important role in successful application of these high-gain laser amplifiers. After the two amplifier tubes,

TABLE II—PARAMETERS OF THE TRANSMITTING AND RECEIVING SYSTEMS

Wavelength ( $\mu$ )	0.63	3.5	10.6
Laser oscillator	He-Ne	He-Xe	CO <sub>2</sub>
Transmitter power (mW)	50	5	500
Transmitting beamwidth (rad)	10 <sup>-4</sup>	2 × 10 <sup>-4</sup>	10 <sup>-3</sup>
Receiving aperture diameter (cm)	5	12.5	15
Laser amplifier	None	He-Xe	None
Detector	Photo-multiplier	In-Sb (77°K)	Thermopile
Measuring range (dB)	65	45	50

the signal passes through a calcite polarizer, a quartz lens, and an iris, to a liquid-nitrogen-cooled indium-antimonide photovoltaic infrared detector whose output is fed into a synchronous detection system. The receiver acceptance angle, about 1 minute of arc, is determined by the dimensions of the amplifier tubes and the telescope. A signal-to-noise ratio of 45 dB is obtained on a clear day. The receiver sensitivity is limited by the laser amplifier noise.

#### 4.3 $10.6\mu$ Equipment

A  $\text{CO}_2$  laser with an output of 0.5 W and a thermopile at the focal plane of a 15 cm collecting mirror comprise the  $10.6\mu$  transmitting and receiving systems. The laser is operated with a continuous flow of gas. Therefore, virtually uninterrupted measurement has been possible for a period of more than one year.

#### 4.4 3 mm Wavelength Radar

The 3mm wavelength radar, based on a method used earlier for study of absorption by atmospheric gases at millimeter wavelengths,<sup>20</sup> provides an independent measure of the liquid water content of fogs. The system uses a klystron, modulated linearly in frequency. Two precisely constructed trihedral corner reflectors are placed on the propagation path, one near the center of the path and the other at the optical transmitter terminal (see Figure 12). Measurement of the relative power reflected from the two reflectors results in attenuation data, accurate to about 0.2 dB per km, for that portion of the path between the reflectors.

#### 4.5 Rain Gauge System

Three gauges of the tipping-bucket type which register a pulse for each 0.25 mm of rain, are located at the transmitting site, path midpoint and the receiving site (see Figure 12). Data from the three gauges are recorded at the site of the optical receivers. No quantitative measurements are made during snow.

### V. MEASURED RESULTS

#### 5.1 Fog

In spite of available signal-to-noise ratios of 65 dB for  $0.63\mu$ , 45 dB for  $3.5\mu$ , and 50 dB for  $10.6\mu$ , the received signal at all three wavelengths has often fallen below their noise levels during dense fog. Thus our ability to measure the wavelength dependence of attenuation by

fog is limited to relatively light fogs with attenuations less than 25 dB per km. Figure 13(a) shows that in a typical morning fog (September 21, 1965) the attenuation (in decibels) of the  $3.5\mu$  wave is about half that of the  $0.63\mu$  wave. This result may be explained by fog droplets of about  $1\mu$  diameter.

The measured data occasionally reveal a much smaller ratio as in Figure 13(b) where the  $3.5\mu$  attenuation (September 15, 1965) amounts to only one sixth of the  $0.63\mu$  attenuation; this result implies a fog with many droplets smaller than one micron.

The measured attenuation of  $10.6\mu$  in a light fog is lower than at  $3.5\mu$ , as shown in Figure 13(c). At the beginning of this record (1.30 p.m. January 4, 1967), the signal at  $0.63\mu$  and  $3.5\mu$  are equal at a level of about  $-15$  dB while the  $10.6\mu$  signal is at about  $-2$  dB. This result can be explained, for example, by entering Figure 6(d) at a maximum drop radius of  $1.3\mu$ ; there, one sees that the attenuations at  $0.63\mu$  and  $3.5\mu$  are equal and exceed the  $10.6\mu$  attenuation by a factor of eight, roughly the observed value. But at 3 p.m. in Figure 13(c), the situation has changed significantly, and the ratios of the  $0.63\mu$ ,  $3.5\mu$ , and  $10.6\mu$  attenuations are now about 15:6:1. However, if we enter Figure 6(d) at a maximum drop radius of  $0.7\mu$ , the attenuation ratios are found to be very close to the observed values; thus it is found that small changes in the drop sizes can drastically affect wavelength dependence.

A percentage time distribution for the ratio of attenuation by light fog at  $3.5\mu$  and  $0.63\mu$  is plotted in Figure 14. The data, taken during seven separate fogs, were accumulated over sixteen hours during which the attenuation at either wavelength over the 2.6 km path was between 5 and 50 dB. It is seen that the median value of the ratio is 0.62 and the attenuation at  $3.5\mu$  is less than at  $0.63\mu$  85 per cent of the time. The 15 per cent of the time that the attenuation at  $3.5\mu$  exceeds that at  $0.63\mu$  may be caused in part by equipment instability; but it can be real for certain fog parameters, such as, in Figure 6(d),  $a_m = 2$  microns.

The data of Figures 4 and 6 predict that attenuation of  $10.6\mu$  is insensitive to the drop-size distribution in light fog where drop radii are about  $1\mu$ . Therefore, one expects close correlation between the liquid-water density of a light fog and the measured  $10.6\mu$  attenuation.

During measurement of attenuation of the laser beams by a morning fog May 20, 1966 (Figure 15), the liquid water density of the fog was determined by measuring the attenuation of 3 mm waves. At

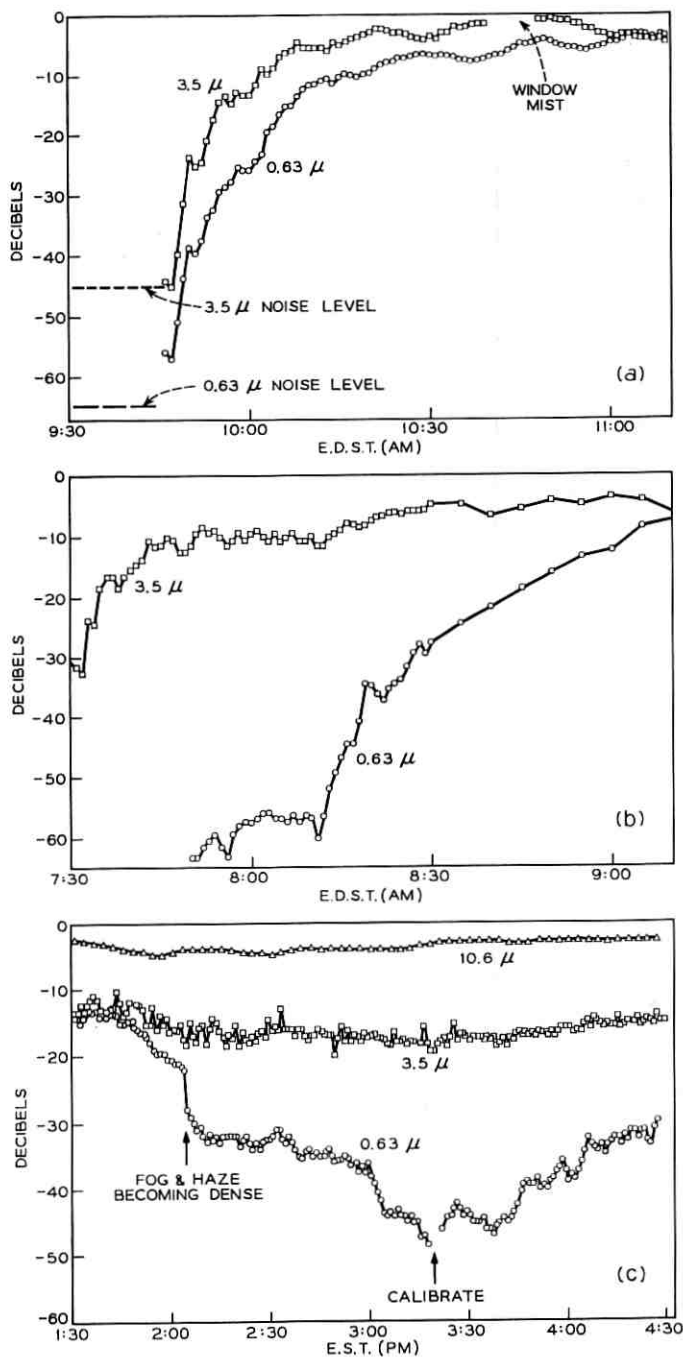


Fig. 13—Measurement of 2.6 km transmission loss in light fog. 0 dB-signal level in clear weather.

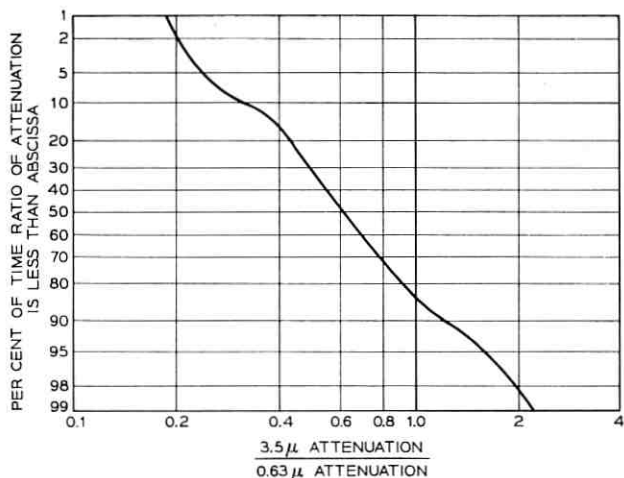


Fig. 14—A distribution for the ratio of attenuation by light fog at  $3.5\mu$  and  $0.63\mu$ .

3 mm, where the wavelength is certainly much greater than the fog-drop radius, the liquid water content is given by  $M = 0.25\gamma \text{ gm/m}^3$ ,<sup>18</sup>  $\gamma$  being the 3 mm attenuation coefficient in dB/km.

As shown in Figure 15, at 9:30 a.m. the laser beams could not be detected and the 3 mm data indicate a fog density of  $0.3 \text{ gm/m}^3$ . As the fog gradually lifted, the optical signals emerge in sequence above

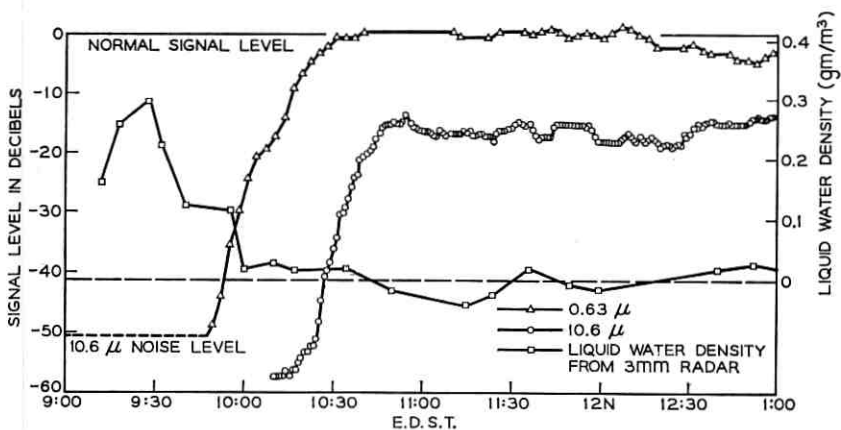


Fig. 15—Correlation between attenuation of laser beams and liquid water content measured by a 3 mm wavelength radar in fog.

the noise level but because dense haze lingered throughout the day, the  $0.63\mu$  wave remained below the clear weather level. There is good correlation between the attenuation of the laser beams and the liquid water content of the fog obtained by the 3 mm wavelength measurement. The zero reference of the liquid water density is taken at the vanishing of the attenuation of the  $10.6\mu$  laser beam. However, precise agreement between the measured attenuation of  $10.6\mu$  and that calculated from the liquid water content obtained at 3 mm is difficult to establish because of the very small attenuation at 3 mm for light fogs. It should also be kept in mind that the fog density measured by the 3 mm radar is an average over only about half of the propagation path (see Figure 12).

### 5.2 Rain

Transmission through some light rains is difficult to interpret because the rain is mixed with fog; however, summer showers are very suitable for evaluating attenuation by rain. Figure 16 shows typical measured data during a summer shower; attenuation of  $3.5\mu$  is consistently about 20 per cent greater than that of  $0.63\mu$ . The attenuation is well correlated with the rain rate averaged over the path. The average path rain rate is taken to be the arithmetic average of the readings of the three rain gauges described in Section 4.5, with that of the midpoint gauge carrying a double weight.

Owing to the variation in raindrop terminal velocity and drop size distribution, the relationship between the attenuation coefficient and the rain rate can be hardly expected to be linear. However, the predicted attenuation coefficient for the rain rate between 12.5 and 100 mm per hour is almost linear as shown in Figure 8. Therefore, it is justifiable to determine a least square line for measured data of attenuation by rain above a rate of 12.5 mm per hour. Figure 17 shows a least square line

$$\alpha\left(\frac{\text{dB}}{\text{km}}\right) = 0.155p\left(\frac{\text{mm}}{\text{hr}}\right) + 2.66$$

for the measured  $0.63\mu$  data of Figure 16 and two other showers.

The calculated curves for  $0.63\mu$  attenuation by rain with and without forward scattering correction (from Figure 8) have been included in Figure 17 for comparison. The good agreement between the measured line and the curve calculated with forward scattering may appear somewhat fortuitous in view of the rms deviation 2.8 dB/km. How-

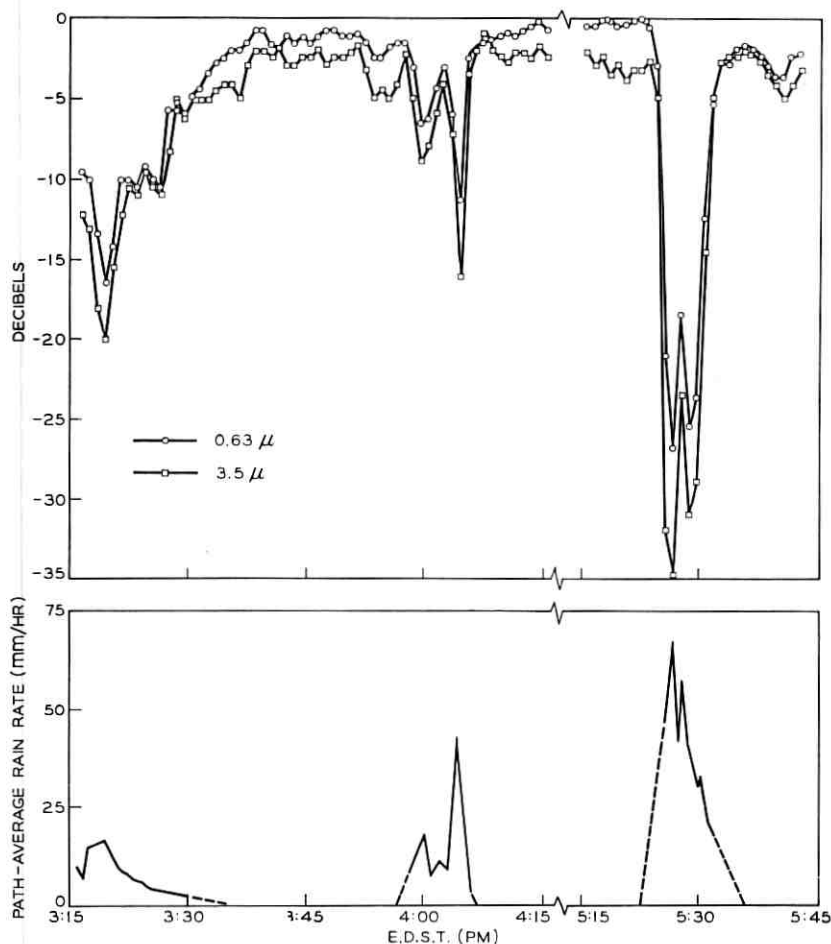


Fig. 16 — Measurement of 2.6 km transmission loss in rain showers on September 24, 1965. 0 dB-signal level in clear weather.

ever, only peak attenuations of summer showers which are relatively free of foggy conditions have been taken as measured data in Figure 17.

The relatively large rms deviation is explained as follows: the sampling of a spatially nonuniform shower by three rain gauges does not provide a satisfactory average rain rate over the 2.6 km path; the attenuation depends upon drop size distribution which may vary from one shower to another; since optical attenuation by fog is orders of

magnitude higher than that by rain, any slight mist or haze within the rain can appreciably change the measured values.

Simultaneous measurements at all three wavelengths were carried out in an unusually heavy rainstorm of September 21, 1966, during which more than 125 mm of rain accumulated. A sample of the measured data from this storm is given in Figure 18.

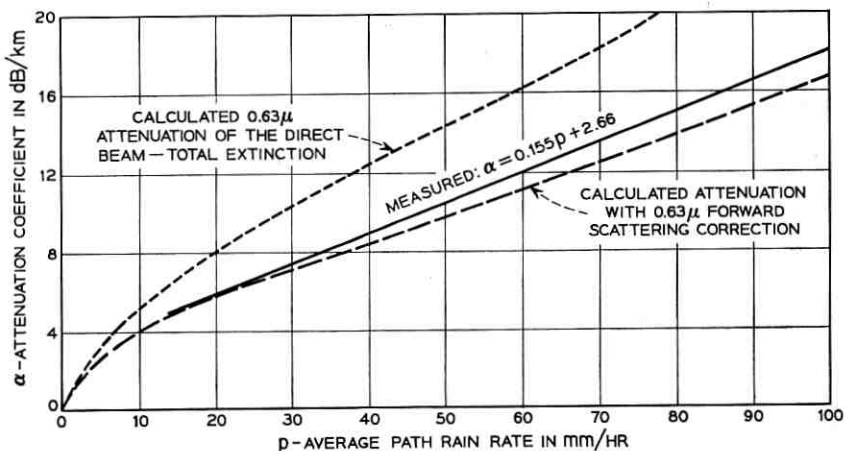


Fig. 17—Measured rain attenuation coefficients of  $0.63\mu$  for a 2.6 km path; standard deviation is  $\pm 2.8$  dB per km at a rain rate of 50 mm/hr.

Points corresponding to the peak attenuations of the separate showers in the storm are plotted in Figure 19 and least-square lines for each wavelength have been drawn for rain rates between 10 and 60 mm per hour. The attenuation by rain at  $10.6\mu$  and  $3.5\mu$  is consistently greater than that at  $0.63\mu$ . At  $0.63\mu$  the agreement between calculated and measured values is again rather good. Notice that the measured points at 95 mm per hour fall below the predicted curve.\* When we compare Figure 19 with Figure 13(c), say, it is obvious that the wavelength dependence in propagation through rain is inverse to that through fog.

\* The  $0.63\mu$  data in Figures 18 and 19 were not taken with the same receiving telescope as those of Figure 16 (5 cm diameter, see Table 1). Rather, a near-field cassegrain telescope with a collecting aperture of 600 cm was used. This change was made to determine whether or not a large receiving aperture would intercept more of the energy forward scattered by the rain (see Figures 10 and 21a) and thereby further decrease the attenuation. However, the attenuations (relative to the clear-day value) measured with the large aperture did not turn out to be significantly less than those measured with the small one.

Another sample of measured data is shown in Figure 20;† it is of particular interest because the attenuation at  $0.63\mu$  is much lower (about 18 dB) than in previous measurements and calculation for the same rain rates. The attenuation at  $3.5\mu$  and  $10.6\mu$  is only slightly below the prediction. Examination of the raw data shows that the rain distribution along the path was characterized by higher rates

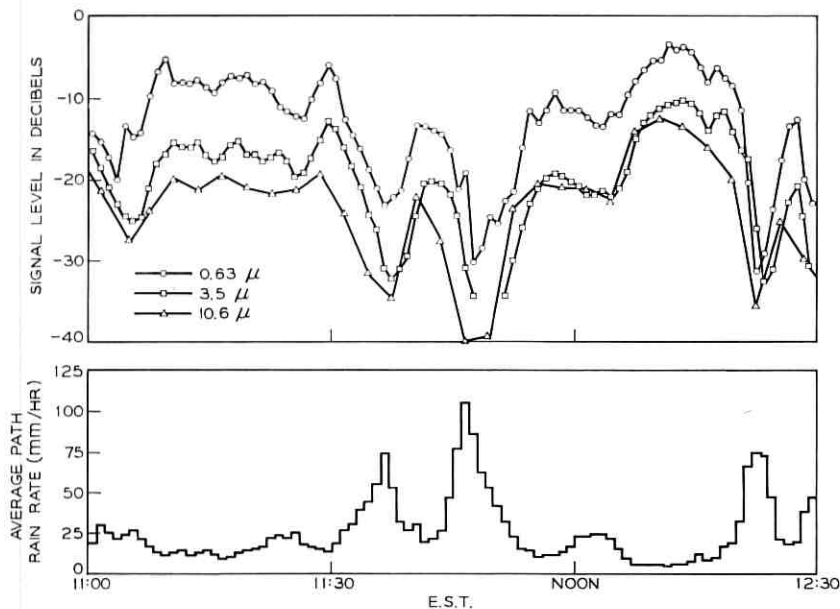


Fig. 18— Measurement of 2.6 km transmission loss in a rain storm. 0 dB-signal level in clear weather.

near the receiving site. This observation suggests that this very low attenuation at  $0.63\mu$  is caused by a strong forward scattering contribution which is most effective when the scattering particles are near the receiver. This result is also confirmed by the measured data of the rain showers in Figure 16. There the relatively low  $0.63\mu$  attenuation coefficient measured in the second shower is also associated with a rain distribution with high concentration near the receiving site.

† The data in Figure 20 were taken with a  $0.63\mu$  transmitter beamwidth of  $5 \times 10^{-4}$  radians.

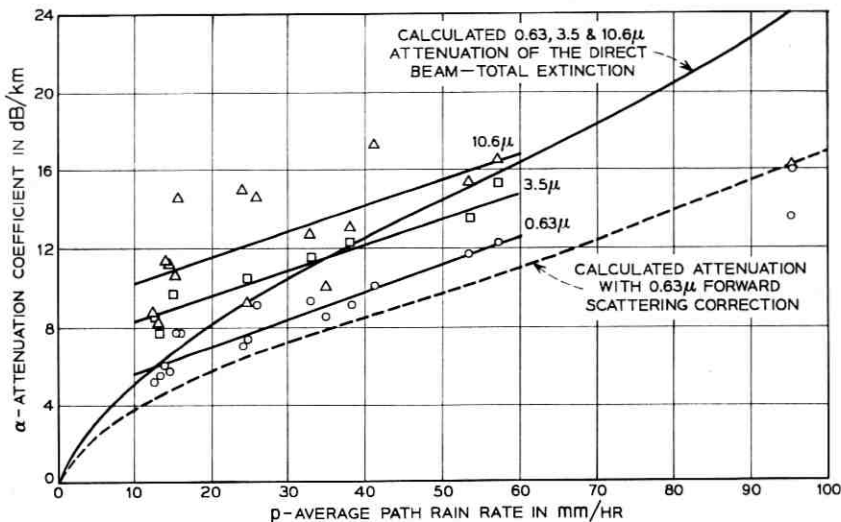


Fig. 19—Measured attenuation coefficients of a rain storm for a 2.6 km path.

### 5.3 Snow

Figure 21 shows measurements of transmission loss through a light snow shower. The accumulation never exceeded about 12.5 mm per hour. Snows heavier than this have caused the signals at all three wavelengths to fall below the noise levels. The  $10.6\mu$  wave often appears to suffer greater attenuation in snow as illustrated in Figure 21; however, no definite wavelength dependence is consistently observed.

### 5.4 A Cumulative Distribution of Attenuation at $10.6\mu$

In Section 4.3 we mentioned that the  $10.6\mu$  equipment operated continuously. Signal levels for the period June 1966 to May 1967 have therefore been analyzed and reduced to a cumulative distribution of attenuation as shown by the central curve in Figure 22. For example, one sees that attenuation on the 2.6 km path, resulting from all causes, exceeded 30 dB (11.5 dB/km) three per cent of the time. Also shown in the figure are distributions for the months with the highest (March) and lowest (July) outage times. Clearly, during July, a system operating at  $10.6\mu$  would be quite reliable; however, during March, heavy attenuations, mainly caused by fog, occur all too often on a 2.6 km path.

5.5 Beam Broadening at  $0.63\mu$ 

Typical measured results on the beam broadening effects of rain, snow, and fog are presented in Figures 23, 24, and 25, respectively. Curve 1 in each figure is a typical clear-weather beam (about 20-second half-power beamwidth); this broadening is essentially determined by the inhomogeneities of the refractive index in the atmosphere. Notice that the clear weather beam itself is subject to modest variation but this variation is generally much less than the beam broadening observed under conditions of precipitation. The beam

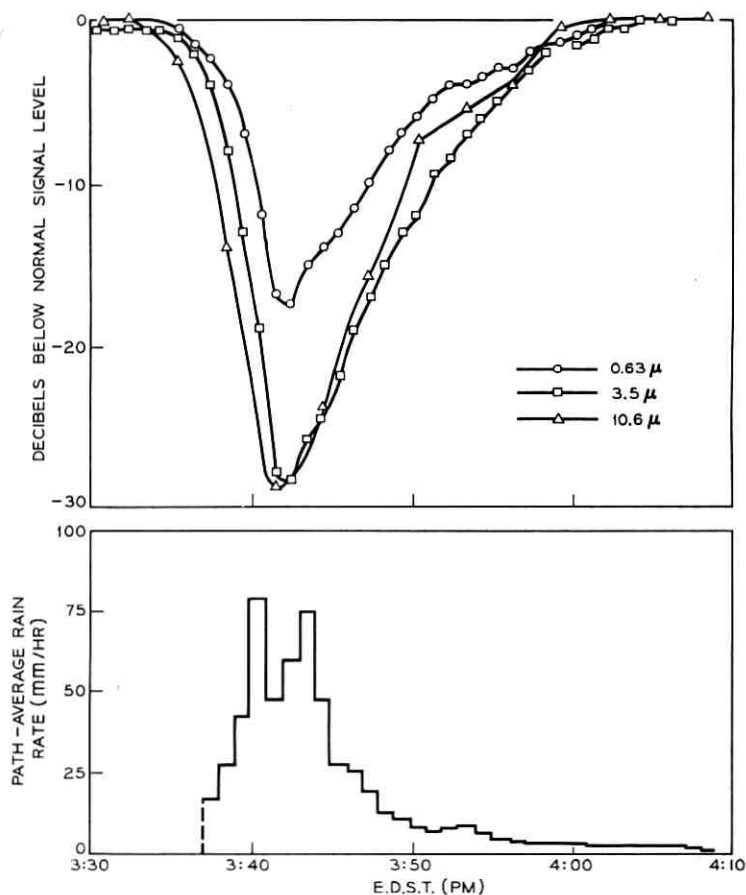


Fig. 20 — Measured attenuation over 2.6 km during a rain shower on July 11, 1967. 0 dB-signal level in clear weather.

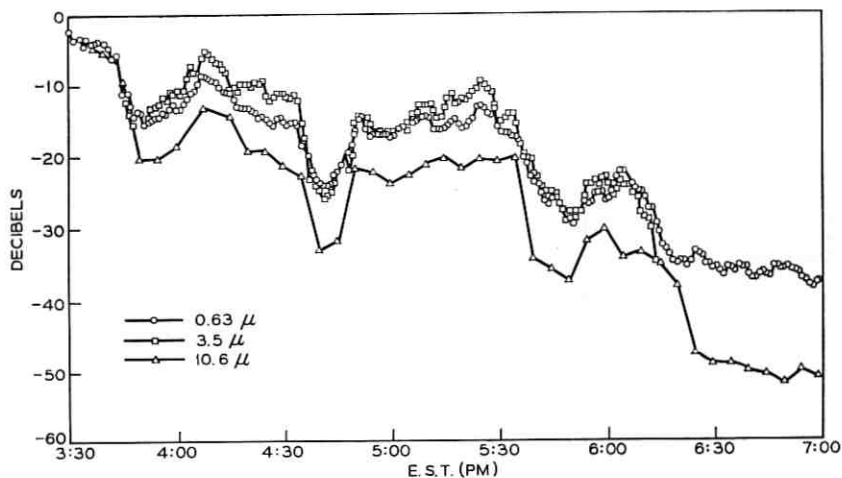


Fig. 21 — Measurement of 2.6 km transmission loss during a light snow shower on January 26, 1966. 0 dB-signal level in clear weather.

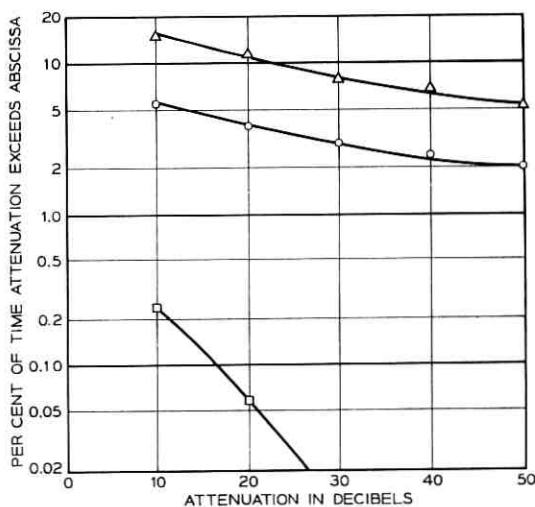


Fig. 22 — A cumulative distribution of attenuation at  $10.6\mu$  over a 2.6 km path.  $\circ$  = Average attenuation from June 1966 to May 1967.  $\triangle$  = March 1967, highest month.  $\square$  = July 1966, lowest month.

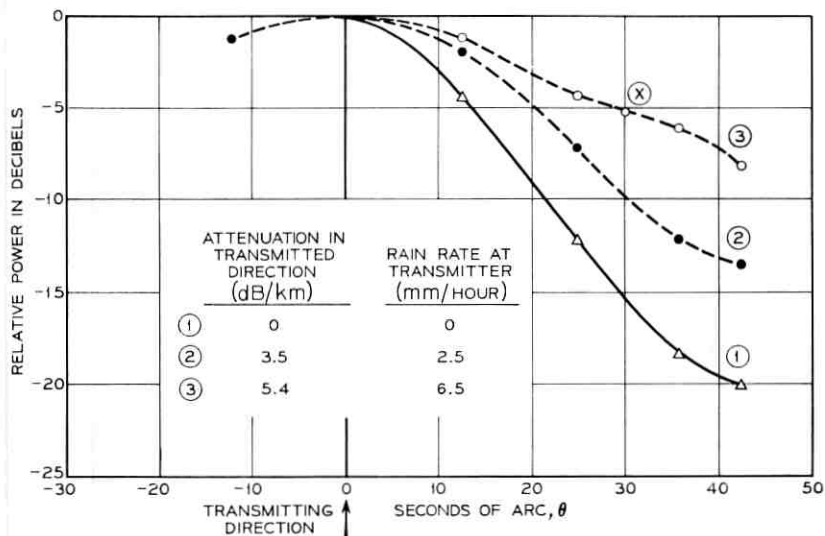


Fig. 23 — Beam broadening caused by rain.

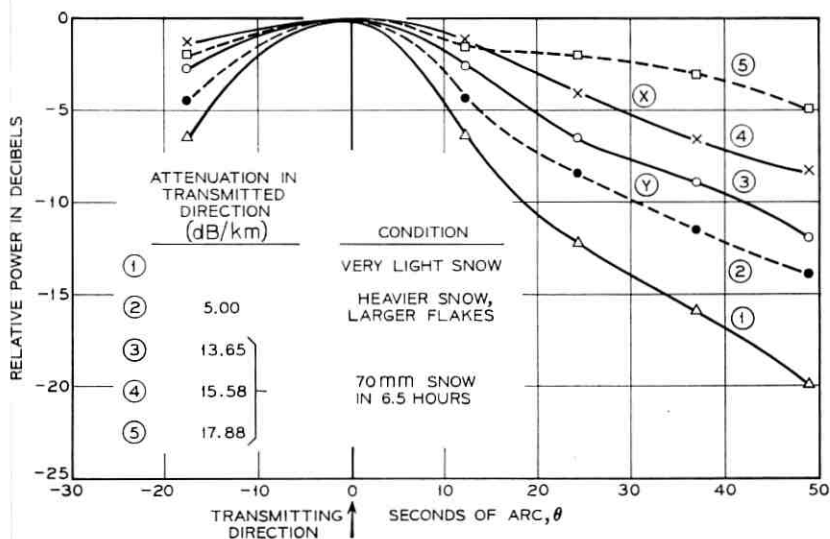


Fig. 24 — Beam broadening caused by snow.

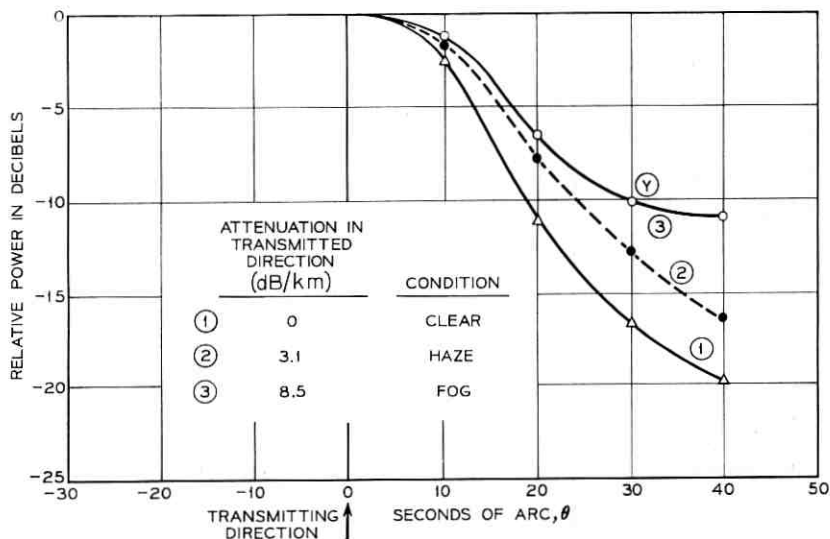


Fig. 25 — Beam broadening caused by fog.

broadening is measured by moving the receiver on a horizontal track transverse to the axis of the incident beam.

The other measured curves show beam broadening resulting from precipitation and the corresponding attenuations along with descriptions of precipitation; the curves are normalized at  $\theta = 0$ , the direction of the beam axis. In general, the highest attenuations correspond to the greatest beam broadening. In Figure 24, we see that the onset of beam broadening caused by snow occurs when the attenuation is fairly high. Broadening effects in the case of rain are observable at much lower attenuations (Figure 23). This is because raindrops produce more forward scattering than snow flakes which suffer from poor geometry and random orientations. Thus, the X points show the same amount of beam broadening in Figures 23 and 24; but the corresponding attenuations are 5.4 dB/km for the rain and 15.6 db/km for the snow.

Although the beam broadening, caused by fog also is readily measurable, the fog drop, being comparable in size with wavelength, is even less efficient in forward scattering than the snow flake. The Y points in Figures 24 and 25 show that the attenuation by fog is about twice that of snow for the same degree of beam broadening.

The measured beam broadening due to rain exceeds the prediction

of a single-scattering gaussian model as discussed in Section 3.2. Quantitative correlations are difficult because of the time variability and inhomogeneity of rainfall along the path.

#### VI. DISCUSSIONS

A simple picture of the vast difference in attenuation of micron waves by fog and rain has been substantiated by theory and experiment. The relatively low attenuation by rain is, in part, the result of forward scattering. Owing to the difficulty of obtaining independent physical data on snow, quantitative correlation between physical measurements of precipitation and transmission has been made only for rain and fog. The predictability of attenuation of optical waves by rain is comparable to that for microwaves.<sup>21</sup> Indeed, visible wavelengths are attenuated less than millimeter wavelengths.

Attenuation by dense fogs often exceeds 20 dB/km. The wavelength dependence of attenuation by light fog, that is, progressively less attenuation with increasing wavelength, has been observed as expected, but the dependence is a strong function of the drop-size distribution. Similar results for incoherent light have been reported in the literature.<sup>15, 22</sup> Although the predicted wavelength dependence for heavy fogs which consist of drops with average radius of  $5\mu$ , is weaker than for light fogs, the attenuation at  $10.6\mu$  would still be significantly less than at visible and shorter infrared wavelengths (see Figure 4). However, a typical dense fog of  $0.1 \text{ g/m}^3$  liquid water density is calculated to attenuate  $10.6\mu$  by at least 40 dB/km. Attenuation by fog at  $10.6\mu$  is characterized by strong absorption and relative insensitivity to drop-size distribution.

The measured attenuation by rain, about  $0.2 \text{ (dB/km)/(mm/hr)}$  at  $0.63\mu$ , is consistently less (about 20 to 40 per cent) than at  $3.5\mu$  and  $10.6\mu$ . Rain drops, which are absorbing spheres at  $3.5\mu$  and  $10.6\mu$ , offer less scattering than at visible wavelengths and also have a less directional scattering pattern owing to the longer wavelengths.

The scattering patterns of fog drops have little directivity compared with the laser beams themselves therefore the forward scattering correction for the fog attenuation of narrow laser beams is small. If the beamwidth of the incident laser beam is comparable with the width of the scattering patterns of precipitation particles, the forward scattering will reduce the scattering loss significantly which, indeed, is mentioned in Section 5.2 for the propagation of  $0.63\mu$  through

rain. Naturally the absorptive loss is not subject to any reduction. But the scattering loss of a laser beam propagating through fog cannot increase indefinitely as the fog density increases.\* In particular, for a visible source radiating into a homogeneously distributed dense fog, the energy must ultimately diffuse outward in all directions, thus the free space loss of an isotropic point source appears to be the limit of the scattering loss.

When the scattering by precipitation particles is added to the attenuated original beam, a broadened beam is observed at the receiving plane; this has been illustrated by a single scattering gaussian model in Section 3.2 and by measured results in Section 5.5.

The apparent attenuation on the beam axis is reduced by the scattered component. For heavy rain, the received signal is dominated by the scattering as illustrated in Figure 10(b) and the reduction in attenuation becomes significant. When the scattering correction is small, estimates by the single scattering model (Section 3.2) and the multiple scattering model (Section 3.1) are practically the same. For relatively large corrections the multiple scattering model is expected to give a better estimate.

The precise prediction of attenuation of laser beams by precipitation in the atmosphere is hampered by the uncertainty of particle size distributions. A better knowledge of the drop size distribution is certainly desirable to provide a firm ground for the prediction of attenuation, but even a measured drop-size distribution might lead to ambiguous interpretation when the variability and inhomogeneity of the natural fog or rain is unaccounted for. Summations over unreliable drop size distributions introduce complicated-looking problems but provide little more information than a simple relation such as equation (10).

Although it is convenient to distinguish between rain and fog by a classification of drop size, one should be aware of the frequent occurrence of the intermediate states in the form of a drizzle or a mixture of rain and fog. The attenuation under these conditions has been observed to exhibit transition characteristics; however, little can be said beyond this trivial observation.

The prediction of attenuation by snow has not been touched upon here, but the experimental data indicate that it lies intermediate be-

---

\* A common experience is to observe a heavy fog during daylight hours; although the sun is completely obliterated, the observer still has considerable scattered light in his environs.

tween that of rain and fog for a given amount of equivalent liquid water.

In order to evaluate relative merits of systems using different wavelengths, it is interesting to compare the attenuation by precipitation at optical wavelengths with that in other parts of the electromagnetic spectrum. Figure 26 presents the approximate attenuation coefficients for a typical dense fog and a representative shower in the frequency range from  $10^{10}$  to  $10^{15}$  cps.<sup>18, 21</sup> The absorption for a water layer containing the same amount of liquid water as the rain is also shown in Figure 26 for reference. The attenuation by rain decreases slowly from millimeter to visible wavelengths. However, the attenuation by fog is about two orders of magnitude less than that of rain at upper microwave frequencies, while the optical attenuation by fog is about two orders of magnitude greater than that of rain. Notice that, even

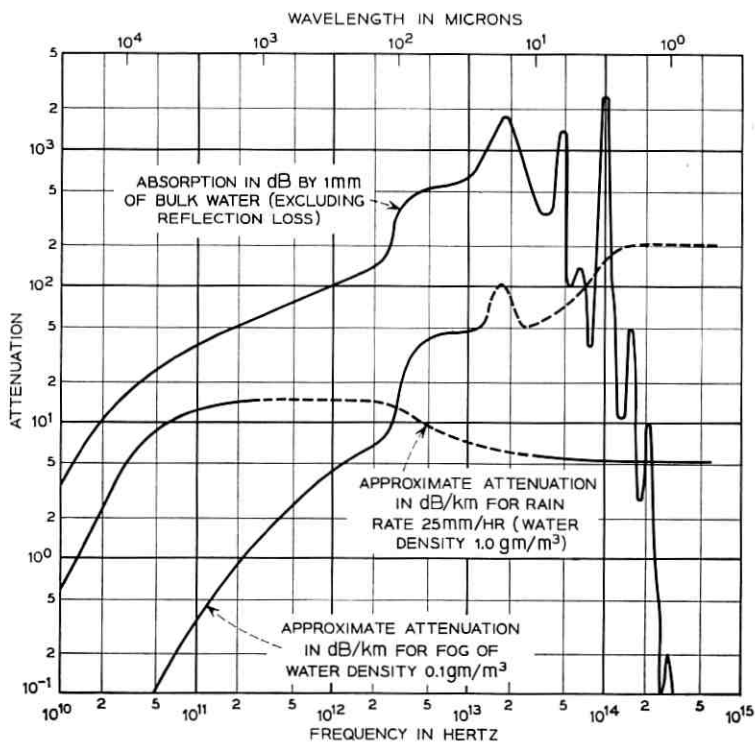


Fig. 26—Attenuation due to liquid water in various forms as function of frequency.

at  $10\mu$ , where attenuation by fog passes through a weak minimum (see Figure 26), the attenuation is still rather large as far as a practical communication system is concerned.

## ACKNOWLEDGMENT

The authors are indebted to R. W. Wilson, A. A. Penzias, and A. W. Norris for the experimental data at  $10.6\mu$  and the distribution in Figure 22. Technical assistance was given by R. A. Desmond and C. A. Davison and R. A. Semplak; the computations were made by Mrs. E. Kerschbaumer.

## REFERENCES

1. Chu, T. S. and Hogg, D. C., "The Attenuation of  $3.392\mu$  He-Ne Laser Radiation by Methane in the Atmosphere," *B.S.T.J.*, *45* (February 1966), pp. 301-306.
2. Middleton, W. E. K., *Vision Through the Atmosphere*, University of Toronto Press, (1952) p. 43.
3. Hogg, D. C., "Scattering and Attenuation Due to Snow at Optical Wavelengths," *Nature*, *203* (July 25, 1964), p. 396.
4. Wilson, R. W. and Penzias, A. A., "Effect of Precipitation on Transmission Through the Atmosphere," *Nature*, *211* (September 3, 1966), p. 1081.
5. H. C. Van de Hulst, *Light Scattering by Small Particles*, New York: John Wiley and Sons (1957), chapter 11.
6. Centeno, M., "The Refractive Index of Liquid Water in the Near Infrared Spectrum," *J. Opt. Soc. Amer.*, *31* (March 1941), pp. 244-247.
7. Bayly, J. G. and others "The Absorption Spectra of Liquid Phase  $H_2O$ ,  $HDO$ , and  $D_2O$  from  $0.7\mu$  to  $10\mu$ ," *Infrared Phys.*, *3* (December 1963), pp. 211-223.
8. Kislovskii, L. D., "Optical Characteristics of Water and Ice in the Infrared and Radio Wave Regions of the Spectrum," *Opt. Spectroscopy*, *7* (September 1959), pp. 201-206.
9. Curcio, J. A. and Petty, C. C., "The Near Infrared Absorption Spectrum of Liquid Water," *J. Opt. Soc. Amer.*, *41* (May 1951), pp. 302-304.
10. Draeger, D. A., and others, "Far-Infrared Spectrum of Liquid Water," *J. Opt. Soc. Amer.*, *56* (January 1966), pp. 64-69.
11. Eldridge, R. G., "A Few Fog Drop-Size Distributions," *J. Meteorology*, *18* (October 1961), pp. 671-676.
12. Diermendjian, D., "Scattering and Polarization Properties of Polydispersed Suspensions With Partial Absorption," *Electromagnetic Scattering* (Proc. Interdisciplinary Conf. Electromagnetic Scattering), ed. M. Kerker, New York: Pergamon Press, pp. 171-189, 1963.
13. Erkovich, S. P., and others, "Influence of Fog on the Range of Ground Communication Using an Optical Carrier," *Telecommunications and Radio Eng.*, (December 1965), pp. 12-16. trans. from Russian.
14. Junge, C., "The Size Distribution and Aging of Natural Aerosols as Determined From Electrical and Optical Data on the Atmosphere," *J. Meteorology*, *12* (February 1955), pp. 13-25.
15. Kurnick, S. W., Zitter, R. N., and Williams, D. B. "Attenuation of Infrared Radiation by Fog," *J. Opt. Soc. Amer.*, *50* (June 1960), pp. 578-583.
16. Saunders, M. J., unpublished work.
17. Laws, J. O. and Parsons, D. A., "The Relation of Rain Drop Size to Intensity," *Trans. Amer. Geophys. Union*, *24* (1943), pp. 452-460.

18. Kerr, D. E., Propagation of Short Radio Wave, New York: McGraw-Hill Book Co., Inc., 1951, Chapter 8.
19. Chu, T. S., "An Approximate Generalization of the Friis Transmission Formula," Proc. IEEE, 53 (March 1965), pp. 296-297.
20. Crawford, A. B. and Hogg, D. C., "Measurement of Atmospheric Attenuation at Millimeter Wavelengths," B.S.T.J., 35 (July 1956), pp. 907-916.
21. Medhurst, R. G., "Rainfall Attenuation of Centimeter Waves: Comparison of Theory and Measurement," IEEE Trans. Antennas and Propagation, AP-13 (July 1965), pp. 550-564.
22. Arnulf, A., and others, "Transmission by Haze and Fog in the Spectral Region 0.35 to 10 Microns," J. Opt. Soc. Amer., 47 (June 1957), pp. 491-498.



# The Stream Guide, a Simple, Low-Loss Optical Guiding Medium

By P. KAISER

*Heat generated by viscous friction in a high speed gas flow in a pipe causes a transverse refractive index variation that can continuously focus a light beam passing through this pipe. The comparatively simple construction, together with the low losses inherent in gaseous guiding media, makes the stream guide attractive as an optical beam waveguide. This article presents theoretical and experimental results.*

In thermal gas lenses, temperature gradients and ensuing refractive index variations are caused by heat transfer from an external heat source.<sup>1</sup> The tubular gas lens power is supplied by resistive heating; the figure of merit, that is, the focusing strength per unit of applied power is a criterion for its efficiency.<sup>2</sup> The efficiency may be improved by using Peltier heat as it has recently been suggested in connection with the proposal for an alternating gradient, thermo-electric beam waveguide.<sup>3</sup> In still another way, heat is generated by viscous dissipation which exists in a high-speed gas stream in a pipe. The temperature rise creates a refractive index variation capable of continuously focusing a light beam passing through this pipe.

The adiabatic flow of a compressible fluid is treated in the literature.<sup>4, 5</sup> The axial density variation resulting from frictional pressure loss and the transverse density variation caused by viscous dissipation, together with the assumption of a parabolic transverse velocity and temperature profile, lead, after simplification, to the following expression for the refractive index  $n(r, z)$ :

$$n(r, z) = 1 - \frac{r^2}{a^2} (n_0 - 1) \frac{\kappa - 1}{2} R \frac{p_1}{p_0} M_1 M(z). \quad (1)$$

In this equation,  $a$  is the radius of the pipe,  $n_0$  the refractive index at atmospheric pressure  $p_0$ ,  $\kappa$  the ratio of the specific heats ( $c_p/c_v$ ),  $R$  ( $\approx 0.90$ ) the so-called recovery factor,\*  $p_1$ ,  $M_1$  and  $M(z)$  the pressure

\* See p. 211 of Ref. 4.

and the Mach number at the beginning and along the pipe, respectively.

Provided that the absolute velocity is small compared with the velocity of sound, and that simultaneously the relative change of the velocity along the guide also is kept small, it can be shown that the eikonal equation yields as ray path  $r(z)$ :

$$r(z) = (1 + \beta z)^{\frac{1}{3}} \left[ C_1 J_{\frac{1}{3}} \left( \frac{2}{3} \frac{\alpha}{\beta} (1 + \beta z)^{\frac{1}{3}} \right) + C_2 N_{\frac{1}{3}} \left( \frac{2}{3} \frac{\alpha}{\beta} (1 + \beta z)^{\frac{1}{3}} \right) \right] \quad (2)$$

with

$$\alpha = \frac{M_1}{a} \left[ (n_0 - 1)(\kappa - 1) R \frac{p_1}{p_0} \right]^{\frac{1}{2}} \quad \text{and} \quad \beta = \frac{f\kappa}{a} M_1^2$$

whereby  $J_{1/3}(x)$  and  $N_{1/3}(x)$  are the Bessel and Neumann functions of fractional order  $1/3$ ,  $C_1$  and  $C_2$  are integration constants and  $f$  represents the average friction coefficient. Equation 2 describes an undulating trace with steadily decreasing amplitude and period as the result of the ever increasing velocity and, consequently, focusing strength downstream.

If one considers the flow parameters to be locally independent of  $z$  one obtains for the period of the beam size variation  $L_b(z)$  (with  $R = 0.90$ ; see Ref. 6):

$$L_b(z) = 3.3a \left[ (n_0 - 1)(\kappa - 1) M_1 M(z) \frac{p_1}{p_0} \right]^{-\frac{1}{2}}. \quad (3)$$

The  $1/e$  half width of the beam which does not change its size in this pseudouniform guide is given by  $w_o = (\lambda L_b(z))^{1/2} / \pi$  ( $\lambda$  = light wavelength). One notices that small spot sizes can be achieved by choosing a monatomic gas with high refractive index, by selecting a small pipe diameter and by increasing either the initial velocity or the pressure, or both. However, a characteristic feature of frictional flow is a comparatively large axial velocity gradient for high initial velocities, a fact which directly affects the total pipe length employable for a specified exit speed.

The experimental setup is shown in Fig. 1. The gas was injected into the pipe through a large number of radial jets. The gas flow and pressure were adjusted in such a way that a light beam which entered the guide collimated ( $w_{1/e} \approx 0.9$  mm) left it either collimated or with a focal point coinciding with the end of the pipe. Thus the total pipe length represented an even or odd multiple of  $L_b/2$ , respectively. For a pipe length of 3.07m and at air flow rates between 40

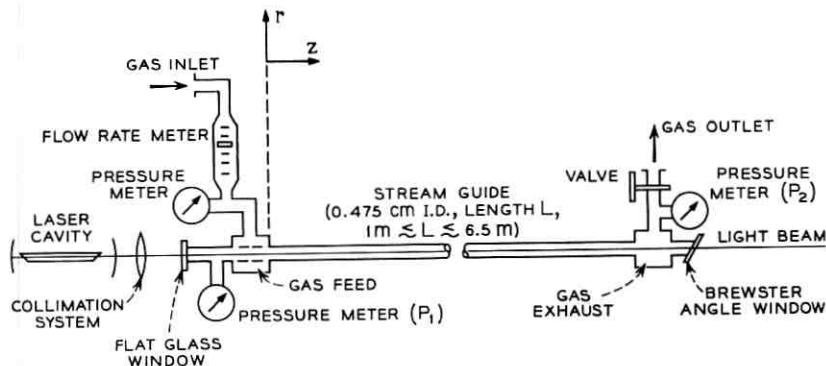


Fig. 1—Experimental setup for measurements with the stream guide.

to 55 liters per minute ( $23.2 \leq p_1 \leq 64.7$  psi,  $p_2 = 14.7$  psi) the averaged period of the beam size variation ranged between approximately 6.14 and 1.53m. Typical values for the Reynolds number were in the order of 40,000.

In Fig. 2 the pressure and flow rate is varied in such a fashion as to keep the averaged focusing strength constant ( $L_b =$  length of pipe  $L$ ). For a given focusing strength, by increasing the pressure the required velocity decreases and the final velocity approaches more and more the initial velocity. The use of argon instead of air increased the focusing strength as expected. The corresponding theoretical periods of the beam size variation at the beginning and the end of the pipe as computed via the experimental pressure and flow rate from (3) are also shown ( $L_{b_1}$  and  $L_{b_2}$ , respectively). Their average value  $L_{av}$  is roughly constant and the results for both air and argon are in close agreement. However, for  $L = 6.42\text{m}$ ,  $L_{av}$  was approximately 36 percent lower than the experimental value. In general, different pipe lengths and varying operating conditions resulted in values of  $L_{av}$  which varied around the experimental results.

The axial velocity distribution depends largely on the friction coefficient  $f$ . Its value may be determined theoretically, but owing to its involved dependence on various factors, an experimental evaluation is more reliable. From Fig. 2 follows that  $f$  is smaller for smaller absolute velocities. Thus, for comparable focusing action, an increase in pressure not only results in smaller velocity gradients because of a reduced initial velocity but also because of a reduced friction coefficient.

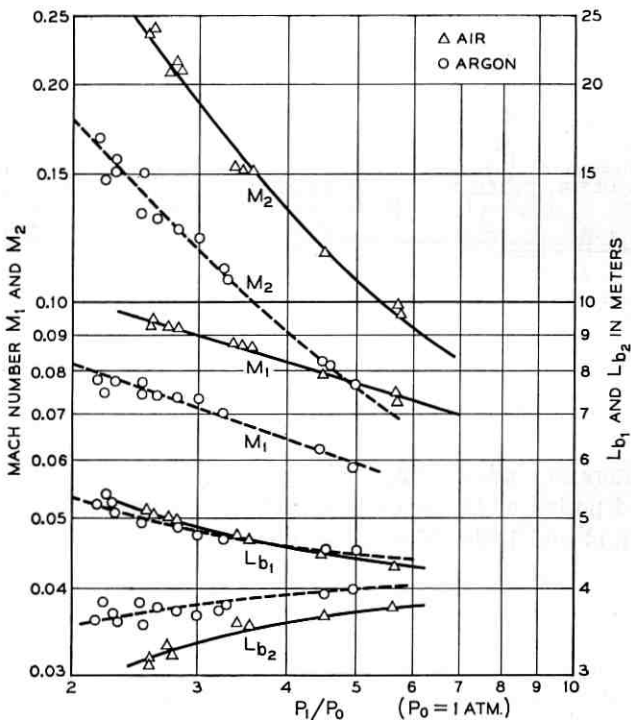


Fig. 2—Experimental Mach number and theoretical period of the beam size variation  $L_{b_1}$  and  $L_{b_2}$  (according to equation 3) at the beginning and the end of the pipe as a function of the initial pressure  $p_i/p_0$  for air and argon (temperature 22°C). The experimental period of the beam size variation was constant and corresponded to the total length of the pipe (6.42m).

The eventual application of the stream guide for long distance communication requires that the pressure be reestablished periodically, whereby the period is expected to be in the range of a few meters. This can be accomplished by alternately injecting gas from a high pressure supply line and exhausting it into a lower pressure pipe running parallel to the guide.

Focusing properties which are close to those of a uniform guide can be achieved if the stream guide is operated at high absolute pressures together with small pressure drops along the guide. Rayleigh scattering losses impose an upper pressure limit of approximately 500 psi for a maximum transmission loss of 1 dB per km (for air) if losses resulting from turbulent scattering are neglected. Also, eventual mode

conversion losses caused by a non-parabolic refractive index variation are not taken into account.

Whether the stream guide has actual applications as a simple, continuous guiding medium depends on the results of further studies of its optical properties, especially the effects of velocity gradients and turbulence on beam fluctuations and power loss.

I gratefully acknowledge valuable comments by C. A. Fritsch, T. J. Kessler, and R. J. Port, about the characteristics of compressible fluid flow, and I appreciate the assistance of H. W. Astle in carrying out the experiments.

## REFERENCES

1. Berreman, D. W., "A Lens or Light Guide Using Convectively Distorted Thermal Gradients in Gases," *B.S.T.J.*, 43 (July 1964), pp. 1469-1475.
2. Marcuse, D. and Miller, S. E., "Analysis of a Tubular Gas Lens," *B.S.T.J.*, 43 (July 1964), pp. 1759-1782 and Marcuse, D., "Theory of a Thermal Gradient Gas Lens," *IEEE Trans. Microwave Theory and Technique*, *MTT-13*, No. 6 (November 1965), pp. 734-739.
3. Kaiser, P., "A Thermoelectric Alternating Gradient Optical Guiding Apparatus," U. S. Patent application 703-742, February 7, 1968.
4. Shapiro, A. H., *The Dynamics and Thermodynamics of Compressible Fluid Flow*, 2 vols., New York: The Ronald Press Company, 1953, p. 159.
5. Ward Smith, A. J., "Subsonic Adiabatic Flow in a Duct of Constant Cross-Sectional Area," *J. Royal Aeronautical Soc.* 68 (February 1964), pp. 117-126.
6. Tien, P. K., Gordon, J. P., and Whinnery, J. H., "Focusing of a Light Beam of Gaussian Field Distribution in Continuous and Periodic Lens-Like Media," *Proc. IEEE* 53 (February 1965), pp. 129-136.



# Pulse Shuttling in a Half-Mile Optical Lens Guide

By D. GLOGE and W. H. STEIER

*To investigate the distortion of a gaussian light beam in a long lens guide a light pulse was shuttled back and forth up to 150 times in a straight underground conduit with lenses (quality  $\lambda/10$ ) positioned focally every 140 m. The pulse was formed by suddenly "dumping" the light stored in a He-Ne laser cavity into the guide. Part of the round-trip loss was replenished by a He-Ne amplifier. In scanning the intensity in the guide cross-section on various round trips of the pulse it was found that the gaussian profile was virtually undisturbed.*

## I. INTRODUCTION

Lens guides with widely separated glass lenses for long distance optical communication have been proposed in several varieties<sup>1, 2</sup> and investigated in various laboratory and field experiments.<sup>3-5</sup> The use of dielectric coatings reduces the loss to one per cent per lens or less,<sup>3</sup> an estimate which has been confirmed by the experiments reported here. This loss figure permits 1000 lenses to be placed in the beam path before the beam intensity is down by 40 to 50 dB and a repeater or amplifier is necessary.

An average distance of 100 m between lenses would lead to a repeater spacing of 100 km. There is legitimate doubt that a light beam can be kept bundled and centered on the guide axis over this distance. Measurements in a 140 m underground air-filled pipe showed a slow beam drift of several mm per week correlated with the ground temperature field.<sup>5</sup> Thermal insulation of the pipe could reduce this effect, but eventually along the line there will have to be some beam position control to cope with this and with an expected slow ground drift.

Careful investigation in the same pipe revealed that density fluctuations or any short time influence of the gas in a well-shielded

conduit 5 feet below the surface can be neglected even over distances of 100 km.<sup>7</sup>

However, these measurements give no information about any time-independent distortion of the beam caused, for example, by imperfect lens surfaces. Abberations are most likely negligible for the low power lenses used in the lens guide, but random irregularities may lead to severe damage of the beam profile in a long sequence of lenses.<sup>8, 9</sup> This will impede detection, increase the diffraction loss, and hamper any active position control of the beam.

The difficulty of measuring these distortions lies in the sensitivity required. If 10 per cent deviation from the correct intensity profile of the beam is tolerable after 1000 lenses a check in one section has to be sensitive to 0.01 per cent deviation. In addition, this has to be done for many different lenses to gain a reasonable average. The shuttle pulse technique is one method for measuring these small deviations.

## II. THE SHUTTLE PULSE LINE

A straight 3- $\frac{1}{2}$ -inch-diameter iron pipe 5 feet below ground with lenses roughly every 140 m was used as a test line. The lenses had a focal length of 70 m, a diameter of 60 mm, a quality of  $\lambda/10$ , and antireflection coatings on both sides. There were six 140 m sections with a total length of about  $\frac{1}{2}$  mile. For further information about this line see Reference 5.

After a passage of 6 lenses no distortion of the beam could be measured reliably. To increase the minute effects involved the beam was folded back on itself, passing the same lenses many times. To distinguish between the various transits a light pulse shorter than the round trip travel time had to be launched. This "pulse shuttling technique" was used before<sup>3</sup> and was adopted here with some variations which are shown in Figure 1.

A polarization switch consisting of a KD\*P crystal and a calcite Wollaston prism was positioned inside the cavity of a He-Ne laser oscillating at 6328Å. Activated by a voltage pulse this switch "dumped" the energy stored in the oscillator cavity into the test line. This light pulse passed through a He-Ne amplifier and a mode matching two-mirror telescope before entering the lens guide. When the pulse returned from its first round trip through the line it found no voltage on the switch, passed it once, and another time upon reflection from the mirror at the back of the switch, and entered the line once again.

On every reflection from one of the telescope mirrors about one

per cent of the light pulse was transmitted and fed into a receiver. This loss and the loss in the switch were compensated by the He-Ne amplifier.\* By counting the number of pulses in the receiver the number of round trips in the line was determined. The total loss in the line was calculated from the decay of the pulse train.

The use of a polarization switch to generate high power pulses from

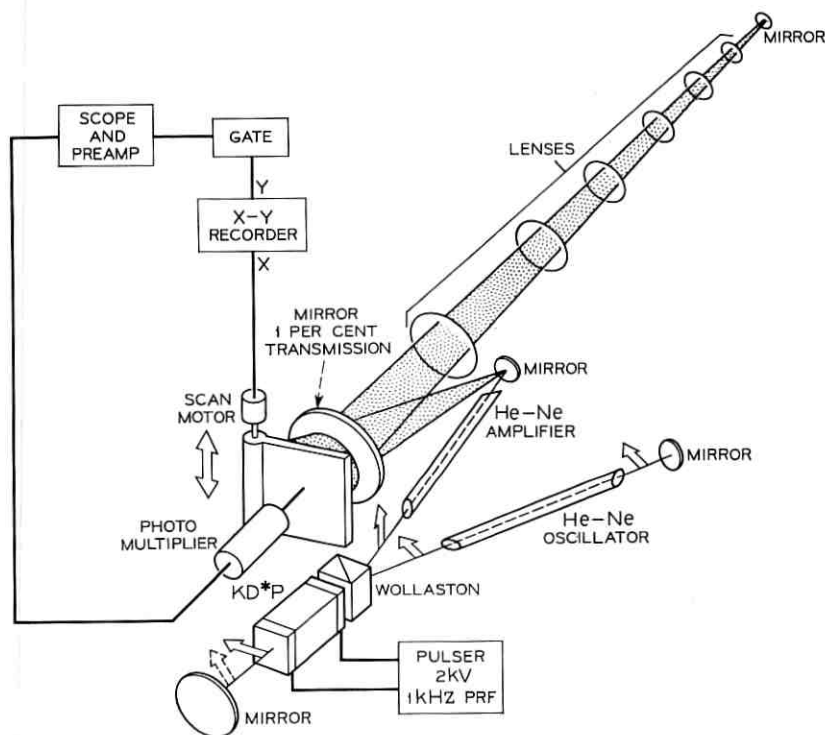


Fig. 1—Shuttle pulse line showing pulse injection, receiver, and processing apparatus.

a He-Ne laser has been described before.<sup>10</sup> To reduce the losses in the switch both the KD\*P crystal and the calcite prism were immersed in a matching oil chamber with antireflection coated quartz windows. Figure 2 shows the refractive indices for the polarization of the oscillator light. The z-cut KD\*P crystal was  $3 \times 3 \times 12$  mm, the longitudinal field was applied by silver-painted rims around both

\* Its use was suggested by Mr. E. A. J. Marcetili.

ends. A loss of one or two per cent per transit may be expected for this switch.

The 2 m long oscillator cavity was almost confocal. An iris inside the cavity limited oscillations to the fundamental mode which had a  $1/e$  diameter of 1.25 mm at the mirrors. The gas tube was 1 m long with a bore of 4 mm.

The 2 kV pulse from a commercial unit\* had a rise time of 50 ns. During this time about half the oscillator light was rotated into the perpendicular plane of polarization and deflected into the shuttle pulse line by the Wollaston prism. The cavity was emptied com-

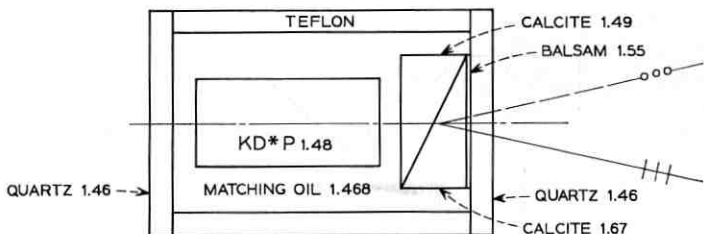


Fig. 2—Optical switch with numbers giving the refractive indices for light polarized in the plane of the figure.

pletely after about 150 ns. The deflected pulse is shown in Figure 3. The peak power of the pulses entering the line was about 100 mw.<sup>10</sup>

The amplifier tube was 1 m long with a 4 mm bore. The telescope magnified the 1.25 mm diameter beam to the 10 mm diameter of the lens guide mode. The spacing of the telescope mirrors was 1.25 m, large enough to neglect spherical aberration and astigmatism. All mirrors used in the experiment had dielectric coatings.

As a necessary shield against turbulence the beam had to be enclosed everywhere. In the laboratory acetate tubes were used. In addition a wooden cover provided a shield against dust and acoustic vibrations. All parts of the launching system were mounted on a solid concrete table. The laboratory was an underground concrete room of 5×5 m. Air currents and convection in the underground conduit were prevented by an air-tight seal closing the tube where it entered the laboratory. One of the antireflection coated lenses already described was used for this purpose.

The mirror at the far end of the line had a 140 m radius of curva-

\* Pulse Engineering Inc., Velonex Div. Model 350.

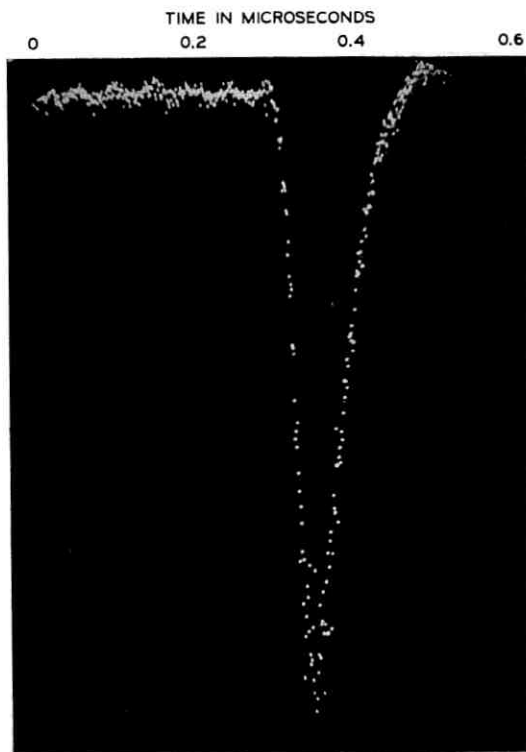


Fig. 3 — Pulse injected into the lens guide (amplitude not calibrated).

ture and was adjusted by remote control. It could be mounted in place of any of the lenses thus changing the guide length from 140 m to  $6 \times 140$  m. The change in the decay rate of the pulse train was observed as the guide length was changed. From this it was concluded that each section added about 2 per cent to the round-trip loss of the pulses. Consequently there was about one per cent section loss per transit of which a large fraction can be attributed to the lenses. Notice that these lenses had been in use for about a year in previous field experiments where moisture and dust might have affected their coatings.

With the amplifier turned off the round-trip loss in the switch, the mirrors and the amplifier tube was about 18 per cent. The switch and the mirrors probably account for the largest part of the loss. The loss in the switch will be somewhat higher for the shuttle pulse polari-

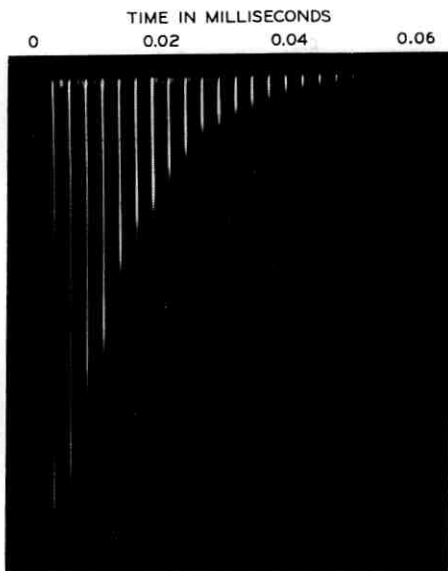


Fig. 4 — Pulse decay in the 3-section line with the amplifier turned off.

zation than for the oscillator polarization. For the perpendicular polarization of the shuttle pulse the indices in the calcite are interchanged from those shown in Figure 2, producing a larger mismatch. Figure 4 shows a pulse train received from a line with three sections corresponding to a round-trip loss of 24 per cent.

With the amplifier turned on, the 3-section line went into oscillation with modes up to the third order being observed. Though not as bright as in a cavity with one or two sections these modes were stable in time and showed no noticeable distortion of their intensity profile. Oscillating modes were a good indication for the optimum alignment of all components. In a line with more than three sections the gain was not sufficient to cause oscillations. Figure 5 shows a pulse train in a 3-section line after the amplifier gain was reduced enough to prevent oscillation.

The detection of the pulses was not limited by detector noise but by cw-light leaking from the switch into the cavity during the interval between pulses. If this light is at a resonant frequency of the shuttle pulse cavity a relatively large amount of power can be coupled from the oscillator and large field strengths will build up in the line. Fortunately this long cavity changes its length randomly

during the round-trip time thus avoiding resonance. However, in this random case some power will still be coupled into the line and the oscillations will build up to an extent determined by the line losses. Therefore the amplifier gain had to be set to balance the background light and pulse decay so that a maximum number of pulses could be seen. This condition is studied quantitatively in the appendix.

Figure 6 shows the optimum round-trip loss, resulting in the maximum number of round trips  $N$ , for a given extinction ratio of the switch and a desired signal to noise ratio at the detector. The lines show the idealized situations of perfect resonance and completely random phase buildup. The experimental condition was somewhere in between, but close to complete randomness. To get the 150th pulse with an S/N of 20 dB, the amplifier gain was set for a round-trip loss of about one per cent. This suggests an extinction ratio of about 50 dB (see Figure 6). This extinction ratio has to be understood as the ratio of the peak pulse power to the power that leaks in between pulses and propagates in the line. Only the small part of the light leakage that is in the lower order modes can propagate.

The initial high amplitude pulses in Figure 5 suffered a larger attenuation than one per cent as they drove the amplifier into satura-

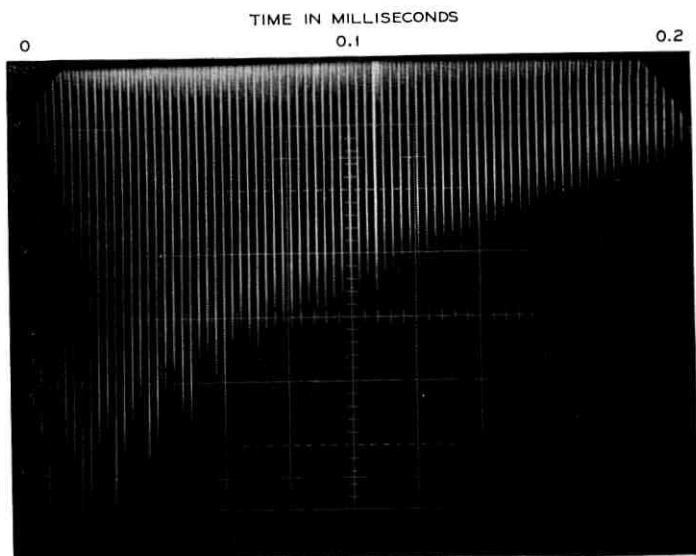


Fig. 5 — Pulse train from the 3-section line with the amplifier working.

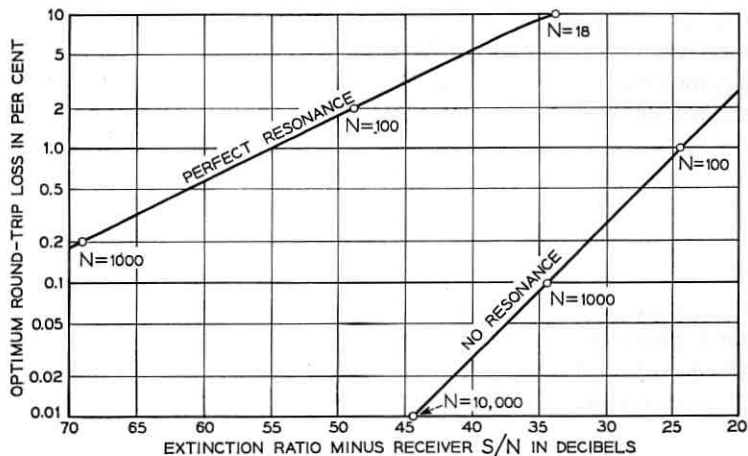


Fig. 6—Round-trip loss versus extinction ratio of the pulse injector for the maximum number of pulses detectable. The lines indicate the limits of perfect resonance and of complete phase randomness.

tion. Some of the background light in Figure 5 is caused by acoustic resonances in the KD\*P crystal following the high voltage pulse. Since this did not obstruct the detection of the initial pulses and vanished rapidly no measure was taken to prevent it.

### III. THE SCANNING OF THE BEAM PROFILE

The light transmitted by the larger telescope mirror in Figure 1 was used to measure the lateral intensity profile of the light pulses impinging on this mirror. The technique was to measure the intensity at a certain point of the mirror with a pinhole receiver when, say, the 50th pulse comes by, then move to another point, launch a new pulse, and wait again for the 50th round trip. This can be repeated point by point for any detectable round trip. Since in the experiment the round-trip time was several microseconds a new pulse could be launched every millisecond.

The pinhole receiver consisted of a photomultiplier with a small iris and a diffusing ground glass plate behind it. The hole diameter was a fraction of a millimeter. The light pulses had a spot diameter of 10 mm at that mirror.

The multiplier received all pulses arriving from the far end of the line. The transmitted intensity from pulses traveling in the opposite

direction was deflected to the side and did not reach the pinhole. A diode gate, triggered after the proper delay time, picked the wanted pulse out of the amplified multiplier signal. The signal from the gate was amplified by a narrow band resonance amplifier which was tuned to the 1-kHz repetition rate of the injected pulse. The rectified amplitude of the 1-kHz signal was displayed on the y-axis of an x-y recorder. The x-deflection corresponded to the location of the pinhole receiver which was moved slowly across the back of the mirror. One scan took several minutes, the scanning speed being determined by the bandwidth of the rectified signal. This bandwidth was reduced to a fraction of 1 Hz to suppress time dependent effects as far as possible. The accuracy of the scan was set by variations affecting the tremendously sensitive alignment of the system. This limited the reproducibility to about 5 per cent of the total signal.

Figures 7, 8, and 9 show scans taken in a line with three sections. The intensity units in these figures are arbitrary and different for each scan as the amplifier settings were changed between scans. All these scans were taken along a horizontal line across the center of the light beam. The dotted lines show a gaussian intensity distribution calculated for the theoretical  $1/e$ -spot diameter of 10 mm for comparison.

Figure 7 represents a check of the profile launched into the line. The bumps and spikes on this scan are attributed to variations with

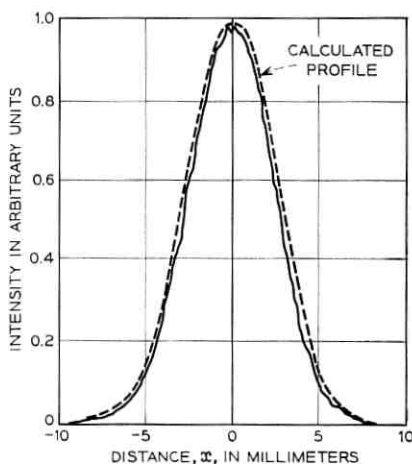


Fig. 7 — Intensity scan across the guide cross-section for light after one round trip in the 3-section line.

time and the injected beam may be considered gaussian within the accuracy of the scan. Figures 8 and 9 are scans taken after 75 and 150 round trips, respectively. The 3-section line was about 400 m long. Consequently, after 150 round trips the light pulse had traveled 120 km and passed 900 lenses.

The slight tilt of the profile may be interpreted as light which accompanied the beam in higher order modes.<sup>9</sup> Many more scans were taken in this and longer lines for various numbers of round trips. Figures 7, 8, and 9 are representative of the results.

#### IV. DISCUSSION OF THE EXPERIMENT

A question that has to be investigated in more detail is whether a 120 km lens guide would actually cause the same negligible distortion on a light beam as found for the shuttle pulse experiment. There are three important points to be considered:

- (i) The distortion added to the beam by the optical components other than the lenses.
- (ii) The finite apertures of these components.
- (iii) The periodic nature of a shuttle pulse experiment.

In the shuttle pulse line there were, in addition to the lenses under investigation, several other optical components, such as the switch,

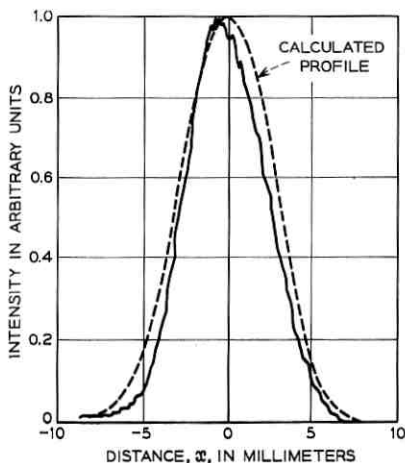


Fig. 8—Intensity scan across the guide cross-section for light after 75 round trips in the 3-section line.

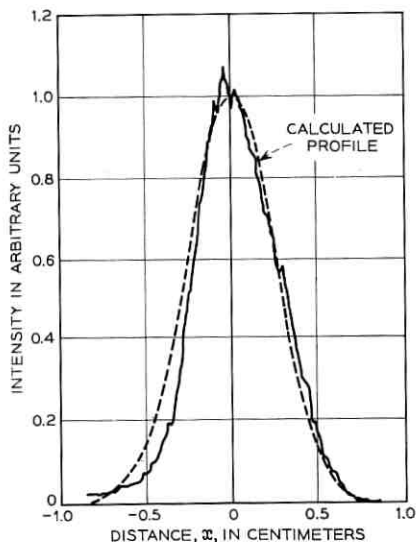


Fig. 9—Intensity scan across the guide cross-section for light after 150 round trips in the 3-section guide.

the amplifier, and the telescope, which the light passed twice on every round trip. To find their contribution to the beam distortion, the nature of the expected irregularities on an optical surface has to be considered.

Any irregularity on an optical surface will distort the beam, but not all of this distortion will accumulate in a lens guide, because the finite aperture of the guide smooths out the intensity and phase-front of the beam. This is equivalent to saying that only low order modes will be transmitted in the guide. Consequently these modes are the only growing source of distortion. They are generated by irregularities correlated over areas comparable to the beam cross section: smooth bumps whose heights determine the amount of light coupled into these modes.<sup>9</sup>

The polishing process will normally cause those bumps to be the highest which extend furthest over the surface. Hence it is expected that a large beam will be distorted more than a small one. This implies that those optical components on which the beam had only a 1 mm diameter contributed very little to the distortion. So only the two large mirrors facing the line are left as major additional sources of beam distortion. Since they had the same optical quality

and beam size as the lenses, their contribution may be considered approximately the same as an additional lens in the line.

The second point deals with the effective beam aperture of the shuttle pulse line. The amplifier had an inner diameter of 4 mm, and the KD\*P crystal had a cross section of 3×3 mm. Both were in the 2 m section between the small telescope mirror and the end mirror. For a wavelength of 6328Å, an aperture of 3 mm, and a spacing of 2 m, one calculates an effective Fresnel number of 1.8. In this section the beam had the same shape and phase front as in the confocal 2 m oscillator cavity from which it was originally ejected.

Applying Slepian's propagation coefficients for modes in a diffraction-limited confocal cavity one finds, for a Fresnel number of 1.8, a diffraction loss of about  $10^{-6}$ ,  $10^{-5}$ ,  $10^{-4}$ ,  $10^{-3}$  per transit for the first, second, third, and fourth parasitic mode, respectively.<sup>11</sup> More significantly, all these modes except the fourth one went into oscillation in the 3-section line. Hence the aperturing in the system should not suppress the mode buildup for modes up to at least the third order.

Further investigation of the individual modes shows that the first and second parasitic modes are not only generated by irregularities on the lens surfaces, but also by additional lens effects, for example, in the gain medium of the amplifier tube or by lens displacements, laterally and along the axis. In turn these modes can be suppressed, even in a line with imperfect lenses, by proper alignment of these lenses.<sup>8</sup> This means that the first and second parasitic modes cannot be used to determine the lens imperfections in the experimental guide. They could be and were avoided by proper alignment.

Let us look therefore at higher modes, say, the third one. Figure 9 in Reference 9 shows the profile of a gaussian beam with 5 per cent of its power in the third mode. Comparing this with the recorded profile in Figure 8 one may assume that its distortion was of the same order. Without pushing the quantitative analysis of the experiment too much, it can be said that the power collected in the third mode after 900 lenses was apparently not larger than a few per cent of the beam power.

Gloge<sup>9</sup> predicts this amount (and only a fraction of this in the next higher modes) for the lenses used, if the irregularities on the surfaces are correlated over distances about twice the beam diameter. On the basis of these calculations it may be assumed that the detection of the higher order modes would be beyond the experimental accuracy.

The third point has to do with the iterative structure of the lens

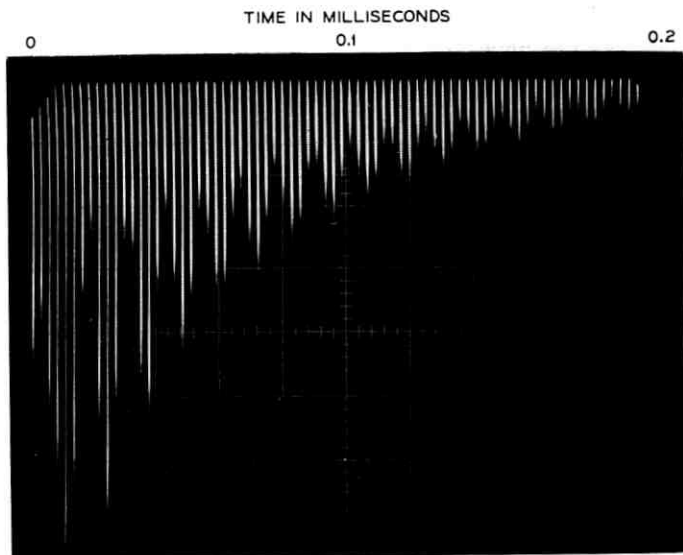


Fig. 10— Pulse train from the 3-section line after one lens was misaligned.

guide simulated by the shuttle pulse line. Obviously on every round trip the light pulse suffers the same kind of distortion, whereas in a real lens guide this distortion would be completely at random.

Consider for example the most simple irregularity: a displaced lens. Figure 10 shows a pulse train similar to Figure 5 but after one lens was misaligned. Apart from the expected decay there is a periodic fluctuation of the signal. This can be explained by an oscillation of the beam center about its correct position or, which is equivalent, by periodically generated and annihilated parasitic modes. One can show that the modes, because they travel with a propagation constant slightly different from that of the gaussian beam, should do exactly that in a periodic structure.

Only if the round trip is an integral number of beat periods for a specific mode will the power in that mode grow continuously. To multiply the minute effects expected per section in the experiment this condition was arranged for the third order mode. This was done by changing the distance of the telescope mirrors and watching the periodic fluctuations of the pulse train. One can calculate that the third mode builds up if the fluctuation period is three pulses on the pulse train. In this case we should observe the maximum third order mode distortion of the beam. Scans taken under this condition indi-

cated no major deviation from the scans shown. The explanation might be that the power generated per round trip in the third mode was smaller than, or at most, equal to the attenuation of that mode.

In a lens sequence with independent random irregularities, the relative phases are completely arbitrary and the average power in the parasitic modes would grow proportional to the number of lenses passed, at least as long as reconversion can be neglected. If, as an upper limit, the generation rate per round trip is assumed equal to the loss of  $2 \times 10^{-4}$ , the third mode would increase to 3 per cent of the beam intensity after 900 equivalent lenses.

#### V. CONCLUSIONS

A 1/2-mile underground lens guide with six confocally spaced lenses was investigated by sending a light pulse back and forth in this guide. The lateral intensity profile of the light beam could be checked after any round trip by scanning the intensity in the cross section. It was found that the gaussian profile after passing 900 lenses was still virtually undistorted.

The lenses had a quality of  $\lambda/10$ , a diameter of 60 mm, and were antireflection coated to give a reflection and absorption loss of one per cent per pass. The effective aperture of the guide was determined by an amplifier tube and an optical switch within the path of the light. The diffraction losses for modes up to at least third order were negligibly low. Even for the condition of critical buildup of the third mode the distortion of the light profile after 900 lenses was negligible.

#### ACKNOWLEDGEMENTS

The authors wish to thank Mr. E. A. J. Marcatili for many fruitful discussions, and they gratefully acknowledge the constructive assistance of Mr. H. E. Earl.

#### APPENDIX

Assume that the peak pulse power entering through the switch is  $I_1$  and that the pulse loses a fraction  $p$  of its intensity on every round trip. Consequently, after  $N$  round trips, the intensity

$$I_N = I_1 10^{N \log(1-p)} \quad (1)$$

is left in the pulse. At the same time a power  $I_s$  leaks in through the switch continuously and increases the background light  $I_b$  to a level,

where  $I_s$  just replenishes the loss per round trip. If  $I_s$  adds in phase to the light already circulating, as in a perfect resonator, the comparison of amplitudes yields

$$\sqrt{I_b(1-p)} + \sqrt{I_s} = \sqrt{I_b}. \quad (2)$$

If the phases are completely at random because either the resonant frequency or the entering light frequency changes within the round trip time one has instead

$$I_b(1-p) + I_s = I_b. \quad (3)$$

By introducing a stability parameter  $\alpha = 1$  or  $2$ , both (2) and (3) can be expressed by the relation

$$I_b = I_s[1 - (1-p)^{1/\alpha}]^{-\alpha} \quad (4)$$

which for  $p \ll 1$  reduces to

$$I_b = I_s \left( \frac{p}{\alpha} \right)^{-\alpha}. \quad (5)$$

It is convenient to define a signal to noise ratio

$$R = 10 \log \frac{I_N}{I_b}$$

required at the receiver to analyze the  $N$ th pulse and an extinction ratio

$$E = 10 \log \frac{I_1}{I_s}$$

inherent in the switch. By combining (1) and (5) and solving for  $N$ , one now finds the number of round trips which can be properly detected:

$$N = \frac{R - E - 10\alpha(\log p - \log \alpha)}{10 \log(1-p)}. \quad (6)$$

The derivative  $\partial N / \partial p$  vanishes for

$$N = \alpha \frac{1 - p_{\text{opt}}}{p_{\text{opt}}}. \quad (7)$$

This is the maximum number of round trips that can be achieved with the optimum round-trip loss, for example by adjusting the amplifier gain. Equations (6) and (7) were used to plot Figure 6. It shows  $p_{\text{opt}}$  as a function of the difference  $E - R$  for  $\alpha = 1$  and  $2$ .

These two lines present the limits of perfect resonance and completely random phase buildup. For example, to receive the 150th pulse 20 dB above the noise level in a line that does not resonate, one needs an extinction ratio of 46 dB in the switch and a loss of 0.67 per cent in the shuttle pulse line.

## REFERENCES

1. Goubau, G. and Schwering, F., "On the Guided Propagation of Electromagnetic Wave Beams," *Trans. IRE, AP-9* (May 1961), p. 248.
2. Kompfner, R., "Optical Reflecting System for Redirection of Energy," U. S. Patent 3-224-330 issued December 21, 1965.
3. DeLange, O. E., "Losses Suffered by Coherent Light Redirected and Refocused in an Enclosed Medium," *B.S.T.J.*, 44, No. 2, (February 1965), pp. 283-302.
4. Goubau, G. and Christian, F. R., "Loss Measurements with a Beam Waveguide for Long Distance Transmission at Optical Frequencies," *Proc. IEEE*, 52 (December 1964), p. 1739.
5. Gloge, D., "Experiments With an Underground Lens Waveguide," *B.S.T.J.*, 46, No. 4, (April 1967), pp. 721-735.
6. Marcatali, E. A. J., "Ray Propagation in Beam Waveguides With Redirectors," *B.S.T.J.*, 45, No. 1, (January 1966), pp. 105-116.
7. Gloge, D., "The Effect of Density Fluctuations in a Gas Filled Underground Optical Waveguide," *Proc. Symp. Mod. Opt.*, Brooklyn Polytechnic Press.
8. Marcatali, E. A. J., "Effect of Redirectors, Reforcussers and Mode Filter on Light Transmission Through Aberrated and Misaligned Lenses," *B.S.T.J.*, 46, No. 8, (October 1967), pp. 1733-1752.
9. Gloge, D., "Mode Conversion in an Underground Lens Guide," *B.S.T.J.*, 46, (December 1967), pp. 2467-2484.
10. Steier, W. H., "Coupling of High Peak Power Pulses from He-Ne Lasers," *Proc. IEEE* 54 (November 1966), pp. 1604-1606.
11. Slepian, D., "Some Asymptotic Expansions for Prolate Spheroidal Wave Functions," *J. Math. Phys.* 44 (1965), pp. 99-140.

# Linear Beam Position Control in Optical Waveguides

By JAMES C. DALY

(Manuscript received September 21, 1967)

*This paper studies the effect of an active control system that introduces corrective transverse lens displacements on the propagation of beams in optical waveguides. The induced displacement of the  $n$ th lens is a linear function of the beam displacement at the  $(n + 1)$ th lens. Beam displacements from the ideal design position are caused by transverse displacements of the lenses and sensors from their design positions. Expressions have been obtained for:*

- (i) The conditions for spatial and temporal stability.*
- (ii) The rms beam displacement resulting from uncorrelated displacements of the lenses and sensors.*
- (iii) The beam displacement caused by sinusoidal displacements of the lenses and sensors of arbitrary spatial frequency.*
- (iv) The spatial rate of return to the guide axis of a beam injected into the guide off axis.*

*We also show that the positions of beams, other than the sensed beam, are controlled by the system and that the system can simultaneously guide many different sensed beams. We calculate an upper limit on the probability that the beam will not be contained within a given aperture.*

## I. INTRODUCTION

The ability of a beam waveguide to guide optical frequency electromagnetic energy is severely limited by the tolerances held on the transverse positions of the lenses. Hirano and Fukatsu<sup>1</sup> have shown that uncorrelated transverse lens displacements will cause the expected deviation of the beam from the guide axis to grow as the square root of the number of lenses through which it has passed. Steier<sup>2</sup> has shown that random longitudinal lens displacements and variations in the focal lengths of the lenses couple with random

transverse lens displacements to cause the expected value of the rms beam displacement to grow exponentially with the number of lenses through which it has passed.

This paper describes the performance of linear self-aligning beam waveguides that are subjected to transverse disturbances of the lens and sensor positions. It is quite likely that nonlinear control systems may turn out to be more effective or practical in practice but an understanding of linear systems will facilitate the more involved analysis of nonlinear control systems. The idea of using active guiding media for optical communications was proposed long ago by R. Kompfner<sup>3</sup> and L. U. Kibler,<sup>4</sup> and has been discussed by E. A. J. Marcatili.<sup>5</sup> The improvement that can be obtained with self-aligning beam waveguides has been demonstrated experimentally and with computer simulations by Christian, Goubau, and Mink.<sup>6</sup>

In the guiding systems considered in this paper, the lenses are physically moved an amount that is determined by sensing the position of the beam in the guide.

The axis of the guide is defined as the line joining the centers of the beam sensors. In general in an actual installation this axis will not be straight.

The displacement of paraxial beams from the guide axis is a linear function of the transverse lens displacements. An important consequence of this linearity is that the superposition principle can be applied to the beam displacement. Incremental displacements of the lenses produce incremental displacements of the beam. These increments are independent of any bias positions resulting from an intentional bend. Therefore, when we study the effects of imperfections in a straight guide, the results apply equally well to the effect of imperfections in a curved guide. For example, in studying the effect of the control mechanism on the propagation of a beam through a bend we would proceed as follows:

(i) Specify the guide axis. This is the path of propagation for the beam. The sensors are located along this axis.

(ii) Find the proper set of lens positions that will cause the beam to propagate along this axis. In an analysis these are calculated. In an actual installation these positions would be determined by moving the lenses until the beam is aligned along the sensors.

(iii) Determine the effect of imperfections by assuming that the lenses and sensors are displaced from their proper positions. The consequence of the linearity of the system is that the beam displace-

ment resulting from these imperfections is the same as it would be if the guide axis were a straight line.

This paper emphasizes the case where the design axis for the lens centers and sensors are straight lines and coincident with a reference line. The beam is injected into the guide along the reference line and the center of the first lens of the guide lies on this line.

The optical waveguide consists of a sequence of identical positive lenses, of focal length,  $f$ , and spacing,  $d$ , as shown in Figure 1. In Figure 1,  $g_n$ ,  $s_n$ , and  $r_n$  are the sensor, lens, and beam displacements at the  $n^{\text{th}}$  lens, respectively. We shall consider paraxial ray propagation in two dimensions for simplicity. It has been shown that the three-dimensional problem can be split into two independent two-dimensional problems<sup>1</sup> and that the center of the beam follows a path described by a paraxial ray.<sup>7, 8</sup>

When the guide is subjected to disturbances in time, the transverse displacement of the  $n^{\text{th}}$  lens relative to the reference line is given by  $s(t)_n$ . Similarly, the displacement of the beam center at the  $n^{\text{th}}$  lens from the reference line is given by  $r(t)_n$ . Using geometric optics,<sup>1</sup> and considering the guide to be time-dependent, results in the following difference equation for the paraxial beam in the guide

$$r(t)_{n+2} - (2 \cos \omega_0 d)r(t)_{n+1} + r(t)_n = (d/f)s(t)_{n+1} \quad (1)$$

where  $\cos \omega_0 d = 1 - d/2f$ .

In any lens waveguide there will be transverse displacements of the lenses, owing to the impossibility of holding exact tolerances or the movement of the earth after the guide has been constructed. These lens displacements are unavoidable. They are denoted by  $N_n$ . Here we study the effect of a superimposed corrective lens displace-

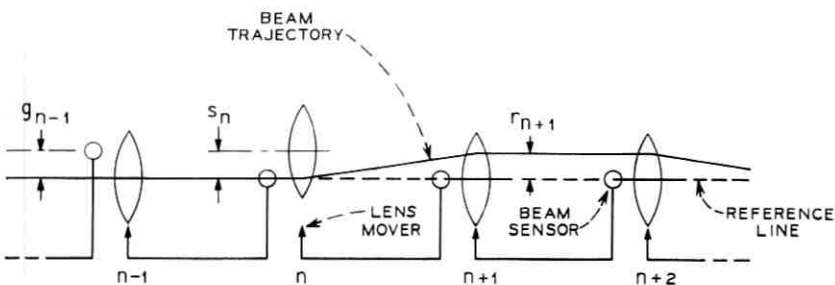


Fig. 1—The beam waveguide and schematic diagram of the feedback system.

ment,  $\delta_n$ , on the performance of the beam waveguide. The total displacement of the  $n^{\text{th}}$  lens is the sum of  $N_n$  and  $\delta_n$

$$s_n = N_n + \delta_n . \quad (2)$$

For most of this paper, the response of the system in time is determined only in the steady-state when the disturbances are either step functions in time or at low enough temporal frequencies to be considered constant functions independent of time. These conditions are relaxed and general time functions allowed in Section 2.2 where temporal stability is considered and in Section 2.4 where the high gain case is considered.

Although the beam control is achieved here by inducing transverse lens displacements, the results can be applied to other beam control mechanisms such as mirrors and prisms, when such mechanisms can be interpreted as an equivalent transverse displacement of the lens.

## II. THE SYSTEM

Figure 2 is a schematic representation of a mechanism for lens position control.

The beam position is sensed at each lens. This beam position signal is used to control the transverse position of the preceding lens. The

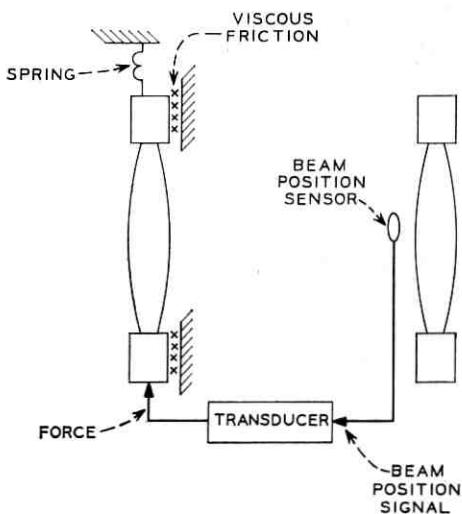


Fig. 2—Schematic diagram of a mechanical device for lens positioning.

difference between the beam and sensor positions at the  $n$ th lens we call the error in the beam position. The corrective displacement of the  $n$ th lens,  $\delta_n(t)$ , is a function of time and the error in the beam position at the  $(n+1)$ th lens.

$$\delta_n = F(e_{n+1}, t) \quad (3)$$

where  $e_{n+1}$  is the position of the beam relative to the sensor at the  $(n+1)$ th lens. The form that the function  $F(e_{n+1}, t)$  takes will depend on the properties of the control mechanism.

In order to study the stability of the beam in the guide it is convenient to transform equation (3) into the temporal frequency domain. Assuming that the control mechanism can be represented by a transfer function  $H_c(s)$ , the Laplace transform of the corrective displacement of the  $n$ th lens for a system at rest at time zero can be written:

$$\delta_n(s) = H_c(s)E_{n+1}(s) \quad (4)$$

where  $s$ ,  $\delta_n(s)$ , and  $E_{n+1}(s)$  are the complex temporal frequency, the Laplace transform of the corrective displacement of the  $n$ th lens, and the Laplace transform of the error in the beam position at the  $(n+1)$ th lens.

In general the transfer function will have the following form

$$H_c(s) = \frac{K(s\tau_a + 1)(s\tau_b + 1) \cdots}{s^N(s\tau_1 + 1)(s\tau_2 + 1)(s\tau_3 + 1) \cdots} \quad (5)$$

It is customary to classify systems in terms of the number,  $N$ , of factors of the form  $1/s$  which appear in the transfer function. This number indicates the number of integrations performed by the components. For example: if  $N = 0$  the system is referred to as a type 0 system, if  $N = 1$  the system is referred to as a type 1 system, and so on.

The number of integrations determines some important properties of the steady state response. Since  $s \rightarrow 0$  as  $t \rightarrow \infty$ , in the steady state equation (5) yields

$$H_c(s) |_{s \rightarrow 0} = A = \frac{K}{s^N} \quad (6)$$

when  $s \rightarrow 0$ . There are two possibilities for  $A$ .  $A$  is either equal to a real constant  $K$  (type 0 system) or  $A$  goes to infinity (type one or more system). We consider both of these possibilities in the following paragraphs.

For the control mechanism shown in Figure 2,  $H_c(s)$ , the control

mechanism transfer function, will be of the form

$$H_c(s) = \frac{K_o}{Ms^2 + Bs + K_s} \quad (7)$$

where  $K_o$  is the gain,  $K_s$  is the spring constant,  $M$  is the mass of the lens, and  $B$  is a friction constant. The steady-state value of  $H_c(s) = A = K_o/K_s$ . This system is reduced to a type 1 system by removing the spring, that is, letting  $K_s = 0$ .

### 2.1 The General Description

The properties of the linear active guiding medium in time and space can be studied using a combination of Laplace and  $Z$  transform techniques.<sup>9-11</sup> Laplace transforms are used to transform from the time domain to the temporal frequency domain. Quantities that depend on position along the guide, given by the lens number  $n$ , are transformed into quantities that depend on axial spatial frequencies using  $Z$  transform techniques.

Taking the Laplace transform of equation (1) results in the following recursion equation for the Laplace transform of the beam displacement.

$$[1 - (d/f)H_c(s)]R(s)_{n+2} - (2 \cos \omega_c d)R(s)_{n+1} + R(s)_n = (d/f) \frac{N_{n+1}}{s} - (d/f)H_c(s) \frac{G_{n+2}}{s} \quad (8)$$

where  $R(s)_n$ ,  $N_n$ , and  $G_n$  are the Laplace transform of the beam displacement at the  $n$ th lens, and the constant displacement of the  $n$ th sensor, respectively. Taking the  $Z$  transform of equation (8) results in the following equation when the boundary conditions are zero, that is, the beam is injected into the guide on axis and the first lens of the guide is on axis

$$R(s, z) \{ [1 - (d/f)H_c(s)]z^2 - (2 \cos \omega_c d)z + 1 \} = z(d/f) \frac{N(z)}{s} - z^2(d/f)H_c(s) \frac{G(z)}{s} \quad (9)$$

where  $R(s, z)$  is the  $Z$  transform of the Laplace transform of the beam position, and  $N(z)$  and  $G(z)$  are the  $Z$  transforms of the constant lens and sensor displacements, respectively. Rewriting equation (9) and introducing the transfer function  $H(s, z)$  results in the following expression.

$$R(s, z) = H(s, z)[N(z) - zH_c(s)G(z)]/s \quad (10)$$

where

$$H(s, z) = \frac{z(d/f)}{[1 - (d/f)H_c(s)]z^2 - (2 \cos \omega_c d)z + 1}. \quad (11)$$

Equation (10) is a simple relationship between functions that contain the information about the performance of the guide. The transfer functions  $H(s, z)$  and  $H_c(s)$  contain the properties of the guide such as  $d/f$  and the characteristics of the control mechanism. The function  $R(s, z)$  contains all the information that is necessary in principle to determine the position of the beam at any lens as a function of time.  $N(z)$  and  $G(z)$  are determined from the constant lens and sensor displacements.

When  $r_n(t)$  can be considered a constant function of time denoted by  $r_n$ , then  $R(s, z)$  is the  $Z$  transform of  $r_n/s$ . Multiplying equation (10) by  $s$  and letting the temporal frequency go to zero yields  $R(z)$ , the  $Z$  transform of the steady-state beam position

$$R(z) = H(z)[N(z) - AzG(z)] \quad (12)$$

where  $H(z)$  is equal to the value of  $H(s, z)$  for  $s$  equal to zero.

## 2.2 Temporal Stability

A function is defined as stable in time if it is bounded for all positive values of time. The position of the beam in the guide will be stable in time if the poles of the Laplace transform of the beam position are in the left half of the complex temporal frequency plane ( $s$  plane). The Laplace transform of the beam position is obtained by taking the inverse  $Z$  transform of equation (10). The following convolution summation<sup>10</sup> is a general expression for the inverse  $Z$  transform and gives the Laplace transform of the beam position.

$$R_n(s) = \frac{1}{s} \sum_{m=0}^n H_m(s)[N_{n-m} - H_c(s)G_{n-m+1}] \quad (13)$$

where  $H_m(s)$  is the inverse  $Z$  transform of  $H(s, z)$ . Assuming that the transfer function  $H_c(s)$  (that describes the control mechanism) has no poles in the right half of the  $s$  plane, the only source of right half plane poles would be in the function  $H_m(s)$ . In order to obtain an expression for  $H_m(s)$  it is convenient to factor the denominator of equation (11) and rewrite the expression for  $H(s, z)$ .  $z_1$  and  $z_2$  are the two roots of the denominator in equation (11) and are given by the

following expression

$$z_{1 \text{ and } 2} = \frac{\cos \omega_o d \pm [\cos^2 \omega_o d - 1 + (d/f)H_c(s)]^{1/2}}{1 - (d/f)H_c(s)}. \quad (14)$$

Therefore

$$H(s, z) = \left[ \frac{d/f}{1 - (d/f)H_c(s)} \right] \frac{z}{(z - z_1)(z - z_2)}. \quad (15)$$

The inverse  $Z$  transform of equation (15) can be found in tables and is given by

$$H_m(s) = \frac{(d/2f)[z_1^m - z_2^m]}{[\cos^2 \omega_o d - 1 + (d/f)H_c(s)]^{1/2}}. \quad (16)$$

A sufficient condition for temporal stability is that the poles  $H_m(s)$  are in the left half of the temporal frequency plane. The  $s$  plane poles of  $H_m(s)$  are the roots of the following two equations

$$1 - (d/f)H_c(s) = 0 \quad (17)$$

and

$$\sin^2 \omega_o d - (d/f)H_c(s) = 0. \quad (18)$$

Equation (17) is the characteristic equation of a single sensor lens loop. Therefore if a single section of guide is stable the roots of equation (17) will be in the left half of the  $s$  plane. Equation (18) is more restrictive. For example, if a single section becomes unstable when the gain,  $K$  in equation (5), is increased beyond a value  $K_u$ , it follows from equation (18) that when many sections are tied together to form the optical waveguide, the value of  $K$  at which the system becomes unstable is reduced by  $\sin^2 \omega_o d$ .

When the  $H_c(s)$  is given by equation (7), the system is stable if

$$A < 1 - d/4f \quad (19)$$

where  $A = K_o/K_s$ .

### 2.3 Spatial Stability

A guide will be defined as spatially stable if the beam remains within a bounded region around the guide axis for all values of  $n$ . A sufficient condition for the steady-state time solution to be spatially stable is that the poles of  $H(z)$  are inside the unit circle in the  $Z$  plane.  $H(z)$  can be obtained by setting  $s = 0$  in equation (11).

$$H(z) = \frac{z(d/f)}{[1 - (d/f)A]z^2 - (2 \cos \omega_c d)z + 1}. \quad (20)$$

Beginning with equations (19) and (20), using standard techniques it can be shown that for the type 0 system described by equation (7) only a negative value of  $A$  will satisfy the conditions for both temporal and spatial stability. For type 1 or higher systems  $A \rightarrow \infty$  and the poles of  $H(z)$  approach the origin of the  $Z$  plane assuring spatial stability.

#### 2.4 The High Gain Case

By high gain we mean large magnitude of  $H_c(s)$ . This is of particular importance, since the performance of the system improves when the magnitude of  $H_c(s)$  becomes large. When the magnitude of  $H_c(s)$  is large, equation (11) becomes

$$H(s, z) \approx \frac{-1}{zH_c(s)}. \quad (21)$$

Using the above approximation for  $H(s, z)$  and relaxing the restriction that the disturbances are constant functions of time and substituting into equation (10) the general expressions  $N(s, z)$  and  $G(s, z)$  for the  $Z$  transforms of the Laplace transforms of the lens and sensor displacements yields

$$R(s, z) - G(s, z) \approx -\frac{N(s, z)}{zH_c(s)}. \quad (22)$$

Division of a  $Z$  transform by  $z$  corresponds to subtracting one from the index of the inverse transform. The inverse  $Z$  transform of equation (22) is

$$R_n(s) - G_n(s) \approx -\frac{N_{n-1}(s)}{H_c(s)} \quad (23)$$

when  $H_c(s)$  is large the Laplace transforms of the beam and sensor positions will be approximately equal. It follows that the functions in the time domain will also be approximately equal. In the steady-state, when the disturbances are independent of time, the displacement of the beam from the guide axis is

$$r_n - g_n = -\frac{N_{n-1}}{A}. \quad (24)$$

For a type 1 or more system  $A \rightarrow \infty$  and in the steady-state the beam follows the sensors.

### 2.5 The Propagation of Unsensed Beams in the Guide

An unsensed beam will differ from the sensed beam primarily because the active guiding mechanism will not respond to deviations of the unsensed beam from the guide axis. The unsensed beam may also be injected into the guide off axis and follow an entirely different trajectory in the guide than does the sensed beam.

The effect of the corrective displacements on beams other than the beam that is sensed by the control system, can be seen by noticing the form of the total lens displacement. The  $Z$  transform of the total lens displacement,  $S(z)$ , is the  $Z$  transform of the constant lens displacement,  $N(z)$ , plus the  $Z$  transform of the corrective lens displacement  $\delta(z) = Az[R(z) - G(z)]$ ,

$$S(z) = N(z) + Az[R(z) - G(z)]. \quad (25)$$

Substituting equation (12) into equation (25), the  $Z$  transform of the total lens displacement becomes

$$S(z) = \frac{z^2 - (2 \cos \omega_0 d)z + 1}{(1 - Ad/f)z^2 - (2 \cos \omega_0 d)z + 1} [N(z) - AzG(z)]. \quad (26)$$

Let  $P_n$  be the displacement of an unsensed beam propagating in the guide with the boundary conditions  $P_{in}$  and  $P'_{in}$  just to left of the first lens which is assumed to be on the reference line. The difference equation that describes the propagation of any beam sensed or unsensed traveling in either direction through the guide is equation (1) rewritten here to describe the unsensed beam.

$$P_{n+2} - (2 \cos \omega_0 d)P_{n+1} + P_n = (d/f)s_{n+1}. \quad (27)$$

Operating on equation (27) using  $Z$  transform techniques<sup>9-11</sup> yields the following expression for the  $Z$  transform of the position of the unsensed beam

$$P(z) = \frac{z(d/f)S(z) + [z^2 - z]P_{in} + zdP'_{in}}{z^2 - (2 \cos \omega_0 d)z + 1}. \quad (28)$$

The substitution of equation (26) and (20) into equation (28) yields the following expression for the  $Z$  transform of the displacement of the unsensed beam.

$$P(z) = H(z)[N(z) - AzG(z)] + \frac{(z^2 - z)P_{in} + zdP'_{in}}{z^2 - (2 \cos \omega_0 d)z + 1}. \quad (29)$$

The displacement of the unsensed beam,  $P_n$ , the inverse  $Z$  transform of (29), is the superposition of two components. The first is represented

by the first two terms in equation (29). A comparison of these two terms with equation (12) shows that this component of the displacement is identical to the displacement of the sensed beam. Comparison of the remaining terms of equation (29) with equation (28) shows that they are identical to the  $Z$  transform of the displacement of a beam traveling in a guide with zero lens displacement,  $S(z) = 0$ .

The second component is identical to the displacement of an unsensed beam injected off axis into a perfectly straight guide. The total displacement of the unsensed beam is the sum of these two components. The unsensed beam will oscillate about the position of the sensed beam just as a beam injected off axis into a perfectly straight guide would oscillate about the guide axis. This result differs from equation (28) of Reference 5, which predicts a growth in the displacement of the unsensed beam as it propagates. In Reference 5 substitution shows equation (28) to be inconsistent with equation (22).

For stability, the sensed beam must travel in the direction of increasing  $n$ , but an unsensed beam may travel in either direction.

### 2.6 The Propagation of Many Sensed Beams in the Guide

Where there are many beams propagating in the positive direction of the guide, the signal obtained from the sensors is the average displacement of all the beams. The  $Z$  transform of the beam position signal is

$$D(z) = \langle P(z) \rangle - G(z). \quad (30)$$

Where  $D(z)$ ,  $\langle P(z) \rangle$ , and  $G(z)$  are the  $Z$  transforms of the position signal, the average beam displacement, and the sensor displacement, respectively. Different beams are injected into the guide differently and follow different trajectories through the guide. When the  $Z$  transform of the total lens displacement is  $S(z)$ , the  $Z$  transform of any beam propagating in the guide is given by equation (28). The  $Z$  transform of the average displacement is given by the average of equation (28) over all beams.

$$\langle P(z) \rangle = \frac{zd/fS(z) + [z^2 - z]\langle P_{in} \rangle + zd\langle P'_{in} \rangle}{z^2 - (2 \cos \omega_s d)z + 1}. \quad (31)$$

Where  $\langle P_{in} \rangle$  and  $\langle P'_{in} \rangle$  are the average displacement and slope of the beams just before propagating through the zeroth lens. It follows from equation (31) that the average displacement of the beams in the guide is the same as the displacement of a beam that is injected

into the guide with slope and displacement equal to  $\langle P'_{in} \rangle$  and  $\langle P_{in} \rangle$ , respectively. Therefore, the control system will respond to the average beam position signal and control the average of the beam displacements just as it would respond to one beam propagating in the guide.

### 2.7 The Response of a Beam to Waves of Displacements

As an example of how the system might perform consider the following particular type of disturbance. Both lenses and sensors are displaced simultaneously. The constant transverse displacements,  $D_n$ , of the lens and sensor assembly relative to the straight reference line form an axial wave of spatial frequency  $\omega$ , and are described by the following equation:

$$D_n = B e^{j\omega nd} \quad (32)$$

then

$$D(z) = \frac{zB}{z - e^{j\omega d}} \quad (33)$$

where  $B$  is the amplitude of the wave,  $\omega = 2\pi/\lambda$ , and  $\lambda$  is the spatial wavelength. When  $n$  is large enough so that boundary effects can be neglected, the  $Z$  transform of the displacement of the beam from the sensor is obtained by using equation (20) and letting  $D(z) = N(z) = G(z)$  in equation (12).

$$R(z) - D(z) = -\frac{(z-1)^2}{(1-Ad/f)z^2 - 2\cos\omega d z + 1} D(z). \quad (34)$$

It follows<sup>10</sup> from equation (34) that at any given spatial frequency,  $\omega$ , the ratio of the amplitude of the wave of the beam's displacement from the lens sensor assembly, to the amplitude of the wave of the lens sensor assembly's displacement from the axis is given by

$$\left| \frac{r_n - D_n}{D_n} \right| = \frac{|1 - \cos\omega d|}{|\cos\omega d - \cos\omega_0 d - A(d/2f)e^{j\omega d}|}. \quad (35)$$

The ratio given in equation (35) is plotted in Figure 3, for various real values of  $A$ , as a function of the spatial phase,  $\omega d$ . It follows from the sampling theorem that the largest spatial phase possible between lenses is  $\omega d = \pi$ .

Figure 4 is a plot of the ratio of the amplitude of the beam displacement to the lens displacement when the sensors remain on axis and the

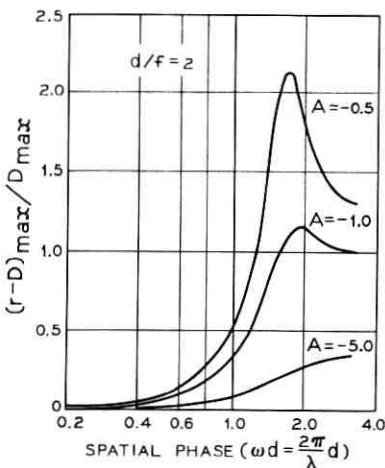


Fig. 3— Spatial frequency response of the beam position relative to the sensor when the lenses and sensors are disturbed simultaneously.

lens displacements  $N_n$  form a wave of axial spatial frequency  $\omega$ . For this case, the ratio of the amplitude of the beam displacement wave to the amplitude of the lens displacement wave is

$$\left| \frac{r_n}{N_n} \right| = \frac{d/2f}{|\cos \omega d - \cos \omega_0 d - A(d/2f)e^{j\omega d}|} \quad (36)$$

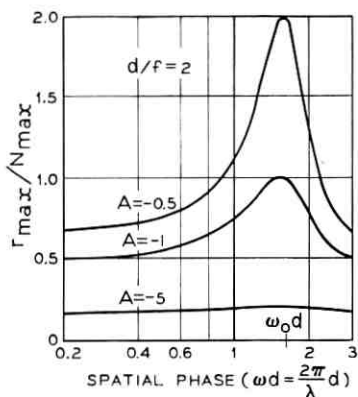


Fig. 4— Spatial frequency response of the beam position relative to the sensor when sensors are undisturbed and the lenses are disturbed.

### 2.8 The Response of a Beam to Random Transverse Displacements

Again assuming that the entire lens sensor assembly moves together, the spatial response of the beam to any general set of displacements,  $D_n$ , is given by the inverse  $Z$  transform of equation (34). The displacement of the beam from the sensor is the following convolution summation

$$r_n - D_n = -D_n + \sum_{m=1}^n (h_{n-m} - Ah_{n-m+1})D_m \quad (37)$$

where  $h_n$  is the inverse  $Z$  transform of the transfer function  $H(z)$ , given in equation (20).

$$h_n = \frac{d/f}{(1 - Ad/f)^{(n+1/2)}} \frac{\sin n\omega_2 d}{\sin \omega_2 d} \quad (38)$$

where  $\cos \omega_2 d = (1 - d/2f)/(1 - Ad/f)^{1/2}$ . We wish to find the expected value of the square of the beam displacement, from the sensor,  $\langle (r_n - D_n)^2 \rangle$ . For uncorrelated displacements, the expected value of the product of any two displacements is given by

$$\langle D_n D_m \rangle = \begin{cases} 0 & \text{if } n \neq m \\ \sigma_L^2 & \text{if } n = m \end{cases} \quad (39)$$

where  $\sigma_L$  is the rms lens and sensor displacement. The expected value of the square of the beam position can be written\*

$$\langle (r_n - D_n)^2 \rangle = \sigma_L^2 \left[ \frac{1 + Ad/f}{1 - Ad/f} + \sum_{m=0}^{n-1} (h_m - Ah_{m+1})^2 \right]. \quad (40)$$

This summation has been evaluated for large  $n$  and plotted in Figure 5 for  $d/f = 1, 2$ , and  $3$  as a function of  $A$ . When the magnitude of  $A$  is large compared with one, the ratio of the rms beam to rms lens and sensor displacement approaches  $1/|A|$ .

### 2.9 The Ability of a Short Section of Stabilized Guide to Return an Initially Off-Axis Beam to the Optical Axis

The preceding sections are concerned with the effect of lens displacements on a beam that is injected into the guide with zero slope

\* Equation (40) can be obtained using equation (37) with the following considerations. (i) The displacements,  $D_n$ , are uncorrelated. (ii) The expected value of a sum is the sum of the expected values. (iii) The expected value of the product of a deterministic function and a random variable is the product of the deterministic function and the expected value of the random variable. (iv) The zeroth lens and sensor are on axis.

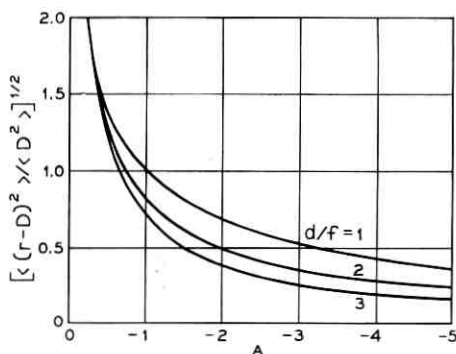


Fig. 5—The statistical response of beam position relative to the sensor when lenses and sensors are disturbed simultaneously.

and coincident with the guide axis. This is equivalent to saying that the boundary conditions of the difference equation are zero.

When a beam is injected into a straight feedback controlled guide off axis and the lens displacements are zero the  $Z$  transform of the beam position is a function of the boundary conditions and is determined using standard techniques.<sup>10</sup>

$$R(z) = \frac{[(1 - Ad/f)z^2 - (2 \cos \omega_0 d)z]r_0 + (1 - Ad/f)r_1}{(1 - Ad/f)z^2 - (2 \cos \omega_0 d)z + 1} \quad (41)$$

where  $r_0$  and  $r_1$  are the beam displacement at the zeroth and first lenses, respectively. The inverse  $Z$  transform of equation (41) can be found in tables and is equal to the following

$$r_n = (1 - Ad/f)^{-n/2} (B \sin \omega_2 nd + C \cos \omega_2 nd) \quad (42)$$

where  $\cos \omega_2 d = (1 - d/2f)/(1 - Ad/f)^{1/2}$  and the constants  $B$  and  $C$  chosen so that equation (42) will satisfy the boundary conditions.

Equation (42) shows that when a beam is injected into the feedback controlled guide off axis the maximum possible deviation from the axis decreases by a factor of  $(1 - Ad/f)^{-1/2}$  at each lens. For example, a beam injected parallel to the axis, one centimeter off axis, into a stabilized guide four lenses long with  $Ad/f = -9$ , will leave the guide with a maximum displacement from the axis that is less than 0.1 mm.

### 2.10 The Probability That the Beam Will Not be Contained Within a Given Aperture

An upper limit on the probability of the beam exceeding a threshold can be calculated using Chebyshev's inequality.<sup>12</sup> The probability of

the magnitude of the beam deviation from the axis of the sensors exceeding a value,  $T$ , at any given lens is less than the mean squared deviation divided by  $T^2$

$$P(|r_n - g_n| \geq T) \leq \frac{\langle (r_n - g_n)^2 \rangle}{T^2}. \quad (43)$$

If the magnitude of "A" is much larger than one, it follows from equation (24) that

$$\langle (r_n - g_n)^2 \rangle = \frac{\sigma_L^2}{A^2} \quad (44)$$

where  $\sigma_L$  is the rms disturbance of the lens position. Equation (44) is quite general and holds for deterministic as well as random lens displacements.

### III. CONCLUSIONS

A beam waveguide using the linear beam control system described here can be made stable in time and space by proper choice of the control mechanism.

If many beams are propagating in the guide it is only necessary that the control system interact with one or more beams propagating in the positive direction for the guide to be stabilized for all beams.

When the magnitude of  $A$ , the low frequency value of  $H_c(s)$  is large, the error in the beam position varies inversely with  $A$ .

It follows from equation (24) that, if  $A$  is large, the probability that the deviation of the beam from the axis of the sensors will exceed a value,  $T$ , at any given lens is equal to the probability that the displacement of the preceding lens will exceed a value of  $T$  multiplied by  $A$ . If  $A = -100$ , and  $T = 1$ , and if the lens displacements have a standard deviation of 0.1 and a gaussian amplitude distribution, then the probability that the deviation of the beam from the guide axis will exceed one is less than the vanishingly small value of  $10^{-10}$ . A more conservative number,  $10^{-6}$ , for this probability, that holds for all amplitude distributions, is obtained using Chebyshev's inequality.

There is no growth in the rms deviation of the beam from the guide axis as the beam propagates down the stabilized guide. Also, since the effects of guide imperfections, for example, transverse lens displacements, do not build up, the construction tolerances on the guide can be relaxed. It is possible to contain the beam within a narrow region of the guide axis, which permits minimizing the guide aperture.

## V. ACKNOWLEDGMENT

The author thanks D. H. Ring for many fruitful discussions and constructive suggestions.

## REFERENCES

1. Hirano, J. and Fukatsu, Y., "Stability of a Light Beam in a Beam Waveguide," Proc. IEEE, 52 (November 1964), pp. 1284-1292.
2. Steier, W. H., "The Statistical Effects of Random Variations in the Components of a Beam Waveguide," B.S.T.J., 45 March 1966, pp. 451-471.
3. Kompfner, R., unpublished work.
4. Kibler, L. U., unpublished work.
5. Marcatili, E. A. J., "Ray Propagation in Beam-Wave Guides with Redirectors," B.S.T.J., 45 (January 1966), pp. 105-115.
6. Christian, J. R., Goubau, G., Mink, J. W., "Self-Aligning Optical Beam Waveguides," Paper 5-6, 1967 IEEE Conf. Laser Eng. and Applications, Washington, D. C., June 6-8, 1967.
7. Tien, P. K., Gordon, J. P., and Whinnery, J. R., "Focusing of a Light Beam of Gaussian Field Distribution in Continuous and Periodic Lens-Like Media," Proc. IEEE, 53 (February 1965), pp. 129-136.
8. For a discussion of the properties of a periodic sequence of lenses, see: Pierce, J. R., *Theory and Design of Electron Beams*, New York: D. Van Nostrand, 1954, Chapter XI.
9. Cheng, D. K., *Analysis of Linear Systems*, Reading, Mass.: Addison-Wesley Publishing Company, Inc., 1959, Chapter 10, Section 3, p. 319.
10. See, for example, Jury, E. I., *Theory and Application of the Z-Transform Method*, New York: John Wiley & Sons, Inc., 1964.
11. Daly, J. C., "The Application of Z Transform Techniques to the Analysis of Paraxial Ray Propagation in Beam Waveguides," IEEE Trans. Microwave Theory and Techniques, MTT-16 (February 1968), pp. 95-98.
12. Feller, W., *An Introduction to Probability Theory and Its Applications*, New York: John Wiley & Sons, Inc., (1957), Chapter IX, Section 6, p. 219.



# Communication of Analog Data from a Gaussian Source Over a Noisy Channel

By A. D. WYNER

(Manuscript received December 20, 1967)

*We consider the problem of the transmission of analog data from a Gaussian source over a memoryless channel with capacity  $C$  nats per second. The source emits  $R$  independent zero mean Gaussian variates per second with variance  $\sigma^2$ . These digits are block-coded  $RN$  at a time into  $N$  second channel inputs. The performance criterion is the mean square error. Let  $\epsilon^2(N)$  be the smallest attainable mean square error with parameter  $N(R, C, \sigma^2)$  fixed. Shannon has shown that  $\epsilon^2(N) \geq \sigma^2 \exp(-2C/R) \triangleq \epsilon_0^2$  and  $\epsilon^2(N) \rightarrow \epsilon_0^2$  as  $N \rightarrow \infty$ . Hence the ideal error  $\epsilon_0^2$  is attainable in the limit as the coding delay  $N \rightarrow \infty$ . We are concerned with the rate at which  $\epsilon^2(N) \rightarrow \epsilon_0^2$ , and our principal result is that  $\epsilon^2(N) - \epsilon_0^2 \leq O[(\log N/N)^{1/2}]$ .*

## I. INTRODUCTION

We are interested in the following problem. Suppose we have an analog data source which emits a sequence of statistically independent Gaussian variates at a rate of  $R$  per second. We wish to transmit this data through a noisy channel of capacity  $C$  nats per second. Our problem is the determination of the minimum possible mean-squared-error.

Specifically we shall study the communication system of Figure 1. The output of the analog source is a sequence  $X_1, X_2, X_3, \dots$  of statistically independent Gaussian variates with zero mean and variance  $\sigma^2$  which appear at the coder input at rate of  $R$  per second. After  $N$  seconds,  $n = NR$  source variates have accumulated at the coder input. Let  $\mathbf{X}$  denote this random  $n$ -vector. The channel is a discrete memoryless channel\* which we assume accepts one input per second, and the coder contains a mapping of  $\mathbf{X}$  to an allowable channel input  $N$ -vector  $\mathbf{S}$ . Since it requires  $N$  seconds to transmit  $\mathbf{S}$ , the system can process the data continuously without a "backup" at the coder input.

\* Actually our results are valid for a broader class of channels. See the remark after Theorem 2 in Section II.

The decoder examines the channel output  $N$ -vector  $\mathbf{R}$  and emits a Euclidean  $n$ -vector  $\mathbf{X}'$  which is hopefully "close" to  $\mathbf{X}$ . The error criterion which we adopt is (the "mean-squared-error")

$$\epsilon^2 = \frac{1}{n} E \|\mathbf{X} - \mathbf{X}'\|^2, \quad (1)$$

where " $\|\cdot\|$ " is the Euclidean norm and  $E$  denotes expectation.

We shall assume that the parameters  $\sigma^2$ ,  $R$ , and  $C$  are held fixed for this entire paper, and denote by  $\epsilon^2(N)$ , the smallest value of  $\epsilon^2$  attainable with parameter  $N$  (and therefore  $n = RN$ ). Shannon<sup>1</sup> has shown that

$$(i) \quad \epsilon^2(N) \geq \sigma^2 \exp(-2C/R) \triangleq \epsilon_0^2, \quad (2a)$$

$$(ii) \quad \epsilon^2(N) \rightarrow \epsilon_0^2 \quad \text{as } N \rightarrow \infty, \quad (2b)$$



Fig. 1 — Communication System.

so that  $\epsilon^2 = \epsilon_0^2$  is attainable in the limit as the delay  $N \rightarrow \infty$ . We are concerned here with the rate at which  $\epsilon^2(N)$  approaches the ideal  $\epsilon_0^2$ , and our principal result is

$$\epsilon^2(N) \leq \epsilon_0^2 \left[ 1 + \frac{2}{R\sqrt{\beta}} \sqrt{\frac{\log N}{N}} + O\left(\frac{1}{\sqrt{N}}\right) \right], \quad \text{as } N \rightarrow \infty, \quad (3)$$

where  $\beta > 0$ , a parameter related to the channel, is defined in equation (13).

This result is related to a result of D. Sakrison<sup>2</sup> which was done independently.\* In fact we have used one of his ideas (Lemma 1 in our paper) to simplify our original proof.

## II. STATEMENT AND DISCUSSION OF RESULTS

Following Shannon's technique,<sup>1</sup> we separate the coder into two parts as shown in Figure 2. The first part, called the *source encoder* or *quantizer*, contains a fixed set  $\mathcal{S}$  of  $M$  Euclidean  $n$ -vectors, and associates with each possible input  $n$ -vector  $\mathbf{X}$  a member of  $\mathcal{S}$  (say  $\hat{\mathbf{X}}$ ). Let us denote

\* This paper and Sakrison's paper were presented at the International Symposium on Information Theory, San Remo, Italy, September 1967.

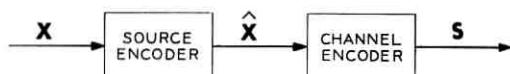


Fig. 2—Decomposition of the Coder.

the resulting (mean-square) "quantization error" by

$$\epsilon_Q^2 = \frac{1}{n} E \| \mathbf{X} - \hat{\mathbf{X}} \|^2. \quad (4)$$

The second part of the encoder, called the *channel encoder*, associates with each  $\hat{\mathbf{X}}$  (one of the  $M$  members of  $\mathcal{S}$ ) a channel input  $N$ -vector (say  $\mathbf{S}$ ). The decoder, at the receiving end of the channel, associates with each received  $N$ -vector  $\mathbf{R}$  one of the members of  $\mathcal{S}$  (say  $\hat{\mathbf{X}}'$ ). Let  $P_e = \Pr \{ \hat{\mathbf{X}}' \neq \hat{\mathbf{X}} \}$  be the probability of a transmission error, and denote the (mean-squared) transmission error by

$$\epsilon_T^2 = \frac{1}{n} E \| \hat{\mathbf{X}} - \hat{\mathbf{X}}' \|^2. \quad (5)$$

Clearly

$$\epsilon_T^2 \leq \frac{1}{n} P_e \max_{\mathbf{u}, \mathbf{v} \in \mathcal{S}} \| \mathbf{u} - \mathbf{v} \|^2. \quad (6)$$

Further, the overall error  $\epsilon^2$  satisfies

$$\epsilon^2 = \frac{1}{n} E \| \mathbf{X} - \mathbf{X}' \|^2 \leq (\epsilon_Q + \epsilon_T)^2. \quad (7)$$

Thus we want to make both  $\epsilon_Q^2$  and  $\epsilon_T^2$  as small as possible.

Consider the parameter  $M$ , the number of members of the approximating set  $\mathcal{S}$ . In the interest of minimizing  $\epsilon_Q^2$  we want to make  $M$  large. However, in the interest of minimizing  $P_e$  and therefore  $\epsilon_T^2$ , we want to make  $M$  small. The proper compromise yields our result, equation (3).

The following theorems indicate just how to choose  $M$ . The first is proved in Section III, and the second was proved by C. E. Shannon (Ref. 3, p. 16).

*Theorem 1: (Source Encoding).* Let  $\mathbf{X}$  be a random  $n$ -vector ( $n = 1, 2, \dots$ ) whose components are zero mean Gaussian variates with variance  $\sigma^2$ . Let  $R_0 > 0$  be given and let  $\{a_n\}_1^\infty$  be a sequence which tends to zero. Then there exists a set  $\mathcal{S}$  of  $M$   $n$ -vectors, where

$$M \leq \exp [n(R_0 - a_n)], \quad (8)$$

and a mapping  $f$  of  $\mathbf{X}$  into  $\mathcal{S}$ , such that as  $n \rightarrow \infty$

$$\frac{1}{n} E \| \mathbf{X} - f(\mathbf{X}) \|^2 \leq \sigma^2 e^{-2R_0} \left( 1 + 2a_n + \frac{\log n}{n} \right) + O(a_n^2) + O\left( \frac{\log \log n}{n} \right). \quad (9)$$

Furthermore,  $\mathcal{S}$  is such that for all  $\mathbf{u} \in \mathcal{S}$ ,

$$\frac{1}{n} \| \mathbf{u} \|^2 \leq \sigma^2. \quad (10)$$

A special case of some interest in itself is that for which  $a_n \equiv 0$ . In this case Theorem 1 asserts the existence of a quantization of  $\mathbf{X}$  with  $M = \exp(nR_0)$  points and mean-squared quantization error no more than  $\sigma^2 \exp(-2R_0)(1 + \log n/n) + O(\log \log n/n)$  as  $n \rightarrow \infty$ . If the channel is noiseless with capacity  $C$  nats second, it can transmit  $e^{CN}$  messages with no error in the  $N$  seconds that it takes for the  $n$ -vector  $\mathbf{X}$  to be emitted from the source. Thus if  $R_0 = C/R$ ,  $M = \exp(R_0 n) = e^{CN}$ , and the members of  $\mathcal{S}$  can be reconstructed perfectly by the receiver. The overall error is therefore

$$\epsilon^2 = \epsilon_0^2 \leq \sigma^2 \exp(-2C/R) \left( 1 + \frac{\log n}{n} \right) + O\left( \frac{\log \log n}{n} \right). \quad (11)$$

Let us turn now to the discrete memoryless channel defined by an input set  $(1, 2, \dots, K)$ , an output set  $(1, 2, \dots, J)$ , and a set of transition probabilities  $P(j | k)$ ,  $1 \leq j \leq J$ ,  $1 \leq k \leq K$ . Corresponding to each input probability distribution  $p_k$ ,  $1 \leq k \leq K$ , there is a joint distribution  $p(k, j) = P(j | k)p_k$  on the product of the input and output sets. Define the random variable (called "information")

$$U(k, j) = \log \left\{ \frac{p(j | k)}{\sum_{k'=1}^K p_k \cdot p(j | k')} \right\}, \quad 1 \leq k \leq K, \quad 1 \leq j \leq J. \quad (12)$$

The channel capacity  $C = \max_{\{p_k\}} EU$ , where the maximization is performed with respect to all possible input probability distributions. Let  $(p_k^*)_{k=1}^K$  be a maximizing input distribution, and let  $U^*(k, j)$  be the corresponding information, then define

$$\beta = (2 \text{ var } U^*)^{-1} = (2EU^{*2} - 2C^2)^{-1}. \quad (13)$$

*Theorem 2: (Shannon): Let  $\{b_N\}_{N=1}^\infty$  be a sequence which tends to zero from above. Then there exists an  $N$ -dimensional code (for the channel*

described above) with  $M$  members

$$M \geq \exp [N(C - b_N)], \quad (14)$$

and (for any a priori distribution on the code words) error probability

$$P_e \leq k \exp (-\beta N b_N^2), \quad (15)$$

where  $k$  is independent of  $N$ , and  $\beta$  is defined by (13).

Actually we can broaden the class of channels for which our main result (3) holds to include that class of channels for which Theorem 2 holds for some constant  $\beta$ . This broadened class includes the Gaussian channel with signal-to-noise ratio  $\rho$  for which  $\beta = [(1 + \rho)^2 / \rho(2 + \rho)]$  (see equation 74 of Ref. 4).

Theorems 1 and 2 lead us directly to the proper choice of  $M$  and our main result. Since the channel encoder must encode each of the members of  $\mathcal{S}$  into channel inputs, we equate the  $M$ 's of Theorems 1 and 2 obtaining (from  $n = NR$ )

$$R_0 = C/R \quad \text{and} \quad b_N = Ra_n. \quad (16)$$

If we then choose

$$b_N = \sqrt{\frac{\log N}{\beta N}}, \quad (17)$$

where  $\beta$  is defined in (13) we have from Theorem 1 a quantization error

$$\epsilon_q^2 \leq \sigma^2 \exp (-2C/R) \left( 1 + \frac{2}{R\sqrt{\beta}} \sqrt{\frac{\log N}{N}} \right) + O\left(\frac{\log N}{N}\right), \quad (18)$$

and from (6), (10), and Theorem 2, a transmission error

$$\epsilon_r^2 \leq 4\sigma^2 P_e \leq 4\sigma^2 k \frac{1}{N}. \quad (19)$$

Thus by combining (7), (18), and (19) we have an over-all mean-squared error

$$\epsilon^2 \leq \sigma^2 \exp (-2C/R) \left( 1 + \frac{2}{R\sqrt{\beta}} \sqrt{\frac{\log N}{N}} \right) + O\left(\frac{1}{\sqrt{N}}\right). \quad (20)$$

This is our result (3).

### III. PROOF OF THEOREM 1

We must establish the existence of a mapping  $f$  of Euclidean  $n$ -space into a set  $\mathcal{S}$  of  $M$   $n$ -vectors such that  $E \| \mathbf{X} - f(\mathbf{X}) \|^2 / n$  satisfies the

upper bound (9). Let  $r_o = E \| \mathbf{X} \|$ . It can be shown that with very high probability, as  $n \rightarrow \infty$ ,  $\mathbf{X}$  will be near the surface of the sphere of radius  $r_o$  with center at the origin. It turns out to be convenient to establish the existence of a mapping  $g$  from the surface  $S_{r_o}$  of this sphere to a set  $\mathcal{S}$ .

Accordingly we shall construct the mapping  $f$  as follows. Let  $\mathbf{X}_p = \mathbf{X}(E \| \mathbf{X} \| / \| \mathbf{X} \|) = \mathbf{X}(r_o / \| \mathbf{X} \|)$  be the projection of  $\mathbf{X}$  onto the surface  $S_{r_o}$ . Let  $g$  be a mapping of  $S_{r_o}$  to some set  $\mathcal{S}$  of  $n$ -vectors ( $g$  has not yet been found, of course), then  $f = g(\mathbf{X}_p)$ . The following lemma of D. J. Sakrisan<sup>2</sup>, is proved in the Appendix.

*Lemma 1: For any mapping  $g$ , and  $f = g(\mathbf{X}_p)$ ,*

$$E \| \mathbf{X} - f(\mathbf{X}) \|^2 = \text{Var} \| \mathbf{X} \| + E \| \mathbf{X}_p - g(\mathbf{X}_p) \|^2. \quad (21)$$

Since, as we shall see,  $\text{Var} \| \mathbf{X} \|$  is relatively small, the principal contribution to  $E \| \mathbf{X} - f(\mathbf{X}) \|^2$  is  $E \| \mathbf{X}_p - g(\mathbf{X}_p) \|^2$ .

Our next task is to find the mapping  $g$ , and to this end we will establish a lemma concerning the covering of  $S_{r_o}$  by spherical caps. First some definitions.

Let  $\mathbf{w}$ ,  $\mathbf{z}$  with and without subscripts denote points on  $S_{r_o}$ , the surface of a sphere in  $n$ -space of radius  $r_o$ . Let  $\alpha(\mathbf{w}, \mathbf{z})$  be the angle\* between  $\mathbf{w}$  and  $\mathbf{z}$ . For  $0 \leq \theta \leq \pi$ , let  $\mathcal{C}(\mathbf{w}, \theta) = \{ \mathbf{z} : \alpha(\mathbf{w}, \mathbf{z}) \leq \theta \}$  be the spherical cap of half angle  $\theta$  centered at  $\mathbf{w}$ . Assign the usual "area" measure to  $S_{r_o}$ . If  $A \subseteq S_{r_o}$  is measurable, let  $\mu(A)$  be its measure. In particular, let

$$C_n(\theta) = \mu[\mathcal{C}(\mathbf{w}, \theta)] = \frac{(n-1)\pi^{n-1}r_o^{n-1}}{\Gamma\left(\frac{n+1}{2}\right)} \int_0^\theta \sin^{n-2} \varphi \, d\varphi \quad (22)$$

be the area (measure) of a cap of half angle  $\theta$ †, so that

$$C_n(\pi) = \frac{n\pi^{n/2}r_o^{n-1}}{\Gamma\left(\frac{n+2}{2}\right)} \quad (23)$$

is the area of  $S_{r_o}$ . We now state

*Lemma 2:‡ Let  $\mathbf{X}_p$  be a random vector which is uniformly distributed*

\* The angle  $\alpha(\mathbf{w}, \mathbf{z})$  is defined by  $\cos \alpha = (\mathbf{w}, \mathbf{z}) / \| \mathbf{w} \| \| \mathbf{z} \|$ , where  $(\mathbf{w}, \mathbf{z})$  is the inner product and  $0 \leq \alpha \leq \pi$ .

† It is shown in Ref. 5 that  $A_n(r)$ , the surface area of an  $n$ -sphere of radius  $r$  is given by  $A_n(r) = n\pi^{n/2} r^{n-1} / \Gamma[(n+2)/2]$ . Equation (22) follows from the fact that  $C_n(\theta) = \int_0^\theta (r_o d\varphi) A_{n-1}(r_o \sin \varphi)$ .

‡ Lemma 2 is related to a result on the covering of the  $n$ -sphere in Ref. 6.

on  $S_{r_n}$ . Let  $M$  (a positive integer) and  $\theta$  ( $0 \leq \theta \leq \pi$ ) be arbitrary. Then (for any dimension  $n$ ) there exists a set of  $M$  points  $\{\mathbf{w}_1, \dots, \mathbf{w}_M\} \subseteq S_{r_n}$  such that

$$Q(\mathbf{w}_1, \dots, \mathbf{w}_M) \triangleq \Pr \left\{ \mathbf{X}_p \notin \bigcup_{j=1}^M \mathcal{C}(\mathbf{w}_j, \theta) \right\} \leq \exp [-MC_n(\theta)/C_n(\pi)]. \quad (24)$$

*Proof:* Let us define the function

$$F(\mathbf{w}_1, \mathbf{w}_2, \dots, \mathbf{w}_M, \mathbf{z}) = \begin{cases} 1 & \text{if } \alpha(\mathbf{w}_j, \mathbf{z}) > \theta, \quad 1 \leq j \leq M, \\ 0 & \text{otherwise.} \end{cases} \quad (25)$$

Then for a fixed set  $\mathbf{w}_1, \dots, \mathbf{w}_M$ ,

$$\begin{aligned} Q(\mathbf{w}_1, \dots, \mathbf{w}_M) &= \Pr \left\{ \mathbf{X}_p \notin \bigcup_{j=1}^M \mathcal{C}(\mathbf{w}_j, \theta) \right\} \\ &= EF(\mathbf{w}_1, \dots, \mathbf{w}_M, \mathbf{X}_p) \\ &= \frac{1}{C_n(\pi)} \int F(\mathbf{w}_1, \dots, \mathbf{w}_M, \mathbf{z}) d\mu(\mathbf{z}). \end{aligned} \quad (26)$$

Now consider a random experiment in which the  $M$  points  $\mathbf{w}_1, \dots, \mathbf{w}_M$  are random vectors chosen independently with uniform distribution on  $S_{r_n}$ .  $Q$  is now a random variable given by

$$Q(\mathbf{W}_1, \mathbf{W}_2, \dots, \mathbf{W}_M) = \frac{1}{C_n(\pi)} \int F(\mathbf{W}_1, \dots, \mathbf{W}_M, \mathbf{z}) d\mu(\mathbf{z}), \quad (27)$$

where upper case  $\mathbf{W}$ 's represent random vectors. We now compute  $EQ(\mathbf{W}_1, \dots, \mathbf{W}_M)$ , the average of  $Q$  over all choices of  $\mathbf{W}_1, \dots, \mathbf{W}_M$ . We will show that  $EQ \leq \exp [-MC_n(\theta)/C_n(\pi)]$ . Since at least one set  $\{\mathbf{w}_1, \dots, \mathbf{w}_M\}$  must satisfy  $Q(\mathbf{w}_1, \dots, \mathbf{w}_M) \leq EQ$ , the lemma will follow.

We can write

$$\begin{aligned} EQ &= E \frac{1}{C_n(\pi)} \int F(\mathbf{W}_1, \dots, \mathbf{W}_M, \mathbf{z}) d\mu(\mathbf{z}) \\ &= \frac{1}{C_n(\pi)} \int d\mu(\mathbf{z}) EF(\mathbf{W}_1, \dots, \mathbf{W}_M, \mathbf{z}), \end{aligned} \quad (28)$$

the interchange of expectation and integration being justified by the fact that  $F \geq 0$ . As indicated in (28),  $EF(\mathbf{W}_1, \dots, \mathbf{W}_M, \mathbf{z})$  is computed

with  $z$  held fixed. Now

$$\begin{aligned} EF(\mathbf{W}_1, \dots, \mathbf{W}_M, z) &= \Pr \{F = 1\} = \Pr \bigcap_{i=1}^M \{\alpha(\mathbf{W}_i, z) > \theta\} \\ &= \left(1 - \frac{C_n(\theta)}{C_n(\pi)}\right)^M \leq \exp[-MC_n(\theta)/C_n(\pi)], \end{aligned} \quad (29)$$

so that

$$E(Q) \leq \exp[-MC_n(\theta)/C_n(\pi)] \int \frac{d\mu(z)}{C_n(\pi)} = \exp[-MC_n(\theta)/C_n(\pi)] \quad (30)$$

which concludes the proof.

We now give the construction of  $g$ . Let  $M = M_n = \exp[n(R_o - a_n)]$  as in Theorem 1, and let  $\theta = \theta_n = \arcsin \exp(-R_o + \delta_n)$ , where  $\delta_n > 0$  will be specified below. Let  $\{\mathbf{w}_1, \mathbf{w}_2, \dots, \mathbf{w}_M\}$  be a set which satisfies (24) for these  $\theta$  and  $M$ . Let  $\mathbf{x} \in S_{r_o}$  and say  $\mathbf{x} \in \bigcup_{i=1}^M \mathcal{C}(\mathbf{w}_i, \theta)$ . Let  $j_o$  be the smallest index  $j$  such that  $\mathbf{x} \in \mathcal{C}(\mathbf{w}_j, \theta)$ . Then

$$g(\mathbf{x}) = (\cos \theta) \mathbf{w}_{j_o}, \quad (31)$$

(see Figure 3), and  $\|g(\mathbf{x}) - \mathbf{x}\| \leq r_o \sin \theta$ . If  $\mathbf{x} \notin \bigcup_{i=1}^M \mathcal{C}(\mathbf{w}_i, \theta)$ , then let  $g(\mathbf{x}) = \mathbf{w}_1$ . In this case  $\|\mathbf{x} - g(\mathbf{x})\| \leq 2r_o$ . Hence

$$E \|\mathbf{X}_p - g(\mathbf{X}_p)\|^2 \leq r_o^2 \sin^2 \theta + 4r_o^2 Q(\mathbf{w}_1, \mathbf{w}_2, \dots, \mathbf{w}_M). \quad (32)$$

Since the set  $\{\mathbf{w}_i\}$  satisfies (24),

$$E \|\mathbf{X}_p - g(\mathbf{X}_p)\|^2 \leq r_o^2 \sin^2 \theta_n + 4r_o^2 \exp[-MC_n(\theta)/C_n(\pi)]. \quad (33)$$

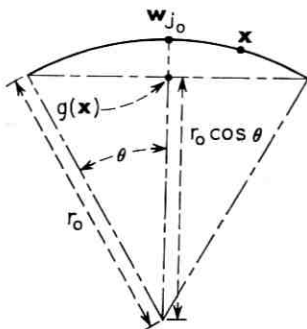


Fig. 3—Construction of  $g(\mathbf{x})$ . The solid line is the cap  $\mathcal{C}(\mathbf{w}_j, \theta)$ .

Combining (33), and Lemma 1, and the fact (proved in the Appendix) that

$$r_o \leq \sigma \sqrt{n} \quad \text{and} \quad \frac{1}{n} \text{var} \|\mathbf{X}\| \leq 0.92\sigma^2/n, \quad (34)$$

we obtain

$$\begin{aligned} \frac{1}{n} E \|\mathbf{X} - f(\mathbf{X})\|^2 \\ \leq \sigma^2 \sin^2 \theta_n + 4\sigma^2 \exp[-M_n C_n(\theta_n)/C_n(\pi)] + 0.92\sigma^2/n, \end{aligned} \quad (35)$$

where  $M_n = \exp[n(R_o - a_n)]$  and  $\theta_n = \arcsin \exp(-R_o + \delta_n)$ , where  $\delta_n > 0$  is to be specified. Our final step is selection of  $\delta_n$  so that (9) is satisfied. For  $\theta_n$  bounded away from  $\pi/2$ , Shannon (equation 27 of Ref. 4) has shown that as  $n \rightarrow \infty$ ,

$$\frac{C_n(\theta_n)}{C_n(\pi)} \sim \frac{1}{\sqrt{2\pi n}} \frac{\sin^n \theta_n}{\cos \theta_n \sin \theta_n} > \frac{1}{\sqrt{2\pi n}} \sin^n \theta_n, \quad (36)$$

so that (using the definitions of  $M_n$  and  $\theta_n$ ) for  $n$  sufficiently large

$$M_n \frac{C_n(\theta_n)}{C_n(\pi)} \geq \frac{\exp[n(\delta_n - a_n)]}{\sqrt{2\pi n}}. \quad (37)$$

We now define  $\delta_n$  by

$$\delta_n = a_n + \frac{1}{2} \frac{\log n}{n} + \frac{\log \log n}{n} + \frac{\log \sqrt{2\pi}}{n}. \quad (38)$$

Then, from (37), for  $n$  sufficiently large

$$\exp[-M_n C_n(\theta_n)/C_n(\pi)] \leq 1/n. \quad (39)$$

Finally, we have

$$\begin{aligned} \exp(2\delta_n) &= 1 + 2\delta_n + O(\delta_n^2) \\ &= 1 + 2\delta_n + O(a_n^2) + O\left[\left(\frac{\log n}{n}\right)^2\right]. \end{aligned} \quad (40)$$

Combining (35), (39), and (40) we obtain

$$\begin{aligned} \frac{1}{n} E \|\mathbf{X} - f(\mathbf{X})\|^2 \\ \leq \sigma^2 e^{-2R_o} \left(1 + 2a_n + \frac{\log n}{n}\right) + O\left(\frac{\log \log n}{n}\right) + O(a_n^2) \end{aligned} \quad (41)$$

which is (9).

Inequality (10) follows from (31) and (34) by simply

$$\|f(\mathbf{X})\| = \|g(\mathbf{X}_p)\| = r_0 \cos \theta < r_0 < \sqrt{n\sigma^2}. \quad (42)$$

#### APPENDIX

In this appendix we establish some facts about the random vector  $\mathbf{X} = (X_1, X_2, \dots, X_n)$  whose coordinates are independent zero-mean Gaussian variates with variance  $\sigma^2$ .

*Proposition:*

$$\begin{aligned} (i) \quad E \|\mathbf{X}\| &\leq (n\sigma^2)^{\frac{1}{2}} \\ (ii) \quad \text{var} \|\mathbf{X}\| &\leq 0.92\sigma^2 \end{aligned}$$

*Proof:* (i) follows from the Schwarz inequality:  $[E(1 \cdot \|\mathbf{X}\|)]^2 \leq E \|\mathbf{X}\|^2 E 1^2 = E \|\mathbf{X}\|^2 = n\sigma^2$ . To establish (ii), consider the  $n$ -fold joint probability density for the vector  $(R, \Phi_1, \dots, \Phi_{n-1})$ , the polar coordinate representation of  $\mathbf{X}^*$ ,

$$g(r, \varphi_1, \varphi_2, \dots, \varphi_{n-1}) = \exp(r^2/2\sigma^2) r^{n-1} h(\varphi_1, \dots, \varphi_{n-1}), \quad (43)$$

where  $h(\varphi_1, \dots, \varphi_{n-1}) = (2\pi\sigma^2)^{-n/2} \cos^{n-2} \varphi_1 \cos^{n-3} \varphi_2 \dots \cos \varphi_{n-2}$ .

The marginal distribution for the random variable  $R = \|\mathbf{X}\|$  is

$$f(r) = \frac{2}{(2\sigma^2)^{n/2} \Gamma\left(\frac{n}{2}\right)} r^{n-1} \exp(-r^2/2\sigma^2),$$

so that an integration yields

$$E \|\mathbf{X}\| = E(R) = \sqrt{2\sigma^2} \Gamma\left(\frac{n+1}{2}\right) / \Gamma\left(\frac{n}{2}\right).$$

Since  $E \|\mathbf{X}\|^2 = n\sigma^2$ , we have

$$\text{var} \|\mathbf{X}\| = n\sigma^2 \left\{ 1 - \frac{2}{n} \left[ \frac{\Gamma\left(\frac{n+1}{2}\right)^2}{\Gamma\left(\frac{n}{2}\right)} \right] \right\}. \quad (44)$$

Using the Stirling formula,

$$e^{-u} u^{u-\frac{1}{2}} \sqrt{2\pi} \left( 1 + \frac{1}{12u} - \frac{1}{360u^3} \right) \leq \Gamma(u) \leq e^{-u} u^{u-\frac{1}{2}} \sqrt{2\pi} \left( 1 + \frac{1}{12u} \right),$$

\* See, for example, M. G. Kendall and A. Stuart, *The Advanced Theory of Statistics*, vol. 1, London: Griffin, 1963, Section 11.2.

to underestimate  $\Gamma(n + 1/2)$  and overestimate  $\Gamma(n/2)$  we obtain

$$\frac{\text{Var} \|\mathbf{X}\|}{n\sigma^2} \leq 1 - e^{-1} \left(1 + \frac{1}{n}\right)^n \left(1 - \frac{7}{36n(n+1)} - \frac{1}{90(n+1)^2}\right)^2. \quad (45)$$

Further

$$\begin{aligned} e^{-1} \left(1 + \frac{1}{n}\right)^n &= \exp[-1 + n \log(1 + 1/n)] \\ &\geq \exp[-1 + n(1/n - 1/2n^2)] \\ &= \exp(-1/2n) \geq 1 - \frac{1}{2n}, \end{aligned}$$

and

$$\frac{1}{36n(n+1)} + \frac{1}{90(n+1)^2} \leq \frac{1}{n^2} \left(\frac{7}{36} + \frac{1}{90}\right) \leq \frac{0.21}{n^2}.$$

Hence,

$$\begin{aligned} \frac{\text{Var} \|\mathbf{X}\|}{n\sigma^2} &\leq 1 - (1 - 0.5n^{-1})(1 - 0.42n^{-2}) \leq \frac{0.5}{n} + \frac{0.42}{n^2} \\ &= \frac{0.5}{n} \left(1 + \frac{0.84}{n}\right) \leq \frac{0.5(1.84)}{n} = \frac{.92}{n}. \end{aligned} \quad (46)$$

This is (ii).

We now give a

*Proof of Lemma 1:*

$$\begin{aligned} E \|\mathbf{X} - f(\mathbf{X})\|^2 &= E \|\mathbf{X} - \mathbf{X}_p + \mathbf{X}_p - g(\mathbf{X}_p)\|^2 \\ &= E \|\mathbf{X} - \mathbf{X}_p\|^2 + E \|\mathbf{X}_p - g(\mathbf{X}_p)\|^2 \\ &\quad + 2E(\mathbf{X} - \mathbf{X}_p, \mathbf{X}_p - g(\mathbf{X}_p)), \end{aligned} \quad (47)$$

where  $(\mathbf{u}, \mathbf{v})$  is the inner product of the  $n$ -vectors  $\mathbf{u}$  and  $\mathbf{v}$ . Now  $\|\mathbf{X} - \mathbf{X}_p\|^2 = \{ \|\mathbf{X}\| - E \|\mathbf{X}\| \}^2$ , so that

$$E \|\mathbf{X} - \mathbf{X}_p\|^2 = \text{var} \|\mathbf{X}\|. \quad (48)$$

Further, the inner product

$$\begin{aligned} &((\mathbf{X} - \mathbf{X}_p, \mathbf{X}_p - g(\mathbf{X}_p))) \\ &= (\mathbf{X}, \mathbf{X}_p) - (\mathbf{X}, g(\mathbf{X}_p)) - (\mathbf{X}_p, \mathbf{X}_p) + (\mathbf{X}_p, g(\mathbf{X}_p)) \\ &= \|\mathbf{X}\| r_0 - r_0^2 - \|\mathbf{X}\| \|g(\mathbf{X}_p)\| \cos \alpha_1 + r_0 \|g(\mathbf{X}_p)\| \cos \alpha_2, \end{aligned} \quad (49)$$

where  $\alpha_1$  is the angle between  $\mathbf{X}$  and  $g(\mathbf{X}_p)$ , and  $\alpha_2$  is the angle between  $\mathbf{X}_p$  and  $g(\mathbf{X}_p)$ . Since  $\mathbf{X}$  and  $\mathbf{X}_p$  are colinear,  $\alpha_1 = \alpha_2 = \alpha(\mathbf{X}_p)$  a function of  $\mathbf{X}_p$ . Now from (43) we see that the random variable  $R = \|\mathbf{X}\|$  and the vector  $(\Phi_1, \dots, \Phi_{n-1})$  are statistically independent. Since  $\mathbf{X}_p$ , depends only on  $\Phi, \dots, \Phi_{n-1}$  and not on  $R$ , we conclude that  $\|\mathbf{X}\|$  is independent of  $g(\mathbf{X}_p)$  and  $\alpha(\mathbf{X}_p)$ . Thus from (49)

$$\begin{aligned} E(\mathbf{X} - \mathbf{X}_p, \mathbf{X}_p - g(\mathbf{X}_p)) \\ = r_0 E \|\mathbf{X}\| - r_0^2 - E \|\mathbf{X}\| E[\|g(\mathbf{X}_p)\| \cos \alpha(\mathbf{X}_p)] \\ + r_0 E[\|g(\mathbf{X}_p)\| \cos \alpha(\mathbf{X}_p)] = 0. \end{aligned} \quad (50)$$

Equations (47), (48) and (50) imply Lemma 1.

#### REFERENCES

1. Shannon, C. E., "Coding Theorems for a Discrete Source with a Fidelity Criterion," *1959 IRE Convention Record Part 4*, pp. 142-163.
2. Sakrisan, D. J., "A Geometric Treatment of the Problem of Source Encoding a Gaussian Random Variable," Tech. Rep., Space Sciences Laboratory, University of California, Berkeley, 1967; also presented at the Int. Symp. Inform. Theory, San Remo, Italy, September 1967.
3. Shannon, C. E., "Certain Results in Coding Theory for Noisy Channels," *Inform. Control, 1*, (September 1957), pp. 6-25.
4. Shannon, C. E., "Probability of Error for Optimal Codes in the Gaussian Channel," *B.S.T.J.*, 38, No. 5 (May 1959), pp. 611-656.
5. Wozencraft, J. and Jacobs, I., *Principles of Communication Engineering*, New York: John Wiley and Sons, Inc., 1965, pp. 355-357.
6. Wyner, A. D., "Random Packings and Coverings of the Unit  $n$ -Sphere," *B.S.T.J.*, 46, No. 9 (November 1967), pp. 2111-2118.

# On Permutation Switching Networks

By A. E. JOEL, JR.

(Manuscript received December 1, 1967)

*Rearrangeable switching networks are considered as permutation generators. Two-by-two network arrays may be implemented in these networks using a  $\beta$  reversing element. Nested tree arrays of these elements may be used to synthesize rearrangeable switching networks which appear minimal. Multistage network arrays of these elements may be implemented within a single coordinate device.*

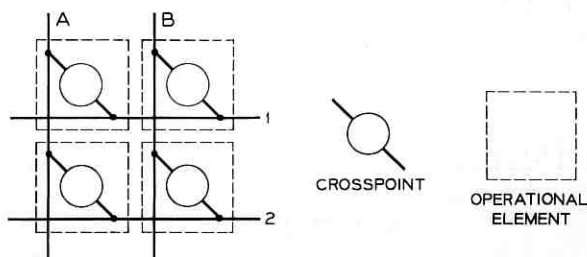
## I. INTRODUCTION

Two-sided communication switching networks with an equal number of input and output terminals ( $N$ ) have been looked upon as permutation generators of order  $N$ .<sup>1, 2</sup> Alteration of the permutation being produced by any state of the network configuration may be achieved by rearranging or changing the state of the switching network. By limiting the switches in each stage to binary action devices certain economies have been achieved.<sup>3</sup> This paper describes additional savings, particularly in the number of required operating elements. Some further savings are achieved by introducing break contacts into switching networks.

## II. THE $\beta$ ELEMENT

A small space division switching network is a two-by-two array of crosspoints (see Fig. 1). Each of these crosspoints is generally considered as either electromechanical make-contacts or electronic two-state devices. Confining our attention to make-contacts, they may be actuated by a coordinate mechanism, as in a crossbar switch, or as individual relays.

Usually in switching networks the crosspoints are controlled so that only one may be operated in any column and row. Such use of  $2 \times 2$  arrays confine the maximum number of states from the 16 possible states to those useful in switching networks. The 16 states

Fig. 1— $2 \times 2$  crosspoint array.

include double connections (two operated in the same column or row) and the zero state. The zero state is useful if the crosspoint devices require holding power. When this state occurs it introduces a vacuous partition into the permutation of the network. Actually the only useful states, particularly when viewed from the standpoint of rearrangeable networks, are the two shown in Fig. 1: ( $A \rightarrow 1$ ,  $B \rightarrow 2$ ), and ( $A \rightarrow 2$ ,  $B \rightarrow 1$ ). In these rearrangeable networks the vacuous states are eliminated.

It is proposed that the equivalent of  $2 \times 2$  arrays of four make-contacts and associated electromagnets be achieved by the simple expedient of two transfer contacts connected in the so-called reversing configuration (see Fig. 2a). Using this two-state or binary ( $\beta$ ) element only two moving contacts and one electromagnet are required. The equivalent of  $\beta$  elements may be achieved in many other ways without break contacts. Figs. 2b and 2c show a  $\beta$  array made from the array of Fig. 1 using only 2 operating elements.

### III. THE USE OF $\beta$ ELEMENTS IN SYMMETRICAL REARRANGEABLE NETWORKS

Methods have been described by V. E. Beneš<sup>3</sup> for using  $2 \times 2$  arrays to form rearrangeable link networks. Improvements result when applying  $\beta$  elements to these networks. For example, the equivalent of a  $4 \times 4$  rearrangeable switching network can be made of three stages of  $2 \times 2$  switches or a total of six  $\beta$  elements (Fig. 3). Here 6  $\beta$  elements replace 16 crosspoints and their operating magnets. An  $8 \times 8$  switch of 64 crosspoints may be replaced by 20  $\beta$  arrays in 5 stages (see Fig. 4).

For extending to larger networks, the method taught by Beneš may be applied, replacing the middle  $4 \times 4$  stage by the three symmetric stages of  $\beta$  elements. A rearrangeable network with  $N$  terminals

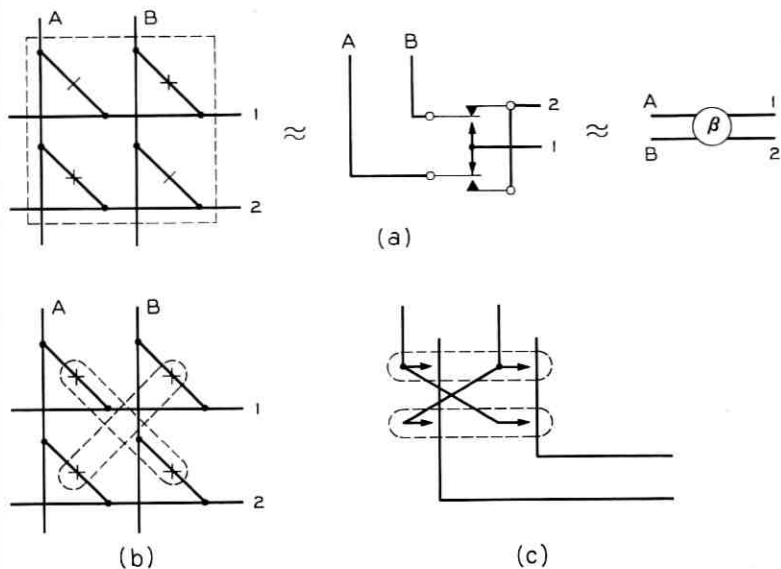


Fig. 2 — Binary  $\beta$  element. (a) One operator. (b) Two operators.

on each side will comprise  $S$  stages of these elements with  $N/2$  elements per stage where

$$S = 2 \log_2 N - 1.$$

The total  $\beta$  elements per input terminal is

$$\frac{N}{2} (2 \log_2 N - 1) \frac{1}{N} = \log_2 N - \frac{1}{2}.$$

For a network with  $N = 1024$  terminals per side (see Fig. 5), then 9.5  $\beta$  elements are used in the network per input terminal. This is considerably less than the 32 coordinate array crosspoints per input required in the network described by Beneš.

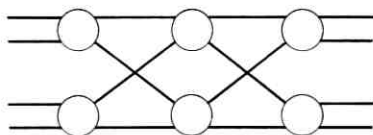


Fig. 3 — Three stage  $4 \times 4$  network of  $\beta$  elements.

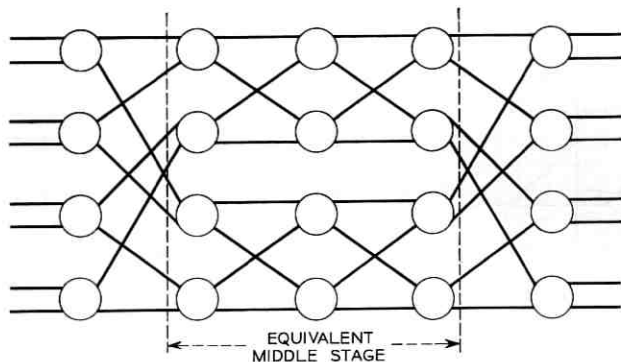


Fig. 4 — Five stage  $8 \times 8$  Beneš type network of  $\beta$  elements.

#### IV. NESTED TREE TYPE PERMUTATION NETWORKS

The  $4 \times 4$  symmetric network may be further simplified by omitting one  $\beta$  element to obtain a network (see Fig. 6), where each input reaches each output through one or more selecting trees of  $\beta$  elements. The  $\beta$  elements in the first stage is used by inputs 2 and 3 to select one of two trees in stages 2 and 3, either of which can reach a given output depending upon the state of the  $\beta$  element to which it is connected.

This  $4 \times 4$  network (Fig. 6) is a trivial case of the "nested trees" concept. The stages 2 and 3 are two superimposed trees with stage 1 a one-stage selecting tree.

The concept is better illustrated with higher order networks. The  $8 \times 8$  array in Fig. 7 uses 17  $\beta$  elements with 1, 2, and 3 stage trees in a total of 6 stages. This compares very favorably with a single stage  $8 \times 8$  array requiring only about one quarter of the number of operating magnets, about one half of the number of moving contacts, and only 4 more contacts. A  $16 \times 16$  array with 49  $\beta$  elements would have 1, 2, 3, and 4 stage trees in a total of 10 stages.

In general with nested trees the first stage connected with the outputs (or inputs) has

$$s_1 = \log_2 N$$

stages of  $N/2$   $\beta$  elements and is the highest order tree group. Then the remaining stages form lower order trees, which might be con-

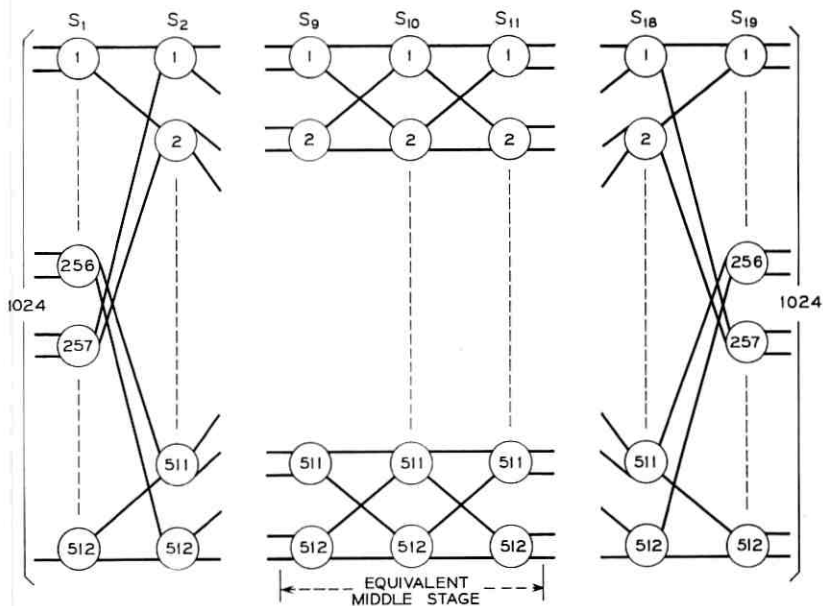


Fig. 5 — Beneš type 1024 terminal network of  $\beta$  elements.

sidered in different spatial dimensions or disjunctive nested parts of the network.

The total  $\beta$  elements in such a network is

$$\sum_{s=1}^{\log_2 N} \frac{N}{2^s} \log_2 \frac{N}{2^{s-1}}$$

This function simplifies to

$$N \log_2 N - N + 1.$$

Derived in another manner this same formula has been obtained by Goldstein and Leibholz<sup>4</sup>

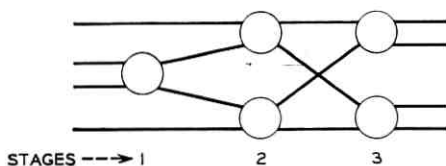


Fig. 6 — Three stage "tree type"  $4 \times 4$  network of  $\beta$  elements.

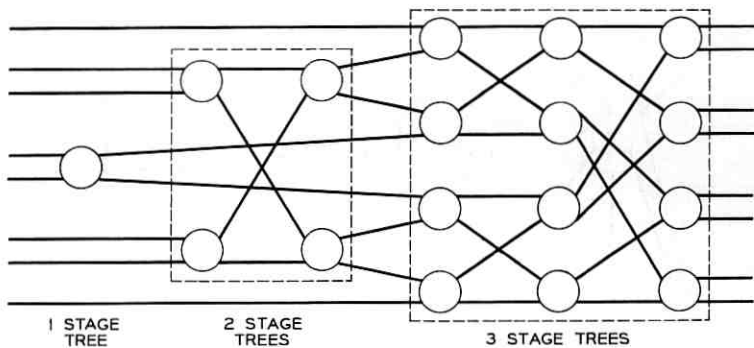


Fig. 7—Six stage "nested tree" type  $8 \times 8$  network of  $\beta$  elements.

Figure 8 shows the derivation of a nested tree network for  $N = 32$  where the different order nested trees are shown as boxes to illustrate the various parts of the network. Figure 9 illustrates the spatial concept for the same network.

The total number of stages in such networks may be defined as the total number of stages in all trees. Thus,

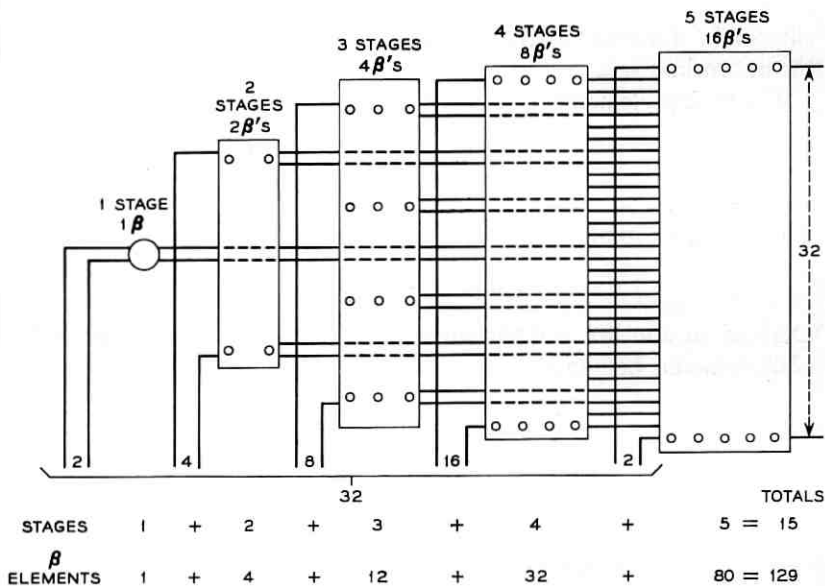


Fig. 8—Schematic of "nested tree" type  $32 \times 32$  network of  $\beta$  elements.

$$S = \log_2 N \left( \frac{\log_2 N + 1}{2} \right).$$

The number of  $\beta$  elements per input is, for large numbers,  $\log_2 N - 1$ . This is an improvement of  $0.5 \beta$  element per input compared with the symmetric network approach described in the previous section.

To double the size of a nested network requires the addition of new higher order trees and doubling the input capacity of the previous network by converting the former output trees to input trees. Increasing the size by this means is much easier than the reassignment of links required when symmetric type networks grow.

#### V. SERIAL PERMUTATION NETWORKS

The nested tree type link network is nonsymmetric. Other nonsymmetric arrangements of reversing devices have been proposed to

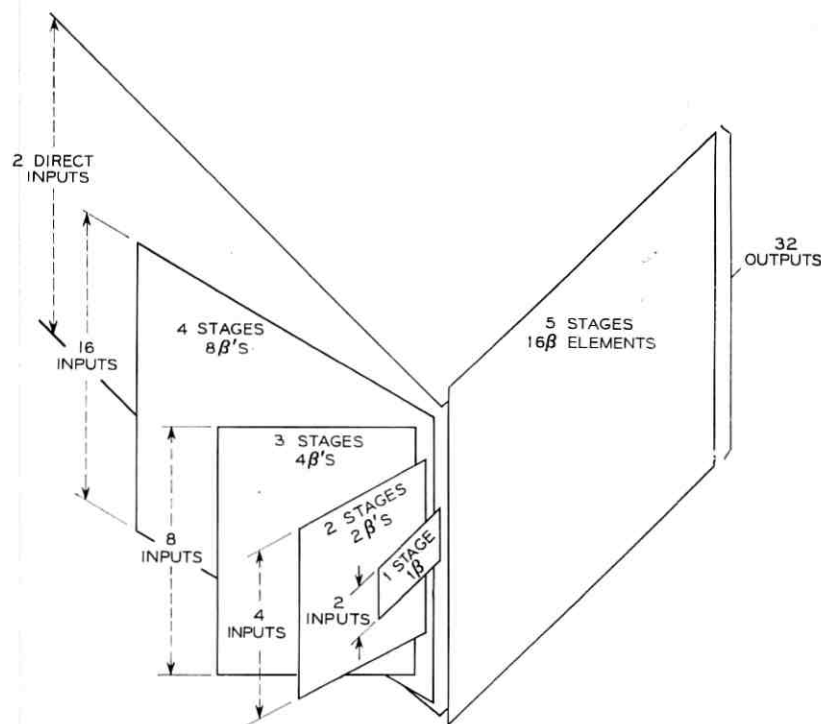


Fig. 9—Pictorial concept of "nested tree" type  $32 \times 32$  network of  $\beta$  elements.

form permutation networks.<sup>5</sup> These networks are serial in character as contrasted to the link type.

As shown in Fig. 10, assuming a permutation generator of  $P_{N-1}$ , then  $(N-1)$   $\beta$  elements will insert the  $N^{\text{th}}$  lead into the permutation to produce  $P_N$ . The total  $\beta$  arrays per input for  $N$  inputs would be

$$\frac{N-1}{2}$$

For  $N=4$  a complete network of 3 stages derived in this manner is shown in Fig. 11. For  $N > 4$ , serial networks of this type require more  $\beta$  elements than the link type. However, these networks are more readily adaptable to networks where  $N$  is small, where  $N$  is not a power of 2, and to obtain network growth in one dimension. However, growth is expensive since when  $N$  inputs are present the addition of another input requires  $(N-1)$   $\beta$  elements.

Since the  $(N-1)$   $\beta$  elements are operated in only  $(N-1)$  combinations to achieve the desired output, then savings may be made by using combinatorial arrangements. Combinations of  $\log_2 N-1$  elements are achieved by trees of  $N-1$  stages where the several  $\beta$  elements of a stage may be actuated by the same magnet. Thus, for the third stage of Fig. 11, we have Fig. 12, where the two of the  $\beta$  elements are actuated by the same magnet.

For  $N=8$ , although 33  $\beta$  elements would be required (almost twice the number required for a link type network) one less magnet would be required, 17 instead of 18. As  $N$  increases the magnet savings become large, but generally it is impractical to actuate the large number of  $\beta$  elements required for the higher order stages.<sup>6</sup> For  $N=1024$ , for example, the last stage would require 10 relays, 3 of which would actuate 128, 256, and 512  $\beta$  elements, respectively.

The smaller the number of paths through an array or switch of a

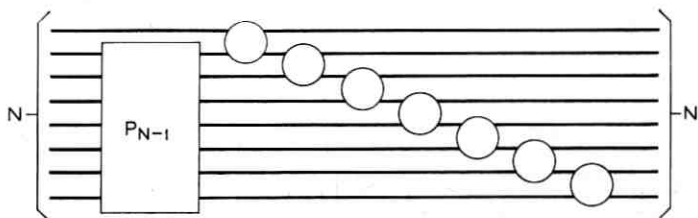


Fig. 10—Serial permutation network extension.

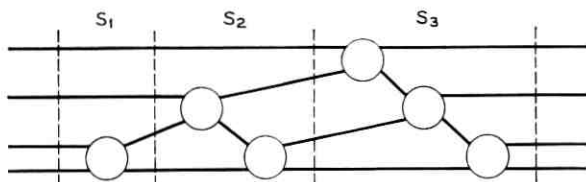


Fig. 11 — Three stage serial  $4 \times 4$  network of  $\beta$  array.

switching stage, the fewer existing elements of a permutation are disturbed by rearranging. The smaller the switches, the greater the number of stages required. However, the number of stages does not increase as rapidly as the switch size decreases. The  $\beta$  array is ideal for rearrangeable switching networks, and the  $\beta$  array is a contribution to keeping the number of operating elements (magnets) small.

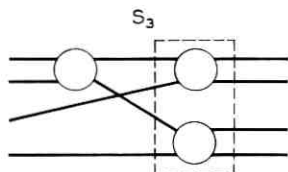


Fig. 12 — Stage 3 of serial  $4 \times 4$  network combining  $\beta$  elements.

#### VI. A NETWORK DEVICE

The  $\beta$  elements in the various arrays just described may be thought of as crosspoints in a coordinate device. For example, the  $8 \times 8$  network has 4 rows and 5 columns of  $\beta$  elements. A  $4 \times 5$  coordinate device could be built which has 4 select and 5 hold magnets or operating elements, like a crossbar switch. First the select elements would be operated in combination to prepare to change the state of  $\beta$  elements in a particular column. Then the column operating element would reset the  $\beta$  elements in this combination. In five such steps the entire  $8 \times 8$  network would be reconfigured. For such a large array as a  $1024 \times 1024$  symmetrical network 19 steps would be required.

Crossbar switches with vertical multiples divided such as in Fig. 2c, could be used as network devices in this sense. The interstage link wiring would be between verticals. A  $128 \times 128$  network requires 769  $\beta$  elements. A 10 horizontal crossbar switch provides 5  $\beta$  elements per vertical so that 16  $10 \times 10$  switches would implement this size

rearrangeable network. This compares with 30 10-vertical crossbar switches for the more familiar three-stage network of  $10 \times 10$  switches for a  $100 \times 100$  rearrangeable network.

Nonblocking networks without interruptions caused by rearrangeability can be made from rearrangeable networks by extension of switch sizes to a full Clos network. For a  $100 \times 100$  network, 20  $10 \times 19$  and 19  $10 \times 10$  switches are required. Nonblocking without interruption may also be achieved by alternately using two permutation networks connected in parallel. For the  $128 \times 128$  network only 36  $10 \times 10$  switches with divided vertical multiples would be required in this configuration.

#### VII. SUMMARY

The  $\beta$  element reduces the number of devices required to implement rearrangeable switching networks. In particular, networks consisting of nested trees of these elements produce minimal permutation switching networks. Crossbar switches or similar coordinate devices may be used to implement networks made of  $\beta$  arrays. Two permutation networks in parallel are equivalent of a nonblocking switching network without rearrangement.

#### REFERENCES

1. Beneš, V. E., "Permutation Groups, Complexes, and Rearrangeable Connecting Networks," B.S.T.J., 43, No. 4, part 2 (July 1965), pp. 1619-1640.
2. Joel, Jr. A. E., "Relay Permutation Type Switching System," U S. Patent 2,625,610, applied for December 5, 1947, issued January 13, 1953.
3. Beneš, V. E., "Optimal Rearrangeable Multistage Connecting Networks," B.S.T.J., 43, No. 4, part 2 (July 1964), pp. 1641-1656.
4. Goldstein, L. J., and Leibholz, S. W., "On the Synthesis of Signal Switching Networks with Transient Blocking," IEEE Trans. Elect. Comm. (October 1967), pp. 637-641.
5. Moore, E. F., "Relay Selecting Circuit," U S. Patent 2,864,008, applied for December 28, 1955, issued December 9, 1958.
6. Shannon, Claude E., "Memory Requirements in a Telephone Exchange," B.S.T.J., 29, No. 3 (July 1950), pp. 343-349.

## Contributors to This Issue

E. T. BAYLISS, B.S.E.E., 1961, and M.S., 1962, both from Oregon State University; Bell Telephone Laboratories, 1962—. Mr. Bayliss has worked on methods of antenna pattern synthesis with special application to large array antennas. He is engaged in system engineering and design of radars and interceptors for ballistic missile defense. Member, Eta Kappa Nu, Pi Mu Epsilon, Sigma Tau, IEEE.

H. RICHARD BEURRIER, Diploma in Radio Engineering, Valparaiso Technical Institute, Valparaiso Ind., 1954; Bell Telephone Laboratories, 1954—. Mr. Beurrier has worked on circuits applied to ultrasonic transmission systems. More recently he has been concerned with vhf and uhf network systems applied to transistor circuits to effect unusually large power capability.

TA-SHING CHU, B.S., 1955, National Taiwan University; M.S., 1957, and Ph.D., 1960, Ohio State University; Bell Telephone Laboratories, 1963—. Mr. Chu has been concerned with problems involving electromagnetic wave propagation and microwave antennas. Member, IEEE, Commission 2 of URSI, American Physical Society, Sigma Xi, Pi Mu Epsilon.

JAMES C. DALY, B.S., 1960, University of Connecticut; M.E.E., 1962, and Ph.D., 1967, Rensselaer Polytechnic Institute; faculty member of the Electrical Engineering Department at Rensselaer, where he taught and did research on bulk semiconductor microwave interactions, 1962-1966. Bell Telephone Laboratories, 1966—. He is now concerned with optical wave guidance. Member, IEEE, Tau Beta Pi, Eta Kappa Nu, Sigma Xi.

ALLEN N. FRIEDMAN, B.S., 1956, City College of New York; M.S., 1958, Yale University; Ph.D., 1964, Columbia University; Bell Telephone Laboratories, 1961—. Mr. Friedman first studied the properties of metallic magnetic materials, then became involved in exploratory development of devices between optical and subaudio frequencies. Recently he has been concentrating on vhf and uhf devices. Member, American Physical Society and its Solid State section, Phi Beta Kappa, Sigma Xi.

DETLEF GLOGE, Dipl. Ing., 1961, D.E.E., 1964, Braunschweig Technische Hochschule (Germany); research staff, Braunschweig Technische Hochschule 1961-1965; Bell Telephone Laboratories, 1965—. In Braunschweig, Mr. Gloge was engaged in research on lasers and optical components. At Bell Telephone Laboratories, he has concentrated in the study of optical transmission techniques. Member, VDE, IEEE.

D. C. HOGG, B. Sc., 1949, University of Western Ontario; M. Sc., 1950, Ph.D., 1953, McGill University; Bell Telephone Laboratories, 1953—. His work has included studies of artificial dielectrics for microwaves, diffraction of microwaves, and over-the-horizon, millimeter wave and optical propagation. Fellow, IEEE; member, Commission 2 of URSI, Sigma Xi, AAAS.

AMOS E. JOEL, JR., B.S., 1940, and M.S., 1942, Massachusetts Institute of Technology; Bell Telephone Laboratories, 1940—. Mr. Joel did relay engineering, crossbar system testing, fundamental development studies of telephone switching systems, design of circuits for early relay digital computers, and preparation of texts to teach switching design.

Later he was concerned with designing automatic message accounting computer circuits, making fundamental engineering studies of new switching systems, and was head of a department responsible for the development planning of the Bell System's first electronic telephone switching systems. Mr. Joel was Director of Bell Laboratories' Common Systems Switching Laboratory from 1961 to 1967. Mr. Joel is now a Switching Consultant at Bell Laboratories. He holds some 50 patents, among which is the largest U. S. patent ever issued (its 884 pages cover a machine to automatically compute the cost of each toll call).

He has been active in national and local IEEE affairs, is a member-at-large of its Communication Technology Group, chairman of its Meetings Committee, and member of its Communication Switching Committee. Member, Sigma Xi, Association for Computing Machinery, AAAS.

PETER KAISER, Diplom Ingenieur, 1963, Technische Hochschule, Munich, Germany; M.S., 1965, and Ph.D., 1966, University of California, Berkeley; Bell Telephone Laboratories, 1966—. At Berkeley, Mr. Kaiser was working on frequency independent antennas. He now is engaged in optical transmission research with emphasis on gas lens beam waveguides. Member, IEEE.

R. E. PARKIN, B.Sc. (Eng.), 1962, Ph.D., 1965, Imperial College (University of London); Bell Telephone Laboratories, 1965—. Mr. Parkin is concerned with computer-aided design techniques applied to telephone development, with particular emphasis on hybrid integrated technology. Associate Member, IEE.

H. SEIDEL, B.E.E., 1943, City College of New York; M.E.E., 1947, and D.E.E., 1954, Brooklyn Polytechnic Institute; Bell Telephone Laboratories, 1953-1961, 1962—. He has been concerned with microwave ferrite propagation studies and parametric amplification in solid-state devices, and active networks in high through microwave frequencies.

WILLIAM H. STEIER, B.S.E.E., 1955, Evansville College; M.S.E.E., 1957, and Ph.D. (E.E.), 1960, University of Illinois; Bell Telephone Laboratories, 1962—. Mr. Steier first worked on the millimeter wave circular waveguide transmission system. More recently he worked on optical transmission lines and gas lenses. Member, IEEE, Sigma Xi.

AARON D. WYNER, B. S., 1960, Queens College; B.S.E.E., 1960, M.S., 1961, and Ph.D., 1963, all from Columbia University; Bell Telephone Laboratories, 1963—. Mr. Wyner has been engaged in research in various aspects of information theory. He is also adjunct associate professor of electrical engineering at Columbia University and Chairman of the Metropolitan New York Chapter of the IEEE Information Theory Group. Member, IEEE, SIAM, Tau Beta Pi, Eta Kappa Nu, Sigma Xi.

